Investigation on transport and magneto-transport properties of 3d transition metal based compounds

Thesis submitted for the award of the degree of

Doctor of Philosophy (Science)

in

Physics (Experimental)

By

Sudipta Chatterjee

Department of Physics

University of Calcutta

2023

Dedicated to my Parents and Sister…

Acknowledgment:

I would like to take this opportunity, as I submit my Ph.D. thesis, to express my sincere gratitude to all of the kind individuals who have supported me throughout the past five and a half years of my academic career at the S. N. Bose National Centre for Basic Sciences.

First and foremost, I would like to express my heartfelt thanks to my supervisor, *Prof. Kalyan Mandal*, for his constant supervision and guidance during my research work and the Ph.D. thesis, which would not have been possible without his invaluable assistance. His constant encouragement to accept the challenges of conducting research in various disciplines has enhanced my experimental skills. I am also thankful to him for giving me the freedom to plan my experiments, which turned out to be very valuable in the end. It is a great pleasure to have a supervisor like him.

I sincerely thank my joint supervisor *Dr. Barnali Ghosh (Saha)* for her constant guidance and support during my research work. Her invaluable advice and guidance will undoubtedly show me the proper direction in my future career and life. She has helped in every way, including with my personal issues, and I am lucky to work with someone as kind as her. I am also very grateful to *Prof. A. K. Raychaudhuri* for his constant support and guidance over these years. His guidance has always inspired my attitude toward research. The mentoring that I received from him has helped me both professionally and personally. I am fortunate enough to work with a scientist like him.

I want to express my sincere gratitude to *Prof. Manoranjan Kumar* and *Dr. Nitesh Kumar* for their constant encouragement and guidance during the last phase of my Ph.D. thesis. The discussions I had with them always helped me to think more clearly. I would like to thank *Dr. V. Raghavendra Reddy* at UGC-DAE, Indore for his help in the high-resolution XRD measurements. I am also very thankful to *Prof. Achintya Singha* at Bose Institute, Kolkata for his kind help in the Raman spectroscopy measurements. I must thank *Prof. Priya Mahadevan* and *Dr. Nitesh Kumar* for their valuable suggestions during my academic talk at S. N. Bose Centre. I am grateful to my B.Sc. teachers *Dr. Sukanya Dasgupta (S.D.G.)* and *Dr. Saugata Bhattacharya* who inspired me to take this journey. I am particularly grateful to *S.D.G.* mam for her invaluable support in my tough times. I am also indebted to my M.Sc. teacher *Prof. Debnarayan Jana*, who helped me tremendously at the start of my research career and is still helping me whenever it is necessary. I am thankful to *Dr. Dirtha Sanyal* from VECC, Kolkata for allowing me to do the superconductivity experiment in his lab during my M.Sc. project at VECC. I consider myself very lucky to have had such excellent professors throughout my academic career.

I am thankful to *Dr. Ravindra Singh Bisht (Ravi da), Saheli*, *Jyotirmay*, *Parushattom*, *Subrata da*, and *Avisek da* for collaborating on different projects. I was very fortunate to have a senior like *Ravi da*, who helped me a lot at the beginning of my research career and is still helping me in my academia and beyond. In my final days, I am glad to have juniors like *Sridhar* and *Sourav*. The late-night chats with them are something I will miss a lot.

Apart from my lab mates, I want to express my gratitude to *Akash da*, *Sayan*, *Satyaki*, *Nikhilesh*, *Satyabrata*, *Anirban*, and *Kali da* for making these years very special. Normal words of gratitude fall short in light of *Akash da's* unwavering love and encouragement. He is like an elder brother to me, someone who is always there to listen and with whom I have shared countless unforgettable moments over these years. I will never forget the late-night chats I had with *Sayan* both within and outside the campus, especially during the Covid periods.

I am grateful to all the technical staff, especially *Shakti da*, *Urmi di*, *Debarghya da*, *Sourav da*, *Amit da*, and *Joy da* for their unfailing assistance during sample characterization and measurements. I thank the student mess, institute canteen, kitchen team, all the group-D staff, and security staff who worked tirelessly to make our campus life healthy, clean, and safe.

Last but not least, I would like to express my deepest respect and gratitude to all of my family members, particularly, my mother (*Maa*), father (*Bapi*), and my sister, *Piu* for their unconditional support, blessings, and care. All of my accomplishments come from my parents, who had to go through a lot of hard times and make a lot of sacrifices to make me who I am now. *Piu* is not just my sister, but also my strength in difficult times. I would also like to thank *Saheli* in particular for always being there for me and letting me take her for granted. I endow my heartiest respect to my uncle (*Alok Das*), *aunty*, and my younger brother, *Saptarshi* for their endless love, support, and care. *Saptarshi* is more than a brother to me; he is also my best friend. He is always there for me during my tough times. A warm thanks to *Pisi*, and *Ammi* for their boundless affection and blessings. The culmination of all these people's blessings, support, affection, and good wishes is the outcome of this Ph.D. thesis that I am about to submit.

Finally, I want to thank the *almighty God* for holding my hand through the ups and downs of my life throughout this amazing journey.

With regards,

Sudipta Chatterjee
S. N. Bose National Centre for Basic Sciences
Kolkata, India
September 2023

List of publications:

[1] Sudipta Chatterjee, Ravindra Singh Bisht, V. Raghavendra Reddy, and A. K. Raychaudhuri**,** "Emergence of large thermal noise close to a temperature-driven metal-insulator transition" *Phys. Rev. B 104, 155101 (2021).*

[2] Ravindra Singh Bisht, Sudipta Chatterjee, Sreyan Raha, Achintya Sinha, D. Kabiraj, D. Kanjilal, and A. K. Raychaudhuri, "Disorder-induced crossover of Mott insulator to weak Anderson localized regime in an argon-irradiated $NdNiO_3$ film" *Phys. Rev. B 105, 205120 (2022).*

[3] Sudipta Chatterjee, Jyotirmay Sau, Subrata Ghosh, Saheli Samanta, Barnali Ghosh, Manoranjan Kumar, and Kalyan Mandal, "Anomalous Hall effect in topological Weyl and nodal-line semimetal Heusler compound Co_2VAl" *J. Phys.: Condens. Matter 35, 035601 (2023).*

[4] Sudipta Chatterjee, Jyotirmay Sau, Saheli Samanta, Barnali Ghosh, Nitesh Kumar, Manoranjan Kumar, and Kalyan Mandal, "Nodal-line and triple point fermion induced anomalous Hall effect in topological Heusler compound Co_2CrGa" *Phys. Rev. B 107, 125138 (2023).*

List of Publications apart from the thesis work:

[1] Parushottam Majhi, Sudipta Chatterjee, Ravindra Singh Bisht, V. Raghavendra Reddy, Barnali Ghosh, and A. K. Raychaudhuri, "Diffused metal-insulator transition in $NdNiO_3$ film grown on $BaTiO_3$: Likely evidence of electronic Griffiths phase" *Phys. Rev. Materials 5, 085005 (2021).*

[2] Saheli Samanta, Subrata Ghosh, Sudipta Chatterjee, Kalyan Mandal "Large magnetocaloric effect and magnetoresistance in Fe-Co doped $Ni_{50-x}(FeCo)_xMn_{37}Ti_{13}$ all-d-metal Heusler alloys" *J. Alloys Compd. 910, 164929 (2022).*

[3] Avisek Maity, Sudipta Chatterjee, A. K. Raychaudhuri, and Barnali Ghosh "Gated Photodetector with a Bipolar Response from Single-Crystal Halide Perovskite Using a Polymeric Electrolyte as the Gate Dielectric" *ACS Appl. Electron. Mater. 4, 4298 (2022).*

[4] Saheli Samanta, Sudipta Chatterjee, Subrata Ghosh, and Kalyan Mandal, "Large reversible magnetocaloric effect and magnetoresistance by improving crystallographic compatibility condition in Ni(Co)-Mn-Ti all-d-metal Heusler alloys" *Phys. Rev. Materials 6, 094411 (2022).*

[5] Saheli Samanta, Sudipta Chatterjee, Jayee Sinha, and Kalyan Mandal, "Giant reversibility of magnetoresponsive properties in all-d-metal Ni-Co-Mn(Cu)-Ti Heusler alloys: Role of phase fraction assisted magnetostructural transition" *Phys. Rev. Materials 7, 084406 (2023).*

List of attended conferences:

[1] **QMAT-2020**, S. N. Bose National Centre for Basic Sciences, Kolkata (oral presentation).

[2] **ICTCMS-2021**, S.N. Bose National Centre for Basic Sciences, Kolkata.

[3] **QMAT-2022**, IIT Kanpur, Uttar Pradesh (oral presentation).

[4] **Focussed Meeting on Quantum Materials-2023,** S. N. Bose National Centre for Basic Sciences, Kolkata.

Table of Contents

Chapter 1 Introduction

In this chapter, we discuss the fundamentals of metal-insulator transition and the anomalous Hall effect in the context of rare-earth nickelates and Heusler alloys. A brief review has been given on some exotic and novel properties of rare-earth nickelates and Co_2-based topological Heusler alloys. An overview of the thesis is also presented to highlight the main observations made in this thesis.

1 Introduction

1.1 Preface

Transition metal-based compounds are unambiguously the main area of interest and the foundation for a large field of physical phenomena: the physics of strongly correlated electrons. They exhibit a variety of fascinating phenomena, like metal-insulator transition (MIT), colossal magnetoresistance, multiferroicity, high-temperature superconductivity, etc [1]. Recently, they have also attracted particular interest due to their topologically non-trivial band structure which leads to various exotic transport properties such as the anomalous Hall effect (AHE), anomalous Nernst effect, Fermi arc surface states, and chiral anomalies [2–10]. The key factor determining the diversity of behavior of these materials is that their electrons can be in two conceptually quite distinct states: they can be either localized at corresponding ions or delocalized, itinerant, as in normal metals. The focus of this thesis is primarily on two particular phenomena in 3d transition metal-based compounds: the MIT and the AHE.

The phenomena of MIT, where a metal with delocalized electrons makes a transition to an insulating state with strongly localized electrons, is one of the oldest topics in condensed matter physics, yet it is also one of the most fundamentally least understood problems. A variety of systems, including oxides, chalcogenides, and doped semiconductors, exhibit MIT [11–19]. In contrast to elemental materials, the physical properties of systems near MIT evolve dramatically with changes in control parameters such as carrier concentration, temperature, pressure, or external magnetic field [14,18,20–26]. Historically, the field of MIT progressed in two major directions. One direction is the correlation-driven Mott transition [27], where strong electron correlation leads to the splitting of the density of states (DOS) at the Fermi level (E_F) and $N(E_F) \rightarrow 0$. These types of transition are generally first-order in nature and the MIT is observed as a function of temperature. The other broad direction is the disorder-driven Anderson transition, where the electronic states close to the E_F are localized although $N(E_F)$ remains finite, i.e., $N(E_F) \neq 0$ [18,28,29]. In general, the concept of a mobility edge is used to distinguish between extended and localized states in the energy space. These types of transition are generally second-order in nature, and often tuned by disorder and/or carrier density, which tune the mobility edge and E_F, respectively. In recent years, there has been a convergence of

the two directions known as the Mott-Anderson transition, in which both disorder and correlation are present [17,30,31]. It has been also demonstrated that the existence of disorder in a Mott transition significantly modifies the $N(E_F)$ [32].

The perovskite rare-earth nickelates, with the generic formula $RNiO_3$ (where R is a lanthanide rare-earth), are a large class of solids for which MIT has been extensively studied due to the strong correlations between the charge, spin, and lattice degrees of freedom [14,15,19]. The rare-earth nickelates show a temperature-driven MIT from a high-temperature orthorhombic (Pbnm) metallic phase to a low-temperature monoclinic ($P2_1/n$) insulating phase, with the exception of $LaNiO_3$, which is rhombohedral ($R\bar{3}c$) and a paramagnetic metal at all temperatures in the bulk [15]. Despite numerous experimental and theoretical studies on MIT in rare-earth nickelates, there are still several fundamental aspects that require a better understanding, such as the issue of slow relaxations, the consequences of electronic phase separation, and the nature of fluctuation dynamics close to MIT temperature. In this thesis, we have studied some of these emerging aspects of MIT in perovskite rare-earth nickelates.

Another phenomenon that we have studied in this thesis is the AHE in cobalt (Co_2)-based ferromagnetic full Heusler compounds (hereafter we will use the word Co_2-based for "cobalt-based" in this whole thesis). The AHE appears in solids with broken time-reversal symmetry, typically in a ferromagnetic phase, as a consequence of spin-orbit coupling (SOC) [33]. The origin of AHE in magnetic materials is one of the most intriguing aspects of condensed matter physics, and the intrinsic or extrinsic contribution of the AHE is still very elusive. In ferromagnetic materials, in addition to the ordinary Hall effect resulting from the Lorentz force deflecting moving charge carriers in a magnetic field, there is an anomalous term that is proportional to spontaneous magnetization [33]. The AHE in these compounds arises by either an intrinsic mechanism [34] that can be explained by the Berry phase effect of the occupied electronic Bloch states [35,36] or an extrinsic mechanism which can be explained by asymmetric scattering of the conduction electrons in the presence of SOC or impurities [37–39]. For a long time, it was considered that anomalous Hall conductivity (AHC) scaled with the magnetization of the sample. According to this concept, any ferromagnetic material possesses an AHE, but it is zero for an antiferromagnet due to magnetic sublattice compensation. Therefore, the AHE has been regarded as the primary indicator of finite magnetization in ferromagnets. However, it was only recently discovered that the intrinsic contribution to AHE is not directly related to the sample's magnetization but, rather, arises from its net Berry curvature (BC) [40,41]. A necessary condition for a finite net BC and thus a

nonzero AHE is the absence of symmetries (e.g. time-reversal symmetry or mirror symmetry). In contrary to previous notions, it is thus possible to control the BC and the intrinsic AHE through appropriate handling of symmetries and band structures, regardless of the finite value of the magnetization [42].

Among various ferromagnetic materials, Co_2-based ferromagnetic full Heusler compounds have attracted immense interest due to their high Curie temperature and tunable electrical and magnetic properties [43,44]. Particularly, the distinctive half-metallic characteristic makes these compounds promising candidates for technological applications [45,46]. Recent band structure calculations for these compounds reveal that the inclusion of SOC results in a unique topological Weyl semimetal state with broken time-reversal symmetry [47]. Even though there exist several topological Weyl semimetals with broken inversion symmetry [48–52], the presence of such a semimetallic state in magnetic systems due to broken time-reversal symmetry is extremely rare [53,54]. The BC associated with this topologically non-trivial band structure leads to many novel and exotic magneto-transport properties [3,6–10,55]. Nevertheless, despite belonging to the same space group, $Fm\bar{3}m$, their non-trivial topological and magneto-transport properties are largely determined by their electronic band structure [2,3,7,8,10,56–58]. In this thesis, we have also studied some of these emerging topological aspects of AHE in Co_2-based ferromagnetic full Heusler compounds.

1.2 Perovskite oxides: an overview

Perovskite oxides have the chemical formula ABO_3, where A and B are the two cations, with A being larger than B, and O is an oxygen anion. The B cations are 6-fold coordinated with the oxygen anions, yielding the BO_6 octahedra that serves as the fundamental structural and functional unit of perovskites. Whereas, the A cations are 12-fold coordinated with the oxygen anions [14,59]. The ideal perovskite structure is cubic with the space group $Pm\bar{3}m$, as shown in Fig. 1.1(a). For an ideal cubic structure, the lattice parameter (a) and ionic radii of A cations (r_a), B cations (r_b), and oxygen anions (r_o) should ideally follow the relation: $a = 2(r_b + r_o) = \sqrt{2}\,(r_a + r_o)$. But, in reality, this relationship does not hold for the majority of the perovskite compounds, and structural distortions take place to optimize the ionic packing, moving the system away from the ideal cubic. The tendency to distort can be measured using the Goldschmidt tolerance factor t, which is defined as: $t = \frac{(r_a + r_o)}{\sqrt{2}(r_b + r_o)}$. Most cubic perovskite

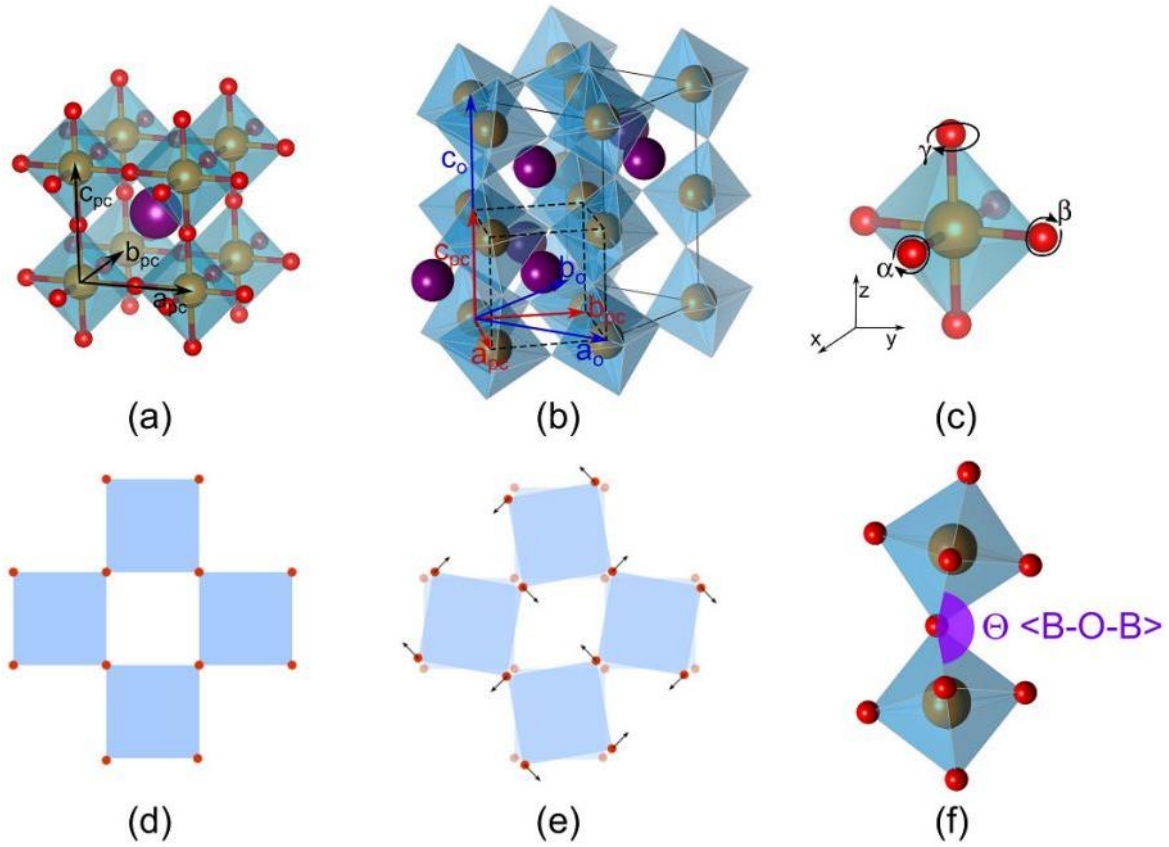

Figure 1.1: (a) and (b) Ideal cubic and orthorhombic structure of perovskite oxide. (c) The BO_6 octahedra in Glazer notation. (d) Top view of BO_6 octahedra in an ideal cubic structure. (e) Top view of BO_6 octahedra in orthorhombic structure. (f) Schematic of the <B-O-B> angle. The A cation is represented by the purple central sphere in all panels, while the B cations are represented by the orange spheres positioned at the corner of the cubic unit cell and 6-fold coordinated with the O anions (red). The image is adapted from the reference [15].

structures are stable at $0.9 < t < 1$, however, other compounds relax to rhombohedral symmetry. For $t < 0.9$, the crystal has a tendency to adopt a rhombohedral or orthorhombic structure as shown in Fig. 1.1(b). When $t > 1$, the crystal typically exhibits ferroelectric instability, and when t is increased further, it forms a hexagonal polymorph. Figure 1.1(e) depicts the octahedral tilts that result in an orthorhombic structure from a cubic structure (figure 1.1(d)). Glazer's pioneering studies [60,61] classified the symmetry-allowed rigid rotations of BO_6 octahedra in perovskite compounds, showing that the most common distortions of the BO_6 network can be described as simple octahedral rotations α, β, γ about the x, y, z principal crystallographic axes of the perovskite lattice, respectively, as shown in Fig. 1.1(c). The B-O-B bond angle (super-exchange angle), depicted in Fig. 1.1(f), which scales proportionally with

t, is commonly used to measure the degree of distortion of perovskite compounds [15]. In the next section, we will discuss a particular example of an electronic phase transition in perovskite oxides: the metal-to-insulator transition.

1.3 Metal-insulator transition

The MIT occurs when a metal with electrons that have extended wave functions enters into an insulating state with strongly localized electrons. A material can be classified as a metal or as an insulator depending on its ability to conduct electrical current at T = 0 K. Generally, the resistivity (ρ) of a metal increases with the temperature ($\frac{\partial \rho}{\partial T} > 0$), while for an insulator the ρ decreases with the temperature ($\frac{\partial \rho}{\partial T} < 0$). However, the pristine definition of a metal and an insulator is $\sigma \neq 0$ and $\sigma = 0$ respectively at $T \rightarrow 0$, where σ is the electrical conductivity [20,26]. In the next subsections, we will discuss how one can achieve a transition from metal to insulator and vice versa. Particularly, we will discuss the correlation-driven Mott and disorder-driven Anderson transitions in this context, as other MITs are beyond the scope of this thesis.

1.3.1 Correlation-driven Mott transition

In a brief description, the energy spectrum of electrons consists of energy bands with forbidden states (energy gaps) between them, and a material can be classified as a metal or insulator based on its filling. Thus, for insulators, the highest occupied band is filled, whereas, for metals, it is partially filled. Although this band theory proved successful in explaining most of the electronic transport properties of solids, several transition metal oxides having a partially full d-band, such as NiO, CoO, MnO, or FeO, are discovered to be insulators, contradicting the conventional band theory [1].

It was N. F. Mott in 1949, aiming to resolve this inconsistency, who proposed strong electron-electron correlations, in order to explain the insulating state in materials with partially filled bands [62,63]. His model consisted of a lattice with one electron occupying each site. In the absence of on-site electron-electron interactions, the atomic orbitals overlap to form a single half-filled band. When each site is occupied by two electrons, one with spin-up and one with

spin-down, the band is considered to be full. However, in the case of strong Coulomb repulsion, the energy cost of hosting two electrons on the same site can be sufficiently large to split the band into a lower band of singly-occupied sites and an upper band of double-occupied sites. With one electron per site, the bottom band will be full and the upper band empty, leading to an insulating system known as a "Mott insulator".

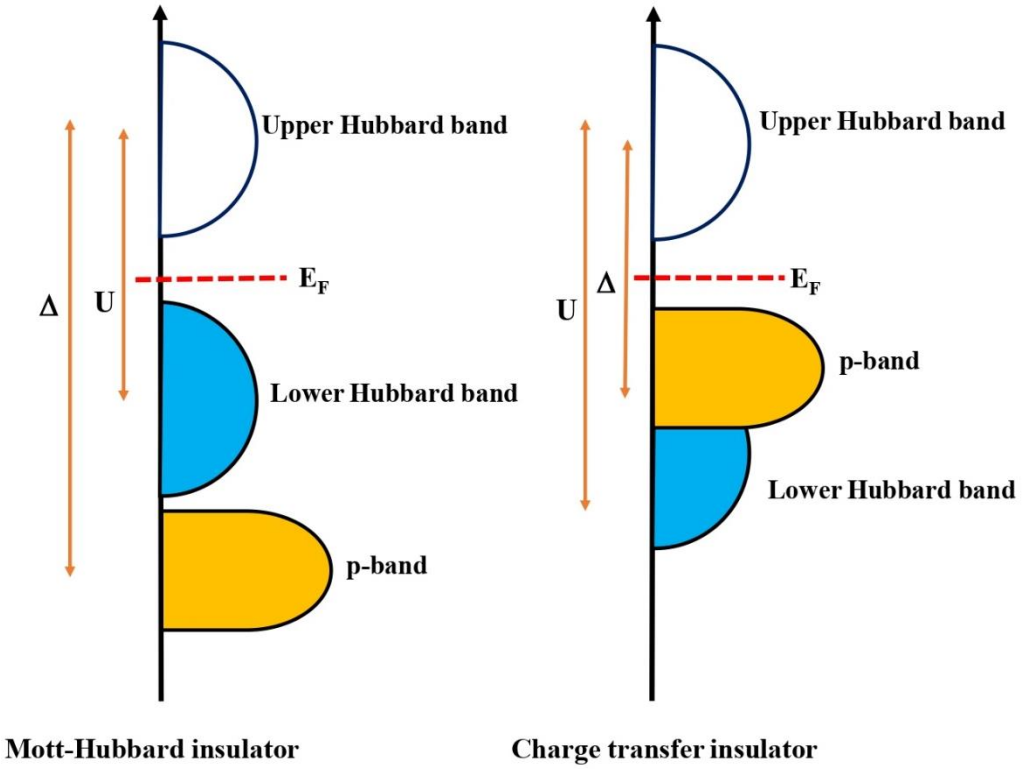

Figure 1.2: (a) Band diagram for Mott-Hubbard insulator and (b) Charge transfer insulator. The Δ stands for the charge transfer energy and U is the Coulomb repulsion.

The first theoretical model was introduced by J. Hubbard in 1963 [64] to explain Mott's idea of the insulating state, who proposed the so-called Hubbard Hamiltonian H_H.

$$H_H = -t \sum_{<ij>\sigma} C_{i\sigma}^{\dagger} C_{i\sigma} + U \sum_i n_{i\uparrow} n_{i\downarrow} \quad (1.1)$$

Where t is the hopping integral and represents the kinetic energy term, U denotes the onsite Coulomb interaction, and n denotes the number operator. The electrical state of the compound is determined by the competition between U, B (bandwidth of the d band before splitting), and t. When $\frac{U}{B} << 1$, the kinetic energy term dominates, and the system is metallic; for $\frac{U}{B} >> 1$, the onsite coulomb energy dominates, and the system is driven to an insulating state. Thus, by

tuning the $\frac{U}{B}$ ratio, a system can be driven from a metallic to an insulating state; such transitions are known as "Mott-Hubbard" transitions.

Furthermore, it has been found that the bandgap is modulated by the type of ligand associated with the transition metal ion [26]. In some transition metal oxides, the direct overlap of d-orbitals is so small that the d-electrons can hybridize with the ligand oxygen atoms. Additionally, if the oxygen p-band is located closer to the Fermi energy, the energy gap is established between the upper Hubbard d-band and the oxygen p band rather than between two d-bands. This type of insulator is known as the charge-transfer insulator, and it is discussed by Zaanen, Sawatzky, and Allen [65]. According to this scheme, cuprates and nickelates would be charge transfer insulators, while titanates and vanadates should be Mott insulators [13]. In Fig. 1.2(a), we demonstrate that when $U < \Delta$, the Mott-Hubbard picture is followed and that the p-band is below the lower Hubbard band. However, when $U > \Delta$, a gap appears between the upper Hubbard band and the ligand p-band because the LHB is below the ligand p-band; these insulators are known as charge transfer insulator and is depicted in Fig. 1.2(b).

1.3.2 Disorder-driven Anderson transition

Both Mott and band insulators were described in the context of a perfect crystal. However, in reality, crystals are never free of disorder. As the degree of the disorder increases, the material may become amorphous and lose its lattice periodicity. The question then arises as to how one would define the insulating state. To be more specific, what will be the wave function of an electron in a random potential?

In 1958, P. W. Anderson was the first to point out that the wave function can change drastically in the presence of strong disorder, i.e., in a random potential [28]. He suggested that the wave function gets localized and its envelope decays exponentially from some point in space r_0, and it can be written as, $|\Psi(r_0)| \sim \exp(|r - r_0|/\xi)$, where ξ is the localization length. Figure 1.3 (a) and (b) illustrate that in the presence of weak disorder, a Bloch wave will lose phase coherence along the length scale of the inelastic scattering length but will stay extended overall. The disorder will cause some randomness in the potential, but nearby localized orbitals will almost degenerate in energy and will thus overlap, forming an extended wave. However, if the disorder is sufficiently large, the random potential fluctuates strongly throughout the characteristic distance of orbital exponential decay, and hence nearby states are very unlikely

to have similar energies. States with similar energies may be very far apart in space, hindering any overlap and thus the formation of an extended state.

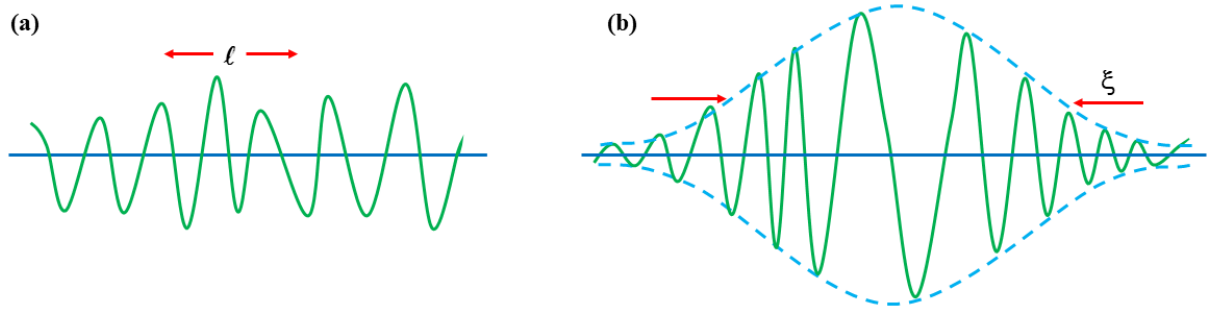

Figure 1.3: (a) The wave functions of extended state with mean free path l. (b) The wave function of localized state with localization length ξ. The figure is adapted from the reference [18].

After a brief overview and some basic knowledge of crystal structure and electronic properties in the context of MIT, in the next section, we will discuss the rare-earth nickelates ($RNiO_3$) system, which is one of the key materials investigated in the thesis.

1.4 Rare-earth nickelates ($RNiO_3$)

Rare-earth nickelates are a fascinating class of materials that displays a strong interplay between charge, spin, lattice, and orbital degrees of freedom. Nickelates are perovskite oxides with the chemical formula $RNiO_3$ where R is a trivalent rare earth R = La, Pr, Nd, Sm,..., Lu. The nickelates were first synthesized in 1971; however, they were not investigated systematically until 1991 [11,66]. Nickelates have generally been disregarded in comparison to other perovskite families such as titanates, manganites, and cuprates. One of the primary reasons for this was the difficulty in synthesizing nickelates due to the poor stability of the Ni^{3+} state at ambient pressure and high temperature [67,68]. Later, certain chemical methods were used to synthesize polycrystalline bulk nickelate samples under ambient oxygen pressure and high temperature. These compounds have a diverse set of structural and physical properties, which are described in the phase diagram as shown in Fig. 1.4. In the next subsections, we will talk more about their electrical, structural, and magnetic properties.

1.4.1 Structural, electrical, and magnetic properties of $RNiO_3$

For a long time, it was believed that the crystal structure of the $RNiO_3$ family was orthorhombic (space group $Pbnm$) in both the metallic and insulating regimes, with the exception of $LaNiO_3$,

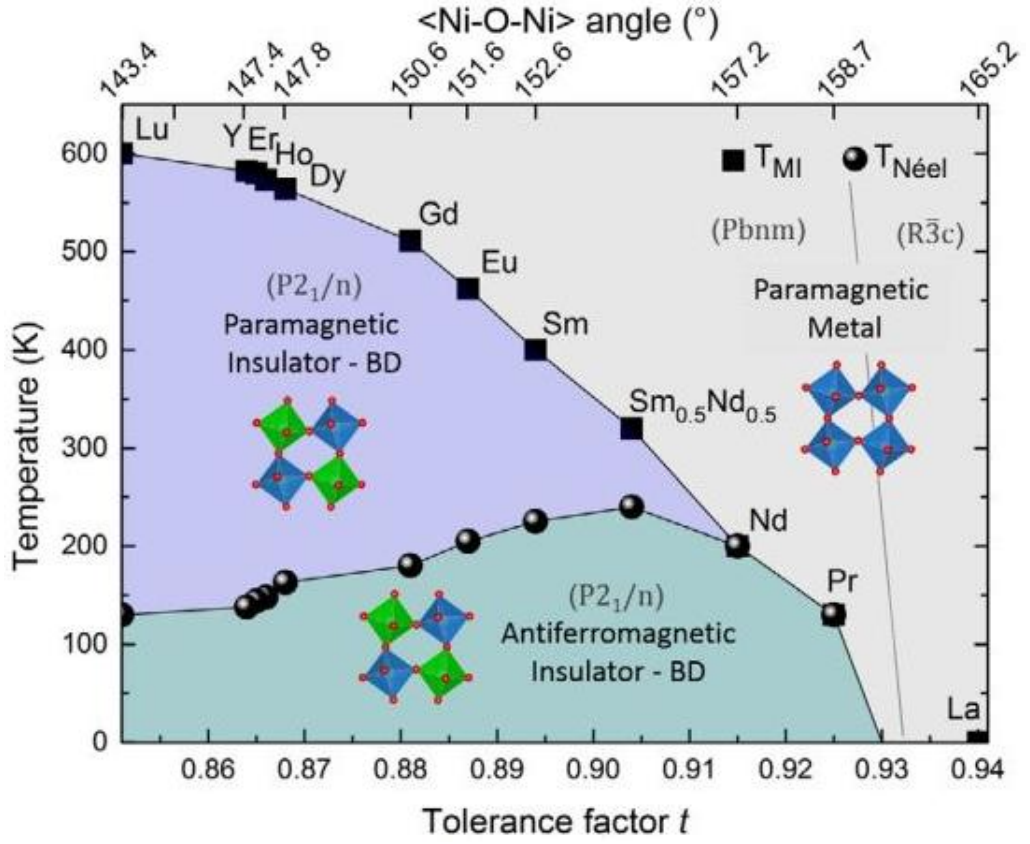

Figure 1.4: The phase diagram of rare-earth nickelates ($RNiO_3$). The image is extracted from the reference [15].

which crystallizes in a rhombohedral structure (space group $R\bar{3}C$) as shown in Fig. 1.4. Early on, it was understood that the MIT occurs simultaneously with an increase in the volume of the unit cell and that sharp MITs often involve a structural phase transition. Neutron diffraction and high-resolution X-ray diffraction measurements were used to study this phase transition. These investigations demonstrated that the insulating phase had two distinct NiO_6 octahedral groups, leading to a monoclinic distortion and the space group $P2_1/n$ [69–72].

The sharp MIT that the rare-earth nickelates exhibit when the temperature falls below a characteristic temperature, T_{MI}, that varies on the rare-earth size, except for $LaNiO_3$, which is metallic at all temperatures and is arguably one of the most remarkable characteristics of these

compounds. The MIT temperature (T_{MI}) is correlated with the extent of orthorhombic distortion in the family. As the distortion increases and the Ni-O-Ni angle decreases from 180° (as well as the tolerance factor t), the $p-d$ orbital overlap and hence the hopping strength decreases as well. As a result, the bandwidth of the system W is reduced and T_{MI} increases from ~ 100 K for $PrNiO_3$ to ~ 600 K for $LuNiO_3$ as shown in Fig. 1.4 [15,73]. In fact, one may tune the T_{MI} by selecting a combination of different rare-earth elements, such as at room temperature for the mixed compound $Nd_{0.5}Sm_{0.5}NiO_3$. Thus, the T_{MI} is strongly related to the chosen rare-earth and thus, the Ni-O-Ni bond angle.

In addition to a structural and electrical transition, a paramagnetic to antiferromagnetic transition also takes place when the temperature of $RNiO_3$ compounds is lowered. At high temperatures, $RNiO_3$ compounds are metallic and paramagnetic, whereas the insulating ground state is antiferromagnetic (shown in Fig. 1.4). On the other hand, $LaNiO_3$ remains paramagnetic at all temperatures. The spin order of these compounds is also linked to the ionic radii at the R site. For instance, when the ionic radius is considerably bigger (e.g. Pr and Nd), it exhibits both the MIT and antiferromagnetic ordering of nickel moments the transition is first-order in nature and the resistance displays hysteresis upon thermal cycling. For R ions with lower ionic radius, the antiferromagnetic transition decouples from the MIT and the Neel temperature $T_N < T_{MI}$, and hence, the system goes through two transitions: from a paramagnetic metallic to a paramagnetic insulating phase at high temperatures, and then to an antiferromagnetic insulating phase at lower temperatures [26,74]. For R ions with lower ionic radius, in the temperature-dependent resistivity curves, no hysteresis is observed [20]. In the next subsection, we will try to understand the MIT in $RNiO_3$ systems.

1.4.2 Understanding of metal-to-insulator transition in $RNiO_3$

The origin of the MIT in rare-earth nickelates and the nature of the insulating state are still being debated. Nickelates have a $3d^7$ structure with a filled t_{2g} band and one electron in the degenerate e_g band. In general, the Ni^{3+} should be Jahn-Teller active [75], which would lift the degeneracy of the e_g orbitals. This kind of lifting of degeneracy is seen in $RNiO_3$, which has smaller rare-earth ions. Interestingly, Jahn-Teller distortion has not been found for $NdNiO_3$ and $PrNiO_3$ due to their large bandwidth [76–80]. Nevertheless, it has been noted that the insulating

state and symmetry lowering are followed by the breathing mode distortion of NiO_6 octahedra, leading to two distinct NiO_6 octahedra with a small volume difference.

There are several experimental and theoretical findings that are present in the literature to understand these observations. Here, we will discuss a few of them. The well-known Zaanen-Sawatzky-Allen (ZSA) diagram places $RNiO_3$ at the boundary between low Δ metals and charge transfer insulators, implying that it has a poor metallic character [65]. The oxygen isotope experiment on $RNiO_3$ by M. Medarde *et al*. revealed that electrons and lattice interactions play a crucial role (other than bandwidth) and should be considered when studying MIT in nickelates [81]. Later infrared spectroscopy experiments confirm this hypothesis [82]. Khomski and Mazine's theoretical prediction indicated charge disproportion ($2Ni^{3+} \rightarrow Ni^{3+\delta} + Ni^{3-\delta}$) at the Ni site is responsible for the charge ordering in nickelates [79]. The experimentally observed value was found to be $0.2e$, where e is electronic charge [79]. Another work by Millis *et al*. revealed that there is no charge ordering in $RNiO_3$, holes in the oxygen cause an asymmetrical coupling of the oxygen, leading to a bond disproportion [80]. The understanding of MIT in $RNiO_3$ is constantly changing due to new hypotheses and findings [83,84]. However, the precise understanding of the insulating condition is still up for debate.

After a brief overview of the MIT and the rare-earth nickelates, in the next section, we will discuss the Heusler alloy, which is one of the important materials investigated in this thesis.

1.5 Heusler compounds: an overview

The history of one of the most fascinating material classes can be traced back to 1903 when Fritz Heusler found that an alloy with the composition Cu_2MnAl behaved like a ferromagnet even though none of its components elements are magnetic [85]. The crystal structure of Cu_2MnAl was not determined until 1934, when Otto Heusler, and Albert Bradley, independently determined the structure [86,87]. Today, Heusler compounds are a vast family of materials that include more than 1,000 compounds with various compositions and lattice structures. Heusler compounds exhibit a variety of intriguing features, including half-metallic ferromagnetism, thermoelectricity, spin-caloricity, and high spin-polarization [44,88–90]. They can also be metallic, semiconducting, superconducting, or half-metallic. The Heusler class of compounds is unique because their structure is stable for a wide range of elements that

can be replaced on any of the three different atomic sites within the unit cell. Heusler compounds have also been found to possess several topological properties in addition to the conventional ones mentioned above, such as topological superconductivity [91,92] and different magnetic topological semimetals [3,6]. Therefore, Heusler compounds have the potential for numerous technologically significant applications. Figure 1.5 depicts an overview of the various elemental combinations that can be used for making these materials [44]. In the next subsection, we will talk about the crystal structure of the Heusler compounds.

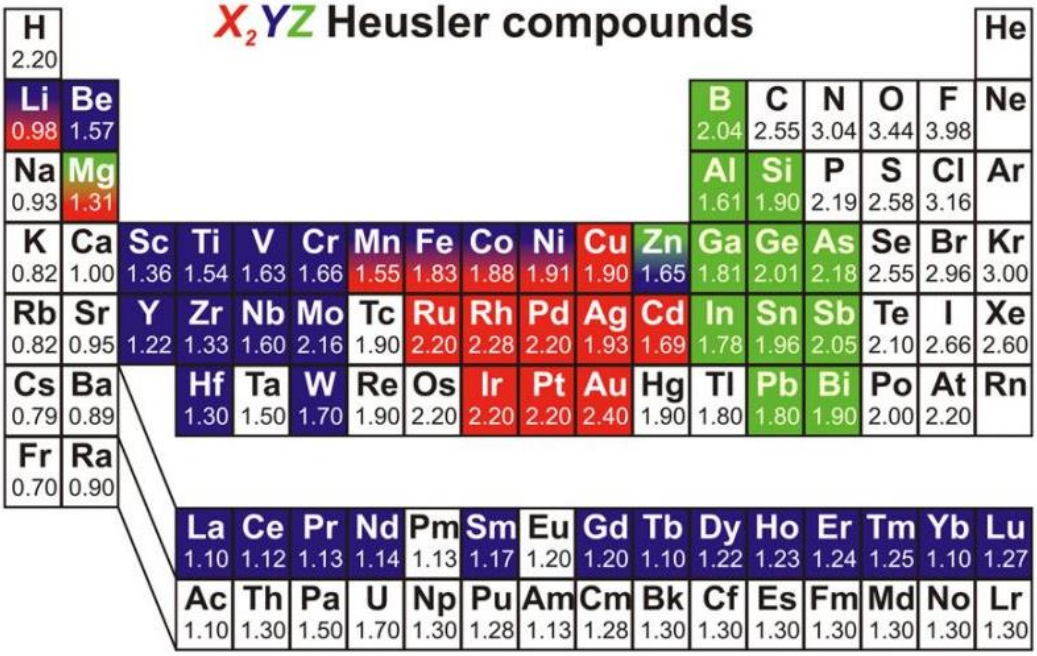

Figure 1.5: The periodic table of the elements. A large variety of Heusler materials can be obtained by combining different elements following the colour scheme. The image is taken from reference [44].

1.5.1 Crystal structure of Heusler compounds

In general, Heusler compounds have a cubic structure and either an X_2YZ (full-Heusler) or XYZ (half-Heusler) composition, where X and Y are transition metals, with X being more electropositive than Y, and Z is a main group element [10]. X atoms occupy (0, 0, 0) and (1/2, 1/2, 1/2) sites whereas Y and Z atoms occupy (1/4, 1/4, 1/4) and (3/4, 3/4, 3/4) sites, respectively. The schematic representations of different Heusler structures are shown in Fig. 1.6. Full-Heuslers can be of two types: full-Heuslers or inverse-Heuslers. Full-Heusler compounds with Cu_2MnAl ($L2_1$ structure) as the prototype, adopt the centrosymmetric $Fm\bar{3}m$ (225) space group. In contrast, inverse-Heusler with Li_2AgSb as the prototype and half-Heusler

(for which MgAgAs is the prototype) compounds have the noncentrosymmetric F$\bar{4}$3m (216) space group. After a brief overview of the crystal structure of the Heusler compounds, in the next subsection, we will discuss the Co_2-based ferromagnetic full Heusler compounds which is one of the investigating compounds in this thesis.

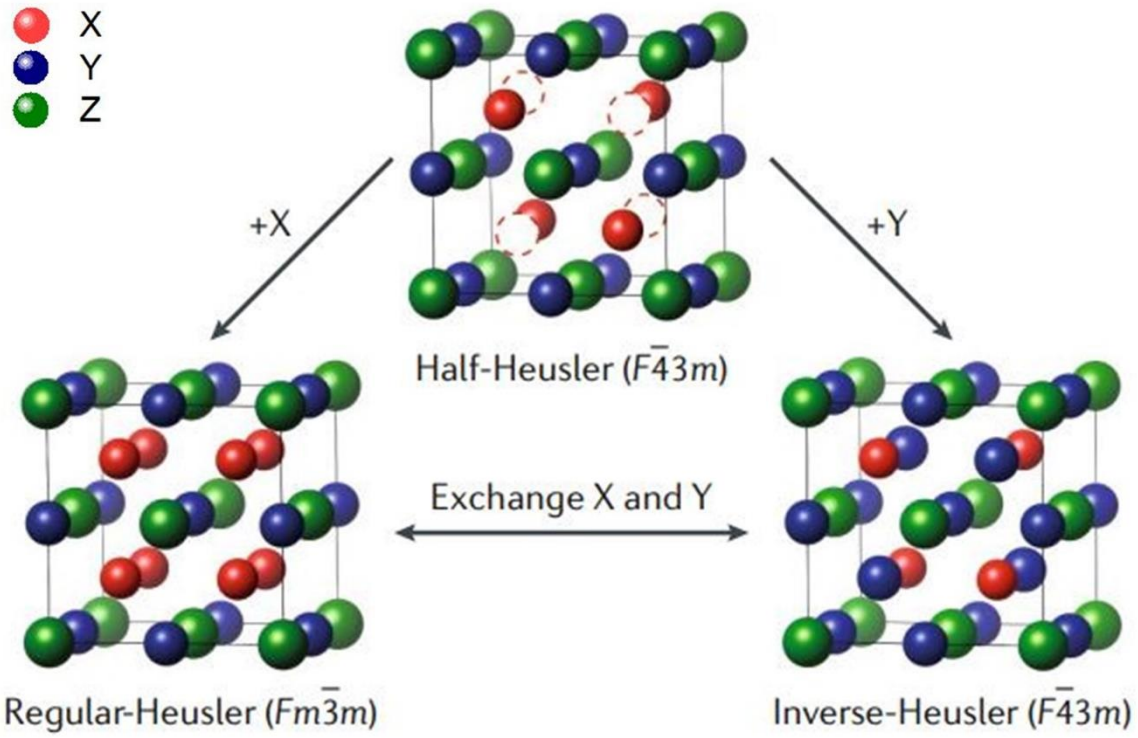

Figure 1.6: Crystal structure of full Heusler, half-Heusler, and inverse-Heusler alloys with their respective space group. The image is adapted from the reference [10].

1.5.2 Co_2-based ferromagnetic full Heusler compounds and Slater-Pauling rule of magnetization

Among these various Heusler compounds, Co_2-based ferromagnetic full Heusler compounds have attracted immense attention in recent times because of their high Curie temperature and tunable magnetic, electrical, and structural properties [44]. Especially, the unique half-metallic character makes them a promising candidate for spintronics applications. It is well-established that Co_2-based half-metallic ferromagnetic Heusler compounds obey the Slater-Pauling (SP) rule [93,94] of magnetization to predict their total spin magnetic moment, which scales linearly with the number of valence electrons [46,95]. The SP rule is a straightforward method for investigating the relationship between valence electron concentration and magnetic moments

in ferromagnetic alloys [46]. Figure 1.7 displays the SP behavior of various Heusler compounds including the Co_2-based ferromagnetic full Heusler compounds. The electronic structure of these compounds shows a minimum in the minority density of states, where the Fermi level is pinned. The minority spin density is therefore fixed at a finite value, and as a result, the number of majority electrons grows proportionally to the total number of electrons. Because of this, the magnetic moment scales linearly with the number of valence electrons.

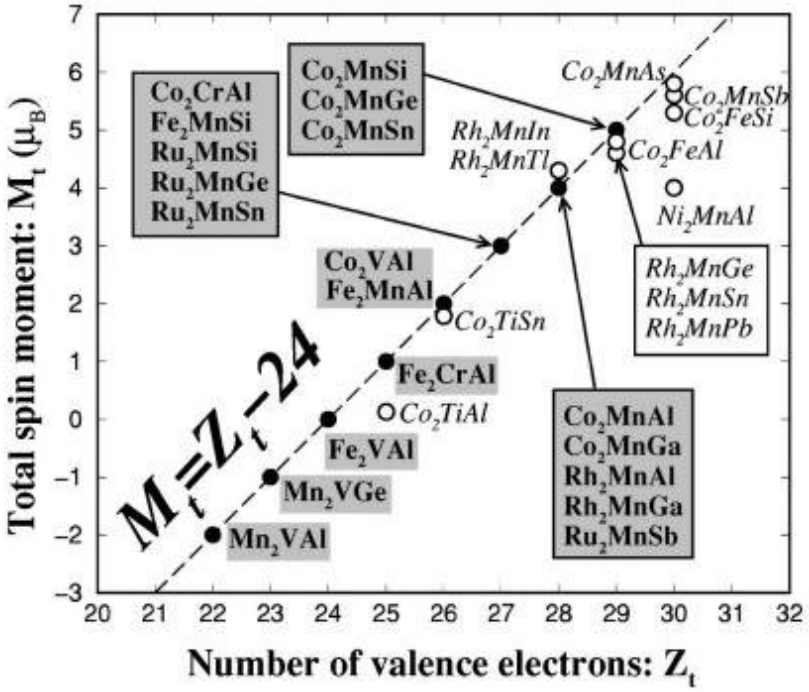

Figure 1.7: Total spin moments for various Heusler alloys. The dashed line represents the Slater-Pauling behavior. The compounds with open circles represent the deviation from the Slater-Pauling behavior. The graph is taken from the reference [46].

Co_2-based half-metallic ferromagnets also exhibit a gap in the minority density of states and the SP rule for them is given as: $m_t = Z_t - 24$, where m_t is the total magnetic moment per formula unit and Z_t is the total number of valance electrons per unit cell of the compound [46]. Recently, some of these Co_2-based ferromagnetic full Heusler compounds have also been predicted to host non-trivial topological states in their electronic band structure [47]. Therefore, Co_2-based ferromagnetic full Heusler compounds provide a perfect platform to study various exotic non-trivial topological phenomena. After a brief overview of the Co_2-based ferromagnetic Heusler compounds, in the next section, we will discuss the different topological semimetals and their important features.

1.6 Classifications of the topological semimetals

It is widely recognized that semimetals exhibit a small or vanishing density of states close to the Fermi level. Among them, there is a particular class of materials in which the three-dimensional (3D) Brillouin zone (BZ) is crossed or touched by conduction and valence bands, leading to a finite density of states. Such band touchings typically lead to a topological phase transition and can be connected to a topological invariant [96]. In other words, semimetals with band touchings are often topologically distinct from others; thus, they are referred to as topological semimetals [97–100]. Nowadays, topological semimetals have emerged as a new frontier in the field of quantum materials. In the next subsections, we briefly discuss some 3D topological semimetal phases of matter, including Weyl semimetals, Dirac semimetals, nodal-line semimetals, and unconventional fermionic semimetals beyond the Dirac and Weyl semimetals.

1.6.1 Weyl semimetal

Weyl semimetals (WSM) are a type of topological semimetal in which Weyl fermions act as low-energy quasiparticle excitations [101]. In a WSM, two singularly degenerate bands cross at distinct points, or Weyl nodes, and disperse linearly away from each Weyl node in all three momentum space directions. Weyl fermions exhibit distinctive chiralities, either left-handed or right-handed. The chiralities of the Weyl nodes produce chiral charges, which can be thought of as monopoles and antimonopoles of Berry flux in momentum space. When the opposite chiral charges are separated in momentum space, they form surface Fermi arcs [102]. The schematic of a WSM is shown in Fig. 1.8(a).

Real materials that contain the WSM state are typically further divided into inversion-symmetry-breaking WSM and time-reversal symmetry-breaking WSM. The non-centrosymmetric TaAs family of crystals is an excellent example of an inversion symmetry-breaking WSM [48,49,103–105]. The WSMs with broken time-reversal symmetry can be generally realized in ferromagnetic materials like pyrochlore irridate [55], $Co_3Sn_2S_2$ [106,107], and Heuslers [3,6]. The electrical transport and magneto-transport properties have been widely studied for different WSM materials. The linear band dispersion and non-trivial phases in the electronic band structure provide a perfect platform to investigate various non-trivial topological phenomena in various WSM materials.

1.6.2 Dirac semimetal

Dirac semimetals (DSMs) host Dirac fermions as low-energy quasiparticle excitations [101]. In a DSM, two doubly degenerate bands cross to form a Dirac node and then disperse linearly in each of the three momentum space directions away from the node. Each Dirac node can be thought of as a pair of degenerate Weyl nodes with opposite chiralities [102] (i.e. Dirac node has zero chiral charges). The schematic of DSM is given in Fig. 1.8(b). As a pair of degenerate Weyl nodes with opposite chiralities is often unstable and may annihilate, extra crystalline point group symmetries are required to achieve a stable DSM phase [108].

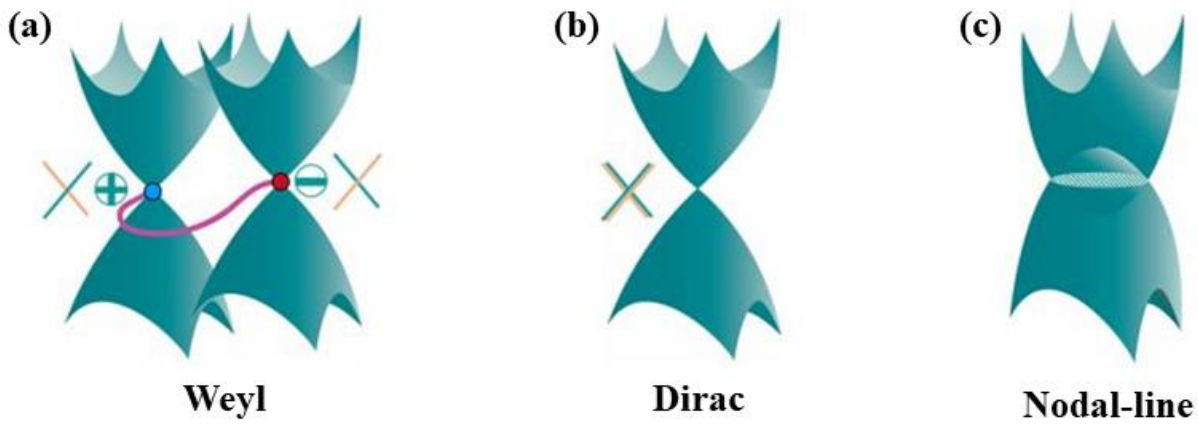

Figure 1.8: Band crossing is shown schematically for the (a) Weyl, (b) Dirac, and (c) Nodal line semimetal. In a Dirac semimetal, all bands are doubly degenerate, but in a Weyl semimetal, the degeneracy is lifted since the inversion symmetry or time-reversal symmetry has been broken. The opposing chirality of the Weyl points is denoted by positive and negative signs. The pink line shows how the surface Fermi arc connects Weyl points at the surface projection. The 2-fold and 4-fold degenerate points are represented in panels a and b, respectively, as crosses of four and two lines. In the case of a nodal line semimetal, the band crossing occurs in a line or ring, and the topological surface state is two-dimensional in nature and is referred to as the drumhead surface state. The image is taken from the reference [102].

One approach is to rely on uniaxial rotational symmetries [108]. A band inversion, in particular, can generate a pair of 3D Dirac nodes at opposing sites of the time-reversal invariant momenta. Typical DSMs of this type are Na_3Bi [109], and Cd_3As_2 [109–111]. The use of non-symmorphic symmetries, such as glide reflections and screw rotations, provides an alternative strategy. Candidates for this type of DSM include deformed spinels [112] and β-BiO_2 [113]. Additionally, the critical point of the topological phase transition between a trivial insulator

and a topological insulator can be realized as a DSM. This has been achieved in the $BiTl(S_{1-x}Se_x)_2$ [114], and $Bi_{2-x}In_xSe_3$ [115] systems.

1.6.3 Nodal-line semimetal

The valence and conduction bands of Dirac and Weyl semimetals cross at a point. However, there may be a more general situation in which the crossing happens along a line or ring that is protected by certain crystalline symmetries. In such cases, they are known as topological nodal-line or nodal-ring semimetals [101] as shown in Fig. 1.8(c). Due to spin-orbit coupling, numerous Weyl and Dirac semimetals originate from nodal lines, highlighting the generality of the nodal line. Such extended states require additional crystalline symmetries for stabilization, usually through a mirror reflection [116]. The degeneracy of the line crossings can be 2-fold, as in a Weyl semimetal, or 4-fold, as in the case of Dirac semimetal.

In addition, there are numerous variations of nodal-line semimetals based on the distinctive band structure and symmetry protection. First, nodal-lines, also known as nodal-circles, can be closed loops within the 3D BZ. Generally, these nodal-lines are formed by a band inversion. Based on symmetry protection, the nodal-lines are further divided into categories. Some nodal-lines are strictly gapless only when spin-orbit coupling is absent [97,117–119]. They are generally protected by the combination of time-reversal and inversion symmetries [97,117,119]. Cu_3N [118], Ca_3P_2 [120], and the ZrSiS family [121,122] are examples of representative materials. Alternately, in noncentrosymmetric crystals protected by a mirror plane, nodal-lines can occur. These nodal-lines maintain their stability even with the inclusion of spin-orbit coupling. $PbTaSe_2$, $TlTaSe_2$, and CaAgAs are examples of such materials [123–125]. Second, nodal-lines can also cross the BZ in a straight line such as the $BaNbS_3$ family [126]. Third, the nodal-lines are capable of building Hopf linkages and nodal-chains in k space [127]. Thus, there are various types of nodal-line semimetals and they are classified depending on their band structure and symmetry protection.

1.6.4 Unconventional fermionic semimetal

Solid-state materials also possess band crossings beyond the Dirac/Weyl semimetals. These band crossings include 3-, 4-, 6-, and 8-fold degeneracies, which are collectively referred to as "unconventional fermions" [128]. Here, we will very shortly discuss a specific type of 3-fold

band crossing, as other higher-order band degeneracies are beyond the scope of this thesis. In triple-point semimetal, three singly degenerate bands cross at distinct points known as the triple-points. These triple points are protected by a uniaxial rotating axis, mirror planes, and time-reversal symmetry. MoC, MoP, and ZrTe are some examples of such materials [129–131]. After a brief overview of the different classes of topological semimetals, in the next section, we will discuss the magnetic topological semimetals (particularly Co_2-based magnetic topological semimetals) and their exotic topological transport properties.

1.7 Co_2-based magnetic topological semimetals

Magnetic topological semimetals display remarkable quantum transport phenomena as a result of the topological structure of their electronic bands in the presence of ferromagnetic ordering, which breaks the system's time-reversal symmetry [132]. Due to the non-trivial band topology, the valence and conduction bands of magnetic topological semimetals have linear band dispersion at the crossing point, and the crossing points can form zero-dimensional discrete points, one-dimensional continuous or extended lines in the BZ.

Among the numerous magnetic topological semimetals, Co_2-based magnetic topological semimetals attracted particular interest because of their high Curie temperature and tunable non-trivial topological properties [44]. A few Co_2-based full Heusler compounds have recently been predicted to have Weyl fermions in their band structure [47]. The Berry curvature associated with this topologically non-trivial state causes a variety of exotic transport phenomena such as the AHE, anomalous Nernst effect, and chiral anomalies [3,5,6,8–10]. After an overall overview of the magnetic topological semimetals, in the next section, we will discuss the AHE which is one of the key phenomena investigated in this thesis.

1.8 Anomalous Hall effect

In 1879, Edwin Hall made a remarkable discovery that a current-carrying conductor experiences the Lorentz force, which presses its electrons against one side of the conductor [133]. Later, he claimed that the effect of his pressing electricity was ten times stronger in ferromagnetic iron than in nonmagnetic conductors [134]. Hall's discovery of a stronger effect in ferromagnetic conductors eventually became known as the anomalous Hall

effect (AHE). Although the AHE was discovered more than a century ago, its origin in magnetic materials remains one of the most intriguing aspects of condensed matter physics. The primary reason appears to be that the AHE problem includes notions based on topology and geometry that have only recently been developed. Early researchers struggled with concepts that would not become evident and fully defined until much later, such as the Berry phase [135]. What is currently known as the Berry-curvature, formerly known as Luttinger's "anomalous velocity," naturally developed in the initial microscopic theory of the AHE by Karplus and Luttinger [34].

Early on, the experimental researchers discovered that the dependency of Hall resistivity ρ_{xy} on applied perpendicular field B_z is fundamentally different in ferromagnetic and nonmagnetic conductors. In the latter, ρ_{xy} grows linearly with B_z, as predicted by the Lorentz force. However, in ferromagnets, ρ_{xy} first rises sharply in weak B_z but saturates at a high value that is almost B_z independent. After a few years, it has been observed that, in Fe, Co, and Ni, the saturation value is approximately proportional to the magnetization M_z. Soon after, Pugh (1930) and Pugh and Lippert (1932) established an empirical relationship between ρ_{xy}, B_z, and M_z [136,137],

$$\rho_{xy} = R_0 B_z + R_s M_z, \tag{1.2}$$

applicable to a wide variety of materials under various external magnetic fields. The second item represents the contribution to the Hall effect caused by spontaneous magnetization.

Unlike R_0, which was previously known to be primarily determined by carrier density, R_s was discovered to be slightly determined by some material-specific factors, including the longitudinal resistivity ρ_{xx}. In 1954, Karplus and Luttinger (KL) proposed a hypothesis for the AHE that, in retrospect, was an essential step in solving the AHE problem [34]. KL demonstrated that electrons receive an additional contribution to their group velocity when an external electric field is introduced to a solid. Because KL's anomalous velocity was perpendicular to the electric field, it may contribute to the Hall effects. In the case of ferromagnetic conductors, the anomalous velocity sum over all occupied band states may not be zero, indicating a contribution to the Hall conductivity σ_{xy}. This contribution has recently been referred to as the intrinsic contribution to the AHE since it primarily depends on the band structure and is mainly independent of scattering.

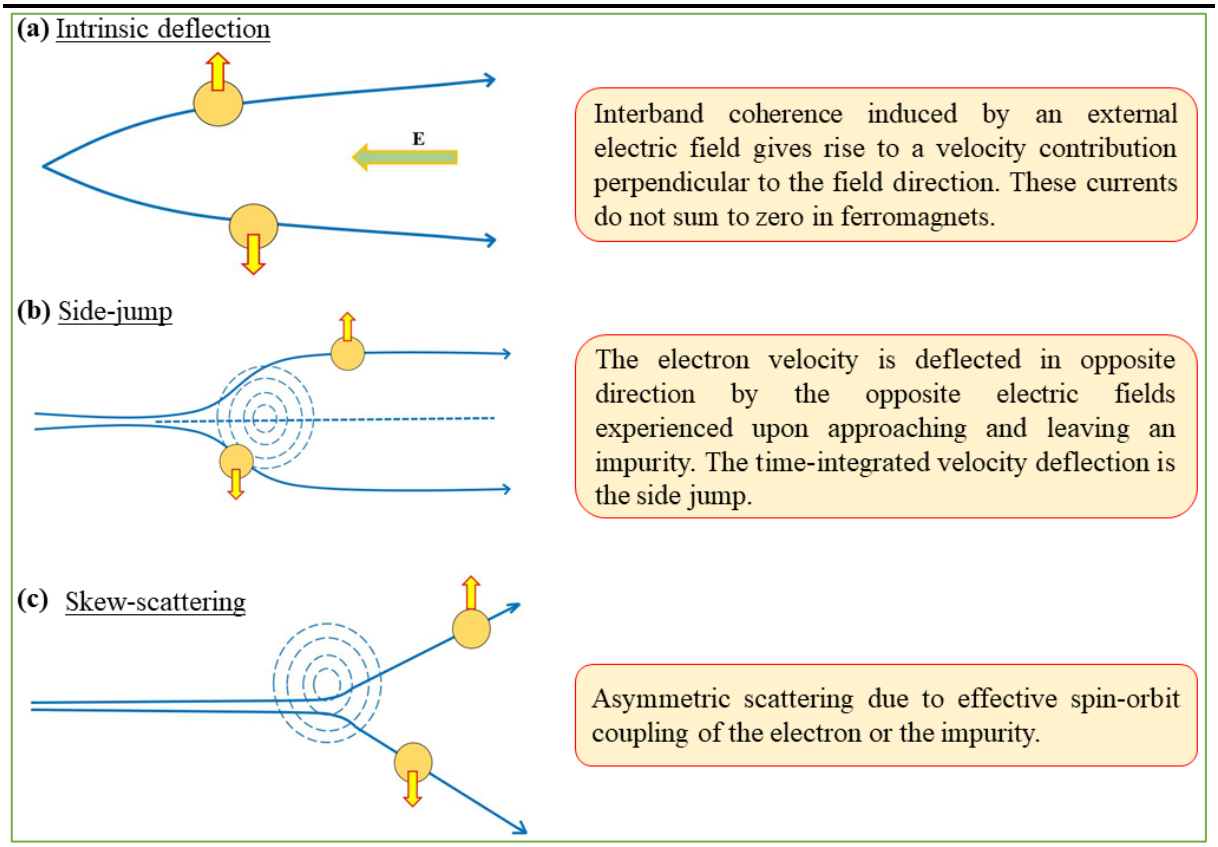

Figure 1.9: The three basic mechanisms that can result in an AHE are illustrated. All of these mechanisms affect the movement of electrons in any real material. The image is partly adapted from the reference [33].

The intrinsic AHE produces a contribution to $\rho_{xy} \approx \frac{\sigma_{xy}}{\sigma_{xx}^2}$ when the conductivity tensor is reversed, making it proportional to ρ_{xx}^2 [33]. The anomalous velocity is only dependent on the Hamiltonian of a perfect crystal and can be correlated with changes in the phase of the Bloch state wave packets when an electric field causes them to evolve in the momentum space of a crystal [119]. Nowadays, the intrinsic AHE has been explained by the Berry phase effect of the occupied electronic Bloch states [35,36].

The primary issue with the intrinsic KL theory was that the obtained Hall response contribution had no evidence of scattering from disorder. Smit and Berger's semiclassical AHE theories, on the other hand, concentrated on the role of disorder scattering in imperfect crystals [37–39]. Smit proposed that the primary source of the AHE currents was asymmetric skew scattering from impurities generated by the spin-orbit interaction. According to this AHE image, $\rho_{xy} \propto \rho_{xx}$. Berger, however, asserted that the fundamental cause of the AHE current was the side

jump that quasiparticles experienced when they were scattered by spin-orbit-linked impurities. The side-jump mechanism could be misinterpreted as the result of a KL anomalous velocity mechanism acting while a quasiparticle was subjected to an electric field caused by an impurity. The side-jump AHE current was thought to be the result of the side jumps per scattering event and scattering rate. One confusing aspect of this semiclassical theory was that all dependence on impurity density and strength appeared to have vanished. As a result, it projected $\rho_{xy} \propto \rho_{xx}^2$ with an exponent similar to that of the intrinsic KL mechanism. However, the side-jump contribution is generally very small for ferromagnetic materials [6–8]. Figure 1.9 depicts schematically the three different mechanisms of AHE.

1.9 Overview of the thesis

In this thesis work, we have investigated some physical phenomena in different 3d-transition metal-based compounds. The thesis mainly focuses on two particular phenomena namely the MIT and the AHE. We have investigated the MIT in $NdNiO_3$ and $Nd_{0.7}La_{0.3}NiO_3$ thin films and we have studied the AHE in Co_2-based ferromagnetic full Heusler compounds.

Specifically, we have addressed the following issues:

a) We have reported that close to a Mott transition there is an emergence of large thermal noise which occurs simultaneously with large flicker noise in $NdNiO_3$ thin films grown on a crystalline substrate of $SrTiO_3$ with different orientations. We have noticed that the thermal noise, which is distinct from the flicker noise, deviates from the canonical Johnson-Nyquist value of $4k_BTR$ and reaches a maximum value at a temperature T^* that is close to but distinct from the MIT temperature. We show that the large thermal noise that occurs along with the large flicker noise both arise from the slow charge carrier dynamics close to T^*. The second spectra calculation reveals strong non-Gaussian fluctuations near the T^*. We also show that the observed large thermal noise has a close dependence on the in-plane strain in the film. It has been also suggested that the co-existence of large noise (both thermal and flicker noise) owes its origin to the electronic phase separation (EPS) that exists near the MIT. A physical model has been proposed that EPS near the MIT temperature can give rise to a sparse phase of nanometric small pockets of metallic phases (nanopuddles) which are surrounded by

and embedded within the minority insulating phase. These isolated metallic nanopuddles act as a source of large noise near the MIT temperature.

b) We have observed that an introduction of disorder in a controlled way using 1 MeV argon ion irradiation, suppresses the correlation-driven MIT in $NdNiO_3$ thin films. The film makes a crossover to a heavily disordered conductor governed by weak localization (WL) and at ever higher disorder, an Anderson localized state. We show that the pristine films of $NdNiO_3$ demonstrate an MIT with the electrical conduction process being governed by variable range hopping (VRH). For disorders up to 1%, the conduction in the film exhibits WL behavior with finite conductivity at temperature $T \rightarrow 0$. At higher fluences ($\sim$ 2%) the conductivity decreases significantly but the electrical conduction follows a power-law temperature dependence with a small but finite zero temperature conductivity σ ($T = 0$) which is expected in a solid with electrons that are Anderson localized. A similar experiment has been performed in $Nd_{0.7}La_{0.3}NiO_3$ thin films. We also observe a significant suppression of non-Gaussian resistance fluctuations in the irradiated films, elucidating the suppression of the correlated nature of the charge carrier dynamics. Raman spectroscopy and x-ray measurements demonstrate that the basic integrity of the NiO_6 octahedra is conserved and the structure preserves its crystallinity.

c) Magnetic topological semimetals with broken time-reversal symmetry are very rare and have drawn significant attention due to their numerous intriguing topological properties. In this regard, the Co_2-based full Heusler compound serves as a fertile playground where various novel topological properties can be investigated. We have studied the AHE in Co_2-based ferromagnetic topological Heusler compound Co_2VAl. We observe that the anomalous Hall resistivity (ρ_{yx}^{A}) scales near quadratically with longitudinal resistivity (ρ_{xx}) and further experimental analysis implies that the AHE in Co_2VAl is dominated by the intrinsic Berry phase mechanism. Experimentally, we have found an AHC of $\sim$ 85 S/cm at 2 K with an intrinsic contribution of $\sim$ 75.6 S/cm, and it is weakly temperature-dependent. The first-principles calculations[1] reveal that the Berry curvature originated from a gapped nodal line and symmetry-protected Weyl

[1] All the first-principles calculations used in this thesis (*Chapter 5* and *Chapter 6*) has been done by the Prof. Manoranjan Kumar's group (in collaboration) at S. N. Bose National Centre for Basic Sciences, Kolkata.

nodes near the Fermi level in the presence of spin-orbit coupling is the main source of the AHE in this compound.

d) We have also studied the AHE in another Co_2-based ferromagnetic topological Heusler compound Co_2CrGa. We show that the AHE in Co_2CrGa is dominated by the intrinsic Berry phase mechanism. Experimental results reveal that the AHC is as large as ~ 569 S/cm at 10 K with an intrinsic contribution of ~ 526 S/cm. In addition to the large AHC, we have also observed an exceptionally large anomalous Hall angle of ~ 8.5% and a large anomalous Hall factor of ~ 0.23 V^{-1} simultaneously at room temperature. First-principles calculations suggest that the Berry curvature originates from the gapped-nodal line and triple point generated Weyl nodes near the Fermi level in the presence of spin-orbit coupling are responsible for the observed large AHC in this compound.

We have arranged this thesis in the following chapters:

Chapter 1: Introduction

Chapter 2: Experimental details

Chapter 3: Emergence of large thermal noise close to a temperature-driven metal-insulator transition

Chapter 4: Disorder-induced crossover of Mott insulator to weak Anderson localized regime in an argon-irradiated $NdNiO_3$ film

Chapter 5: Anomalous Hall effect in topological Weyl and nodal-line semimetal Heusler compound Co_2VAl

Chapter 6: Nodal-line and triple point fermion induced anomalous Hall effect in the topological Heusler compound Co_2CrGa

Chapter 7: Conclusion and Scope for future work

Appendix A: X-ray diffraction data of nickelates nanopowder and rocking curves of nickelates thin films

Appendix B: Scanning electron microscope and energy dispersive X-ray spectroscopy data for nickelates nanopowder and Co_2-based Heusler alloys.

References:

[1] Daniel I. Khomskii, Transition Metal Compounds, Cambridge University Press (2014).

[2] A. Husmann and L. J. Singh, Phys. Rev. B **73**, 172417 (2006).

[3] K. Manna, L. Muechler, T.-H. Kao, R. Stinshoff, Y. Zhang, J. Gooth, N. Kumar, G. Kreiner, K. Koepernik, R. Car, J. Kübler, G. H. Fecher, C. Shekhar, Y. Sun, and C. Felser, Phys. Rev. X **8**, 041045 (2018).

[4] J. Hu, B. Ernst, S. Tu, M. Kuveždić, A. Hamzić, E. Tafra, M. Basletić, Y. Zhang, A. Markou, C. Felser, A. Fert, W. Zhao, J.-P. Ansermet, and H. Yu, Phys. Rev. Appl. **10**, 044037 (2018).

[5] B. Ernst, R. Sahoo, Y. Sun, J. Nayak, L. Müchler, A. K. Nayak, N. Kumar, J. Gayles, A. Markou, G. H. Fecher, and C. Felser, Phys. Rev. B **100**, 054445 (2019).

[6] P. Li, J. Koo, W. Ning, J. Li, L. Miao, L. Min, Y. Zhu, Y. Wang, N. Alem, C.-X. Liu, Z. Mao, and B. Yan, Nat. Commun. **11**, 3476 (2020).

[7] S. Roy, R. Singha, A. Ghosh, A. Pariari, and P. Mandal, Phys. Rev. B **102**, 085147 (2020).

[8] G. K. Shukla, J. Sau, N. Shahi, A. K. Singh, M. Kumar, and S. Singh, Phys. Rev. B **104**, 195108 (2021).

[9] A. Sakai, Y. P. Mizuta, A. A. Nugroho, R. Sihombing, T. Koretsune, M.-T. Suzuki, N. Takemori, R. Ishii, D. Nishio-Hamane, R. Arita, P. Goswami, and S. Nakatsuji, Nat. Phys. **14**, 1119 (2018).

[10] K. Manna, Y. Sun, L. Muechler, J. Kübler, and C. Felser, Nat. Rev. Mater. **3**, 244 (2018).

[11] J. Torrance, P. Lacorre, A. Nazzal, E. Ansaldo, and C. Niedermayer, Phys. Rev. B **45**, 8209 (1992).

[12] G. Catalan, R. M. Bowman, and J. M. Gregg, Phys. Rev. B **62**, 7892 (2000).

[13] A. K. Raychaudhuri, Adv. Phys. **44**, 21 (1995).

[14] G. Catalan, Phase Transitions **81**, 729 (2008).

[15] S. Catalano, M. Gibert, J. Fowlie, J. Íñiguez, J.-M. Triscone, and J. Kreisel, Reports

Prog. Phys. **81**, 046501 (2018).

[16] W. Yamaguchi, O. Shiino, T. Endo, K. Kitazawa, and T. Hasegawa, Appl. Phys. Lett. **76**, 517 (2000).

[17] M. Imada, A. Fujimori, and Y. Tokura, Rev. Mod. Phys. **70**, 1039 (1998).

[18] P. A. Lee and T. V. Ramakrishnan, Rev. Mod. Phys. **57**, 287 (1985).

[19] S. Middey, J. Chakhalian, P. Mahadevan, J. W. Freeland, A. J. Millis, and D. D. Sarma, Annu. Rev. Mater. Res. **46**, 305 (2016).

[20] R. Scherwitzl, Metal-insulator transitions in nickelate heterostructures, Ph.D. thesis, University of Geneva (2012).

[21] M. L. Medarde, J. Phys. Condens. Matter **9**, 1679 (1997).

[22] N. Gayathri, A. K. Raychaudhuri, X. Q. Xu, J. L. Peng, and R. L. Greene, J. Phys. Condens. Matter **10**, 1323 (1998).

[23] E. Mikheev, A. J. Hauser, B. Himmetoglu, N. E. Moreno, A. Janotti, C. G. Van de Walle, and S. Stemmer, Sci. Adv. **1**, (2015).

[24] Y. Kumar, R. J. Choudhary, and R. Kumar, J. Appl. Phys. **112**, 073718 (2012).

[25] A. K. Raychaudhuri, K. P. Rajeev, H. Srikanth, and N. Gayathri, Phys. Rev. B **51**, 7421 (1995).

[26] Ravindra Singh Bisht, Investigation of Metal Insulator Transition in 3D Transition Metal Oxides, Ph.D. thesis, University of Calcutta, India (2019).

[27] N. F. Mott, Proc. Phys. Soc. Sect. A **62**, 416 (1949).

[28] P. W. Anderson, Phys. Rev. **109**, 1492 (1958).

[29] F. Evers and A. D. Mirlin, Rev. Mod. Phys. **80**, 1355 (2008).

[30] D. Belitz and T. R. Kirkpatrick, Rev. Mod. Phys. **66**, 261 (1994).

[31] A. Georges, G. Kotliar, W. Krauth, and M. J. Rozenberg, Rev. Mod. Phys. **68**, 13 (1996).

[32] Z. Wang, Y. Okada, J. O'Neal, W. Zhou, D. Walkup, C. Dhital, T. Hogan, P. Clancy, Y.-J. Kim, Y. F. Hu, L. H. Santos, S. D. Wilson, N. Trivedi, and V. Madhavan, Proc. Natl. Acad. Sci. **115**, 11198 (2018).

[33] N. Nagaosa, J. Sinova, S. Onoda, A. H. MacDonald, and N. P. Ong, Rev. Mod. Phys. **82**, 1539 (2010).

[34] R. Karplus and J. M. Luttinger, Phys. Rev. **95**, 1154 (1954).

[35] T. Jungwirth, Q. Niu, and A. H. MacDonald, Phys. Rev. Lett. **88**, 207208 (2002).

[36] N. Nagaosa, J. Phys. Soc. Japan **75**, 042001 (2006).

[37] J. Smit, Physica **21**, 877 (1955).

[38] J. Smit, Physica **24**, 39 (1958).

[39] L. Berger, Phys. Rev. B **2**, 4559 (1970).

[40] A. K. Nayak, J. E. Fischer, Y. Sun, B. Yan, J. Karel, A. C. Komarek, C. Shekhar, N. Kumar, W. Schnelle, J. Kübler, C. Felser, and S. S. P. Parkin, Sci. Adv. **2**, (2016).

[41] S. Nakatsuji, N. Kiyohara, and T. Higo, Nature **527**, 212 (2015).

[42] R. Shindou and N. Nagaosa, Phys. Rev. Lett. **87**, 116801 (2001).

[43] J. Kübler, G. H. Fecher, and C. Felser, Phys. Rev. B **76**, 024414 (2007).

[44] T. Graf, C. Felser, and S. S. P. Parkin, Prog. Solid State Chem. **39**, 1 (2011).

[45] R. A. de Groot, F. M. Mueller, P. G. van Engen, and K. H. J. Buschow, Phys. Rev. Lett. **50**, 2024 (1983).

[46] I. Galanakis, P. H. Dederichs, and N. Papanikolaou, Phys. Rev. B **66**, 174429 (2002).

[47] Z. Wang, M. G. Vergniory, S. Kushwaha, M. Hirschberger, E. V. Chulkov, A. Ernst, N. P. Ong, R. J. Cava, and B. A. Bernevig, Phys. Rev. Lett. **117**, 236401 (2016).

[48] B. Q. Lv, H. M. Weng, B. B. Fu, X. P. Wang, H. Miao, J. Ma, P. Richard, X. C. Huang, L. X. Zhao, G. F. Chen, Z. Fang, X. Dai, T. Qian, and H. Ding, Phys. Rev. X **5**, 031013 (2015).

[49] H. Weng, C. Fang, Z. Fang, B. A. Bernevig, and X. Dai, Phys. Rev. X **5**, 011029 (2015).

[50] S.-Y. Xu, N. Alidoust, I. Belopolski, Z. Yuan, G. Bian, T.-R. Chang, H. Zheng, V. N. Strocov, D. S. Sanchez, G. Chang, C. Zhang, D. Mou, Y. Wu, L. Huang, C.-C. Lee, S.-M. Huang, B. Wang, A. Bansil, H.-T. Jeng, T. Neupert, A. Kaminski, H. Lin, S. Jia, and M. Zahid Hasan, Nat. Phys. **11**, 748 (2015).

[51] S.-Y. Xu, I. Belopolski, D. S. Sanchez, C. Zhang, G. Chang, C. Guo, G. Bian, Z. Yuan, H. Lu, T.-R. Chang, P. P. Shibayev, M. L. Prokopovych, N. Alidoust, H. Zheng, C.-C. Lee, S.-M. Huang, R. Sankar, F. Chou, C.-H. Hsu, H.-T. Jeng, A. Bansil, T. Neupert, V. N. Strocov, H. Lin, S. Jia, and M. Z. Hasan, Sci. Adv. **1**, (2015).

[52] K. Zhang, C. Bao, Q. Gu, X. Ren, H. Zhang, K. Deng, Y. Wu, Y. Li, J. Feng, and S. Zhou, Nat. Commun. **7**, 13552 (2016).

[53] S. Borisenko, D. Evtushinsky, Q. Gibson, A. Yaresko, K. Koepernik, T. Kim, M. Ali, J. van den Brink, M. Hoesch, A. Fedorov, E. Haubold, Y. Kushnirenko, I. Soldatov, R. Schäfer, and R. J. Cava, Nat. Commun. **10**, 3424 (2019).

[54] N. Morali, R. Batabyal, P. K. Nag, E. Liu, Q. Xu, Y. Sun, B. Yan, C. Felser, N. Avraham, and H. Beidenkopf, Science (80-.). **365**, 1286 (2019).

[55] X. Wan, A. M. Turner, A. Vishwanath, and S. Y. Savrasov, Phys. Rev. B **83**, 205101 (2011).

[56] M. Obaida, K. Westerholt, and H. Zabel, Phys. Rev. B **84**, 184416 (2011).

[57] I.-M. Imort, P. Thomas, G. Reiss, and A. Thomas, J. Appl. Phys. **111**, 07D313 (2012).

[58] R. P. Jena, D. Kumar, and A. Lakhani, J. Phys. Condens. Matter **32**, 365703 (2020).

[59] D. B. Mitzi, Chem. Rev. **119**, 3033 (2019).

[60] A. M. Glazer, Acta Crystallogr. Sect. B Struct. Crystallogr. Cryst. Chem. **28**, 3384 (1972).

[61] A. M. Glazer, Acta Crystallogr. Sect. A **31**, 756 (1975).

[62] N. F. Mott, Metal-Insulator Transition, Taylor & Francis, London (1990).

[63] Patrik Fazekas, Lecture Notes on Electron Correlation and Magnetism, (1999).

[64] J Hubbard. Electron Correlations in Narrow Energy Bands. Proceedings of the Royal Society A: Mathematical, Physical and Engineering Sciences, 276:238– 257, (1963).

[65] J. Zaanen, G. A. Sawatzky, and J. W. Allen, Phys. Rev. Lett. **55**, 418 (1985).

[66] P. Lacorre, J. B. Torrance, J. Pannetier, A. I. Nazzal, P. W. Wang, and T. C. Huang, J. Solid State Chem. **91**, 225 (1991).

[67] S. J. Kim, G. Demazeau, and I. Presniakov, J. Phys. Condens. Matter **14**, 10741 (2002).

[68] S. Ishiwata, M. Azuma, M. Takano, E. Nishibori, M. Takata, M. Sakata, and K. Kato, J. Mater. Chem. **12**, 3733 (2002).

[69] J. A. Alonso, J. L. García-Muñoz, M. T. Fernández-Díaz, M. A. G. Aranda, M. J. Martínez-Lope, and M. T. Casais, Phys. Rev. Lett. **82**, 3871 (1999).

[70] J. A. Alonso, M. J. Martínez-Lope, M. T. Casais, J. L. García-Muñoz, and M. T. Fernández-Díaz, Phys. Rev. B **61**, 1756 (2000).

[71] J. L. García-Muñoz, M. A. G. Aranda, J. A. Alonso, and M. J. Martínez-Lope, Phys. Rev. B **79**, 134432 (2009).

[72] M. Medarde, M. T. Fernández-Díaz, and P. Lacorre, Phys. Rev. B **78**, 212101 (2008).

[73] S. R. Barman, A. Chainani, and D. D. Sarma, Phys. Rev. B **49**, 8475 (1994).

[74] Sara Catalano, Electronic properties of $NdNiO_3$ and $SmNiO_3$ thin films Ph.D. Thesis University of Geneva (2016).

[75] Sagar Sarkar, Role of structure in determining the properties of transition metal/post-transition metal compounds, Ph.D. thesis, University of Calcutta, India (2018).

[76] J.-S. Zhou and J. B. Goodenough, Phys. Rev. B **69**, 153105 (2004).

[77] M. Zaghrioui, A. Bulou, P. Lacorre, and P. Laffez, Phys. Rev. B **64**, 081102 (2001).

[78] U. Staub, G. I. Meijer, F. Fauth, R. Allenspach, J. G. Bednorz, J. Karpinski, S. M. Kazakov, L. Paolasini, and F. D'Acapito, Phys. Rev. Lett. **88**, 126402 (2002).

[79] I. I. Mazin, D. I. Khomskii, R. Lengsdorf, J. A. Alonso, W. G. Marshall, R. M. Ibberson, A. Podlesnyak, M. J. Martínez-Lope, and M. M. Abd-Elmeguid, Phys. Rev. Lett. **98**, 176406 (2007).

[80] H. Park, A. J. Millis, and C. A. Marianetti, Phys. Rev. Lett. **109**, 156402 (2012).

[81] M. Medarde, P. Lacorre, K. Conder, F. Fauth, and A. Furrer, Phys. Rev. Lett. **80**, 2397 (1998).

[82] R. Jaramillo, S. D. Ha, D. M. Silevitch, and S. Ramanathan, Nat. Phys. **10**, 304 (2014).

[83] A. Mercy, J. Bieder, J. Íñiguez, and P. Ghosez, Nat. Commun. **8**, 1677 (2017).

[84] O. E. Peil, A. Hampel, C. Ederer, and A. Georges, Phys. Rev. B **99**, 245127 (2019).

[85] F. Heusler, Ueber magnetische Manganlegierungen [German]. Verh. Dtsch. Phys. Ges. 5, 219 (1903).

[86] O. Heusler, Ann. Phys. **411**, 155 (1934).

[87] Proc. R. Soc. London. Ser. A, Contain. Pap. a Math. Phys. Character **144**, 340 (1934).

[88] T. Graf, S. S. P. Parkin, and C. Felser, IEEE Trans. Magn. **47**, 367 (2011).

[89] H. C. Kandpal, G. H. Fecher, and C. Felser, J. Phys. D. Appl. Phys. **40**, 1507 (2007).

[90] L. Wollmann, A. K. Nayak, S. S. P. Parkin, and C. Felser, Annu. Rev. Mater. Res. **47**, 247 (2017).

[91] F. F. Tafti, T. Fujii, A. Juneau-Fecteau, S. René de Cotret, N. Doiron-Leyraud, A. Asamitsu, and L. Taillefer, Phys. Rev. B **87**, 184504 (2013).

[92] Y. Nakajima, R. Hu, K. Kirshenbaum, A. Hughes, P. Syers, X. Wang, K. Wang, R. Wang, S. R. Saha, D. Pratt, J. W. Lynn, and J. Paglione, Sci. Adv. **1**, (2015).

[93] J. C. Slater, Phys. Rev. **49**, 931 (1936).

[94] L. Pauling, Phys. Rev. **54**, 899 (1938).

[95] G. H. Fecher, H. C. Kandpal, S. Wurmehl, C. Felser, and G. Schönhense, J. Appl. Phys. **99**, 08J106 (2006).

[96] Z. Wang, Y. Sun, X.-Q. Chen, C. Franchini, G. Xu, H. Weng, X. Dai, and Z. Fang, Phys. Rev. B **85**, 195320 (2012).

[97] C. Fang, H. Weng, X. Dai, and Z. Fang, Chinese Phys. B **25**, 117106 (2016).

[98] M. Z. Hasan, S.-Y. Xu, I. Belopolski, and S.-M. Huang, Annu. Rev. Condens. Matter Phys. **8**, 289 (2017).

[99] B. Yan and C. Felser, Annu. Rev. Condens. Matter Phys. **8**, 337 (2017).

[100] N. P. Armitage, E. J. Mele, and A. Vishwanath, Rev. Mod. Phys. **90**, 015001 (2018).

[101] J. Hu, S.-Y. Xu, N. Ni, and Z. Mao, Annu. Rev. Mater. Res. **49**, 207 (2019).

[102] N. Kumar, S. N. Guin, K. Manna, C. Shekhar, and C. Felser, Chem. Rev. **121**, 2780 (2021).

[103] S.-M. Huang, S.-Y. Xu, I. Belopolski, C.-C. Lee, G. Chang, B. Wang, N. Alidoust, G. Bian, M. Neupane, C. Zhang, S. Jia, A. Bansil, H. Lin, and M. Z. Hasan, Nat. Commun. **6**, 7373 (2015).

[104] S.-Y. Xu, I. Belopolski, N. Alidoust, M. Neupane, G. Bian, C. Zhang, R. Sankar, G. Chang, Z. Yuan, C.-C. Lee, S.-M. Huang, H. Zheng, J. Ma, D. S. Sanchez, B. Wang, A. Bansil, F. Chou, P. P. Shibayev, H. Lin, S. Jia, and M. Z. Hasan, Science (80-.). **349**, 613 (2015).

[105] L. X. Yang, Z. K. Liu, Y. Sun, H. Peng, H. F. Yang, T. Zhang, B. Zhou, Y. Zhang, Y. F. Guo, M. Rahn, D. Prabhakaran, Z. Hussain, S.-K. Mo, C. Felser, B. Yan, and Y. L. Chen, Nat. Phys. **11**, 728 (2015).

[106] E. Liu, Y. Sun, N. Kumar, L. Muechler, A. Sun, L. Jiao, S.-Y. Yang, D. Liu, A. Liang, Q. Xu, J. Kroder, V. Süß, H. Borrmann, C. Shekhar, Z. Wang, C. Xi, W. Wang, W. Schnelle, S. Wirth, Y. Chen, S. T. B. Goennenwein, and C. Felser, Nat. Phys. **14**, 1125 (2018).

[107] Q. Wang, Y. Xu, R. Lou, Z. Liu, M. Li, Y. Huang, D. Shen, H. Weng, S. Wang, and H. Lei, Nat. Commun. **9**, 3681 (2018).

[108] B.-J. Yang and N. Nagaosa, Nat. Commun. **5**, 4898 (2014).

[109] Z. K. Liu, B. Zhou, Y. Zhang, Z. J. Wang, H. M. Weng, D. Prabhakaran, S.-K. Mo, Z. X. Shen, Z. Fang, X. Dai, Z. Hussain, and Y. L. Chen, Science (80-.). **343**, 864 (2014).

[110] M. Neupane, S.-Y. Xu, R. Sankar, N. Alidoust, G. Bian, C. Liu, I. Belopolski, T.-R. Chang, H.-T. Jeng, H. Lin, A. Bansil, F. Chou, and M. Z. Hasan, Nat. Commun. **5**, 3786 (2014).

[111] S. Borisenko, Q. Gibson, D. Evtushinsky, V. Zabolotnyy, B. Büchner, and R. J. Cava, Phys. Rev. Lett. **113**, 027603 (2014).

[112] J. A. Steinberg, S. M. Young, S. Zaheer, C. L. Kane, E. J. Mele, and A. M. Rappe, Phys. Rev. Lett. **112**, 036403 (2014).

[113] S. M. Young, S. Zaheer, J. C. Y. Teo, C. L. Kane, E. J. Mele, and A. M. Rappe, Phys. Rev. Lett. **108**, 140405 (2012).

[114] S.-Y. Xu, Y. Xia, L. A. Wray, S. Jia, F. Meier, J. H. Dil, J. Osterwalder, B. Slomski, A.

Bansil, H. Lin, R. J. Cava, and M. Z. Hasan, Science (80-.). **332**, 560 (2011).

[115] M. Brahlek, N. Bansal, N. Koirala, S.-Y. Xu, M. Neupane, C. Liu, M. Z. Hasan, and S. Oh, Phys. Rev. Lett. **109**, 186403 (2012).

[116] G. Chang, S.-Y. Xu, X. Zhou, S.-M. Huang, B. Singh, B. Wang, I. Belopolski, J. Yin, S. Zhang, A. Bansil, H. Lin, and M. Z. Hasan, Phys. Rev. Lett. **119**, 156401 (2017).

[117] C. Fang, Y. Chen, H.-Y. Kee, and L. Fu, Phys. Rev. B **92**, 081201 (2015).

[118] Y. Kim, B. J. Wieder, C. L. Kane, and A. M. Rappe, Phys. Rev. Lett. **115**, 036806 (2015).

[119] C.-K. Chiu and A. P. Schnyder, Phys. Rev. B **90**, 205136 (2014).

[120] L. S. Xie, L. M. Schoop, E. M. Seibel, Q. D. Gibson, W. Xie, and R. J. Cava, APL Mater. **3**, 083602 (2015).

[121] L. M. Schoop, M. N. Ali, C. Straßer, A. Topp, A. Varykhalov, D. Marchenko, V. Duppel, S. S. P. Parkin, B. V. Lotsch, and C. R. Ast, Nat. Commun. **7**, 11696 (2016).

[122] J. Hu, Z. Tang, J. Liu, X. Liu, Y. Zhu, D. Graf, K. Myhro, S. Tran, C. N. Lau, J. Wei, and Z. Mao, Phys. Rev. Lett. **117**, 016602 (2016).

[123] G. Bian, T.-R. Chang, R. Sankar, S.-Y. Xu, H. Zheng, T. Neupert, C.-K. Chiu, S.-M. Huang, G. Chang, I. Belopolski, D. S. Sanchez, M. Neupane, N. Alidoust, C. Liu, B. Wang, C.-C. Lee, H.-T. Jeng, C. Zhang, Z. Yuan, S. Jia, A. Bansil, F. Chou, H. Lin, and M. Z. Hasan, Nat. Commun. **7**, 10556 (2016).

[124] G. Bian, T.-R. Chang, H. Zheng, S. Velury, S.-Y. Xu, T. Neupert, C.-K. Chiu, S.-M. Huang, D. S. Sanchez, I. Belopolski, N. Alidoust, P.-J. Chen, G. Chang, A. Bansil, H.-T. Jeng, H. Lin, and M. Z. Hasan, Phys. Rev. B **93**, 121113 (2016).

[125] X.-B. Wang, X.-M. Ma, E. Emmanouilidou, B. Shen, C.-H. Hsu, C.-S. Zhou, Y. Zuo, R.-R. Song, S.-Y. Xu, G. Wang, L. Huang, N. Ni, and C. Liu, Phys. Rev. B **96**, 161112 (2017).

[126] Q.-F. Liang, J. Zhou, R. Yu, Z. Wang, and H. Weng, Phys. Rev. B **93**, 085427 (2016).

[127] T. Bzdušek, Q. Wu, A. Rüegg, M. Sigrist, and A. A. Soluyanov, Nature **538**, 75 (2016).

[128] B. Bradlyn, J. Cano, Z. Wang, M. G. Vergniory, C. Felser, R. J. Cava, and B. A.

Bernevig, Science (80-.). **353**, (2016).

[129] H. Weng, C. Fang, Z. Fang, and X. Dai, Phys. Rev. B **93**, 241202 (2016).

[130] Z. Zhu, G. W. Winkler, Q. Wu, J. Li, and A. A. Soluyanov, Phys. Rev. X **6**, 031003 (2016).

[131] B. Q. Lv, Z.-L. Feng, Q.-N. Xu, X. Gao, J.-Z. Ma, L.-Y. Kong, P. Richard, Y.-B. Huang, V. N. Strocov, C. Fang, H.-M. Weng, Y.-G. Shi, T. Qian, and H. Ding, Nature **546**, 627 (2017).

[132] B. Q. Lv, T. Qian, and H. Ding, Rev. Mod. Phys. **93**, 025002 (2021).

[133] E. H. Hall, Am. J. Math. **2**, 287 (1879).

[134] E. H. Hall, London, Edinburgh, Dublin Philos. Mag. J. Sci. **12**, 157 (1881).

[135] Proc. R. Soc. London. A. Math. Phys. Sci. **392**, 45 (1984).

[136] E. M. Pugh, Phys. Rev. **36**, 1503 (1930).

[137] E. M. Pugh and T. W. Lippert, Phys. Rev. **42**, 709 (1932).

Chapter 2 Experimental Details

In this chapter, we discuss the growth and characterization of different samples prepared, as well as various measuring techniques used for different work. The basic principles of different instruments that we have used have been also discussed.

2 Experimental Details

2.1 Preface

In this thesis, we discuss the investigation of metal-insulator transition (MIT) in rare-earth nickelates ($RNiO_3$) and the anomalous Hall effect (AHE) in Co_2-based ferromagnetic full Heusler compounds (X_2YZ). To investigate these phenomena we have prepared all the samples using various preparation techniques such as the sol-gel method, pulsed laser deposition system, and electric arc-melting furnace. To characterize the sample we have used various characterization tools like X-ray diffraction (XRD), energy-dispersive X-ray spectroscopy (EDX), scanning electron microscope (SEM), Raman spectroscopy, and atomic force microscopy (AFM). The transport measurements were carried out using liquid nitrogen (LN_2), He-4 cryostat, and 9-T Dynacool Physical Property Measurement System (PPMS, Quantum Design). The magnetic measurements were performed using a vibrating sample magnetometer in a PPMS (Quantum Design, USA). The low-frequency 1/f noise spectroscopy was done in a homemade liquid nitrogen cryostat. The scanning tunneling spectroscopy was performed in a scanning probe microscopy unit from RHK. All the experimental data acquisition and analysis programs were written in either LabVIEW, MATLAB, C++, or PPMS MultiVu.

2.2 Sample preparation

2.2.1 Synthesis of rare-earth nickelates nanopowder and pellet

In a beaker, a stoichiometric amount of high-quality (> 99.9%) precursors of, Neodymium nitrate hexahydrate, Lanthanum nitrate hexahydrate, and Nickel acetate tetrahydrate were dissolved in a 1:1 acetic and deionized (DI) water solution. The proper amount of ethylene glycol was added to the solution. The water-to-ethylene-glycol ratio is very crucial in the synthesis process [1]. In this study, we used 1.5 times the amount of ethylene glycol compared to DI water. The precursor solution had a molarity of 0.2 M and 0.4 M. The solution was stirred in a hot plate fitted with a magnetic stirrer for 2 hours at 70 °C and 6 hours at room temperature. The solution was heated up for 6 hours until sol formed. The sol was allowed to dry and was

stored at 150 °C for 12 hours before pyrolysis at 350 °C and 450 °C for 1.5 and 1 hour, respectively. In a flow of ultra-high purity oxygen gas, the final heating for phase formation was carried out at 650 °C for 8 hours. The main advantage of this procedure is that the nanoparticles are to get homogeneous and uniform dispersion. The as-prepared nanopowder was then compressed into a pellet with 80 MPa pressure and sintered at 800 °C in a tube furnace with a high oxygen flow for 24 hours in order to make the target material for the Pulsed laser deposition (PLD). After being ground, the pellet was once more sintered for 24 hours at 800 °C with a high oxygen flow. This procedure was repeated seven times, and the sintered pellet was then placed in a high flow of oxygen at 650 °C for 24 hours to maintain oxygen stoichiometry. Figure 2.1(a) represents the flow chart for the synthesis and the Fig. 2.1(b) and 2.1(c) shows the rare-earth nickelates nanopowder and pellet.

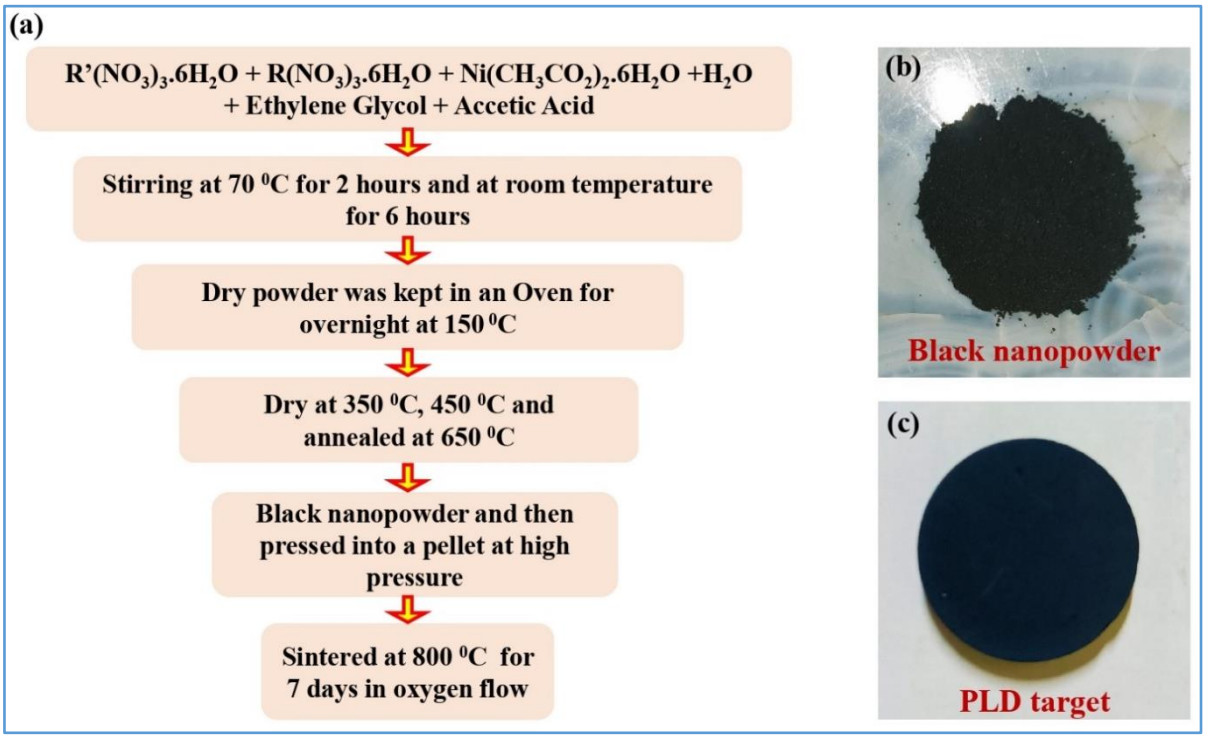

Figure 2.1: (a) The flow chart for the synthesis. (b) The rare-earth nickelates nanopowder. (c) The PLD target is used for the rare-earth nickelates thin film growth.

2.2.2 Growth of rare-earth nickelates thin films

To grow the thin films of rare-earth nickelates, we have used the pulsed laser deposition (PLD) technique. PLD is widely used for growing thin films of complex oxides. T. Venkatesan and his team used the PLD approach for the first time to deposit the high-temperature

superconducting film [2]. A variety of materials, from metal to insulators via semiconductors, can be deposited using this technique [3,4]. However, the most important use of it is to deposit complex materials such as perovskites with perfect stoichiometry [5,6]. In PLD, the deposition takes place in a vacuum or with inert/oxygen gas pressure. A high-power pulsed laser (usually 10-100 MW/cm^2) is focused on a target material to be deposited. The high-powered laser pulse ablates the target material, creating a plume of material that is directed toward the substrate.

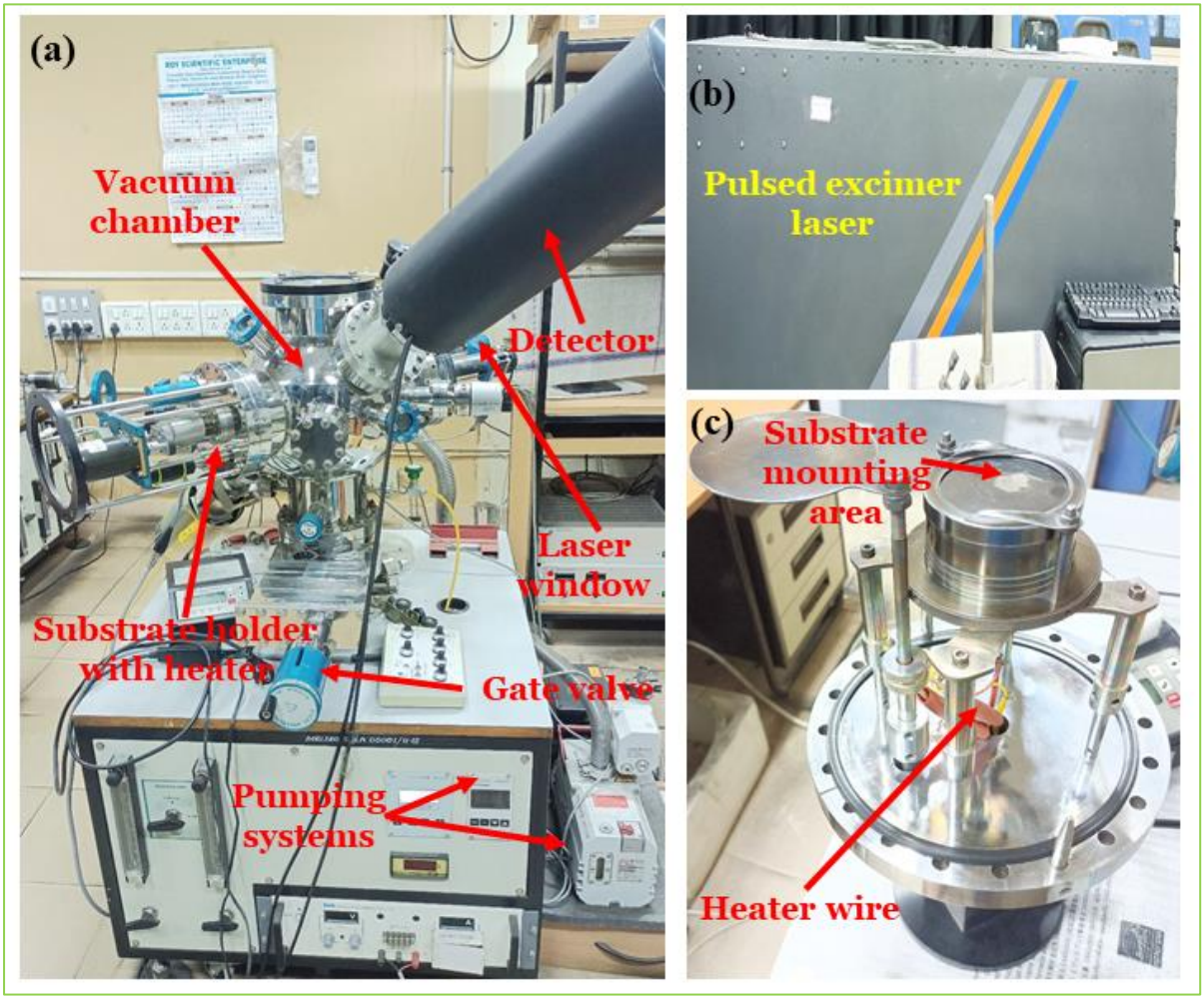

Figure 2.2: (a) The PLD setup in our lab. (b) Image of the pulsed excimer laser. (c) Image of the substrate mounting area.

The plume of the target material is a plasma including energetic species such as atoms, ions, molecules, and electrons that expand in a flow perpendicular to the surface and are collected on a suitable substrate. In PLD, the excimer laser evaporates the target material in a non-equilibrium manner, generating a large quantity of heat in a few nanoseconds in the target material's thin surface layer. The sample stoichiometry in the substrate as the target material is

preserved by this method of laser ablation. We rotate the target during the thin film deposition to achieve uniform ablation on the target (otherwise, high-intensity laser at the same location can damage the target at one location over time). The PLD setup in our lab is shown in Fig. 2.2(a). Figure 2.2(b) displays the image of the pulsed excimer laser and Fig. 2.2(c) represents the image of the substrate mounting area.

In this thesis, the film growth was done using a coherent COMPex pro-201F KrF excimer laser with a 248 nm wavelength [1]. Depending on the laser intensity and spot size, a related value of energy per unit area known as fluence was optimized for the film growth. Our PLD chamber-equipped Reflection High-Energy Electron Diffraction (RHEED) gun was used to carry out layer-by-layer growth. The schematic of the RHEED setup is given in Fig. 2.3(a).

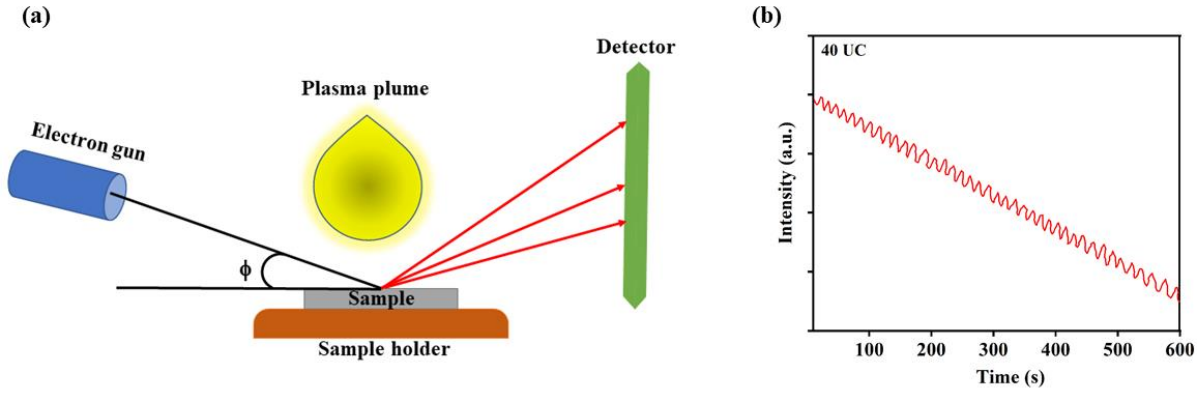

Figure 2.3: (a) Schematic diagram for the RHEED setup. (b) The RHEED oscillations of a 40 UC $NdNiO_3$ film grown on a $SrTiO_3$ (100) single crystal substrate after 1500 laser pulses.

In RHEED, an electron beam created by the electron gun hits the sample surface at a grazing angle, where the electrons diffract. This diffraction pattern can be caught by the detector. In this thesis, we used approximately 1500 laser shots with a repetition rate of 5 Hz to develop thin films with thicknesses of about 15 nm. The growth of a 40 Unit Cell (UC) (~ 15 nm) thick $NdNiO_3$ film on $SrTiO_3$ (100) single crystal substrate is depicted in Fig. 2.3 (b). The target pellets were ablated before all depositions to remove surface contamination from previous depositions in the PLD chamber, and a 30-minute pre-annealing was done to achieve temperature equilibrium between the substrates and the heater. After the deposition, the as-grown films were cooled in situ with 1 bar of high-quality oxygen gas to retain the oxygen stoichiometry.

2.2.3 Growth of polycrystalline full Heusler alloys

To synthesize the polycrystalline Co_2-based ferromagnetic full Heusler compounds, we have used an electric arc-melting furnace. Preparation of the sample in the form of an ingot involves the melting of high-purity raw elements in a tri-arc electric melting furnace under an argon atmosphere [7]. The entire furnace chamber consists of the tri-arc furnace (Centorr Vacuum Industries, Model:5TA), DC power supply, rotary pump, chiller, and vacuum pump unit.

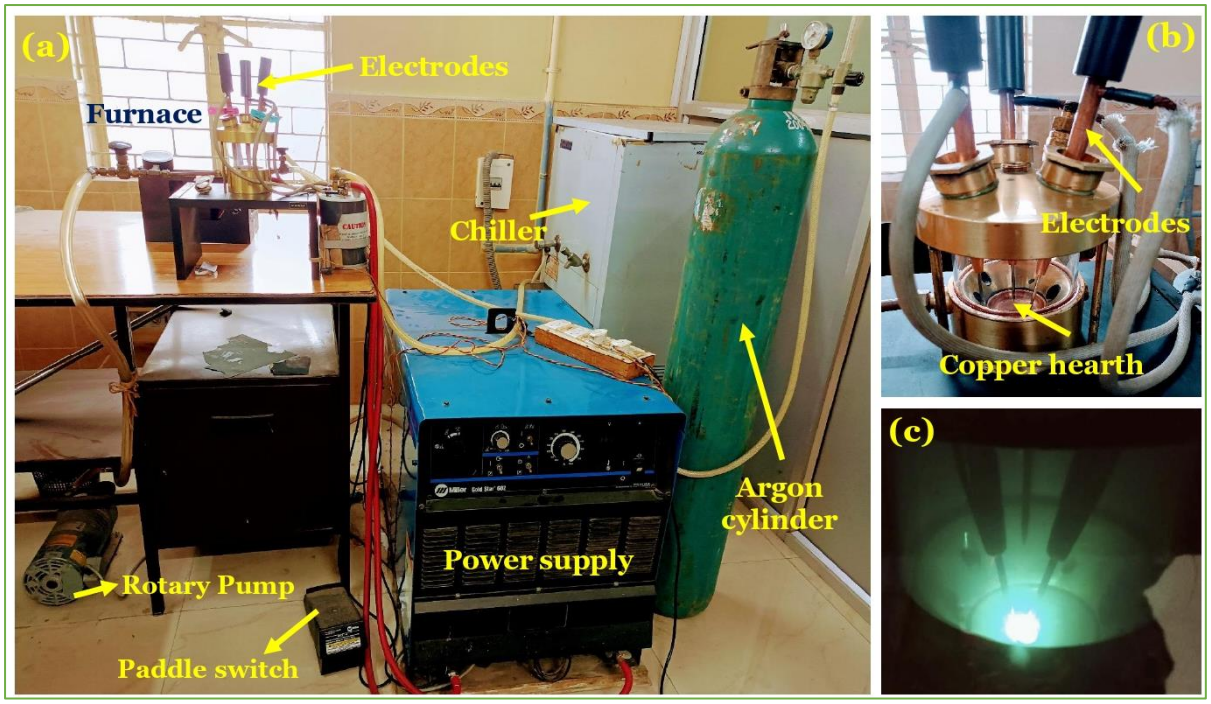

Figure 2.4: (a) An image of the electric arc melting furnace in our lab. (b) The enlarged view near the electrodes. (c) An image of the electrical arc during the sample preparation.

The furnace comprises two primary sections; (i) a copper hearth with positive electrical polarity located in the bottom section and (ii) three electrodes with negative polarity positioned in the upper section, as depicted in Fig. 2.4. To allow for visualization, the water-cooled top and bottom parts of the furnace are separated by a Pyrex glass tube. Moreover, each rod is equipped with a swivel ball to facilitate angular and vertical movements. This system achieves a maximum temperature of 3000°C and a corresponding current of ~120 A.

We have utilized Centorr Vacuum Industries 5TA tri-arc furnace to prepare the sample. First, each raw element is mounted on the copper hearth and set in the furnace. To create an oxygen-free environment within the arc-melting chamber, the initial step involves evacuating the chamber to a pressure of approximately 10^{-3} mbar. Subsequently, high-purity argon gas is

employed for several purging cycles to achieve a condition devoid of oxygen within the chamber. To mitigate heat-related issues resulting from the high-temperature melting process, both the copper-hearth plate and the tungsten tip are continuously cooled using a regular flow of cold water. Once the chamber evacuation process is complete, titanium is melted initially to eliminate any remaining oxygen present in the furnace. Subsequently, the samples were remelted five to six times by being flipped upside down to ensure a uniform homogeneity of the constituent elements.

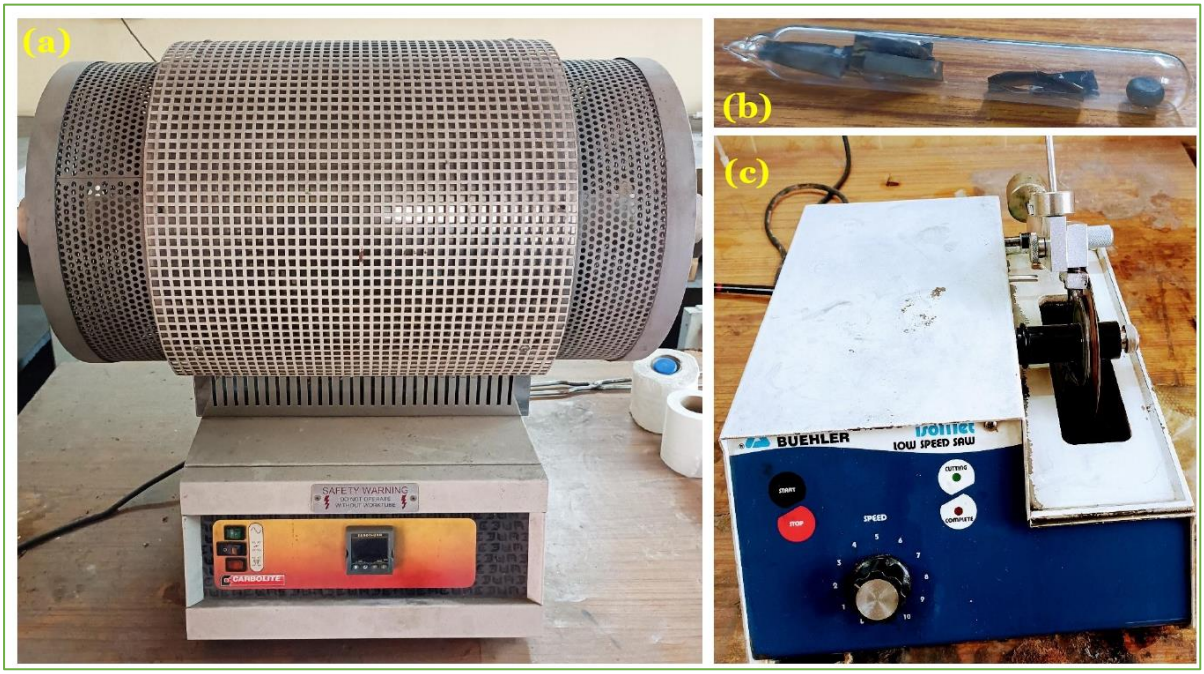

Figure 2.5: (a) An image of the tube furnace in our lab. (b) The image of a sample with a few pieces of tantalum foils inside a quartz tube. (c) An image of the low-speed saw cutter in our lab.

After preparing the ingot, it undergoes ultrasonication in an alcohol bath for thorough cleaning. Subsequently, to prevent oxidation, the cleaned ingot is carefully sealed with tantalum foil within an evacuated quartz tube. Before sealing, the tube is subjected to roughing and purging with Ar gas multiple times to ensure the sample remains free from oxidation. Following the sealing process, the sample is subjected to annealing at their respective temperatures for four days. Once the four-day heat treatment period is complete, the ingot is rapidly quenched in ice water to halt any high-temperature phase transformations. To suit the specific requirements of different experiments, the sample is then cut into various shapes using a low-speed saw,

specifically the (Buehler Isomet^{TM}). For visual reference, Fig. 2.5 presents images of the box furnace, quartz tube, and cutter machine, respectively.

2.3 Structural characterization

2.3.1 X-Ray Diffraction

X-ray diffraction (XRD) is widely used to examine the phase purity and to investigate the crystallographic structure of a material. Through XRD analysis, crucial information about the crystal structure, interplanar spacing, phases, and other crystal-related properties such as lattice strain and average grain size can be extracted [8]. A schematic diagram of the X-ray diffractometer is presented in Fig. 2.6(a). When a monochromatic beam of X-ray with a wavelength compared to lattice spacing of the materials is experienced on the surface of crystalline material, the incident X-ray diffracts from the crystal plane of the material. The diffracted beam from the two collateral plans equal to the multiple integers of the incident beam induces the constructive interference that is determined by following Bragg's law [9]

$$2d\text{Sin}\theta = n\lambda \tag{2.1}$$

Where d is interplanar spacing in the crystal, θ is the angle of diffraction, λ is the wavelength of the incident X-ray beam, and n is an integer (order of diffraction). The diffracted intensity of X-rays is exhibited by the detector in different directions.

There are three different experimental methods for the XRD technique. One is the Lau technique where θ is fixed and λ is variable. The second refers to the Rotating crystal method in which λ remains fixed, where θ varies with respect to the variation of the single crystal. The third method is the powder diffraction technique, similar to the second one. The powder diffractometer divides into two basic segments: θ-θ system and θ-2θ system. In the θ-θ system, both the X-ray source and the detector simultaneously rotate, but the material holder is fixed. Alternately, in the θ-2θ system, the X-ray source remains stationary while the detector moves at a speed equal to twice the rotational speed of the sample holder. In this thesis, a θ-2θ system of Panalytical X-ray diffractometer is used. To check the orientation of the rare-earth thin films we have performed the high-resolution XRD rocking analysis. In the rocking analysis, we fixed the detector at the center of the film's Bragg reflection and followed the diffraction intensity of the sample while it was rocked [10]. Figure 2.6(b) shows a representative example of the XRD

pattern of the Co_2CrGa polycrystalline sample. Due to the polycrystalline nature of some investigating compounds, we have also used the powder diffraction technique in our thesis.

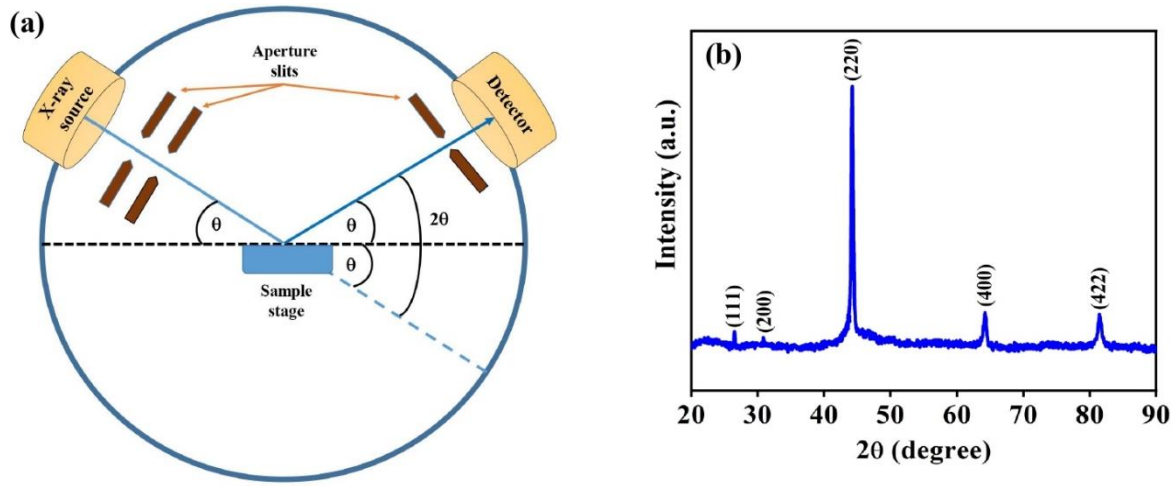

Figure 2.6: (a) Schematic diagram of an X-ray diffractometer. (b) A representative X-ray diffraction pattern for the Co_2CrGa full Heusler compound.

2.3.2 Scanning Electron Microscope

To investigate the material's morphology and composition analysis, a high-resolution field emission scanning electron microscope (FESEM) is widely used in material science as well as the engineering field. SEM acts in a voltage range of 2-50kV and their beam diameter that scans the material's surface is about 5nm- 3µm.

One important segment in SEM is the electron gun from which a branch of electron beams is produced either by conventional thermionically or cold field emission process [11], which is shown in Fig. 2.7(a). The accelerated electrons are propelled by a high-voltage electric field established between the electron source (cathode) and the anode plate. Then these accelerated electron beams are monitored by electromagnetic lenses such as condenser lenses and object lenses. The condenser lens provides the ability to finely adjust the spot size of the electric beam, enabling it to be broader or narrower, while the objective lens focuses the electron beam onto the examined material. In between them, the scan coil serves the purpose of deflecting the electron beam on the material's surface.

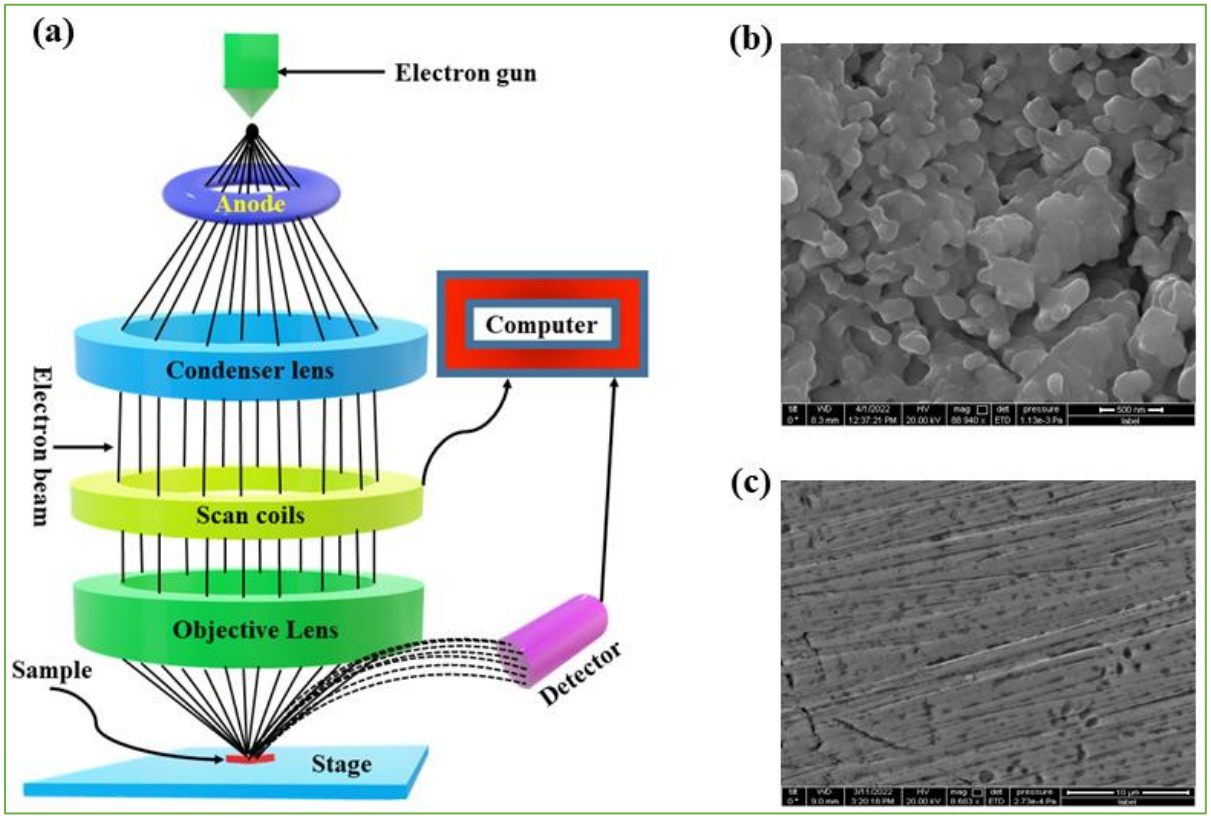

Figure 2.7: (a) Schematic diagram of the scanning electron microscope. (b) SEM micrograph for $NdNiO_3$ nanopowder. (c) SEM micrograph of Co_2CrGa Heusler compound.

When these accelerated electrons interact with the atom of the material, due to an inelastic collision between the electron beam and material, the incident electrons are diminished because of energy dissipation. As a result, various signals such as secondary electrons, auger electrons, characteristic X-rays, backscattered electrons, and cathode luminescence are caused. Depending upon their energy, secondary electrons, and back scattered electrons are separated. The secondary electrons take part in the mapping of the surface image of the material. Figure 2.7(b) and (c) represent the example of SEM micrograph for $NdNiO_3$ nanopowder and Co_2CrGa.

2.3.3 Energy Dispersive X-Ray Spectroscopy

Energy dispersive analysis of X-ray (EDAX) is a convenient technique to determine the chemical composition of bulk material to nanoparticles [12]. The fundamental principle of the EDAX is described in the following paragraph.

When a high-energy electron beam interacts with the atom of the material, it ejects the electron out from the inner shell of the material. For example, the emission of a K-shell electron jumps in an excited state. This causes a position in a particular electronic shell and thus an electron from a higher energy shell jumps into a vacant energy shell. Therefore, the energy difference between these two shells is characterized as a characteristic X-ray that can process direct information about the material's compositions. This characteristic wavelength of the material is inversely proportional to the square root of the atomic number (Z) of the material according to Moseley's law. In EDAX, a Si or Li detector is generally used as an energy dispersive spectrometer that can measure the amount of energy and count the number of emitted X-rays. A typical X-ray spectrum is explained in Fig 2.8(a) and Fig. 2.8(b) depicts the EDAX spectra for the $NdNiO_3$ nanopowder.

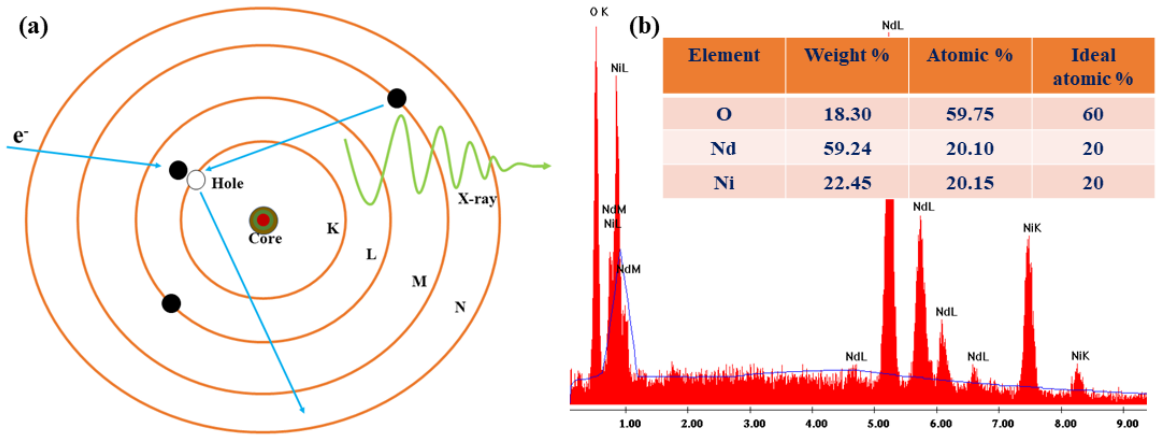

Element	Weight %	Atomic %	Ideal atomic %
O	18.30	59.75	60
Nd	59.24	20.10	20
Ni	22.45	20.15	20

Figure 2.8: (a) The schematic diagram for EDAX analysis. (b) EDAX spectra for the $NdNiO_3$ nanopowder.

2.3.4 Atomic Force Microscope

The Atomic force microscope (AFM) is a type of scanning probe microscope that produces a topographical image of the sample surface based on interactions between a tip and a sample surface. In 1986 at IBM Zurich, Gerd Binning, and other researchers invented the AFM [13]. A typical AFM comprises a cantilever with a tiny tip (probe) at the free end, a laser, a four-quadrant photodiode, and a scanner. Surface characteristics can be explored with very high precision in a range of 100 μm to less than 1 μm. A tip is utilized for imaging in AFM. It is typically made of silicon (Si) or silicon nitride (Si_3N_4) and it approaches the sample at a range of interatomic lengths. Figure 2.9(a) represents the schematic diagram of a basic AFM

operation given below. Figure 2.9(b) illustrates an example of an AFM image of $NdNiO_3$ thin film.

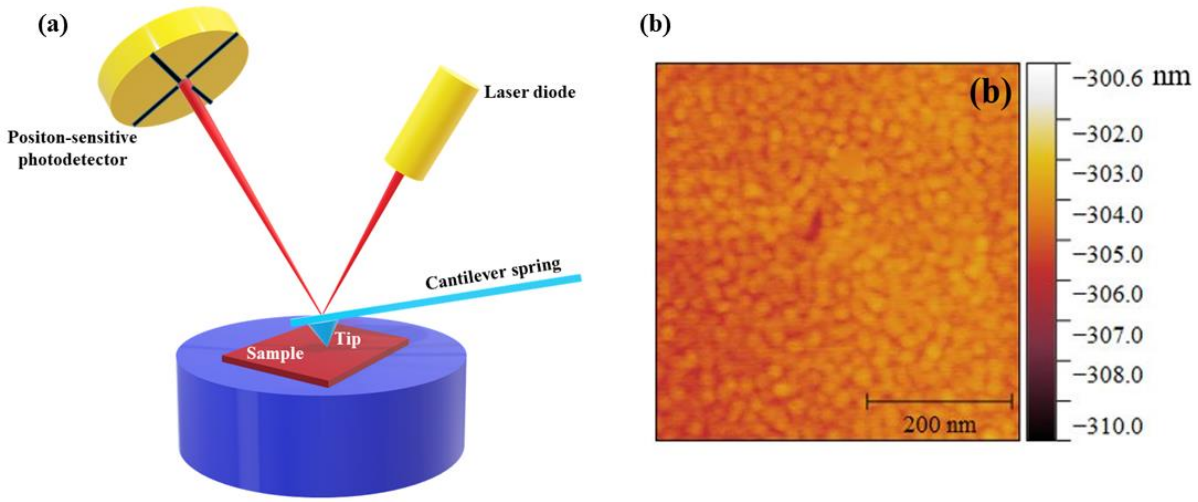

Figure 2.9: (a) The schematic diagram for the basic AFM operation. (b) AFM image of the $NdNiO_3$ film taken over a scan area of 500 nm × 500 nm.

When the tip, which is attached to the free end of the cantilever, comes very close to the surface, attractive and repulsive forces owing to interactions between the tip and the sample surface develop a negative or positive bending of the cantilever. A laser beam is focused on the back of the cantilever. It can be reflected in a four-quadrant photodiode detector. The bending of the cantilever can be precisely monitored with the help of this position-sensitive photodiode. The cantilever deflects in response to changes in atomic force between the tip and the sample, and the detector measures the deflection. The resulting image is a topographical representation of the sample surface.

2.4 Measurement Techniques

2.4.1 Low frequency 1/f noise spectroscopy

In this thesis, we have used low-frequency 1/f noise spectroscopy to measure the thermal noise as well as flicker noise close to MIT. Figure 2.10 illustrates the schematic diagram of the noise measurement setup. In most condensed matter systems, 1/f noise comes from the relaxation of defects or groups of defects with finite relaxation times [14]. While most other measurements

pick up on average characteristics, the presence of noise signifies the existence of a statistical distribution in fluctuating quantities. It is thus a unique and sensitive tool that can provide information on the underlying statistics of defects and the relaxation phenomena that give rise to noise.

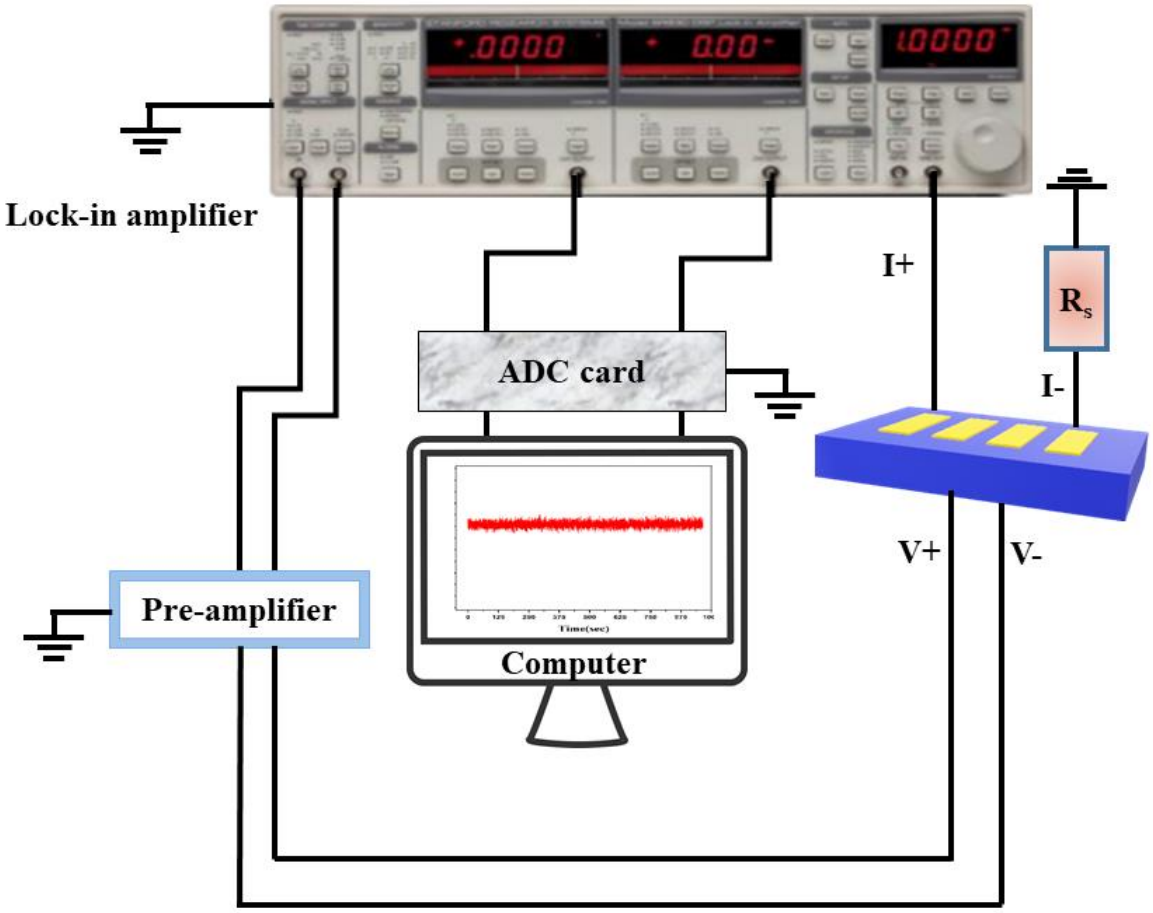

Figure 2.10: The schematic diagram of the experimental setup for the 1/f noise measurement.

Electrical noise in a solid can be classified into three types: Nyquist noise, shot noise, and flicker noise [14]. Nyquist noise (also known as Johnson noise or Thermal noise) emerges from the Nyquist theorem [15,16]. If a resistor of value R kept at a temperature T, the thermal noise has a spectral power density (SPD) in the order of $4k_BTR$, where k_B is the Boltzmann constant [17]. In this case, the $S_v(f)$ is independent of the current passing through the resistor and is not dependent on the materials property of the resistor. It is a very useful tool to measure the effective electron temperature in a solid. The shot noise, which arises from discrete charge carrier motion in a solid, is also independent of frequency. The shot noise has a SPD equivalent to $2qI$, where q is the value of charge carrier and I is the current through the solid [14]. The

magnitude of the charge carrier can be determined using the shot noise. Generally, when the thermal noise is low enough, the shot noise can be seen at low temperatures.

The other type of noise is the flicker noise, which is mostly measured by the condensed matter physicist. In addition to the thermal noise and the shot noise, this noise exists in a solid. It is measurable when a particular conductor is carrying a current. The flicker noise has SPD, $S_v(f) \propto 1/f^{\alpha}$, often referred to as $1/f$ noise when $\alpha \approx 1$. For a given frequency f, the SPD of the flicker noise shows a quadratic dependence on the applied bias V. The quadratic dependence of the flicker noise on the applied bias V is generally used to distinguish it from the thermal noise [14].

In this thesis, we have measured the thermal noise and the flicker noise using four probe ac measurement techniques in the rare-earth nickelates thin films close to MIT [18]. In noise measurements, to measure the voltage fluctuations across the sample we bias the sample with a constant current from a dual channel lock-in amplifier (LIA) SR830 at a frequency f_0 [19,20]. The value of series resistance (R_S) is chosen so that $R_S > r_S$ (at least by 10^2 order), where r_S is the sample resistance. The voltage developed across the sample is amplified by a low noisy preamplifier SR554 and fed into the lock-in inputs and then demodulated by the LIA. Once the signal has been demodulated, it is fed onto the 16 bit analog to digital converter (ADC) card of bandwidth 200 kHz. The time series of voltage fluctuations were recorded for nearly 16 minutes (1 million data points). The obtained time series of the voltage fluctuations were decimated and digitized using digital signal processing techniques.

All the noise measurements reported in this thesis involved the very careful recording of a time series of voltage fluctuations $\delta V(t)$. The SPD of the time series voltage fluctuations can be obtained using the Fourier transformation, which is given as:

$$S_v(f) = \lim_{T\to\infty} \frac{1}{2T}\left[\int_{-T}^{+T} \delta V(t) e^{-2\pi i f t} dt\right]^2 \tag{2.2}$$

Practically, the SPD was determined using the Welch periodogram method [21]. The SPD at the output channel of the LIA is given as:

$$S_v(f,\varphi) = G^2\left\{\left[S_v^{bg}(f - f_0) + I_0^2(f - f_0) S_r(f) cos^2(\varphi)\right]\right\} \tag{2.3}$$

Where $S_r(f)$ and $S_v^{bg}(f)$ is the PSD of the sample and background respectively. φ, f, f_0, and G represents the phase, measurement frequency, excitation frequency, and gain of the LIA respectively [18]. The dual-channel LIA allows us to measure the in-phase and out-of-phase

components altogether and according to equation 2.3, for φ (In-phase component) = 0^0, we measure a sum of the sample and the background noise while for φ (Out of phase component) = 90^0 , we measure only background noise. The contribution of the noise from the sample can be extracted after subtracting the background noise from the sum of the total noise. The method is thus best suited for measuring the two noise components simultaneously [14].

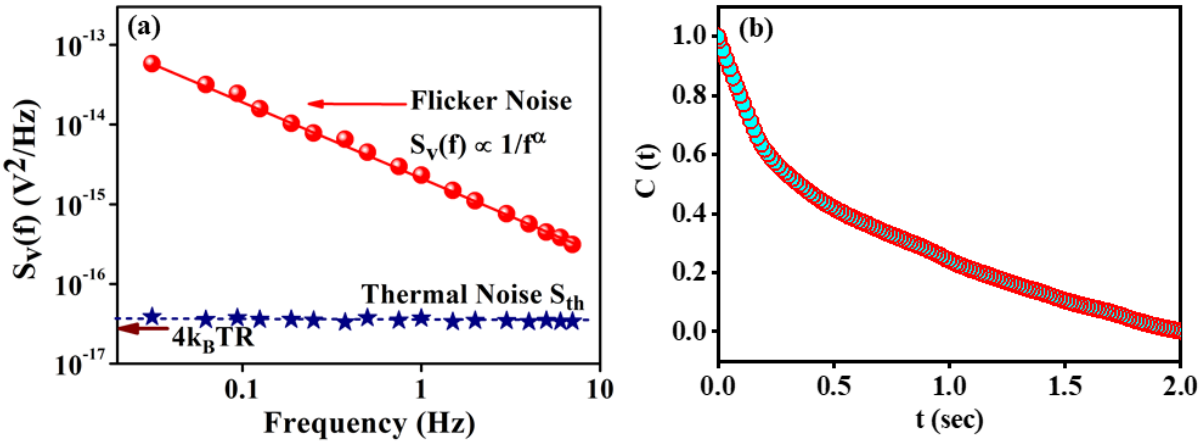

Figure 2.11: (a) An example of spectral power density for the flicker noise varying as $\frac{1}{f^{\alpha}}$ and thermal noise in the $NdNiO_3$ thin film for a particular temperature. The Johnson-Nyquist value of $4k_BTR$ is marked by an arrow. (b) The corresponding autocorrelation function at that temperature for the $NdNiO_3$ thin film.

In order to investigate the electronic correlation near the MIT, we have calculated the autocorrelation function $C(t)$ which can be determined from the time series of voltage fluctuations by using the following relation [22]

$$C(t) \equiv \langle \delta v(t') \times \delta v(t+t') \rangle_{t'} \tag{2.4}$$

Where $\langle \dots \rangle_{t'}$ represents the time average. To investigate the correlated nature of the charge carrier dynamics close to MIT, we have calculated the second spectra from the filtered time series of the voltage fluctuations. The second spectrum is defined as the Fourier transform of four-point correlation in a frequency band. To study the non-Gaussian fluctuations (correlated fluctuations), we have calculated the normalized second spectrum which is given by [14]

$$\Gamma^2 = \int_0^{f_H - f_L} S^{(2)}(f_2) df_2 \tag{2.5}$$

Where

$$S^{(2)}(f_2) = \frac{\int_0^{\infty} \langle \delta v^{(2)}(t) \delta v^{(2)}(t+\varsigma) \rangle \cos(2\pi f_2 \varsigma) d\varsigma}{\left[\int_{f_L}^{f_H} S_v(f_1) df_1\right]^2} \quad (2.6)$$

where f_1 and f_2 are the frequencies associated with the first and second spectra, respectively. The central limit theorem suggests that if fluctuations in any system are independent, their statistics will be Gaussian. However, the statistics will be non-Gaussian if there is a correlation in the fluctuation due to the correlated nature of the electrons. Any deviation from the value 3 of Γ^2 indicates the non-Gaussianity in the fluctuations.

In Fig. 2.11(a), we present an example of measured frequency-independent thermal noise (S_{th}) and the flicker noise with spectral power dependence $S_v(f) \propto \frac{1}{f^{\alpha}}$ at a given temperature for the $NdNiO_3$ thin film. It clearly shows that one can cleanly measure the thermal noise S_{th} along with the flicker noise. Figure 2.11(b) displays the autocorrelation function $C(t)$ vs t for the $NdNiO_3$ thin film for a particular temperature.

2.4.2 Scanning Tunneling Microscope

The basic working principle of a Scanning tunneling microscope (STM) is the tunneling of electrons through a potential barrier in an ultra-high vacuum [23,24]. According to classical physics, an electron with energy $E < V$ (where V is the barrier potential) will not be able to penetrate through the barrier and will reflect, however quantum mechanically, there is a finite possibility that the electron will pass through the barrier. Thus, electron flow is not feasible in classical physics without a direct connection between two surfaces via a wire. However quantum mechanically there is a finite probability of tunneling.

The STM work reported in the thesis (*Chapter 3*) was performed on an RHK UHV 350 SPM machine as shown in Fig. 2.12(a). The system includes two chambers: the main chamber (where measurements of imaging and tunneling conductances are made), and the sample transfer chamber or load-lock chamber. An ion pump maintained the ultra-high vacuum (UHV) level of the main chamber at 10^{-10} mbar, while 10^{-8} mbar was the vacuum level of the load lock chamber. For tunneling measurement, we employed a Pt-Ir tip and a Ni-Al conducting wire. The system is made up of several components, such as an R9 controller, a sample holder, a

scan head, a preamplifier, a bias drive amplifier, a lock-in amplifier, and a CCD camera, among others.

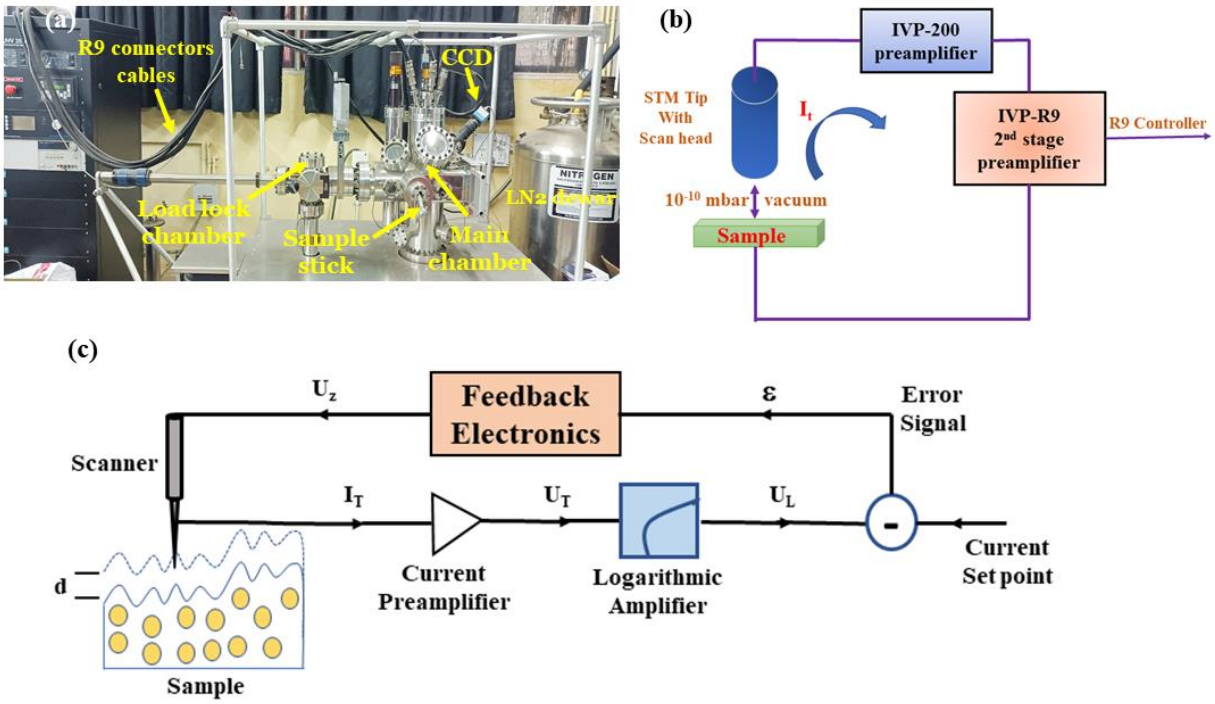

Figure 2.12: (a) Image of the RHK UHV-STM in our lab. (b) Schematic diagram to detect the tunneling current. (c) The schematic diagram for imaging.

The temperature was maintained constant throughout the data scan, and no temperature drift was noticed. In a modulation mode with a small ac bias, the $\frac{dI}{dV}$ was measured. The data was collected by applying a constant direct current (dc) bias and a small alternating current (ac) modulation voltage (much smaller than the dc bias) to measure the differential tunneling conductance $\frac{dI}{dV}$. Performing a raster scan in the presence of ac modulation allows for the simultaneous recording of topography and spectroscopic data. The measuring system's noise floor was below 10 $\frac{pA}{\sqrt{Hz}}$. The local tunneling conductance map (i.e. contour plot of $g = \frac{dI}{dV}$) taken at a constant dc bias V is the. The circuit diagram for measuring the tunneling current is shown in Fig.2.12(b). The schematic diagram for imaging is given in Fig. 2.12(c)

2.4.3 Electrical and magnetic transport measurements

We have used a homemade cryostat for electrical measurements up to LN_2 temperature. For electrical and magneto-transport measurements below LN_2 temperature, we have used a cryogen-free Pulsed tube cycle-based cryocooler and a Dynacool PPMS (Quantum Design, USA) up to a magnetic field of 9T. For the resistivity measurements of rare-earth nickelates thin films, we have used a Keithley source meter 2400/2410. The resistivity and Hall measurements of ferromagnetic Heusler alloys have been done in a 9T-Dynacool PPMS using the electrical transport option (ETO). All the electrical contacts were made with a standard four-probe method using copper wire and conducting silver epoxy. The electrical resistivity (ρ) of all the samples was determined using the following formula:

$$\rho = R\frac{A}{L} \tag{2.7}$$

where A is the cross-sectional area of the samples and l is the distance between the two voltage leads. The schematic diagram of the sample device used for the longitudinal resistivity and Hall resistivity measurements is given in Fig. 2.13(a). Figure 2.13(b) represents the image of the PPMS puck for the ETO measurements.

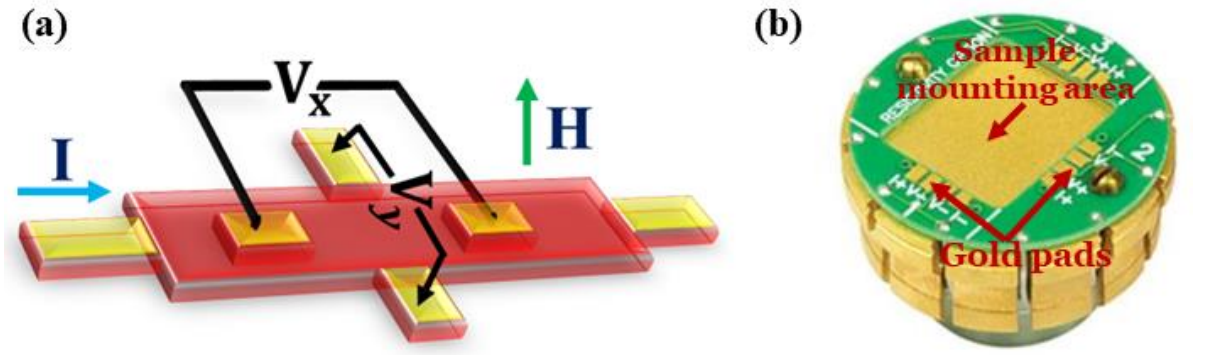

Figure 2.13: (a) Schematic diagram of the sample device used for longitudinal voltage (V_x) and Hall voltage (V_y) measurements. (b) Image of the PPMS puck used for the transport measurements.

2.4.4 Temperature-dependent magnetic measurements

A vibrating sample magnetometer (VSM) is effectively used to determine the dc magnetization of the sample. The VSM module of PPMS made of a linear transport motor for vibrating the sample, a gradiometer pick-up coil detecting the response, and electronics set up for signal detection of the sample as shown in the Fig. 14 [25]. The basic principle of VSM is primarily

governed by Faraday's law of induction. Using a superconducting solenoid magnet, a magnetic field magnetizes the sample when a magnetized sample vibrates inside the pick-up coil, a voltage is produced in the coil. Then the induced voltage is given by

$$V_{coil} = -\frac{d\varphi}{dt} = -\left(\frac{d\varphi}{dz}\right)\left(\frac{dz}{dt}\right) \tag{2.8}$$

Where φ is the magnetic flux enclosed by the pick-up coil and z is the direction of the sample to the coil. When the sample oscillates sinusoidally, the induced voltage in the coil is established in the following form;

$$V_{coil} = \mathrm{CmA\omega Sin(\omega t)}$$

$$= \mathrm{CmA}\sqrt{f}\,\mathrm{Sin}(2\sqrt{f}\,\mathrm{t}) \tag{2.9}$$

Here, C is the calibration constant, m is the magnetic moment of the sample, A is the amplitude of the sample, and f is the frequency of oscillation of the sample.

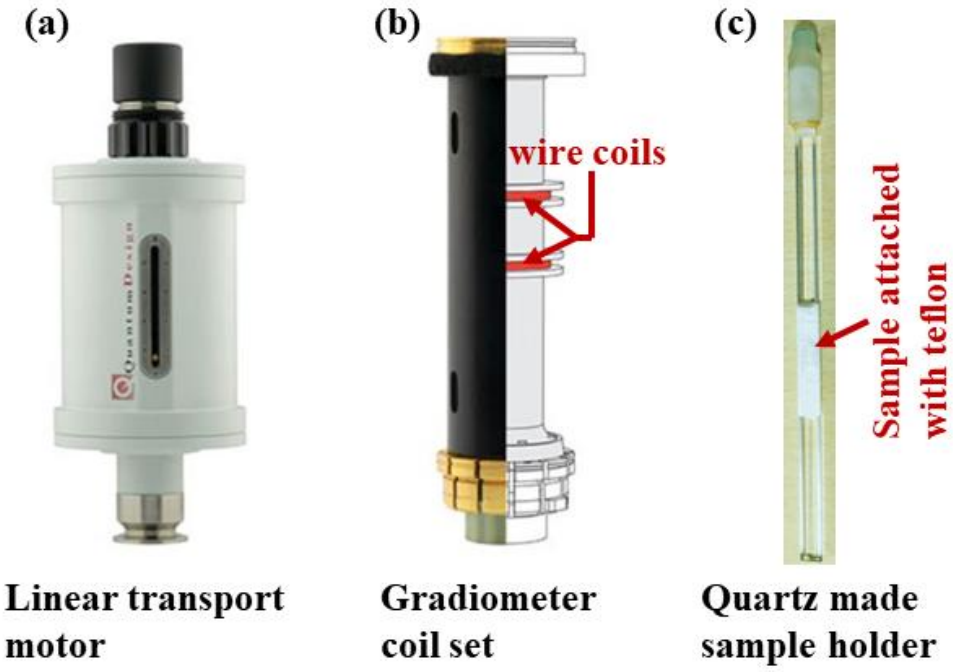

Figure 2.14: (a) Image of the PPMS VSM linear transport motor. (b) Image of the PPMS VSM gradiometer coil set. (c) An image of the PPMS VSM sample holder used to mount the sample.

The output of the pickup coil is connected to the preamplifier along with the VSM module which is attached to a lock-in amplifier providing phase-sensitive detection. Under a certain

magnetic field, the moment is induced inside the material. A vertical sinusoidal mechanical oscillation is provided to the sample so that magnetic flux is enclosed with the help of a pick-up coil as a function of time. The moment is measured as a function of time, magnetic field, and temperature. The system has high resolution which means it can detect the change of magnetic moment less than 10^{-6} emu.

For the measurement, the investigating sample is usually wrapped in an insulating Teflon tape and attached in a non-magnetic quartz paddle /copper sample holder, and then the sample holder is mounted inside the chamber. The chamber is roughed and purged three times after mounting the sample. Then the supreme position of the sample is set through the output signal scanning process. Once the sample position is optimized, then we start the measurement. The magnetic moment is determined in terms of emu by induced voltage with respect to the sinusoidal vibration. We have measured the magnetization (M) as a function of temperature (T) using two protocols and magnetic field (H) from 2-400 K under a fixed magnetic field. In the zero field cooling (ZFC) process, the sample is cooled to a low temperature from room temperature without a magnetic field and then M-T data has been recorded in the heating process under the magnetic field. In the case of field cooling (FC) mode, M-T data is taken under H during the cooling process. M-H measurements have been performed in the field range of $-5\ T \leq H \leq +5\ T$ at different temperature ranges.

References:

[1] Ravindra Singh Bisht, Investigation of Metal Insulator Transition in 3D Transition Metal Oxides, Ph.D. thesis, University of Calcutta, India (2019).

[2] T. Venkatesan, X. D. Wu, A. Inam, and J. B. Wachtman, Appl. Phys. Lett. **52**, 1193 (1988).

[3] T. J. Jackson and S. B. Palmer, J. Phys. D. Appl. Phys. **27**, 1581 (1994).

[4] Y. Hiroshima, T. Ishiguro, I. Urata, H. Makita, H. Ohta, M. Tohogi, and Y. Ichinose, J. Appl. Phys. **79**, 3572 (1996).

[5] M. A. Paranjape, K. S. Shankar, and A. K. Raychaudhuri, J. Phys. D. Appl. Phys. **38**, 3674 (2005).

[6] R. Bachelet, D. Pesquera, G. Herranz, F. Sánchez, and J. Fontcuberta, Appl. Phys. Lett. **97**, 121904 (2010).

[7] M. Ohring and A. Haldipur, Rev. Sci. Instrum. **42**, 530 (1971).

[8] P. B. Hirsch, Phys. Bull. **8**, 237 (1957).

[9] J. C. Woolley, J. Mech. Phys. Solids 6, 83 (1957).

[10] Rajib Nath, Investigation of novel electrical and magnetic properties of perovskite oxides, Ph.D. thesis, University of Calcutta, India (2018).

[11] D. McMullan, Scanning **17**, 175 (2006).

[12] M. Scimeca, S. Bischetti, H. K. Lamsira, R. Bonfiglio, and E. Bonanno, Eur. J. Histochem. (2018).

[13] G. Binnig, C. F. Quate, and C. Gerber, Phys. Rev. Lett. **56**, 930 (1986).

[14] A. K. Raychaudhuri, Curr. Opin. Solid State Mater. Sci. **6**, 67 (2002).

[15] J. B. JOHNSON, Nature **119**, 50 (1927).

[16] H. Nyquist, Phys. Rev. **32**, 110 (1928).

[17] H. B. Callen and T. A. Welton, Phys. Rev. **83**, 34 (1951).

[18] A. Ghosh, S. Kar, Aveek Bid, and A. K. Raychaudhuri, arXiv: Cond-Mat./0402130 v1,

4th Feb (2004).

[19] Sh. Kogan, Electronic noise and fluctuations in solids, Cambridge University Press, 1996.

[20] J. H. Scofield, Rev. Sci. Instrum. **58**, 985 (1987).

[21] P. D. Welch Modern Spectral Analysis, Edited by D.G.Childers (IEEE press, John Wiley and Sons, New York, 1978) page 17.

[22] S. Kundu, T. Bar, R. K. Nayak, and B. Bansal, Phys. Rev. Lett. **124**, 095703 (2020).

[23] G. Binnig and H. Rohrer, Surf. Sci. **126**, 236 (1983).

[24] E. L. Wolf, Principles of Electron Tunnelling Spectroscopy, Oxford University Press, Oxford, 1989.

[25] Q. Design, Physical Property Measurement System Vibrating Sample Magnetometer (VSM) Option, User's Manual, Design 152 (2008).

Chapter 3 Emergence of large thermal noise close to a temperature-driven metal-insulator transition

In this chapter, we report that close to a Mott transition there is an emergence of large thermal noise which occurs concomitantly with large correlated flicker noise (1/f noise) with significant non-Gaussian content. This was observed in $NdNiO_3$ films grown on crystalline $SrTiO_3$ substrates with different crystallographic orientations that show a hysteretic transition from a high-temperature metallic phase to a low-temperature insulating phase. It has been also proposed that the existence of large noise (both thermal and flicker noise) owes its origin to electronic phase separation that exists near the metal-insulator transition.

Content of this chapter has been published in: **S. Chatterjee**, R. S. Bisht, V. R. Reddy, and A. K. Raychaudhuri, "Emergence of large thermal noise close to a temperature-driven metal-insulator transition," **Phys. Rev. B,** 104, 155101 (2021).

3 Emergence of large thermal noise close to a temperature-driven metal-insulator transition

3.1 Preface

In modern condensed matter physics, the physics of metal-insulator transition (MIT), in which a metal with delocalized electrons makes a transition to an insulating state with strongly localized electrons, has been an intensively researched topic. Even though this topic has received key contributions that have enriched it, there are still fundamental issues that need to be addressed. What distinguishes the MIT phenomenon is its generality, which has been seen in a variety of systems, and the presence of particular aspects in MIT physics that are present regardless of material details. The field of MIT has historically progressed in two primary directions. One direction is the disorder-driven Anderson transition [1–3], where at the transition the density of states (DOS) at the Fermi level $N(E_F) \neq 0$. However, the localized nature of the electronic states at about Fermi level E_F gives birth to a unique character for electronic transport. In general, the concept of a mobility edge is used to distinguish between extended and localized states in the energy space. This transition is typically influenced by disorder and/or carrier density, which modulate the mobility edge and Fermi level, respectively. The other broad direction is the correlation-driven Mott transition [4], in which significant electron correlation drives the DOS at E_F to split into two bands and $N(E_F) \rightarrow 0$. In recent years, there has been a convergence of the above two directions, known as the Mott-Anderson transition, when both disorder and correlation are present [5–7]. It has been demonstrated that the presence of disorder in a Mott transition substantially modifies $N(E_F)$ [8].

The thermodynamics of MIT has significant implications. Whereas the Mott transition is typically conceived of as a first-order transition that can be broadened by disorder [5,9–12], the Anderson transition is generally thought of as a continuous transition [1,3]. Like any other phase transition, one may anticipate divergence in the correlation length and a critical slowing down in MIT. Recently, such critical slowing down at a Mott transition temperature has been found using noise measurements and nuclear magnetic resonance relaxation time

measurements in polymeric/organic conductors with the controlled disorder [9–11] as well as oxides like V_2O_3 experiencing Mott transition [12].

In this chapter, we explore one aspect of the temperature-driven MIT. We observe that in a narrow temperature range close to the transition temperature T_{MI}, together with a slowing down of relaxation time, the thermal noise has a significant value that is substantially larger than the canonical Johnson-Nyquist (JN) thermal noise spectral power density (SPD) $4k_BTR$ [13,14]. JN spectral power density $4k_BTR$ is the thermal noise in a resistor R maintained at a temperature T. At temperatures close to the MIT temperature (T_{MI}), the large thermal noise also arises together with large non-Gaussian low-frequency flicker noise with SPD, $S_V(f) \propto \frac{1}{f^{\alpha}}$ with characteristic $\alpha \sim 1$. Large flicker noise has been seen in oxides such as VO_2 [15], $SmNiO_3$ [16], and $NdNiO_3$ (NNO) [17–19]. However, large thermal noise, as reported in this chapter, has not been observed in previous investigations on flicker noise. We also address the possible origin of such large noise that can emerge from electronic phase separation (EPS) near MIT.

The experiments presented here measured thermal noise at the MIT temperature in films of NNO grown on single crystalline substrate $SrTiO_3$ (STO) with three different orientations: (100), (110), and (111). NNO undergoes temperature-driven Mott MIT, which has received a lot of interest in recent years [20,21]. Although the exact nature of the MIT in this material is unknown, it has been demonstrated that the temperature-driven MIT in NNO contains a significant contribution from electron correlation. As a result, we refer to it as a Mott transition. Despite being performed on a specific system NNO, the presented phenomena are of general validity and should be observed in any correlation-driven transition. JN noise is the spontaneous thermal noise that occurs when a resistor R is held at a fixed temperature T and exhibits a voltage fluctuation δv_{th}. Thermal noise [13,14] is a result of the fluctuation-dissipation theorem (FDT) [22] and manifests itself as a voltage fluctuation (without an applied bias) across a dissipative circuit element such as a resistor R maintained at a bath temperature T. The subscript "th" in δv_{th} refers to thermally induced spontaneous voltage fluctuations. The mean square voltage fluctuation of thermal noise δv_{th}^2 measured over a bandwidth Δf is described by the relationship [13,14].

$$\langle(\delta v_{th}^2)\rangle = (4k_BTR)\Delta f \tag{3.1}$$

Equation (3.1) assumes that the electron system at temperature T_e is in equilibrium with the phonon thermal bath at temperature T, so that $T_e = T$. The fluctuation provides a fundamental measurement of the bath temperature T and acts as the basis for noise thermometry in metrology [23]. The frequency-independent SPD of equilibrium JN thermal noise is given as [13,14].

$$S_{th} = 4k_B TR \tag{3.2}$$

The effective electron temperature T_e can be determined using equation (3.2). In a hot electron system $T_e > T$ and the thermal noise $S_{th} > 4k_B TR$ [24]. The JN noise relation is a manifestation of the FDT's validity [22,25,26]. The deviation of the thermal noise S_{th} from the canonical value of $4k_B TR$ is frequently interpreted as a symptom of FDT violation. Thermal noise emerges in the absence of a bias and is bias independent. When a bias V is put across the resistor R, it coexists with the flicker noise. The flicker noise has SPD, $S_V(f) \propto \frac{1}{f^{\alpha}}$, and is typically referred to as $\frac{1}{f}$ noise when $\alpha \sim 1$. For a particular frequency f, $S_V(f) \propto V^2$. The flicker noise is usually distinguished from the thermal noise by its quadratic dependency on the bias V [27].

3.2 Experimental methods

NNO films with thicknesses of ~ 15 nm and rms roughnesses of ~ 0.4 nm were grown on single crystalline STO substrates with different crystallographic orientations using pulsed laser deposition with a KrF (= 248 nm) laser at a fluence of 2.5 J/cm^2. Temperature and oxygen pressure throughout growth were 0.15 mbar and 625°C, respectively. In addition to conventional X-ray diffraction (XRD), the XRD data was employed to produce reciprocal space mapping (RSM). The X-ray RSM measurements are performed using the Bruker D8-Discover system, which is outfitted with Cu K_α radiation, an Eulerian cradle, a Goebel mirror, and a LynxEye detector. Leptos software is used to analyze the acquired data. Both symmetric (002) and asymmetric (103) reflections are used for the RSM measurements. The dc electrical resistivity (ρ) of the films was measured in a closed cycle cryostat (pulsed tube) in a colinear four-probe configuration with Cr/Au contact pads down to 3 K. Both heating and cooling cycle data were collected. The noise measurements (80 < T < 300 K) were carried out in a liquid nitrogen cryostat using a four-probe ac excitation technique [28], which enables the simultaneous measurements of the flicker noise and the frequency-independent thermal noise

S_{th}. The temperature was maintained at ±5 mK. The lock-in amplifier-based ac modulation noise detection technique allows us to concurrently measure the spectral power of voltage fluctuation $\delta v(t)$ from the sample and the background noise [29,30]. Whereas the former contains information about flicker noise, the latter contains information about thermal noise. The thermal noise S_{th} has been calibrated against a standard 1-kΩ resistor to ensure that it is near to the JN value of $4k_BTR$ and that the shielding process is effective in mitigating spurious noise that contributes to the background and frequently causes S_{th} to deviate from the JN value. An ultrahigh vacuum scanning tunnelling microscope was used to capture a spatially resolution image of local tunneling conductance $G(V)$ over an aerial range of 0.5 × 0.5 μm at a fixed bias V. The measurements were made at a base pressure of 10^{-10} mbar. $G(V)$ represents the spatial dependency of the DOS at the E_F and was measured using a modulation method with a small ac bias added to the dc bias V, which is utilized to hold the tip above the film at a constant height. The small ac modulation voltage ($\Delta v \ll V$) was used to determine the differential tunneling conductance $g(V) = \frac{\Delta i}{\Delta v}$ from the modulation Δi current. Doing a raster scan in the presence of ac modulation allows for the simultaneous recording of topography and spectroscopic data. The system has a current noise level of ≤10 $\frac{pA}{\sqrt{Hz}}$. The local tunneling conductance map (LCMAP) is a contour plot of $G(V)$ taken in raster scan mode with a fixed dc bias $V = 0.5\,V$. The color code represents the equivalent value of $G(V)$, with higher tunneling conductance regions being metallic.

3.3 Results

3.3.1 Structural data

Figure 3.1(a)-(c) displays the RSM data measured along (103) reflections for all three films investigated. The grown films are highly oriented, as revealed by the XRD data. The RSM data also indicated that the films are strain relaxed with residual strain (see Table 3.I) due to a finite mismatch lattice constants of the film and the substrate. Figure 3.1(d)-(f) illustrates the atomic force microscopy images of all the films collected over a 500 nm × 500 nm area. The film is compact and has coherent grains, which we attribute to strain relaxation. As observed in the atomic force microscope (AFM) image, strain relaxation produces coherent grains with typical sizes of ≈ 35–40 nm.

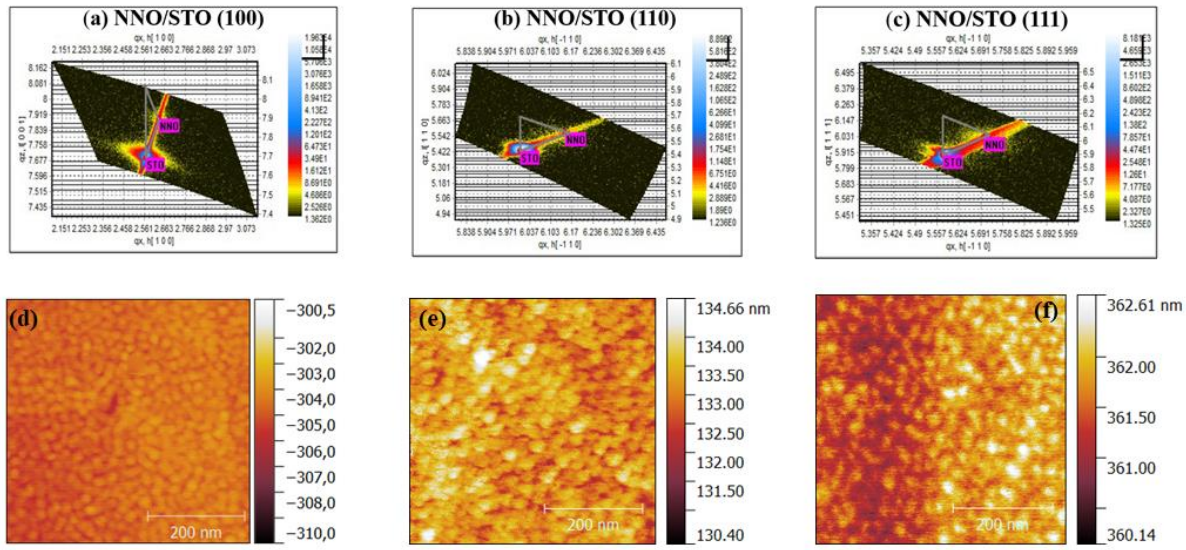

Figure 3.1: (a)-(c) The RSM data for NNO thin films grown on STO single crystalline substrate with different orientations measured along (103) reflection. q vectors are in units of nm^{-1}. The grey solid lines show the relaxation triangle. (d)-(f) The AFM images of the NNO thin films grown on STO single crystal substrate with different orientations taken over an area of 500 nm × 500 nm.

Strain inhomogeneity is caused by strain relaxation and the formation of misfit dislocations, which modifies the nature of the EPS in the coexisting phases of the film. Table 3.I display the relevant parameters derived from RSM data. As the orientation of the STO substrate is altered from (100) → (110) → (111), there is a progressive shift in the in-plane strain $\epsilon_{||}$ (and concomitantly the out-of-plane strain $\epsilon_{\perp}$). The film grown on STO (100) has a small, positive value for $\epsilon_{||}$, whereas the film grown on STO (111) has a large, negative value for $\epsilon_{||}$. This pattern is also seen in the values of relax, which are close to unity, indicating almost perfect relaxation ($R = \frac{a_{film} - a_{substrate}}{a^{R}_{substrate} - a_{substrate}}$). We also observe a steady increase in the full width at half maximum (FWHM) of the rocking curve of the films, which initially stood at a value of 0.373^0 in the film on STO (100) and eventually rose to a value of 0.607^0 in the film on STO (111). In Table 3.I display all the related parameters. Hence, there is progressive disordering in the films of NNO grown on STO with different orientations in the order (100) → (110) → (111). This observation has crucial implications for transport and thermal noise data, as detailed below.

Table 3.I: Relevant structural data obtained from RSM: Out-of-plane strain = $\epsilon_{\perp}=\frac{c_{film}-c_{film}^{R}}{c_{substrate}}$, in-plane strain = $\epsilon_{||}=\frac{a_{film}-a_{film}^{R}}{a_{substrate}}$, a = in-plane lattice constant, and c = out-of-plane lattice contant. Subscripts "film" and "substrate" refer to the fully relaxed film and the substrate, respectively. The subscript R refers to the fully relaxed film. Lattice constants of STO (cubic) a, $c_{substrate}$ = 0.3905 nm; lattice constant of NNO (pseudocubic), a, c_{film}^{R} = 0.3807 nm; $\delta\omega°$ is the full width at half-maximum of the rocking curve in degrees.

Sample	$\epsilon_{\perp}$ (%)	$\epsilon_{||}$ (%)	a_{film} (nm)	c_{film} (nm)	$\delta\omega$ (°)
NNO/STO(100)	-0.081	0.094	0.38107	0.38038	0.373
NNO/STO(110)	0.015	-0.017	0.38063	0.38076	0.489
NNO/STO(111)	0.359	-0.419	0.37906	0.38210	0.607

3.3.2 Transport data

The resistivity (ρ) data for all of the films as a function of temperature are displayed in Fig. 3.2(a). All of the films feature MIT with hysteresis. Hysteresis occurs in a Mott transition due to its underlying first-order nature and can be controlled by the extent of coexisting phase fractions [31,32], as demonstrated in systems such as $PrNiO_3$ and V_2O_3. The T_{MI} is determined by changing the sign of the derivative $\frac{d\rho}{dT}$ as shown in Fig. 3.2(b)-(d). All the T_{MI} values are given in Table 3.II. The transition temperatures vary according to the heating and cooling cycles. T_{MI} is lowest in the film grown on STO (100), which also has the lowest resistivity at 300 K, and T_{MI} is almost similar in the films grown on STO (110) and STO (111). In Fig. 3.2(a), the graph for the film NNO/STO (110) has been shifted vertically for clarity. The T_{MI} for these two films is almost 50 K higher than that of NNO/STO (100) (see Table 3.II). Higher values of ρ in the films on STO (110) and (111) arise from more disorders as noted before (see Table 3.I). This particular aspect, however, is outside the scope of this chapter and is not discussed further.

In the transition region, EPS results in the coexistence of insulating and metallic phases, as observed by spatially resolved techniques [18,33]. The temperature dependence of the volume fractions of the coexisting phases can be determined from the ρ vs T plots using effective

medium theory [34]. The insulating fractions f_i of all the three films and their temperature dependence are presented in Fig. 3.3(a)-(c) (the metallic fraction $f_m = 1 - f_i$). For all the

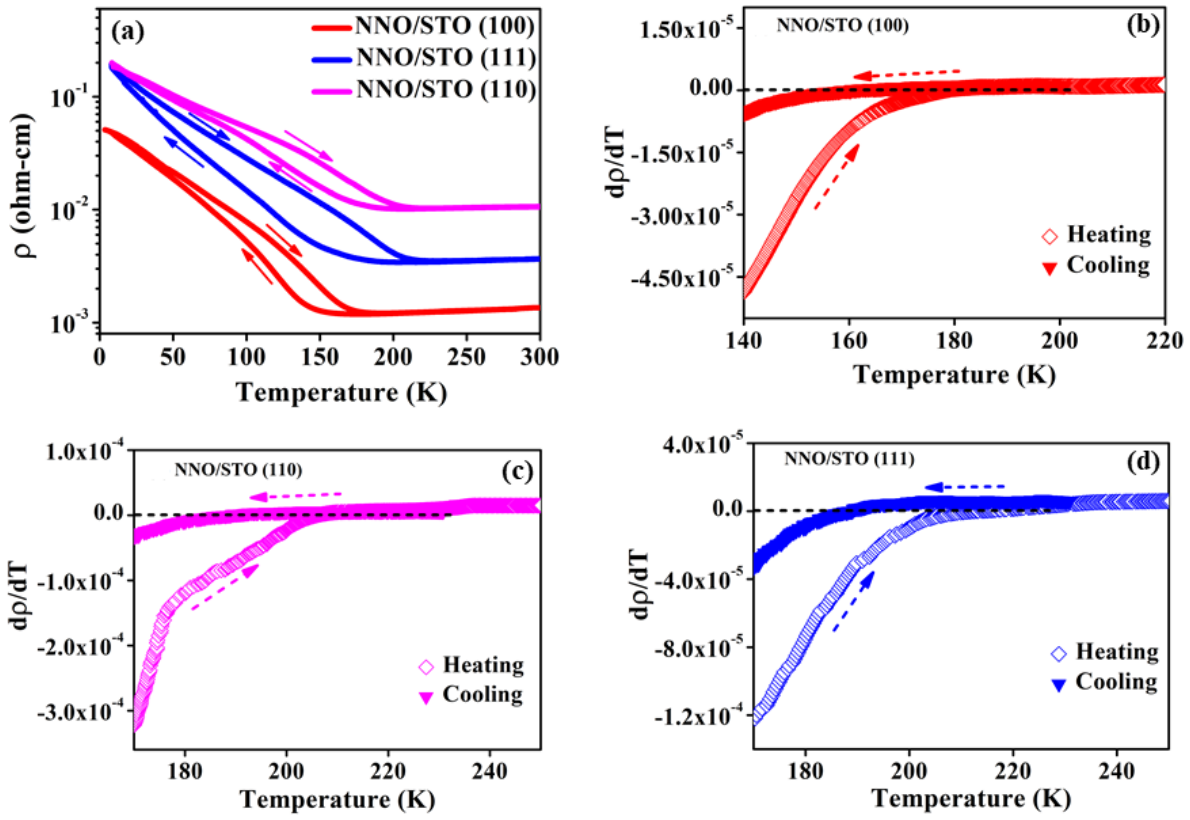

Figure 3.2: (a) Temperature-dependent resistivity data for all three NNO films grown on STO single crystal substrate with different orientations. The curve for the film NNO/STO (110) has been shifted for clarity. (b)-(d) The $\frac{d\rho}{dT}$ curves for all three films studied.

films, the insulating fraction f_i at $T = T_{MI}$ ranges between 0.09 and 0.11. The width of the transition δT_{MI} is defined as the temperature range over which the insulating volume fraction changes from a value of 10 to 90 %. Both the heating and cooling cycles δT_{MI} values are indicated in Fig. 3.3. These values are shown in Table 3.II. The width of the transition δT_{MI} rises from STO (100) to STO (110) to STO (111). This is most likely owing to increased disorder in the films when the orientations shift, as previously mentioned.

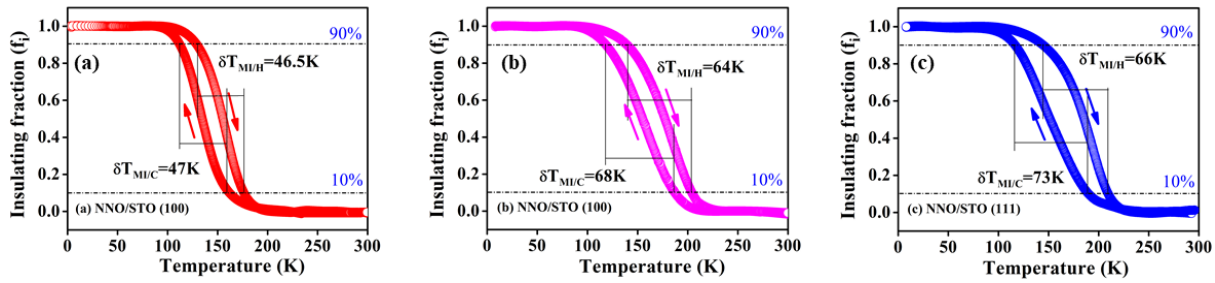

Figure 3.3: (a)-(c) Insulating fractions (f_i) for the NNO films grown on STO substrates with different crystallographic orientations. The figure also marks the width of the transition δT_{MI} defined as the temperature region between 10% and 90% of the transition. Data is shown for both heating and cooling cycles.

Table 3.II: Parameters from electrical transport and noise measurements: H, heating cycle; C, cooling cycle; T_{MI}, metal-insulator transition temperature; δT_{MI}, the width of transition; T^*, the temperature where thermal noise (S_{th}) exhibits a peak; ζ_M, the peak value of the ratio $\frac{S_{th}}{4k_BTR}$.

Sample	T_{MI} (K)		δT_{MI} (K)		$T^*(K)$		$\frac{T^*}{T_{MI}}$		ζ_M	
	H	C	H	C	H	C	H	C	H	C
NNO/STO(100)	177	160	47	47	160	142	0.90	0.89	10	4
NNO/STO(110)	206	189	68	64	200	182	0.97	0.96	11	7
NNO/STO(111)	211	187	73	66	228	202	1.08	1.08	12	10

3.3.3 Thermal noise

Figure 3.4(a)-(c) show examples of observed frequency-independent thermal noise (S_{th}) and flicker noise with spectral power dependency $S_V(f) \propto \frac{1}{f^\alpha}$ for the three films at a given temperature. In the figures, the two kinds of noises are indicated. Figure 3.4(a)-(c) indicates that the thermal noise S_{th} in the films, as well as the flicker noise, can be measured accurately. At the temperatures, the values of S_{th} presented in the figures are nearly $4k_BTR$.

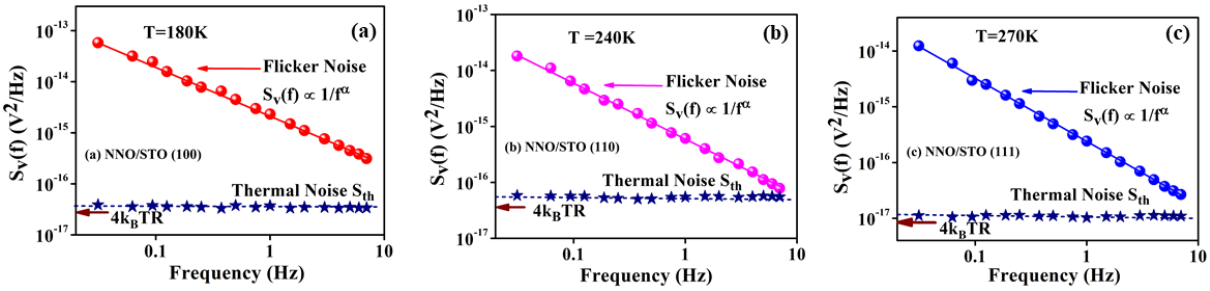

Figure 3.4: (a)-(c) Spectral power density $S_v(f)$ for the flicker noise varying as $\frac{1}{f^{\alpha}}$ and thermal noise S_{th} (frequency-independent power spectrum) in the three NNO films shown in a temperature region away from the transition region. The Johnson-Nyquist value of $4k_BTR$ for the resistance R at the temperature of T is marked by an arrow.

The variation of the measured thermal noise $S_{th}(T)$ in the three films compared to the canonical JN value of $4k_BTR$ is illustrated in Fig. 3.5(a)-(b). To quantify the extent of thermal noise deviation from the JN value, we defined the ratio $\zeta(T) \equiv \frac{S_{th}(T)}{4k_BTR}$, which is the measured thermal noise $S_{th}(T)$ scaled by the JN value. In Fig. 3.5(a)-(b), we showed the ratio $\zeta(T)$ as a function of temperature T for all films for both heating and cooling cycles.

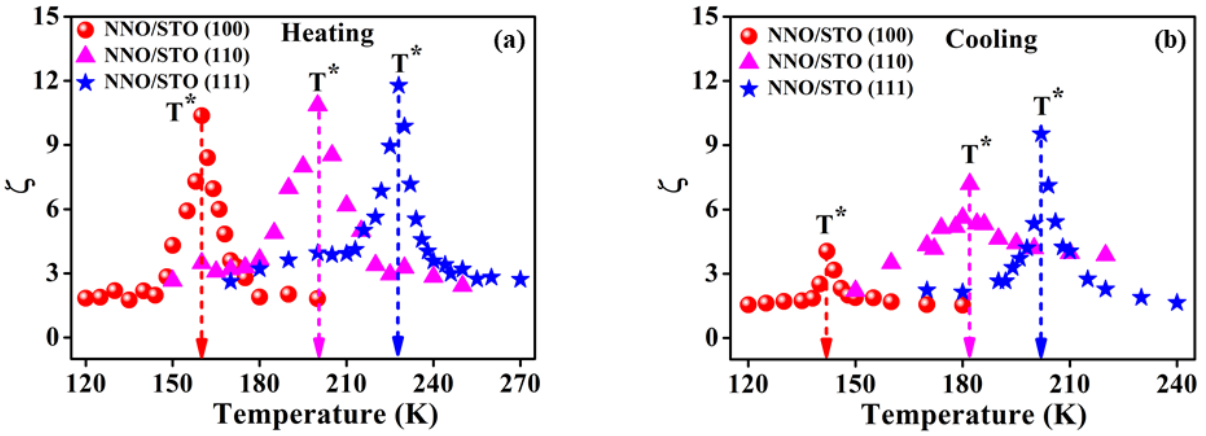

Figure 3.5: (a)-(b) Temperature dependence of the ratio ζ for the three NNO films grown on STO substrates with different orientations. Data are shown for both heating and cooling cycles. The arrows mark the temperature T^*, where the ratio ζ shows a peak.

It is evident that a clear maximum is visible in $\zeta(T)$ around a particular temperature, which we designate as T^*. In the narrow temperature range close to the MIT, all the films studied during

the cooling cycle $\zeta_M > 5$ and the heating cycle $\zeta_M > 10$. Additionally, it is noted that, despite being very close to the MIT transition temperature T_{MI}, the temperature T^*. where $\zeta(T)$ peaks are distinct from it. Table 3. II shows the parameters derived from the noise data. The magnitude of the thermal noise and the scaled value ζ need to be clarified. The as-measured frequency-independent thermal noise can get mixed with extraneous contributions which can add on to the observed noise and thus can make ζ higher than the expected value of 1 as would happen when the background noise only rises from the JN thermal noise. However, extraneous contributions can be reduced by shielding them from external noise sources. It is possible to acquire a measure of the mitigation of extraneous contributions by measuring the background noise with a calibrated resistor of value R_{calib} held at a known temperature T. If the extraneous noise contributions are correctly removed, the measured background noise will be close to the intended value of $4k_BTR_{calib}$. In our experiment, $R_{calib} = 1$ kΩ was used. From these measurements, we establish that the maximum value of ζ that can arise from extraneous noise sources would make $\zeta \leq 1.5$–2. Hence, the observed increase of to greater than 2 is not due to external noise sources. The presence of large thermal noise at temperatures close to but distinct from T_{MI} is an important finding of the study. The enhancement of thermal noise is dependent on substrate orientation and in-plane strain, as shown in Table 3.I derived from RSM data. The value of ζ_M and the ratio $\frac{T^*}{T_{MI}}$ increase progressively for films grown on STO(100) → STO(110) → STO(111) (see Table 3. II).

3.3.4 Flicker noise

The appearance of large S_{th} near MIT is accompanied by the appearance of significant low-frequency flicker noise, as illustrated in Fig. 3.6(a)-(c), which displays the temperature variation of the exponent α of the SPD of the flicker noise $S_V(f) \propto \frac{1}{f^\alpha}$ measured on the three films. A higher value of α indicates that lower frequency fluctuations contribute more to the SPD. It is found that for $T \sim T^*$, α deviates significantly from the expected value of α ≈ 1.0 ± 0.1 and reaches a high at $T \sim T^*$, where ζ also reaches a peak. The value of α at $T \sim T^*$ in all the films reaches a value of ≈ 1.2–1.3, which signifies a substantial shift in the spectral power to lower frequency. The predominance of lower frequency fluctuation results from the slowing down of relaxation time, as we will see later. The relative variance of the resistance

fluctuation $\frac{\langle \Delta R^2 \rangle}{R^2}$ also becomes large, reaching a peak at $T \sim T^*$. As demonstrated in Fig. 3.6(d)-(f),

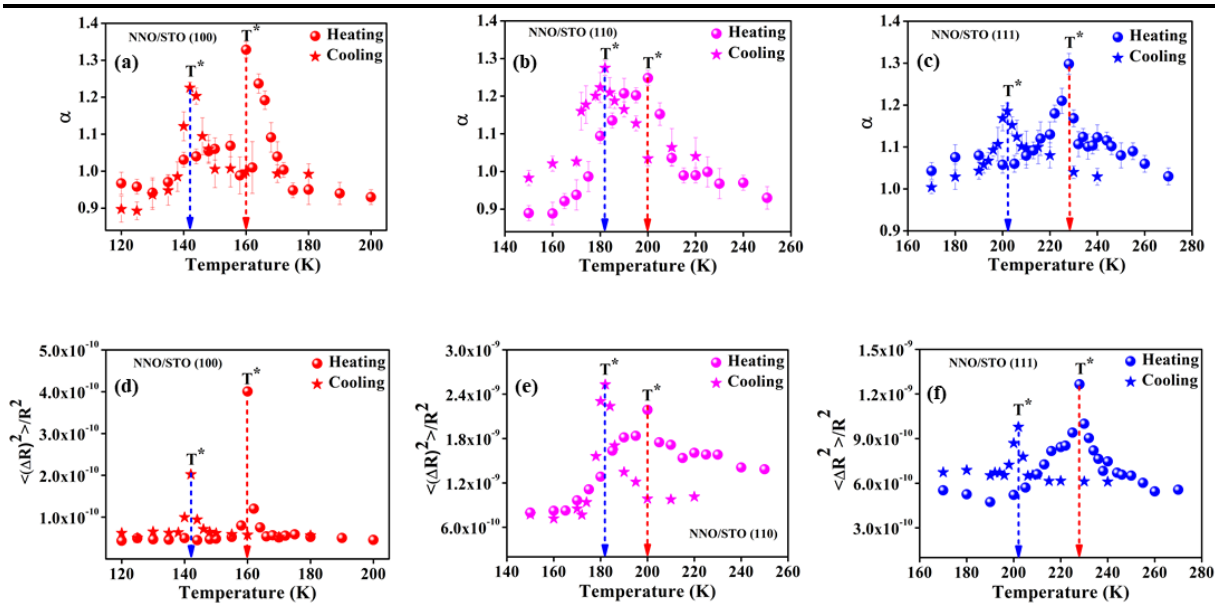

Figure 3.6: (a)-(c) Temperature dependence of the exponent α for the flicker noise spectral power density $\left(S_v(f) \propto \frac{1}{f^{\alpha}}\right)$, for all three NNO films grown on STO substrates with different orientations. The arrows mark the temperature T^* where the ratio ζ shows a peak. (d)-(f) Temperature-dependent relative variation of resistance fluctuation $\frac{\langle \Delta R^2 \rangle}{R^2}$ for the three NNO films grown on STO substrates with different orientations. The arrows mark the temperature where the ratio ζ exhibits a peak.

the peak value of the relative variance might be a factor of 2-3 more than the value at the baseline that occurs away from T^*. (Note: $\frac{\langle \Delta R^2 \rangle}{R^2} = \int_{f_{min}}^{f_{max}} \frac{S_V(f)}{V^2}\, df$ evaluated over the bandwidth of the measurement f_{max}, f_{min}). Interestingly, the peaks in α and $\frac{\langle \Delta R^2 \rangle}{R^2}$ do not occur at $T = T_{MI}$ but at T^* where the thermal noise also peaks. The low-frequency fluctuation that contributes to substantial flicker noise around the transition region is correlated, making the fluctuation non-Gaussian. This can be assessed using the normalized second spectrum, as shown in Fig. 3.7(a)-(c) for the films. The normalized second spectrum is denoted by [15,18,29]

$$\Sigma^2 = \int_0^{f_H - f_L} S^{(2)}(f_2) df_2 \tag{3.3}$$

where

$$S^{(2)}(f_2) = \frac{\int_0^{\infty} <\delta v^{(2)}(t)\delta v^{(2)}(t+\tau)> \cos(2\pi f_2 \varsigma) d\varsigma}{\left[\int_{f_L}^{f_H} S_V(f_1) df_1\right]^2} \quad (3.4)$$

where f_1 and f_2 are the frequencies associated with the first and second spectra, respectively. $\delta v(t)$ is the measured voltage fluctuation.

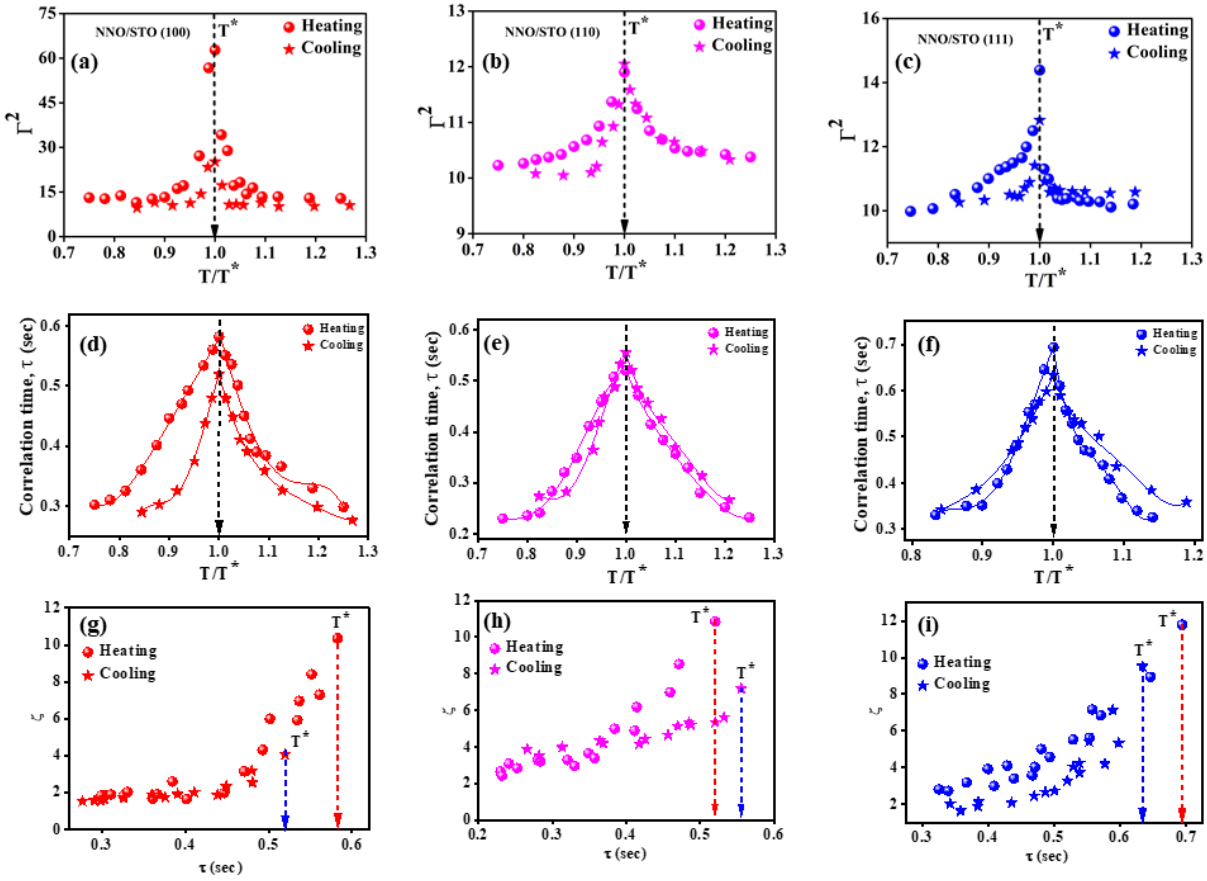

Figure 3.7: (a)-(c) The second spectra Γ^2 of the noise spectra for all three NNO films grown on STO substrate with different orientations with scaled temperature $\frac{T}{T^*}$ for heating and cooling cycles. (d)-(f) The correlation time τ as a function of scaled temperature $\frac{T}{T^*}$ for heating and cooling cycles for all three NNO films grown on STO substrates with different orientations. (g)-(i) Plot of ζ vs τ for heating and cooling cycles for all the three NNO films grown on STO substrate with different orientations.

When the noise sources from which fluctuations arise are correlated in nature, a large value of Γ^2 as observed close to T^* would be expected. The appearance of large noise is correlated with the emergence of slow fluctuations which can be observed from a longer correlation time (τ). τ can be determined from the autocorrelation function $[C(t)]$, which is related to the fluctuation times series $\delta v(t)$ by the relation

$$C(t) = < \delta v(t') \times \delta v(t+t') >_{t'} \quad (3.5)$$

where $< \cdots >_{t'}$ represents the time average. $C(t)$ shows an approximate exponential dependence for a small time and a non-exponential tail for a longer time. The representative plots $C(t)$ vs. t are shown in Fig. 3.8(a)-(c).

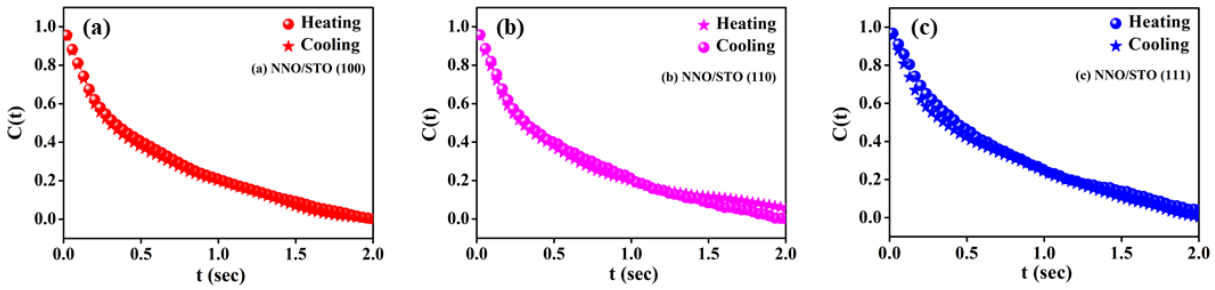

Figure 3.8: (a)-(c) Representative correlation function $C(t)$ as a function of t for all the three NNO films grown on STO single crystal substrate with different orientations at the T^*.

τ has been approximated as the time when $C(t) = \frac{1}{e}C(0)$. Figure 3.7(d)-(f) depicts a plot of τ vs scaled temperature $\frac{T}{T^*}$ for the three films. It can be seen that at $T \sim T^*$, the value of τ increases by a factor of three or more when compared to its value away from T^*. Correlation of the appearance of large S_{th} with the enhanced value of τ can be seen from a plot of ζ vs τ given in the insets of Fig. 3.7(g)-(i). This demonstrates a direct correlation between the two, indicating that the appearance of large thermal noise happens when there is a slowing down of time scales of fluctuation. As previously noted, prior findings of noise spectroscopy in polymeric conductors [9,10], as well as transition metal oxides [12,15–19] have indicated the formation of low-frequency correlated fluctuations near the MIT as detected from exponent α, variance $\frac{\langle \Delta R^2 \rangle}{R^2}$, and second spectra Γ^2. However, no report exists that shows a large deviation of S_{th} from the JN value.

3.4 Discussions

In the context of the Anderson transition, it has been observed that while crossing the metal-insulator transition from metallic samples to insulating samples in both two-dimensional metal-oxide-semiconductor field-effect transistors [35–37] and three-dimensional systems of doped

Si [38], the magnitude of the noise increases rapidly and by orders of magnitude as the electron localization length decreases $T \rightarrow 0$. The $\frac{1}{f}$ type flicker noise at the Anderson transition has been found to be a manifestation of Coulomb glass formed by localized electrons associated by long range Coulomb contact. These issues have been extensively theoretically explored [39], and it was argued that the slow relaxation of a finite number of fluctuators needed for the emergence of large $\frac{1}{f}$ originates from a slow rate of simultaneous tunneling of many localized electrons and by large activation barriers for their subsequent rearrangements. This concept has been used to study large flicker noise in quantum dot arrays [40], where the scenario proposed is a majority metallic phase coexisting with weakly connected dispersed nanoparticles. The appearance of long relaxation times is needed for the appearance of large flicker noise, which can be obtained by considering the correlated motion of extended clusters of charges [39,41].

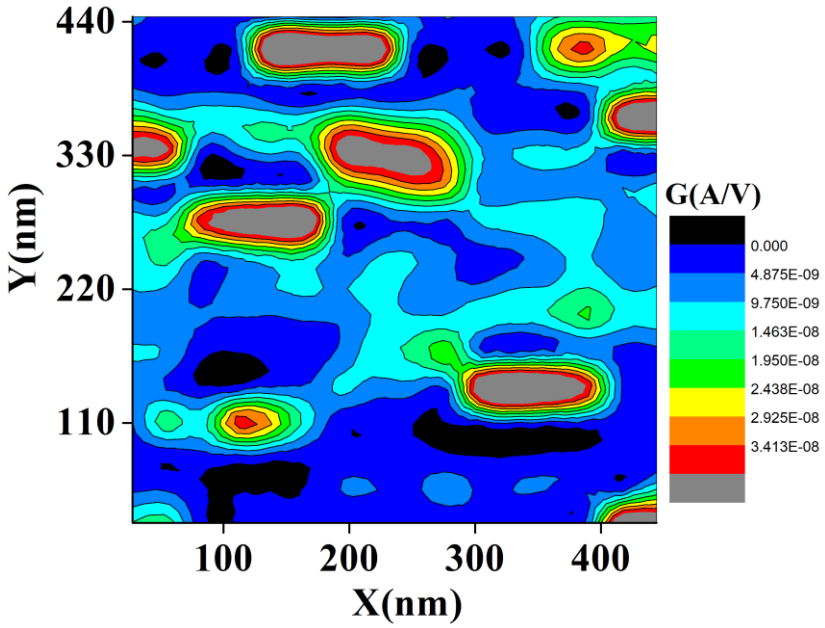

Figure 3.9: Local tunneling conductance map of an NNO film near the region of electronic phase separation. The color-coded conductance $G(A/V)$ is shown in the right bar.

It has been claimed that in such systems, there are a few main conductive channels, around which there are weakly coupled charged clusters with mobile charges, and it is the displacement of these charges that controls the mobility in the paths as well as acting as a source of long relaxation time and gives birth to large flicker noise [39,40]. We describe below how, with

some modifications, such a physical approach can be utilized in the context of Mott transitions where there is a coexistence of phases originating from EPS to understand the generation of large correlated flicker noise as well as large thermal noise. The physical prerequisite for both phenomena is the emergence of fluctuation with a lengthy correlation time.

Mott-type MIT is characterized by a shift in carrier density (n) at $T \sim T_{MI}$. Coexisting phases, as shown in EPS near MIT, introduce significant variation in n. This may be seen in the spatially resolved image taken by scanning tunneling spectroscopy (STS) on a film of NNO near MIT, as shown in Fig. 3.9. The STS image is an LCMAP that depicts existing heterogeneity in the local DOS near the Fermi level E_F. These heterogeneities can range in size from a few nanometers to tens of nanometers. The heterogeneous local DOS will result in a spatially varying local n [18]. The flicker noise in an EPS system, like in a percolating network, is large [42,43]. We would like to propose, as explained below, that the source of the large thermal noise can also be directly traced to EPS, which can result in a longer relaxation period. We present a simple physical scenario to this effect.

We propose the following physical scenario for an EPS near MIT with majority and minority phases. Figure 3.10 depicts a schematic of the proposed physical scenario. This is analogous to the physical model described above [39,40], which is made up of conductive paths with weakly connected charged clusters.

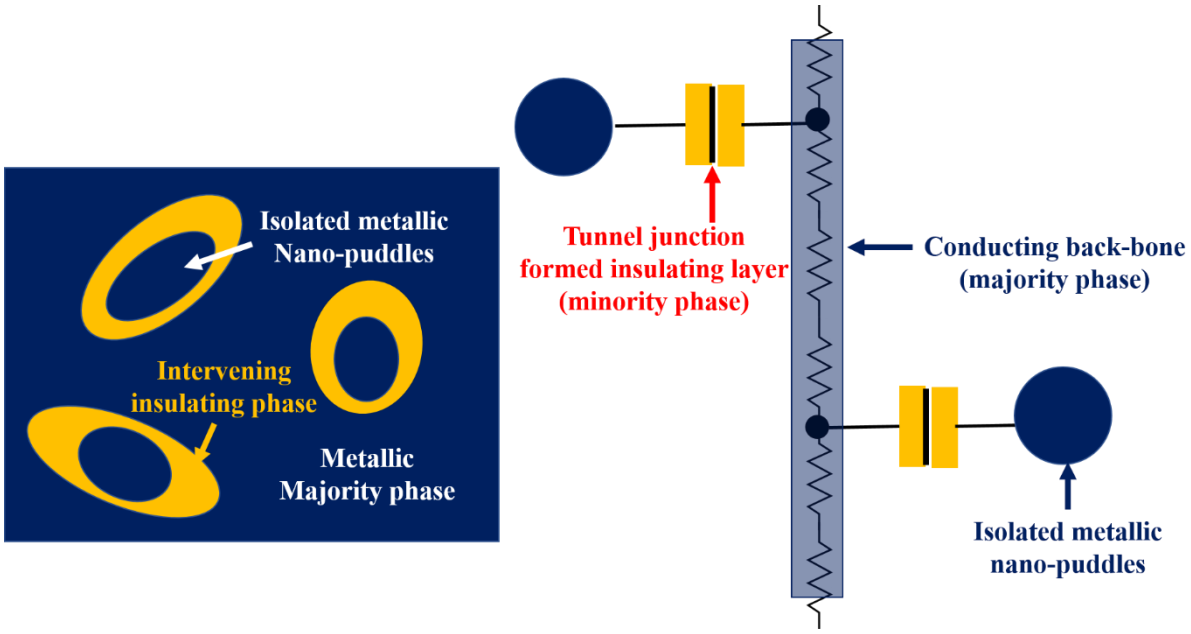

Figure 3.10: Schematic model of isolated metallic nanopuddles in the transition region connected to the metallic majority phase backbone by tunneling through the intervening minority insulating phase.

Noise, both thermal and flicker noise, will be large if there is a sparse phase of nanometric isolated metallic islands (which we describe as "nanopuddles") separated from the main backbone conducting phase (the majority phase) by an intervening insulating layer (the minority phase) that surrounds the nanopuddles. By tunneling through the intervening insulating layer, these metallic nanopuddles would serve as small capacitors coupled weakly to the main conducting phase backbone. (Fig. 3.3(a)-(c) shows that the insulating phase is the minority phase in the temperature range $T \sim T^*$.) The concept of a sparse majority phase trapped within the minority phase and separated from the main body of the majority phase has been presented in the context of the Griffiths phase [44], where slow electronic relaxation is observed [10,11,45]. So, the scenario provided here can be related to the general setting of EPS near a phase change.

The isolated metallic nanopuddles with a small enough average diameter ($\langle d \rangle$) and weakly connected to the main conducting path would show Coulomb charging when the charging energy $E_C \geq k_B T$ [46,47]. This notion has been widely applied in the context of charge transport in granular metal films and other granular metal-insulator composites. One would expect similar notions to be applicable in an EPS system, which is essentially a metal-insulator composite [48–51]. The Coulomb-charged weakly connected nanopuddles will have slow relaxation dynamics, yielding in nonequilibrium electron distribution. As a result, the Coulomb-charged nanopuddles will serve as a source of heating [52–54] and the polarization fluctuations around such charged nanopuddles would generate large noise [55]. Therefore, weakly coupled Coulomb-charged nanopuddles that may exist in the MIT region due to EPS are the source of both slow relaxation and large noise. The noise will significantly increase around the temperature T^* if the average size of the nanopuddles ($\langle d \rangle$) is such that the associated Coulomb charging energy E_C exceeds T^*.

The temperature T^* at which the thermal noise peaks are dictated by two factors: the number density (N_d) of such isolated nanopuddles and their average size ($\langle d \rangle$). As schematically depicted in Fig. 3.11, the N_d of such isolated nanopuddles embedded in the minority insulating phase is anticipated to depend on T. At the temperature range where N_d exhibits a broad maximum, the maximum noise will manifest for the reasons given below. Cooling below T_{MI} causes N_d to decrease as the insulating fraction expands to become the majority phase, progressively subsuming the nanopuddles. At $T \gg T_{MI}$, when the majority metallic phase fraction increases, it gradually subsumes the residual insulating phase, separating the

nanopuddles from the main phase and causing N_d to decrease. It is thus suggested that there will be an optimum temperature range where the phase fraction is such that a significant number of weakly connected nanopuddles can exist as part of the EPS and N_d has a broad maximum.

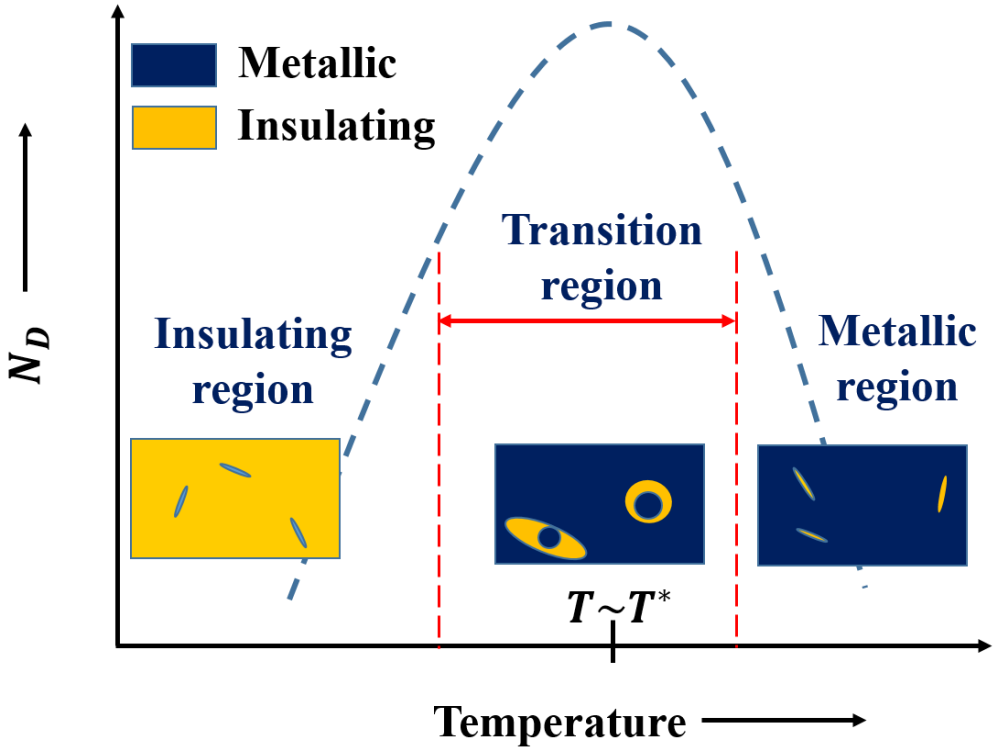

Figure 3.11: Schematic model of phase separation in the three temperature regions and a suggested qualitative dependence of N_d, number density isolated nanopuddles embedded in the minority insulating phase.

The temperature T^* can be used to calculate the average size of the nanopuddles. The $\langle d \rangle$ of the Coulomb-charged nanopuddles can be estimated from $E_C = \frac{e^2}{2C_d}$ (e = elementary charge), where $C_d = 2\pi\epsilon_0\epsilon_d\langle d \rangle$ = capacitance of a metal nanopuddle of diameter $\langle d \rangle$ embedded in a medium with the dielectric constant ϵ_d and ϵ_0 = free space permittivity [48]. As previously proposed for $T \sim T^*$, where the noise is high, the nanopuddles will be Coulomb charged, and this will occur when $E_C \geq k_B T^*$. Using the measured T^* and $\epsilon_d \approx 5$ as the dc dielectric constant of NNO [56], an estimate of $\langle d \rangle \leq$ 15–20 nm was obtained. $\langle d \rangle \leq$ 20 nm for NNO/STO (100) and it decreases to $\leq$ 15 nm for NNO/STO (111) that has larger ζ and higher T^*. Such nanopuddles have been found in LCMAPs obtained with STM (see Fig. 3.9) as well

as in previous studies in the context of EPS near MIT in NNO [18]. We should highlight that the estimate of $\langle d \rangle$ was made assuming a spherical shape for the nanopuddles, which may have an ellipsoidal shape in actuality. For very large nanopuddles, the Coulomb charging energy E_C is small (since it is $\propto \frac{1}{d}$), hence the relevant energy scales are pushed much below T_{MI}, where the number density of such puddles is very low due to the insulating phase's large volume fraction. The charging scale will be high for nanopuddles with very small diameters ($\ll \langle d \rangle$), and they will exhibit Coulomb charging at $T \leq T_{MI}$. However, as was previously mentioned, their number density N_d will be small (see Fig. 3.11), which will result in a negligible contribution to the thermal noise observed. So, it appears that an interplay between the temperature dependent N_d and the distribution of the diameter $\langle d \rangle$ of the nanopuddles will determine the temperature T^* as well as the extent of the temperature range over which the noise remains large. The size distribution and $\langle d \rangle$ are supposed to determine the value of and the maximum value ζ_M. A lower value of $\langle d \rangle$ will result in higher values of T^*. The smaller the size of the nanopuddles, the larger the thermal noise, and hence the larger the ζ_M. The observed emergence of large noise near MIT is presumably a manifestation of EPS in the transition region.

The temperature T^* at which the ratio ζ peaks, as well as the peak value ζ_M, are shown to be highly dependent on the STO substrate orientation on which the NNO films are grown. The substrate orientation, as shown in Table 3.I, affects both the residual strain and the strain relaxation. As a result, T^* and ζ_M are affected by the substrate orientation. This dependence is illustrated in Fig. 3.12 by plotting ζ_M and the ratio $\frac{T^*}{T_{MI}}$ on the in-plane strain ($\epsilon_{||}$%). It can be observed that the two quantities are dependent on the residual in-plane strain. The change in in-plane strain from small tensile strain [in NNO/STO (100)] to significant compressive strain [in NNO/STO (111)] increases the ζ_M and the ratio $\frac{T^*}{T_{MI}}$. This dependence can be justified, as detailed further below. The ζ_M and ratio $\frac{T^*}{T_{MI}}$ are determined by two factors: the average size of the nanopuddle $\langle d \rangle$ and its temperature distribution N_d. The nanopuddles are formed by EPS, and the size scale of the EPS determines the size and size distribution of the nanopuddles that constitute the sparse phase. As previously discussed, this determines ζ_M and the ratio $\frac{T^*}{T_{MI}}$. Since EPS is a result of strain relaxation in the film, which depends on substrate orientation, it is

anticipated that the correlation of ζ_M and ratio $\frac{T^*}{T_{MI}}$ with in-plane residual strain will emerge from this particular dependence on the extent of strain relaxation on substrate orientation.

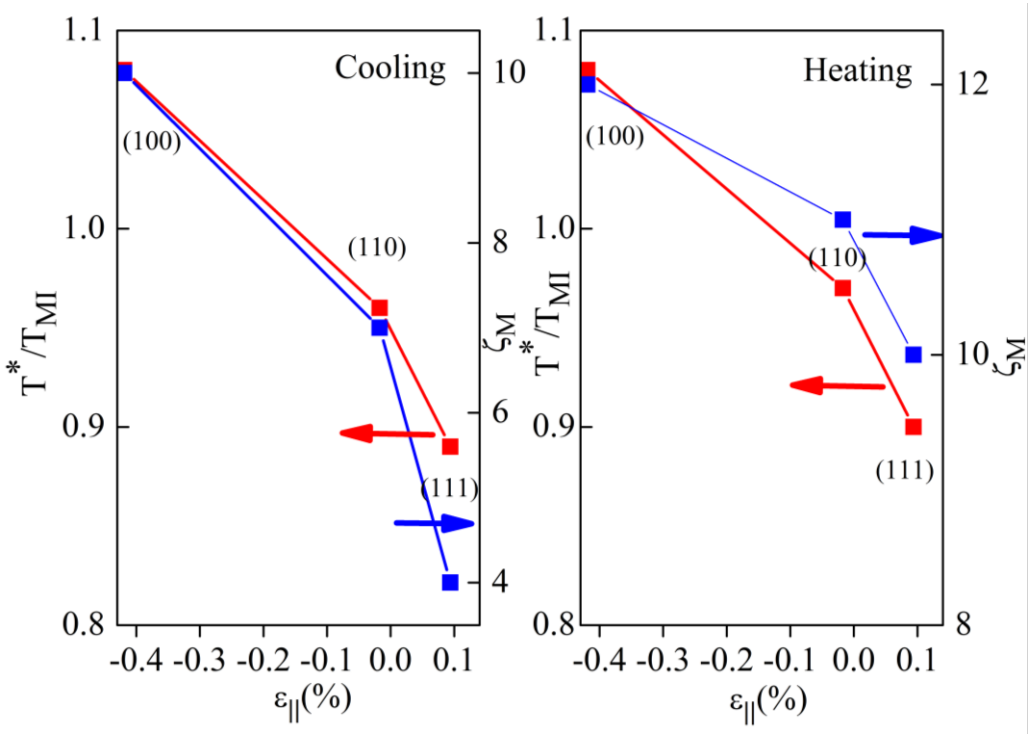

Figure 3.12: Dependence of ζ_M and $\frac{T^*}{T_{MI}}$ on in-plane strain $\epsilon_{||}$.

The size scale in EPS increasingly decreases with increasing strain, as does the disorder caused by the misfit dislocation, which gives rise to the FWHM of the x-ray diffraction peaks (see Table 3.I). The FWHM is the largest in NNO/STO (111), as is the ζ_M and $\frac{T^*}{T_{MI}}$. The specific issue of how the residual strain field and strain field inhomogeneity caused by misfit dislocations might alter the dependence of the size scale of the EPS has been extensively explored, particularly on films of perovskite transition metal oxides [57,58]. This has also been reported in several film systems grown on various substrates, as well as in specific bulk alloys [59–62] and even on VO_2 nanobeams [63–65].

3.5 Conclusion

We report the emergence of large thermal noise (S_{th}) at the Mott transition in $NdNiO_3$ films grown on STO substrates with different crystallographic orientations. This large thermal noise

arises concurrently with largely associated flicker noise ($\frac{1}{f}$ noise) with significant non-Gaussian content. Thermal noise and flicker noise were measured simultaneously, and S_{th} deviated significantly from the canonical Johnson-Nyquist value of $4k_BTR$. We demonstrated that the substantial rise in noise (thermal and flicker noise) results from the dominance of slow relaxations close to the transition. We further demonstrated that the broad peak of the thermal noise, as measured by the ratio $\zeta(T) \equiv \frac{S_{th}(T)}{4k_BTR}$, does not appear at the transition temperature T_{MI} but rather at a noticeably different but nearby temperature T^*. It has been demonstrated that the temperature T^* and the maximum value of ζ (ζ_M) are closely related to the in-plane strain $\epsilon_{||}$%, which increases when the orientation of the substrate STO is changed from (100) to (111). A scenario has been suggested in which the large noise is generated by EPS around MIT temperature, which can result in a sparse phase of nanometric small pockets of metallic phases (nanopuddles) surrounded by and embedded within the minority insulating phase. The nanopuddles are coupled to the majority metallic phase by tunneling through the minority insulating phase layer. If the charged nanopuddles are small enough, they can serve as a source of noise. It has been proposed that the size distribution and average size of the nanopuddles will affect the scale of charging energy E_C and temperature T^*. The dependence of T^* and ζ_M on in-plane strain may arise from the strain-induced variation of the size scale of the nanopuddles. It is likely that our observation that thermal noise increases near a Mott MIT is generic and can be observed in other materials as well if there is EPS present, resulting in the formation of nanopuddles.

References:

[1] P. W. Anderson, Phys. Rev. **109**, 1492 (1958).

[2] F. Evers and A. D. Mirlin, Rev. Mod. Phys. **80**, 1355 (2008).

[3] P. A. Lee and T. V. Ramakrishnan, Rev. Mod. Phys. **57**, 287 (1985).

[4] N. F. Mott, Proc. Phys. Soc. Sect. A **62**, 416 (1949).

[5] D. Belitz and T. R. Kirkpatrick, Rev. Mod. Phys. **66**, 261 (1994).

[6] A. Georges, G. Kotliar, W. Krauth, and M. J. Rozenberg, Rev. Mod. Phys. **68**, 13 (1996).

[7] M. Imada, A. Fujimori, and Y. Tokura, Rev. Mod. Phys. **70**, 1039 (1998).

[8] Z. Wang, Y. Okada, J. O'Neal, W. Zhou, D. Walkup, C. Dhital, T. Hogan, P. Clancy, Y. J. Kim, Y. F. Hu, L. H. Santos, S. D. Wilson, N. Trivedi, and V. Madhavan, Proc. Natl. Acad. Sci. U. S. A. **115**, 11198 (2018).

[9] B. Hartmann, D. Zielke, J. Polzin, T. Sasaki, and J. Müller, Phys. Rev. Lett. **114**, 216403 (2015).

[10] T. Itou, E. Watanabe, S. Maegawa, A. Tajima, N. Tajima, K. Kubo, R. Kato, and K. Kanoda, Sci. Adv. **3**, e1601594 (2017).

[11] R. Yamamoto, T. Furukawa, K. Miyagawa, T. Sasaki, K. Kanoda, and T. Itou, Phys. Rev. Lett. **124**, 46404 (2020).

[12] S. Kundu, T. Bar, R. K. Nayak, and B. Bansal, Phys. Rev. Lett. **124**, 95703 (2020).

[13] J. B. JOHNSON, Nature **119**, 50 (1927).

[14] H. Nyquist, Phys. Rev. **32**, 110 (1928).

[15] S. Samanta, A. K. Raychaudhuri, X. Zhong, and A. Gupta, Phys. Rev. B - Condens. Matter Mater. Phys. **92**, 195125 (2015).

[16] A. Sahoo, S. D. Ha, S. Ramanathan, and A. Ghosh, Phys. Rev. B - Condens. Matter Mater. Phys. **90**, 085116 (2014).

[17] A. M. Alsaqqa, S. Singh, S. Middey, M. Kareev, J. Chakhalian, and G. Sambandamurthy, Phys. Rev. B **95**, 125132 (2017).

[18] R. S. Bisht, S. Samanta, and A. K. Raychaudhuri, Phys. Rev. B **95**, 115147 (2017).

[19] G. N. Daptary, S. Kumar, M. Kareev, J. Chakhalian, A. Bid, and S. Middey, Phys. Rev. B **100**, 125105 (2019).

[20] S. Middey, J. Chakhalian, P. Mahadevan, J. W. Freeland, A. J. Millis, and D. D. Sarma, Annu. Rev. Mater. Res. **46**, 305 (2016).

[21] S. Catalano, M. Gibert, J. Fowlie, J. Íñiguez, J.-M. Triscone, and J. Kreisel, Reports Prog. Phys. **81**, 046501 (2018).

[22] H. B. Callen and T. A. Welton, Phys. Rev. **83**, 34 (1951).

[23] S. P. Benz, A. Pollarolo, J. Qu, H. Rogalla, C. Urano, W. L. Tew, P. D. Dresselhaus, and D. R. White, Metrologia **48**, 142 (2011).

[24] J. P. Nougier, IEEE Trans. Electron Devices **41**, 2034 (1994).

[25] R. Kubo, Reports Prog. Phys. **29**, 306 (1966).

[26] T. M. Mishonov, I. M. Dimitrova, and A. M. Varonov, Phys. A Stat. Mech. Its Appl. **530**, 121577 (2019).

[27] R. F. Voss and J. Clarke, Phys. Rev. B **13**, 556 (1976).

[28] J. H. Scofield, Rev. Sci. Instrum. **58**, 985 (1987).

[29] A. K. Raychaudhuri, Curr. Opin. Solid State Mater. Sci. **6**, 67 (2002).

[30] A. Ghosh, S. Kar, A. Bid, and A. K. Raychaudhuri, arXiv:cond-mat/0402130v1.

[31] X. Granados, J. Fontcuberta, X. Obradors, and J. B. Torrance, Phys. Rev. B **46**, 15683 (1992).

[32] C. Grygiel, A. Pautrat, W. Prellier, and B. Mercey, Epl **84**, 47003 (2008).

[33] K. W. Post, A. S. McLeod, M. Hepting, M. Bluschke, Y. Wang, G. Cristiani, G. Logvenov, A. Charnukha, G. X. Ni, P. Radhakrishnan, M. Minola, A. Pasupathy, A. V. Boris, E. Benckiser, K. A. Dahmen, E. W. Carlson, B. Keimer, and D. N. Basov, Nat. Phys. **14**, 1056 (2018).

[34] D. S. Mc Lachlan, J. Phys. C Solid State Phys. **20**, 865 (1987).

[35] S. Bogdanovich and D. Popović, Phys. Rev. Lett. **88**, 236401 (2002).

[36] J. Jaroszyński, D. Popović, and T. M. Klapwijk, Phys. Rev. Lett. **89**, 89 (2002).

[37] J. Jaroszyński, D. Popovíc, and T. M. Klapwijk, Phys. Rev. Lett. **92**, 226403 (2004).

[38] S. Kar, A. K. Raychaudhuri, A. Ghosh, H. v. Löhneysen, and G. Weiss, Phys. Rev. Lett. **91**, 216603 (2003).

[39] A. L. Burin, B. I. Shklovskii, V. I. Kozub, Y. M. Galperin, and V. Vinokur, Phys. Rev. B - Condens. Matter Mater. Phys. **74**, 075205 (2006).

[40] H. Liu, E. Lhuillier, and P. Guyot-Sionnest, J. Appl. Phys. **115**, 154309 (2014).

[41] K. Shtengel and C. C. Yu, Phys. Rev. B - Condens. Matter Mater. Phys. **67**, 1651061 (2003).

[42] J. V. Mantese and W. W. Webb, Phys. Rev. Lett. **55**, 2212 (1985).

[43] L. F. Fonseca and I. Balberg, Phys. Rev. B **48**, 14915 (1993).

[44] T. Vojta, *AIP Conf. Proc.* ***1550,*** *188* (2013).

[45] P. Majhi, S. Chatterjee, R. S. Bisht, V. R. Reddy, B. Ghosh, and A. K. Raychaudhuri, Phys. Rev. Mater. **5**, 085005 (2021).

[46] S. Dutta, *Electronic Transport in Mesoscopic Systems* (Cambridge University, Cambridge, England, 1995).

[47] *Single Charge Tunneling: Coulomb Blockade Phenomena in Nanostructures*, edited by H. Grabert and M. H. Devoret (Plenum, New York, 1992).

[48] B. Abeles, P. Sheng, M. D. Coutts, and Y. Arie, Adv. Phys. **24**, 407 (1975).

[49] D. Toker, D. Azulay, N. Shimoni, I. Balberg, and O. Millo, Phys. Rev. B - Condens. Matter Mater. Phys. **68**, 041403(R) (2003).

[50] K. H. Mller and M. M. A. Yajadda, J. Appl. Phys. **111**, 123705 (2012).

[51] C. Duan, Y. Wang, J. Sun, C. Guan, S. Grunder, M. Mayor, L. Peng, and J. Liao, Nanoscale **5**, 10258 (2013).

[52] Y. I. Rodionov, I. S. Burmistrov, and N. M. Chtchelkatchev, Phys. Rev. B - Condens. Matter Mater. Phys. **82**, 155317 (2010).

[53] A. Glatz and I. S. Beloborodov, Phys. Rev. B - Condens. Matter Mater. Phys. **81**, 033408

(2010).

[54] C. Liu and Q. Niu, arXiv:cond-mat/9510063v2.

[55] K. T. Kenshi Tada, Y. F. Yoshinobu Fujii, and K. T. Kenji Taniguchi, Jpn. J. Appl. Phys. **40**, 2050 (2001).

[56] J. Ruppen, J. Teyssier, O. E. Peil, S. Catalano, M. Gibert, J. Mravlje, J. M. Triscone, A. Georges, and D. Van Der Marel, Phys. Rev. B - Condens. Matter Mater. Phys. **92**, 155145 (2015).

[57] K. H. Ahn, T. Lookman, and A. R. Bishop, Nature **428**, 401 (2004).

[58] L. Marín, L. A. Rodríguez, C. Magén, E. Snoeck, R. Arras, I. Lucas, L. Morellón, P. A. Algarabel, J. M. De Teresa, and M. R. Ibarra, Nano Lett. **15**, 492 (2015).

[59] Y. Y. Zhao, F. X. Hu, J. Wang, L. Chen, W. W. Gao, J. Shen, J. R. Sun, and B. G. Shen, J. Appl. Phys. **111**, 07D721 (2012).

[60] A. Lahiri, T. A. Abinandanan, M. P. Gururajan, and S. Bhattacharyya, Philos. Mag. Lett. **94**, 702 (2014).

[61] F. Xue, Y. Li, Y. Gu, J. Zhang, and L. Q. Chen, Phys. Rev. B **94**, 220101(R) (2016).

[62] T. D. Ha, J.-W. Chen, M. Yen, Y.-H. Lai, B.-Y. Wang, Y.-Y. Chin, W.-B. Wu, H.-J. Lin, J.-Y. Juang, and Y.-H. Chu, ACS Appl. Mater. Interfaces **12**, 46874 (2020).

[63] J. Cao, E. Ertekin, V. Srinivasan, W. Fan, S. Huang, H. Zheng, J. W. L. Yim, D. R. Khanal, D. F. Ogletree, J. C. Grossman, and J. Wu, Nat. Nanotechnol. **4**, 732 (2009).

[64] J. Wu, Q. Gu, B. S. Guiton, N. P. De Leon, L. Ouyang, and H. Park, Nano Lett. **6**, 2313 (2006).

[65] J. Cao and J. Wu, Mater. Sci. Eng., R **71**, 35 (2011).

Chapter 4 Disorder-induced crossover of Mott insulator to weak Anderson localized regime in an argon-irradiated $NdNiO_3$ film

In this chapter, we show that an introduction of disorder in a controlled way using 1 MeV argon (Ar) ion irradiation, suppresses the correlation-driven metal-insulator transition (MIT) in $NdNiO_3$ films. The films make a crossover to a heavily disordered conductor governed by weak localization and at even higher disorder, an Anderson localized state. Evidence of suppression of correlated behavior can also be found in the irradiated films, where the non-Gaussian nature of resistance fluctuation close to MIT, a signature of correlated electron systems, is suppressed on irradiation, leading to the collapse of the MIT. Raman spectroscopy and X-ray examinations revealed evidence of increasing disordering of the films after irradiation, indicating that the basic integrity of the NiO_6 octahedra is intact and the structure preserves its crystallinity.

Content of this chapter has been published in: R. S. Bisht, **S. Chatterjee**, S. Raha, A. Singha, D. Kabiraj, D. Kanjilal, and A. K. Raychaudhuri, "*Disorder-induced crossover of Mott insulator to weak Anderson localized regime in an argon-irradiated $NdNiO_3$ film*," **Phys. Rev. B** 105, 205120 (2022).

4 Disorder-induced crossover of Mott insulator to weak Anderson localized regime in an argon-irradiated $NdNiO_3$ film

4.1 Preface

The metal-insulator transition (MIT) is an intriguing phenomenon in which a metal with extended wave functions enters an insulating state with strongly localized electrons when one or more physical parameters are varied [1–5]. In one MIT class, the transition is primarily regulated by a crystallographic transition that opens a gap in the conduction band, resulting in a shift in the density of states (DOS) at the Fermi level (E_F) as a result of the change in lattice symmetry [6]. Another MIT class that has recently received a lot of attention is an electronic transition. This form of MIT is broadly classified into two categories. One class is the correlation-driven transition (similar to a Mott-type transition), in which the DOS develops a gap such that the DOS at E_F, $g(E_F) = 0$. The transition is of first order in nature, and the MIT is observed as a function of temperature [1,7,8]. The other major class is the disorder-driven Anderson transition, where the electronic states close to the E_F are localized even while $g(E_F)$ is still finite, i.e., $g(E_F) \neq 0$ [9,10]. The MIT can be ushered in by adjusting the disorder parameter Δ. The transition to the insulating state happens when the disorder parameter is scaled by the bandwidth B, $\delta = \frac{\Delta}{B}$, reaches a critical value $\delta_c \sim 1$. Similarly, for correlation driven transitions, the scaled parameter $u = \frac{U}{B}$, which quantifies the on-site Coulomb repulsion U, is tuned, and the transition occurs at a critical value $u_c \sim 1$ [1,7,8]. Extensive investigations that have been undertaken over the years have established that in a real physical system the transition has aspects of both disorder and correlation. The phenomenon becomes more complicated when both δ and u have finite values, especially when δ and u are close to their critical values and the strength of the correlation and disorder are comparable ($\delta \sim u$) [11]. The MIT is known as an Anderson-Mott transition when a Mott transition occurs with disorder. Despite the complexity of the topic, several unifying scenarios have emerged throughout time. For example, it has been demonstrated that destabilization of the gapped insulating state beyond a certain level of the disorder can result in a transition from insulating to a correlated disordered metallic state, which at a higher level of disorder δ can change over to an Anderson

insulator (AI) [12–14]. At zero temperature [12], as well as at finite but low temperature [13], a phase diagram with parameters δ and u has been provided [15], which shows how a steady enhancement of δ can drive a Mott insulator (with $u > u_c$) to a disordered metallic state and eventually to AI depending on the values of the parameters δ and u. Figure 4.1 depicts a schematic phase diagram taken from Ref. [13] for simplicity of discussion. Although the phase diagram was established in the context of the Mott-Anderson MIT, it may also be used to show how the level of the disorder can modify a correlation-driven MIT. The specific context of the Mott insulator is utilized to illustrate a general class of similar transitions.

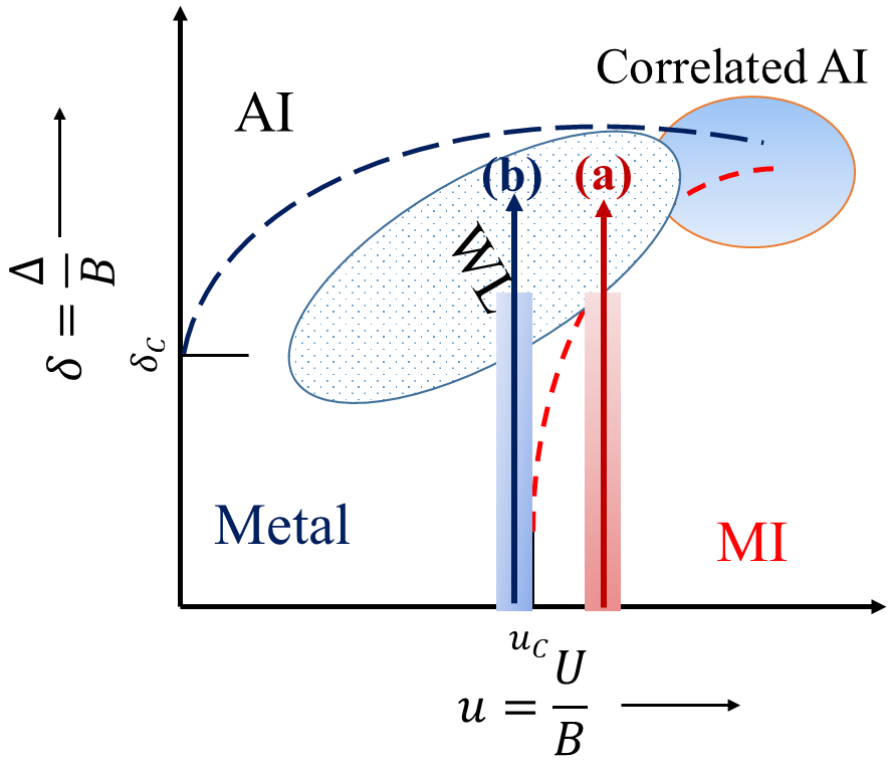

Figure 4.1: Schematic of the phase diagram with correlation and disorder: MI: Mott insulator, AI: Anderson insulator, WL: weak localization regime. The vertical arrows illustrate the schematic path of disordering by 1 MeV Ar ions for (a) $NdNiO_3$ film and (b) $Nd_{0.7}La_{0.3}NiO_3$ film. Shading around the arrows represents expected variations arising from the strain for films grown on different substrates. The phase diagram has been adapted from [13].

The schematic of a qualitative phase diagram in Fig. 4.1 is placed in context with the experimental realization presented in this paper. If we start from a region deep inside the insulating region where $u > u_c$ and increase the disorder by tuning the δ, we can crossover to a region of AI or at least a region of weakly localized metal for sufficiently large. If the

disordering process does not affect u, the disordering path following vertical (a) can be realized. In this situation, it is expected that when the crossover happens, the conductivity will increase on the collapse of the gapped insulator as the gap at E_F closes, and then decreases as the disorder increases. It will also be intriguing to investigate the case where such a disordering process follows vertical (b), where the initial sample is not in a gapped insulating state but rather in a weakly localized regime that is close to the critical boundary ($u \geq u_c$). In this case, unlike the disordering following vertical (a), the disordering following vertical (b) would result in a continuous decrease of conductivity due to disorder enhancement because there is no crossover involved. Hence, qualitative differences are likely to be noticed when disordering occurs following vertical (a) and (b).

The substitution of isovalent ions with different ionic radii is one method to introduce disorder into a system [2,16,17]. Although this approach is commonly used, it has co-lateral difficulties such as changes in crystal structure and changes in ionic radii that might cause internal pressure, resulting in a change in bandwidth B. This would not only change δ, but it may also change u as well. A cleaner strategy to change δ solely and move along vertical (a) and (b) in Fig. 4.1 is to use energetic heavy ion irradiation in a controlled way as a tool to induce disorder without modifying the chemistry. High-energy ion irradiation can create high-density defects in a short period. When the sample utilized is thin enough (such as a thin film on a substrate), the projected ions do not stop inside the film and, as a result, the irradiation does not change the chemistry. Consequently, an extremely useful investigation will be to use irradiation to induce controlled disorder and investigate the progressive destabilization of the gapped insulator, as indicated in the schematic illustrated in Fig. 4.1. It will be especially important to study the nature of electrical conduction in solids when the insulating state is suppressed by the disorder.

In strongly correlated organic conductors, X-ray irradiation was used to investigate disordering a Mott insulator [18]. The radiation-induced disorder increases conductivity, yet the insulating condition is retained at low temperatures. At low temperatures, hydrostatic pressure can be used to induce the disordered insulating state to change over to a weakly localized conducting state, hence increasing the conduction bandwidth by increasing the transfer integral. Whilst high energy, swift heavy ions have been utilized in the past to disorder oxides such as $NdNiO_3$ films, these studies did not address the issue of the collapse of an insulating state such as a Mott insulator when it is disordered progressively [19–21]. The energy of the ions used in these studies was extremely high (200 MeV). In these energy ranges the defects created are distinct due to the predominance of the electronic energy loss mechanism. In this work, we have

investigated the disordering of $NdNiO_3$ (NNO) films of thickness about 15 nm which were grown on (001) oriented crystalline substrates $LaAlO_3$ (LAO) and $SrTiO_3$ (STO) using 1 MeV Ar ions. The stopping distance of 1 MeV Ar ions in such oxides is about 500 nm, which is substantially greater than the film thickness. As a result, the ions do not stop inside the film, but rather deep within the substrate. The route of disordering thus follows the vertical (a) depicted in Fig. 4.1.

The $RNiO_3$ (R = rare earth except for La) is known to have a first-order MIT. The MIT is also associated with a structural transition from a high-temperature orthorhombic phase to a low-temperature monoclinic phase [22,23]. Several scenarios have been addressed in the literature to understand the nature of the insulating state in $RNiO_3$. However, the exact mechanism remains elusive and controversial [22–24]. One possibility suggested that a charge disproportionate Ni site could be responsible for charge ordering in nickelates [25]. Charge ordering in $RNiO_3$ has also been proposed as a cause of the MIT, which is caused by a site-specific Mott phase [24]. A negative charge transfer scenario for the MIT the $RNiO_3$ has been advanced experimentally [26]. Although we are aware that $RNiO_3$ may not be the best example for a Mott system, we placed the $RNiO_3$ close to the Mott insulators in the current investigation. We have also performed similar ion irradiation-induced disordering on a film of $Nd_{0.7}La_{0.3}NiO_3$ (NLNO), which is close to the critical region of MIT obtained by Nd substitution with La [27,28]. The ($Nd_{1-x}La_xNiO_3$) film exhibits substitution attributed to MIT due to bandwidth change around a critical concentration $x = 0.3 - 0.35$, the exact value of which depends on the strain arising from the substrate. When Nd is substituted by La close to the critical region of a composition driven MIT, as in an Anderson type transition, the nature of the first order MIT in $NdNiO_3$ changes [28]. Consequently, the disordering of NLNO films by Ar irradiation follows path (b) in Fig. 4.1. Suppression of the Mott transition where a substitution driven closing of the gap at E_F has also been observed in $Sr_3(Ir_{1-x}Ru_x)_2O_7$, where the introduction of disorder can lead to the opening of a power-law gap in the system on Ru substitution [29]. The observations made by us in this experiment using ion irradiation are comparable to the observations made above. The experimental findings of this study confirm the general validity of the qualitative phase diagram depicted in the schematic in Fig. 4.1, which was developed from earlier theoretical studies on Mott-Anderson transitions [13]. The present research demonstrated that ion induced disordering, even at low fluence, suppresses the insulating phase, resulting in a weakly localized regime with a negative temperature coefficient (NTC) ($\frac{d\rho}{dT} < 0$) but a finite zero temperature conductivity [$\sigma\ (T = 0) \neq 0$]. In fact, the resistivities at low temperature for

the films disordered at low fluence are much lower than those of the pristine film that shows an MIT.

4.2 Experimental details

The NNO and NLNO films with thicknesses of about 15 nm were prepared using a 248 nm KrF pulsed laser deposition (PLD), and their growth was monitored using in situ reflection high energy electron diffraction (RHEED), which was also used to calculate the thickness of the films based on the number of oscillations in RHEED intensity. The films were grown at 625°C and 0.11 Torr oxygen pressure. The laser fluence during deposition was about 2.5 J/cm^2 [30,31]. Ion irradiation was carried out utilizing 1 MeV Ar^{4+} ions and a beam current of 250 particle nA (pnA) at the electron cyclotron resonance (ECR) ion source-based irradiation facility. Using the Monte Carlo method-based software "Stopping and Range of Ions in Matter" (SRIM) and "Transport of Ions in Matter" (TRIM) [32], the relevant parameters for ion-irradiation were computed. During the irradiation, the Ar^{4+} ion beam was scanned uniformly over an area of 1 cm^2, which was greater than the area of the material used. A greater beam scan area in comparison to sample size enables homogeneous irradiation. To prevent temperature rise during ion irradiation, the films were mounted on a liquid nitrogen-cooled copper back plate. Figure 4.2(a) depicts a schematic of heavy ion irradiation geometry and ion stopping in the substrate. Figure 4.2(b) depicts the electronic energy loss and nuclear energy loss for Ar ions in NNO films as determined by SRIM [33]. Table 4.I show how the effects of Ar^{4+} irradiation varied by varying the irradiation time. The fluences used to irradiate the films were 1×10^{14}/cm^2, 5×10^{14}/cm^2, and 1×10^{15}/cm^2. The range of 1 MeV Ar ions in materials such as NNO, STO, and LAO is approximately 490–500 nm. Since this is greater than the film thickness, the ions stop deep in the substrate after disordering the film. The irradiation causes the film to become progressively disordered, but it contains no implanted Ar. The energy loss for the Ar ions employed is predominantly nuclear in nature, causing ions to be directly displaced from the lattice locations. TRIM [32,33] was used to calculate the number of vacancies generated by Ar ions in NNO.

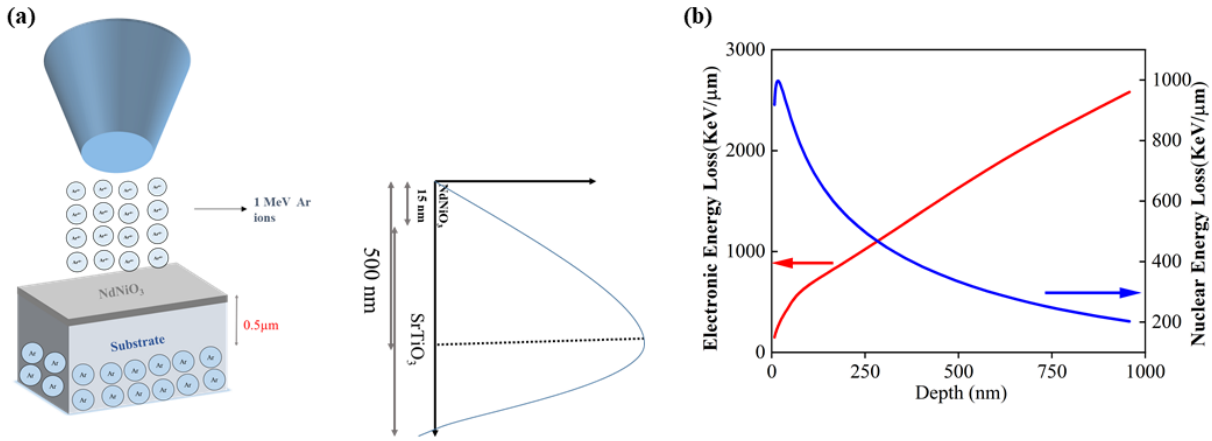

Figure 4.2: (a) Schematic of the geometry of ion irradiation and the projected ranges calculated using TRIM. (b) Electronic and Nuclear energy loss of Ar ions as a function of depth in $NdNiO_3$.

The total knocked-out atoms (atomic displacements) is ≈ $3.5 \times 10^{22}/cm^3$ for a fluence of $1 \times 10^{15}/cm^2$. In general, ≈ 99% of the damage anneals instantly at room temperature and the nominal vacancy created for the fluence is 0.35 vacancies/target atom [33]. After thermal annealing, the retention was ≈ $3.5 \times 10^{20}/cm^3$. Scaling by atomic density results in a nearly 2% disorder in the NNO film. Table 4.I summarize the sample details (including acronyms), fluences employed in the experiment, and the disorder (atomic displacement) generated.

Table 4.I: Details of the samples (and acronyms), the fluence used in the experiment, and the disorder (atomic displacement) generated are summarized.

Fluence (cm^{-2})	Disorder (%)	Film NNO/STO	Film NNO/LAO	Film NLNL/STO	Film NLNO/LAO
0	0	NNO/S0	NNO/L0	NLNO/S0	NLNO/L0
1×10^{14}	0.2	NNO/S1	NNO/L1	NLNO/S1	NLNO/L1
5×10^{14}	1.0	NNO/S2	NNO/L2	NLNO/S2	NLNO/L2
1×10^{15}	2.0	NNO/S3	NNO/L3	NLNO/S3	NLNO/L3

Following irradiation, samples were examined using X-ray diffraction (XRD) and Raman spectroscopy, as well as pristine films, to determine progressive disordering when fluence was

increased. Raman data were collected utilizing a LABRAM HR micro-Raman system with an Ar ion laser (wavelength 488 nm) as an excitation source. In a pulsed tube cryocooler, resistivity (ρ) measurements were carried out in a collinear four-probe geometry down to nearly 3 K. Electrical contacts were made using Cr/Au contact pads placed on the films using a thermal evaporator through a shadow mask. Using an ac-biased digital signal processing approach, the $\frac{1}{f}$ noise spectroscopy measurement was performed in a four-probe geometry [34–36].

4.3 Results

4.3.1 Structural data

The θ-2θ XRD scans on the pristine and irradiated films reveal that the films are free of any impurity phase and that the texture of the film is preserved. Because of the lattice mismatch between films (NNO and NLNO) and LAO [a_{pc}(Å) ≈ 3.79] and STO [a_{pc}(Å) ≈ 3.90], the films formed on them will undergo in-plane compressive and tensile strain (a_{pc} represents a pseudocubic lattice constant). Figures 4.3(a)-(d) show the full-range XRD scans of the pristine and irradiated films. Figures 4.4(a)-(d) represent the XRD scans of the pristine and irradiated films around the most prominent (002) peaks. Except for the pristine films, all samples showed an extra feature in the substrate peaks. The additional feature in the substrate's Bragg peak can be attributed to x-ray scattering from the damaged area of the underlying substrate as a result of ion radiation. The stopping of the ions within the substrates causes strain. This has been noticed, for instance, for the titanium-irradiated $SrTiO_3$ substrate [37]. The growth directions of the films have been designated as $(002)_{pc}$, where the pseudocubic notation is represented by the subscript pc. Table 4.II summarizes the line locations and FWHM values of the XRD lines corresponding to the (002) indexed lines of the films. The positions of the (002) peaks suggest that the out-of-plane (in-plane) lattice constant is smaller (larger) in NNO/S0 than in NNO/L0. Thus, the NNO/L0 film exhibits a minor in-plane compressive strain. Progressive irradiation causes the XRD peaks to shift to the lower 2θ values, indicating that the out-of-plane (in-plane) lattice parameters expand (compress). However, the line shifts caused by irradiation are negligible and only range from 1% to 2%. The indicated (002) lines in both NNO and NLNO films grown on STO exhibit distortions for the highest fluence values. It is possible that the contraction in the lattice happens as a result of the irradiation-induced vacancy and the

subsequent relaxing of the lattice around the vacancy. This is likely to increase the FWHM of the observed XRD peaks. The retention of the Bragg peaks after irradiation demonstrates that the films retain their crystallinity, albeit with the disorder.

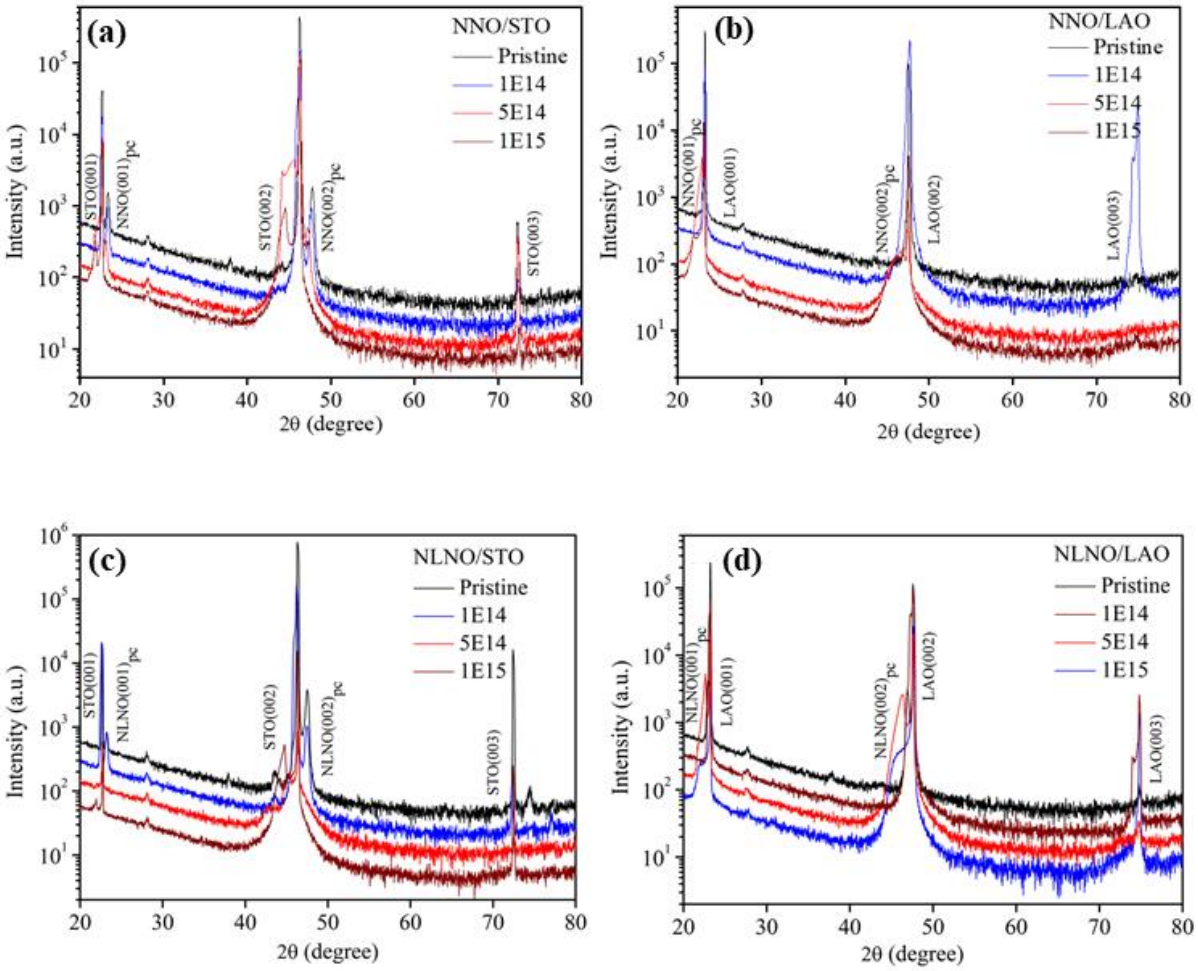

Figure 4.3: (a)-(b) Full range x-ray diffraction data for pristine and irradiated films of $NdNiO_3$ (NNO) grown on $SrTiO_3$ (STO) and $LaAlO_3$ (LAO). These two figures are reproduced from reference [38]. (c)-(d) Full range x-ray diffraction data for pristine and irradiated films of $Nd_{0.7}La_{0.3}NiO_3$ film grown on STO and LAO substrate. The corresponding fluence has a unit of cm^{-2}.

Raman spectroscopy was used to analyze the structural evolution and integrity of the NNO structure in irradiation films. Raman spectroscopy is a local structure-sensitive tool that can reveal what happens to the NiO_6 octahedron at the heart of the NNO structure. The LAO substrate's strong Raman signal ensures that Raman spectra are acquired from scattered light that covers the whole thickness of the film and a portion of the substrate. NNO has an orthorhombic ($Pbnm$) crystal structure at ambient temperature. According to group theoretical

considerations, there are 24 Raman active modes expected for structurally distorted oxides such as NNO [39].

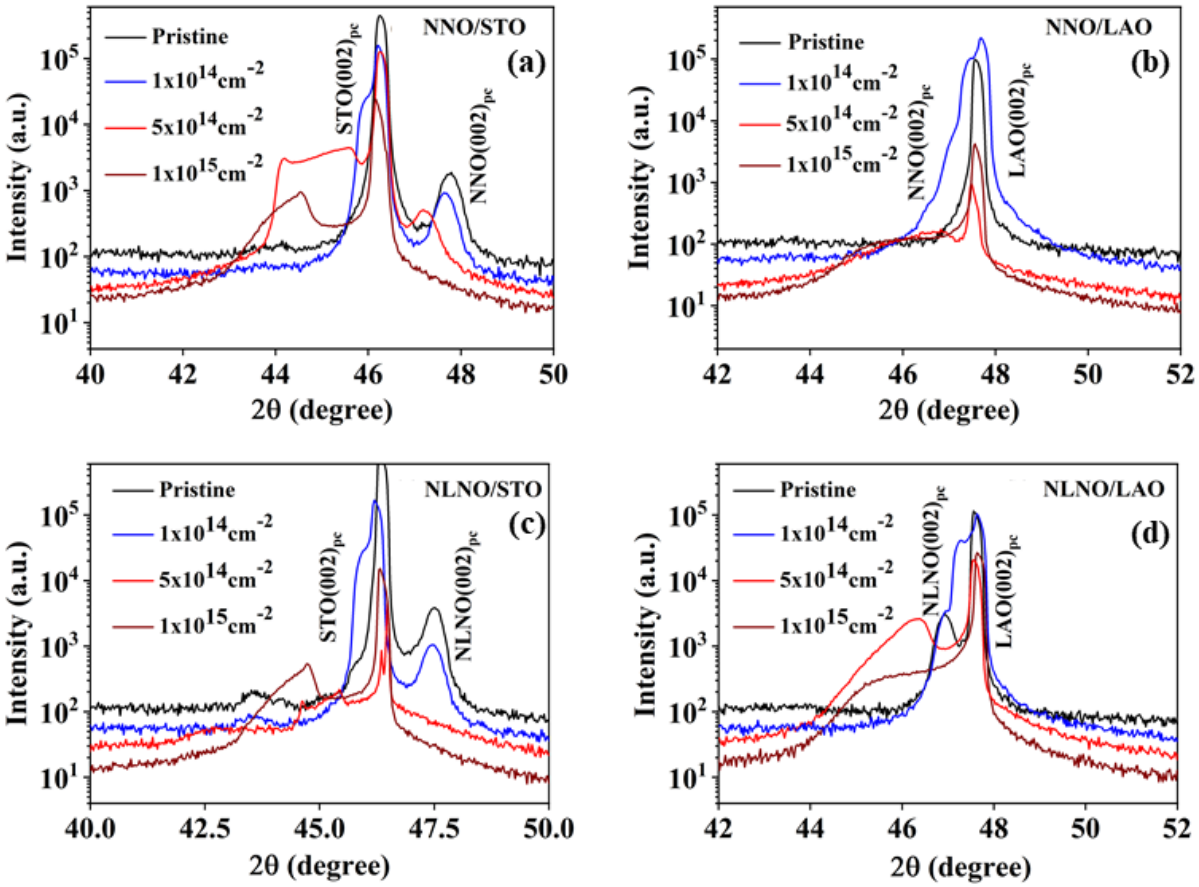

Figure 4.4: (a)-(b) X-ray diffraction data around indices (002) in pristine and irradiated films of NNO grown on STO and LAO. (c)-(d) X-ray diffraction data around indices (002) in pristine and irradiated films of NLNO grown on STO and LAO.

However, only a few Raman modes have been seen experimentally, and our observations are in line with past studies [40,41]. The major detected modes feature E_g and A_g symmetries related to the NiO_6 octahedra. Any changes in these modes indicated by Raman spectroscopy data would provide information on the structural integrity of the NiO_6. The Raman spectra of pristine and irradiated films of NNO and NLNO grown on LAO are shown in Figs. 4.5(a) and 4.5(b). It is noteworthy that the Raman modes of NNO and NLNO films grown on STO substrates were too weak to detect due to the high background from the STO substrate and the small thickness of the film. Table 4.II summarizes the positions of the Raman lines measured in pristine and irradiated films, as well as the modes assigned.

Table 4.II: The table summarizes the peak position ($2\theta_{002}$) and the FWHM ($\Delta(2\theta_{002})$ of the pristine and irradiated samples along the (002) plane as obtained from the XRD data. The ω_1 (cm^{-1}), ω_2 (cm^{-1}), ω_3 (cm^{-1}) represent the different Raman modes for the measured samples.

Sample	XRD data		Raman Spectrum		
	$2\theta_{002}$ (°)	$\Delta(2\theta_{002})$ (°)	ω_1(cm^{-1})	ω_2 (cm^{-1})	ω_3 (cm^{-1})
Film NNO/STO					
NNO/S0	47.77	0.411			
NNO/S1	47.66	0.412			
NNO/S2	47.23	0.410			
NNO/S3	-	-			
Film NNO/LAO					
NNO/L0	47.55	0.10	443.9	305.5	251.1
NNO/L1	47.44	0.288	444.9	305.5	251.1
NNO/L2	46.57	2.10	444.5	304.8	-
NNO/L3	46.55	2.71	-	-	-
Film NLNO/STO					
NLNO/S0	47.50	0.362			
NLNO/S1	47.46	0.404			
NLNO/S2	-	-			
NLNO/S3	-	-			
Film NLNO/LAO					
NLNO/L0	46.93	0.384	437.6	284.3	246.2
NLNO/L1	46.89	0.372	437.4	282.6	238.2
NLNO/L2	46.26	1.42	437	-	-
NLNO/L3	46.22	2.20	-	-	-

The observed values for the Raman mode positions in films [41] and bulk [39] are comparable to those found in NNO/L0 and NLNO/L0. The most intense peak at 443.9 cm^{-1} and the weak shoulder at 431 cm^{-1} in NNO/L0 are caused by E_g modes, where the former is bending of the NiO_6 octahedral cage and the latter is a breathing mode with out-of-phase oxygen oscillations

in the apical and basal planes. The medium-strong line at 305.5 cm^{-1} in NNO/L0 is caused by A_g modes that reflect octahedral rotation out-of-phase and in-phase, respectively.

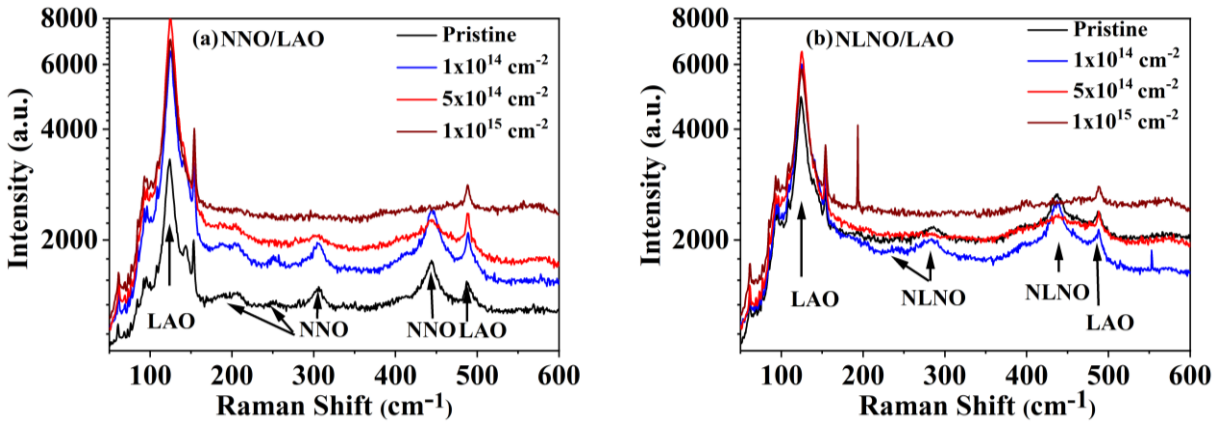

Figure 4.5: The Raman spectra on pristine and irradiated films on LAO substrate for (a) NNO and (b) NLNO. Progressive smearing of NNO peaks on disordering can be seen.

Table 4.III: The full width at the half maxima (FWHM) $\Delta\omega_1$ (cm^{-1}), $\Delta\omega_2$ (cm^{-1}), $\Delta\omega_3$ (cm^{-1}) for the samples marked in Table 4.II.

Sample	$\Delta\omega_1$ (cm^{-1})	$\Delta\omega_2$ (cm^{-1})	$\Delta\omega_3$ (cm^{-1})
NNO/L0	16.46	12.93	14.20
NNO/L1	18.49	16.93	10.01
NNO/L2	21.85	22.05	-
NLNO/L0	16.76	26.41	1.45
NLNO/L1	16.44	29.15	10.42
NLNO/L2	32.63	-	-

These modes also give rise to weaker peaks at shorter wavelengths. The corresponding Raman modes in NNO/L0 soften in NLNO/L0 when La is added, increasing the length of the Ni-O bond. Additionally, some of the weak lines in NNO/L0 could not be seen in NLNO/L0 [40]. Most Raman lines soften a little bit after being exposed to radiation. Although the intensity of the lines decreases with a line broadening as measured by the full-width at half-maxima as shown in Table 4.III, there are negligible changes ($< 0.5\%$) for fluences $\leq 5\times10^{14}$ cm^{-2} for

some of the Raman lines. The retention of Raman lines (albeit widened) at relatively low fluences indicates that the integrity of the metal-oxide octahedra is mostly preserved, despite the fact that the creation of oxygen vacancies on irradiation reduces the number of unaffected octahedra and leads to progressive matrix disordering. The Raman modes are entirely suppressed at higher fluence (1×10^{15} cm^{-2}) due to substantial disorder in the lattice [42]. Hence, the XRD and Raman measurements demonstrate that on 1 MeV Ar ion irradiation, the films become gradually disordered without undergoing any major structural changes up to a fluence of 5×10^{14} cm^{-2} when the disorder (atomic displacement) is ≈ 1%.

4.3.2 Electronic transport in pristine and disordered films of NNO/STO and NNO/LAO

This section discusses changes in resistivities/conductivities caused by the progressive disordering of NNO films grown on STO and LAO substrates in the vertical (a) path seen in Fig. 4.1. Figures 4.6(a) and 4.6(b) exhibit resistivity data for NNO films deposited on STO and LAO substrates, respectively. As the temperature is reduced, the resistivity of the pristine NNO films changes from a negative temperature coefficient of resistivity (NTC) to a positive temperature coefficient of resistivity (PTC). The metal-insulator transition temperature (T_{MI}) was discovered as a change in resistivity slope. T_{MI} ≈ 180 K for the NNO/STO film, and T_{MI} ≈ 75 K for the NNO/LAO film.

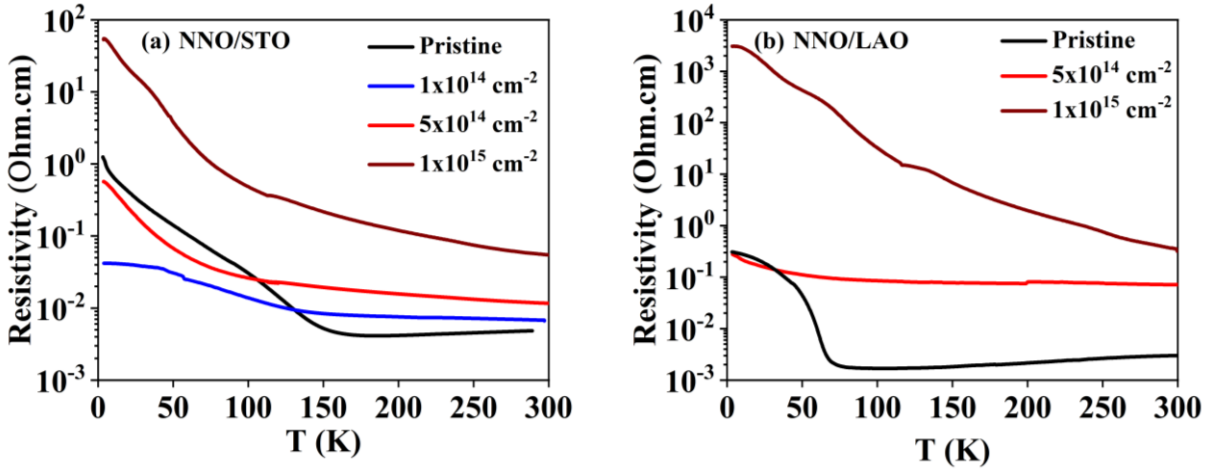

Figure 4.6: Temperature-dependent resistivity data for pristine and irradiated films of NNO grown on (a) STO and (b) LAO substrates. Figure 4.6(a) is reproduced from reference [38].

The significant decrease in T_{MI} in NNO/LAO is attributed to compressive strain in the film stabilizing the high-temperature metallic phase [30]. The measurements on the irradiated samples show that irradiation completely suppresses the MIT even at the lowest fluence (1×10^{14} cm^{-2}). As expected, the resistivity in the insulating side of the pristine $NdNiO_3$ films grown on STO and LAO (i.e., NNO/S0 and NNO/L0) follows the Mott VRH relation as described in Eq. (4.1) [43,44]. Figures 4.7(a) and 4.7(b) present the data as well as the fit. These results are in line with those previously reported for the pristine NNO films [43]:

$$\sigma(T) = \sigma_{0M} T^{-1/4} \exp\left(-\frac{T_0}{T}\right)^{1/4} \tag{4.1}$$

where σ_{0M} and T_0 are constants derived from the fit. T_0 is related to the density of localized states [1,45].

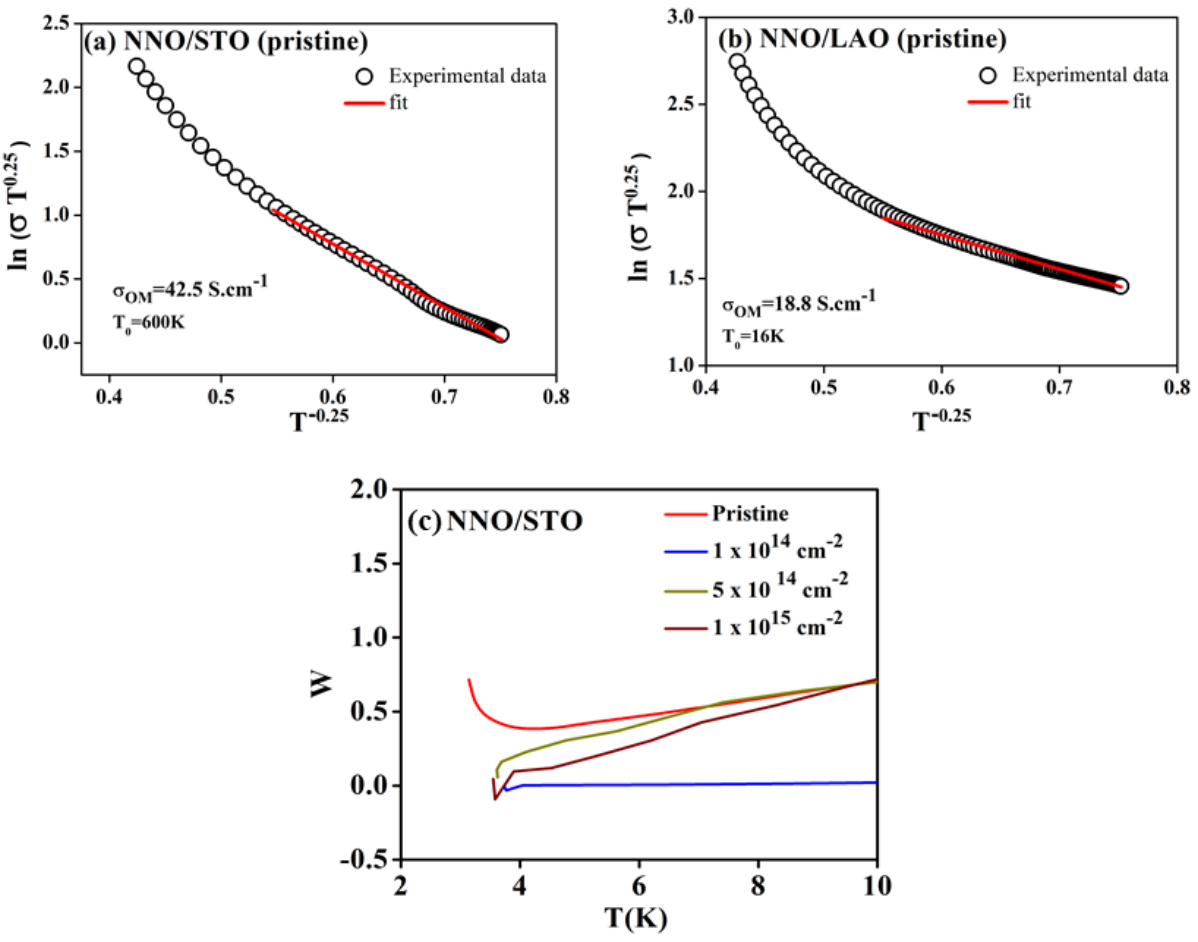

Figure 4.7: Low temperature fit to VRH law for pristine NNO films grown on (a) STO, and (b) LAO. The red line through the data shows the fit. (c) The logarithmic derivative W = $\frac{dln\sigma}{dlnT}$ for the pristine and irradiated samples to show a crossover from insulating to a weakly localized metal with $\sigma \neq 0$ as $T \rightarrow 0$. Figure 4.7(a) is reproduced from reference [38].

The values obtained from the fits for the NNO/S0 are σ_{0M} = 42.5 S/cm and T_0 = 600 K, respectively, and the values for the film NNO/L0 are 18.8 S/cm and 16 K. We also notice, as a test of the insulating character of the pristine films, that the quantity W ≡ $\frac{dln\sigma}{dlnT}$ diverges as the temperature approaches zero [46,47], indicating that σ (T = 0) → 0 as T → 0. It is worth noting that W → 0 when the conductivity σ (T = 0) becomes a finite value as T → 0. Figure 4.7(c) for the NNO/STO films illustrates this.

As previously stated, this progressive disordering occurs along the direction denoted by the vertical (a) in Fig. 4.1. In the section below, we look at how the conductivity $\sigma(T)$ of the films evolved after being subjected to radiation. Figures 4.8(a) and 4.9(a) illustrate the conductivities (σ) as a function of atomic displacement for films grown on STO and LAO at 300 and 3 K. The electrical data are summarized in Table 4.IV. The conductivities gradually decrease upon irradiation for both films at 300 K.

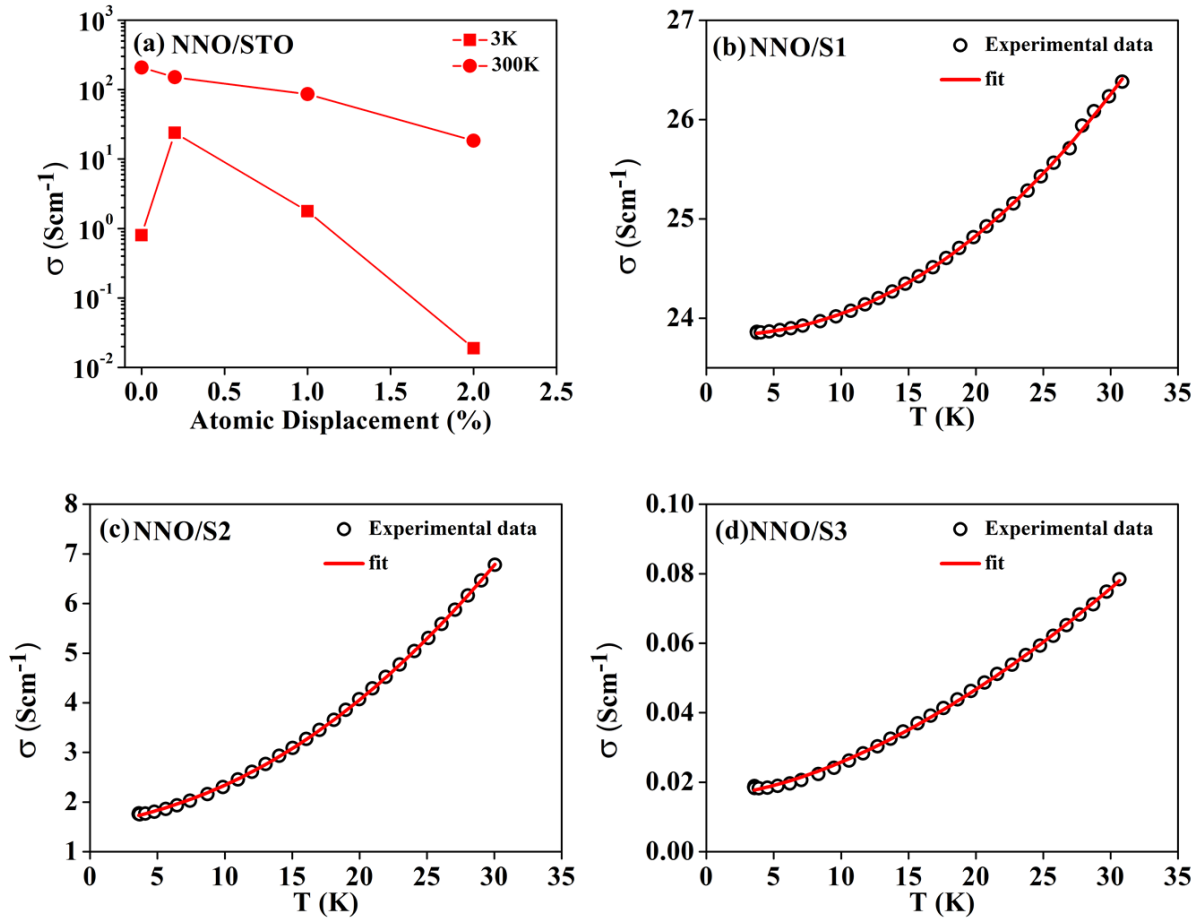

Figure 4.8: (a) Evolution of room temperature (300 K) and low temperature (3 K) conductivity (σ) as a function of atomic displacement in NNO/STO film on Ar ion irradiation. (b)-(d) Low-temperature power low dependence of σ on T.

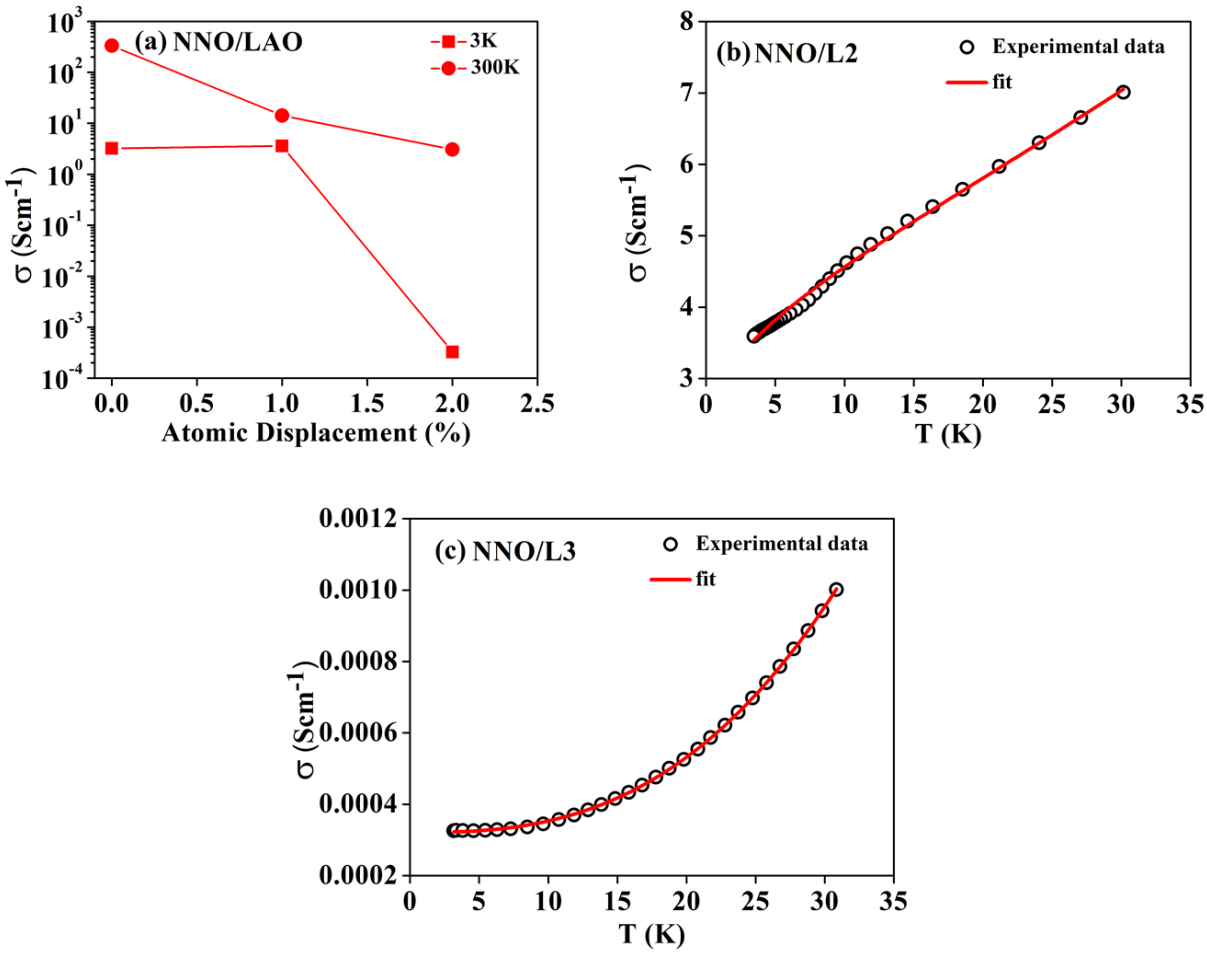

Figure 4.9: (a) Evolution of room temperature (300 K) and low temperature (3 K) conductivity (σ) as a function of atomic displacement in NNO/LAO film on Ar ion irradiation. (b) and (c) Low-temperature power low dependence of σ on T.

This is to be expected in a conventional solid where disordering by ion irradiation increases resistance. The conductivity at T = 3 K, however, demonstrates that stunningly distinct behavior is seen at low temperatures. In this case, there is a nonmonotonous dependence of σ (3 K) on the disorder. The conductivity of the sample NNO/S1 with 0.2% atomic displacement is 30 times higher than the conductivity of the pristine sample NNO/S0. Even though the fluence is increased by a factor of 5, as in the sample NNO/S2 with a 1% atomic displacement, σ (3 K) is higher by a factor of 2.25 than in the pristine sample NNO/S0. For the sample NNO/S3, when the fluence of radiation increases, resulting in a larger disorder (atomic displacement of 2%), σ (3 K) decreases precipitously and drops to less than 2% of the value of (3 K) of the pristine sample. The temperature dependence of the conductivities of the irradiated samples differs significantly from that of the pristine NNO/S0 sample.

Table 4.IV: The Fitting parameters obtained from the VRH (equation 4.1) and power law equations (equation 4.2) as described in the text for different samples. For NLNO/L0 and NLNO/L1, the metallic resistivity follows power law $\rho(T) = \rho_0 + BT^m$

Sample	Observed conductivity		Low-temperature fit of data ($T < 30$ K)				
	σ(3K) S/cm	σ(300K) S/cm	VRH fit		Power law fit		
			σ_{0M}	T_0 (K)	σ_0	m	A
Film NNO/STO							
NNO/S0	0.8	207	42.5	600	-	-	-
NNO/S1	23.86	151	-	-	23.82	2.17	1.5×10^{-3}
NNO/S2	1.8	86	-	-	1.64	1.83	1×10^{-2}
NNO/S3	1.7×10^{-2}	18			1.6×10^{-2}	1.64	2.3×10^{-4}
Film NNO/LAO							
NNO/L0	3.2	333	18.8	16	-	-	-
NNO/L2	3.6	14	-	-	2.83	0.8	0.26
NNO/L3	3.3×10^{-4}	3			3.2×10^{-4}	2.7	6.28×10^{-8}
Film NLNO/STO							
NLNO/S0	31.4	31.4	-	-	30.81	1.86	2×10^{-3}
NLNO/S1	16.0	20.6	-	-	15.96	1.56	2×10^{-3}
NLNO/S2	0.052	1.2	1.71	407	7.6×10^{-2}	1.17	7.4×10^{-4}
NLNO/S3	4.6×10^{-3}	2.3	-	-	4.7×10^{32}	1.87	1.1×10^{-5}
Film NLNO/LAO							
NLNO/L0	1533	362			$\rho_0 = 6.29 \times 10^{-4}$ Ω.cm	2	$B = 6.53 \times 10^{-8}$
NLNO/L1	660	207			$\rho_0 = 1.47 \times 10^{-3}$ Ω.cm	2	$B = 1.27 \times 10^{-7}$
NLNO/L2	0.18	1.02			0.18	1.26	2.5×10^{-4}
NLNO/L3	0.14	0.77			0.135	1.52	3.3×10^{-5}

This demonstrates that the Mott insulating state with VRH-type transport observed in the pristine sample transitions to a disordered conductor in the irradiated samples, which exhibit

power-law conductivity with limited conductivity at zero temperature. This is illustrated in Figs. 4.8(b)-(d), where the conductivities of the irradiation samples NNO/S1, NNO/S2, and NNO/S3 are displayed below 30 K, where they follow a power law:

$$\sigma(T) = \sigma(0) + AT^m, \tag{4.2}$$

where $\sigma(0)$ is the conductivity at T = 0 K, A and the exponent m are constants. $\sigma(0)$ is significant for NNO/S1, and it reduces as fluence increases in NNO/S2 and NNO/S3. A disordered conductor with WL is predicted to have power-law conductivity before approaching an AI state with increasingly decreasing values of $\sigma(0)$. The progressive disordering of the pristine NNO/S0 film suppresses the insulating state with a relatively low disorder, as seen in the sample NNO/S1 with atomic displacements as low as 0.2%, and results in a disordered conductor with WL. As a result, the proposed scenario for increasing the disordering of a Mott insulator to a WL-disordered metal along the pathway vertical (a) of Fig. 4.1 is validated. The $\sigma(0) = 1.6 \times 10^{-2}$ S/cm for the sample NNO/S3 with the highest disorder is very low to support a metallic state and can be considered on the verge of Anderson localization [16].

Another set of samples made from the film NNO/LAO showed a crossover of a correlation-driven insulator to a disordered metal (likely with WL) and subsequently to a highly resistive state but with σ (T = 0) ≠ 0. Because of the compressive strain in the NNO/LAO film, the metallic state is maintained at a lower temperature, lowering the T_{MI}, and the film has a higher conductance than the NNO/STO film. The full data on the pristine and irradiated samples are given in Figs. 4.9(a)-(c). Table 4.IV presents a summary of the data. The conductivity of pristine sample NNO/L0 at low temperatures follows VRH. Irradiation-induced progressive disordering in the samples NNO/L2 and NNO/L3 follows a similar pattern as in irradiated NNO/STO films, where irradiation-induced disordering leads to disordered conductors with power-law conductivity [Eq. (4.2)] due to WL and approaches disordered induced Anderson localization. Thus, our observations show that the insulating state in $NdNiO_3$ that exhibits a temperature-driven MIT like a Mott insulator, on progressive disordering by ion irradiation, does crossover to a disordered conductor with WL and moves to a verge of Anderson localization. This is depicted schematically in Fig. 4.1 as the method of disordering a Mott insulator down the vertical (a).

4.3.3 Radiation-induced disordering in NLNO/STO and NLNO/LAO films

In this section, we compare the radiation-induced disordering found in pristine $NdNiO_3$ films to that observed in a metallic NLNO film grown on LAO or a weakly localized disordered conductor in an NLNO film grown on STO [28]. Both unirradiated pristine films thus differ qualitatively from pristine NNO films grown on STO or LAO, which exhibit low-temperature insulating states. The disordering of the films by 1 MeV Ar irradiation follows the path (b) in Fig. 4.1, which differs from the pathway illustrated by vertical (a) in the previous section. Figures 4.10(a)-(b) exhibit temperature-dependent resistivity data for NLNO films grown on STO and LAO (pristine and irradiated).

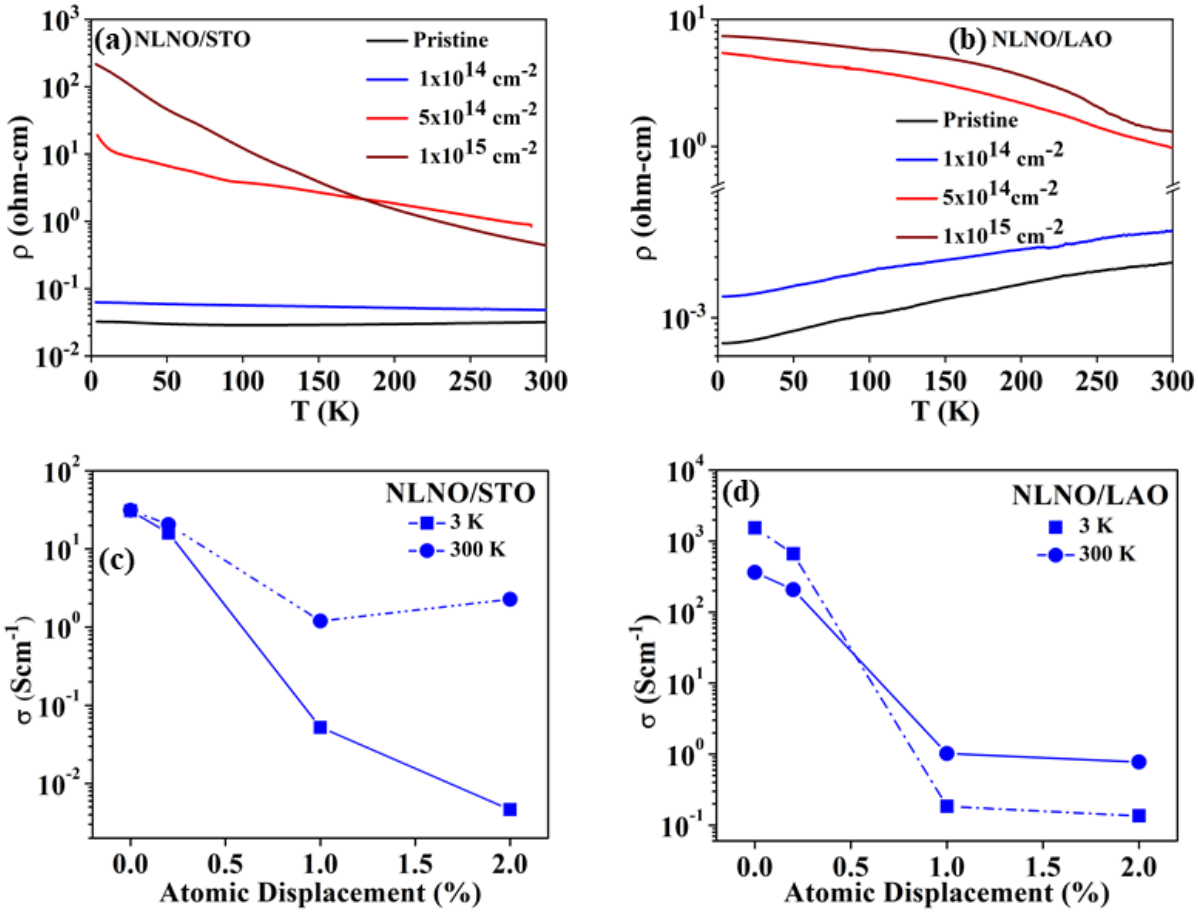

Figure 4.10: Temperature-dependent resistivity for pristine and irradiated films of NLNO grown on (a) STO and (b) LAO substrates. Evolution of room temperature (300 K) and low temperature (3 K) conductivity (σ) as a function of atomic displacement in NLNO film grown on (c) STO and (d) LAO substrates.

Table 4.IV summarizes the data, which may be compared to the data reported in the previous part on the NNO/STO and NNO/LAO films (pristine and irradiated). The pristine NNO films and the NLNO films exhibit qualitatively different characteristics. However, there are significant similarities in the temperature dependence of the irradiated films' resistivities. The resistivities exhibit shallow negative temperature coefficients (NTC) for the NLNO/S0 and NLNO/S1 films. The resistivities in the NLNO/S2 and NLNO/S3 films have a strong NTC and exhibit disordered conductor behavior, as detailed below. Due to compressive stress, the pristine sample NLNO/L0 and the sample irradiated with the lowest fluence NLNO/L1 exhibit metallic resistivities with positive temperature coefficients for NLNO/LAO films. However, the resistivity of NLNO/L1 is approximately 2.5 times greater than that of NLNO/L0. Further disordering increases resistivities rapidly, resulting in NTC. Figures 4.10(c) and 4.10(d), which are displayed σ at T = 3 and 300 K, respectively (see also Table 4.IV), quantify the aforementioned claims for the NLNO/STO and NLNO/LAO films.

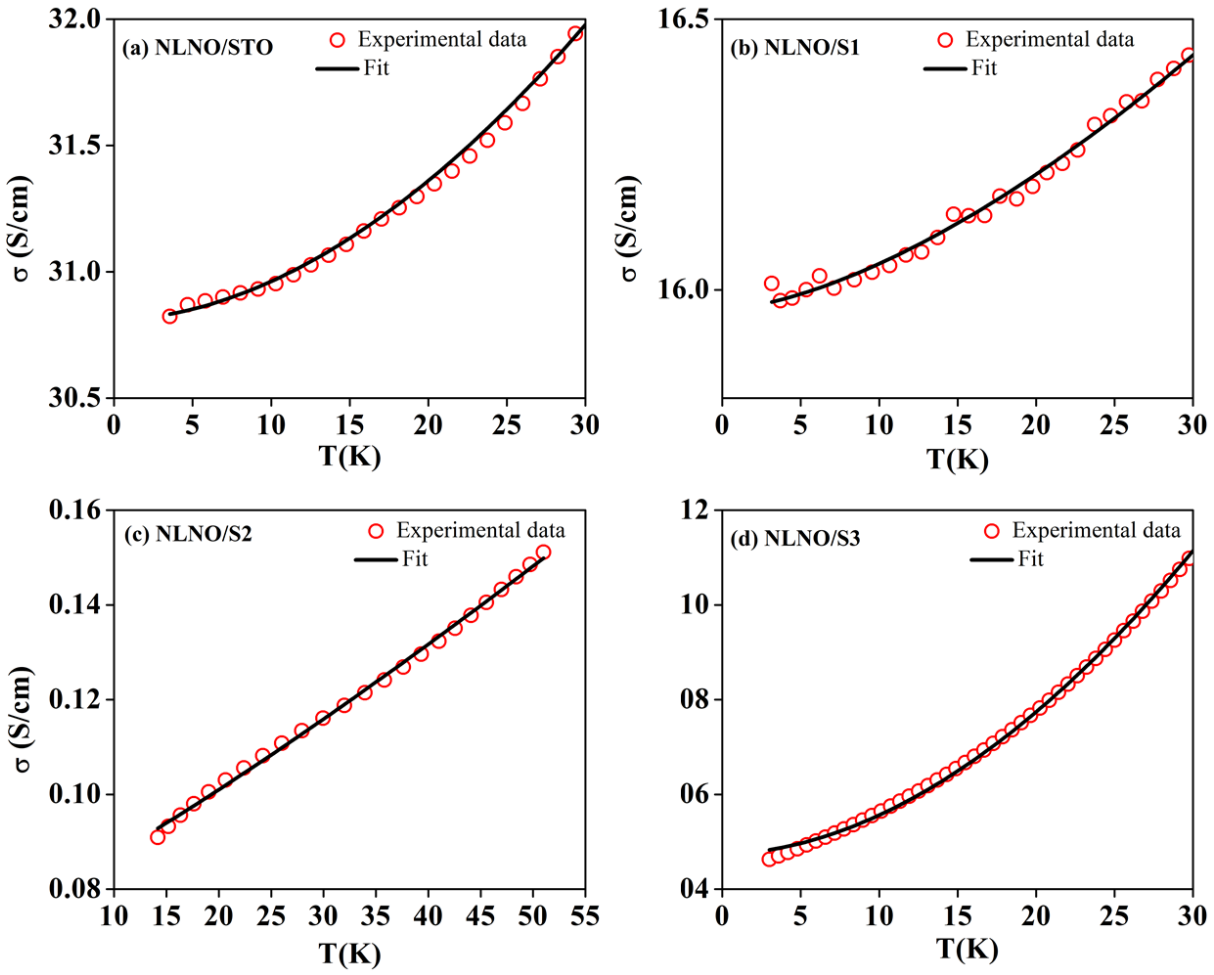

Figure 4.11: (a)-(d) The power law dependence of low-temperature conductivity of pristine and irradiated films of NLNO on STO.

For both NLNO/S0 and NLNO/S1, shallow temperature dependency with a small NTC ensures σ (300 K) ≥ σ (3 K), whereas for larger fluences, σ (300 K) ≫ σ (3 K). As demonstrated in Fig. 4.11(a)-(d) and Table 4.IV, the conductivities of all NLNO/STO films obey power law [Eq. (4.2)]. The pristine layer NLNO/S0 has a significantly greater extrapolated zero temperature conductivity σ(0) than the suppressed Mott insulator NNO/S1. The metallic-type temperature-dependent resistivities (with positive temperature coefficient) of the NLNO/LO and NLNO/L1 are comparable to those observed in a vast class of metallic oxides at low temperatures [16] as demonstrated in Fig. 4.12(a)-(d) and Table 4.IV).

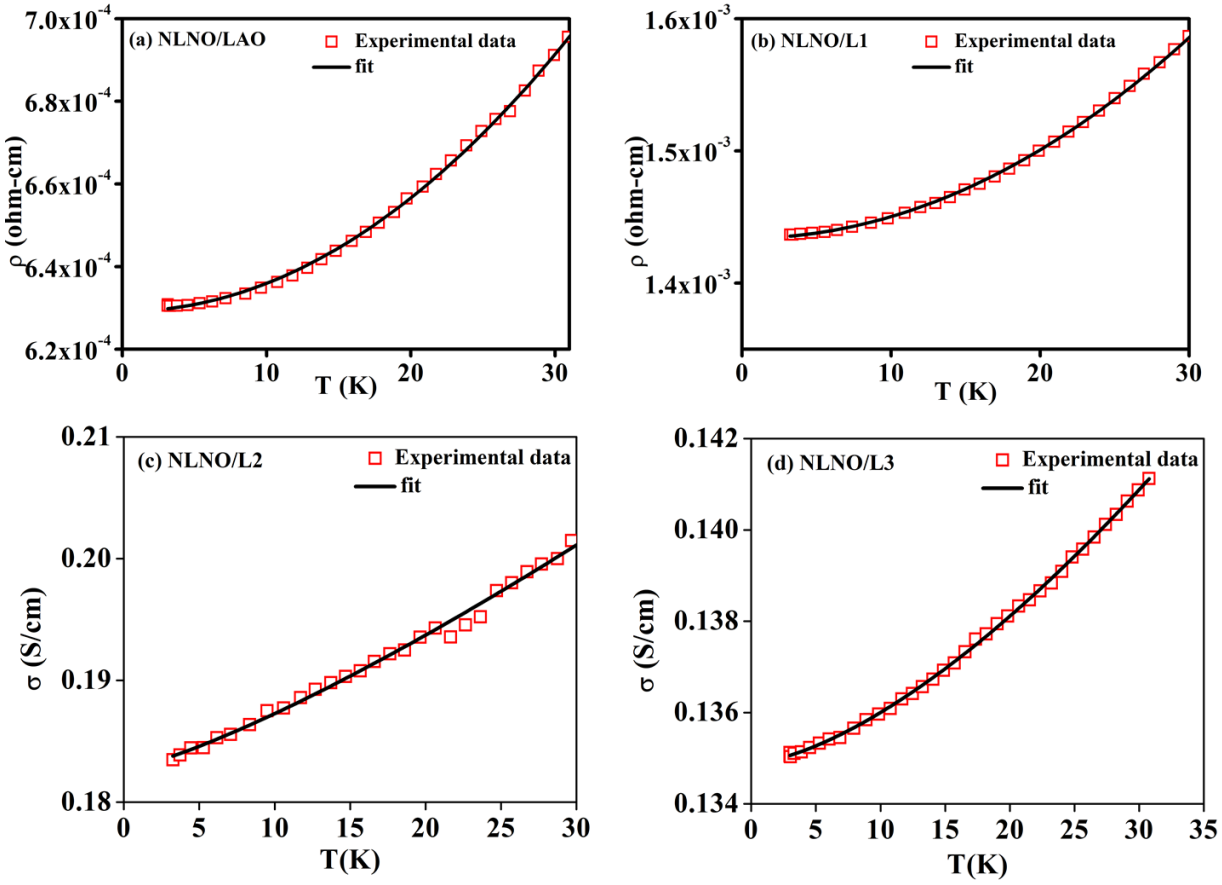

Figure 4.12: (a)-(d) The power law dependence of low-temperature conductivity of pristine and irradiated films of NLNO on LAO.

The increasing irradiation changes the metallic behavior to that of a disordered conductor with power-law conductivity and an extremely low σ(0). We conclude from the preceding discussion that irradiation produces a disordered conducting state on the verge of Anderson localization, regardless of whether the starting pristine sample is an insulator, such as a Mott-insulator, following the pathway shown schematically in vertical (a), or a metallic sample with

a positive temperature coefficient of resistivity following the pathway shown schematically in vertical (b).

4.3.4 Noise spectroscopy near the MIT and the effect of disorder

The influence of irradiation-induced disordering on the $NdNiO_3$ film formed on STO was investigated using flicker noise spectroscopy. Significant flicker noise has been seen in correlated electron systems such as $NdNiO_3$, V_2O_3, and VO_2 at MIT in the past [28,31,48–52]. This flicker noise has a spectral power density $S(f) \propto \frac{1}{f^{\alpha}}$. The representative plot of the frequency-dependent spectral power density is shown in Fig. 4.13(a) for the pristine and irradiated samples of NNO/STO. The exponent α is close to 1 away from T_{MI} in the pristine film as shown in Fig. 4.13(b)]. However, it exhibits a sharp rise at $T = T_{MI}$, indicating a shift in the spectral weight to a lower frequency. In the irradiated films for $T > T_{MI}$, $\alpha > 1$ denotes the dominance of lower frequency fluctuations. However, at lower temperatures, α exhibits similar temperature dependence as the pristine film, albeit without a large surge in α at the transition region $T = T_{MI}$. The MS fluctuations $\frac{<\Delta R^2>}{R^2}$ for each film are presented in Fig. 4.13(c). The pristine films have a nearly temperature-independent $\frac{<\Delta R^2>}{R^2}$ except at $T = T_{MI}$, where the variation increases by an order of magnitude over a short temperature range. The MS variations in the irradiated films are higher than those in the pristine film due to disordering, and $\frac{<\Delta R^2>}{R^2}$ has a shallow T dependence, as found in metallic oxide films that do not show MIT, such as $LaNiO_3$ [53,54]. However, there is no increase in the MS fluctuations as a result of the lack of any observable MIT in them. The absence of an MIT signature in the irradiated film is also observed in the second spectra displayed in Fig. 4.13(d). In pristine film Γ^2, it has a shallow temperature dependency and a value of ≈ 12 throughout most of the temperature region, but at $T = T_{MI}$, it leaps to a value as high as 70 due to the emergence of a substantial non-Gaussian component in the fluctuation. In the irradiated films, Γ^2 has a shallow temperature dependency with values ≈ 10-12, and there is no indication of a large Γ^2 near MIT, in contrast to the pristine film, indicating the lack of strong correlated non-Gaussian fluctuations.

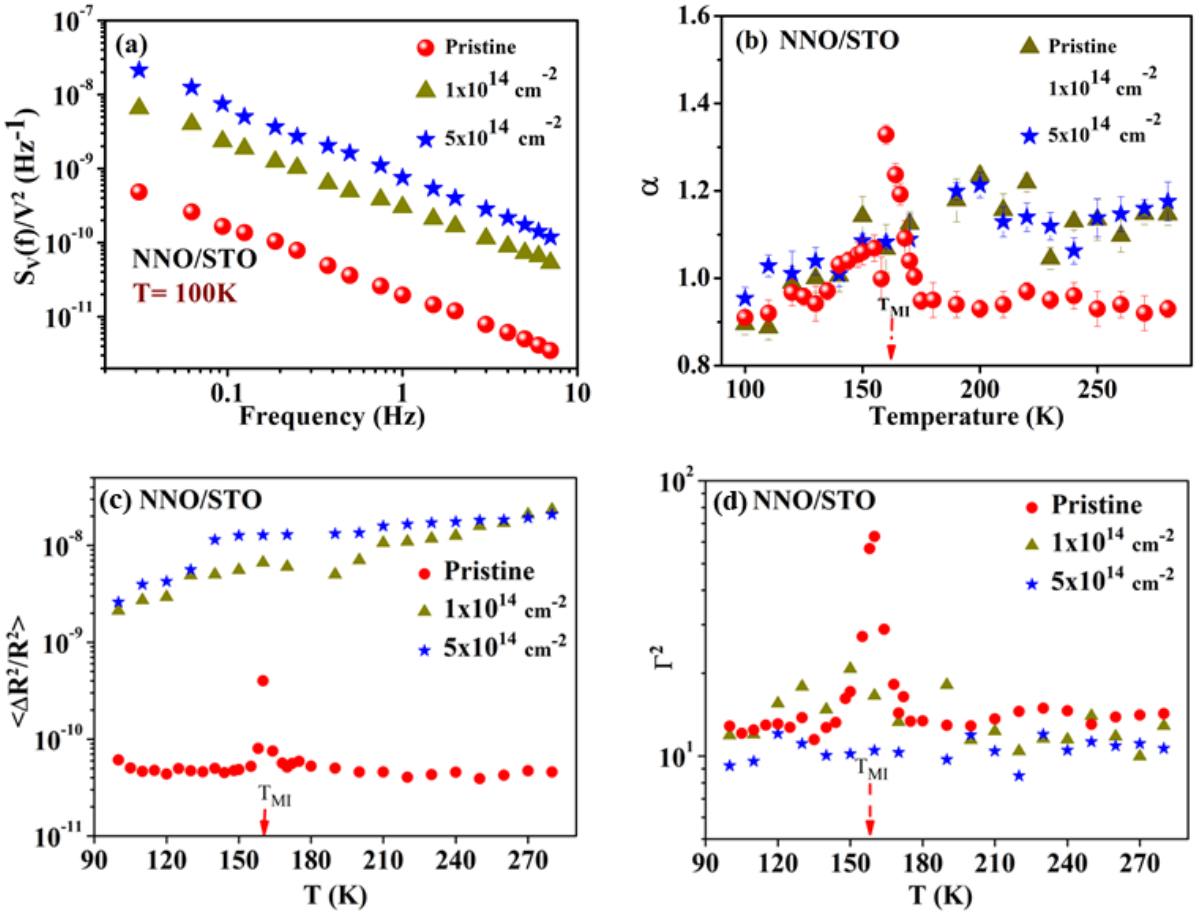

Figure 4.13: (a) Representative data of the frequency-dependent spectral power density at T = 100K for the pristine and irradiated samples of NNO/STO. (b) Temperature variation of the exponent α for the pristine and irradiated samples of NNO/STO. (c) Normalized mean square resistance fluctuation $\frac{\langle \Delta R^2 \rangle}{R^2}$ as a function of temperature for the pristine and irradiated samples of NNO/STO. (d) Temperature-dependent normalized second spectra Γ^2 in the pristine and irradiated films of NNO/STO. The metal-insulator transition temperature is marked as T_{MI}.

4.4 Discussion

4.4.1 Ion irradiation on oxide conductors

The nature of defects created by energetic ions is determined by their energy, with lower energy ions producing point defects such as vacancies and interstitials by nuclear collisions. Higher energy ions with energies well above a few MeV produce extended defects as a result of electronic excitation and electron energy loss mechanisms. In the energy range we use, nuclear collisions will be the main source of energy loss, resulting in the creation of mainly point

defects, with small contributions from electronic energy loss. The formation of defects in oxides formed by energetic ions has been studied extensively for many years [55–58]. The dynamics of defect formation are complicated and depend on the target's structure and chemical contents, as well as the energy of the ions utilized. Nonetheless, certain broad characteristics are shared by the majority of oxides. The energetic ions displace atoms into the interstitial space, leaving vacancies. In an irradiated solid, the defects created are generally vacancies in the top layer of a few tens of nanometers, which is of the same order as the thickness of the films used here, while deep inside the solid, cascade formation may lead to more complex defect structures, which in our case may occur within the substrate [32,33]. The displacement of the oxygen sublattice is important in oxides. This results in the formation of three types of vacancies: neutral oxygen atoms in interstitial places, neutral oxygen vacancies, and singly or doubly charged vacancies formed by electron localization within the vacancies. The creation of vacancies leads to the formation of strong electron localization sites. The charged vacancies that are randomly positioned also operate as strong random scatterers, which can lead to disordered induced localization. Amorphization can occur beyond a critical temperature of irradiation, which is typically $>$ 450 K in oxides depending on the ionic radii of the constituent cations, at higher fluences and ion energy of more than a few MeV [56,57]. To avoid heating, the sample in our experiment is kept mounted on a liquid nitrogen-cooled copper plate. As a result, it is envisaged that considerable amorphization will not occur in the films. The films primarily preserve their crystalline structure. To put our findings into context, a summary of previous investigations on $NdNiO_3$ irradiation is provided below.

Previous experiments on thick (200 nm) $NdNiO_3$ films grown on $SrTiO_3$ and $LaAlO_3$ substrates with very high energy (200 MeV) heavy ions (Ag) ions revealed suppression of the T_{MI} and its shift towards lower temperatures. This has been accompanied by increased resistivity [19–21]. The fluence was used in this energy range at a rate that was more than two orders lower than in the current work. The defects created by an ion with an energy of 200 MeV are not point defects but rather of an extended character. These investigations focused mostly on the enhancement of resistivities due to ion irradiation. However, the suppression of the MIT and the insulating state, as well as its crossover to a disordered conductor with WL and eventual approach to the Anderson localized state, remain unaddressed. The observations were explained as the result of stresses caused by irradiation.

4.4.2 Nature of electrical conduction in the irradiated films at low temperature

The evolution of low-temperature conductivity σ ($T \leq 30$ K) in the disordered conducting state that arises as a result of ion irradiation follows a power law as shown in Eq. (4.2). The evolution of the exponent m on disordering and the way to Anderson localized state would need comments. In substitutional systems such as $LaNi_{1-x}Co_xO_3$, Na_xWO_3, and $LaNi_{1-x}Sr_xO_3$, the exponent is $0.5 \leq m \leq 1$. However, the exponent $1 \leq m \leq 2$ in the $Nd_{0.7}La_{0.3}NiO_3$ system with La doping. In such disordered systems, the exponent m can evolve due to the relative weights of the WL component (which provides a correction to conductivity) as well as an electron-electron interaction term (EEI). While the EEI term contributes a $\sqrt{T}$ temperature to conductivity, the contribution from the WL term comes from the term correction to conductivity that depends on the temperature-dependent phase coherence length $L_\varphi(T)$ given as [3]

$$\delta\sigma_{WL}(T) = \frac{e^2}{2\pi^2\hbar}\left(\frac{1}{L_\varphi(T)}\right) \tag{4.3}$$

The temperature dependence of $L_\varphi(T)$ is determined by the scattering process, which is derived from the relationship $L_\varphi(T) = (D\tau_\varphi)^{1/2}$, where D is the electron diffusivity and τ_φ is the phase relaxation time. Generally, $\tau_\varphi \propto T^p$ with $1.5 < p < 4$. When electron-electron scattering dominates the phase relaxation, $1.5 < p < 2$ is obtained, and when electron-phonon scattering dominates the phase relaxation, $2 < p < 4$ is obtained. Thus, the observed m is $\approx \frac{p}{2}$. In our experiment, $1 < m < 2$ demonstrates that the scattering is dominated by electron-phonon scattering, which is expected in the temperature range of the investigation, as well as strong electron-phonon coupling in oxide systems. Taking both the EEI and the WL contributions into account, we formulate the temperature dependency of σ at $T \leq 30$ K as [16].

$$\sigma_{(T)} = \sigma_0 + A\sqrt{T} + BT^2 \tag{4.4}$$

Figures 4.14(a) and 4.14(b) provide several illustrative examples to fit Eq. (4.4). Thus, it can be assumed that the variation of the exponent m results from relative changes in the weight of the two contributions, which change as the disorder changes the electron diffusivity D. The progressive disordering significantly decreases $\sigma(0)$ and changes m as well. The samples with the highest disorder have low $\sigma(0)$ values, indicating that they are most likely nearing a

disordered-induced localized insulating state with $\sigma(0) \rightarrow 0$.

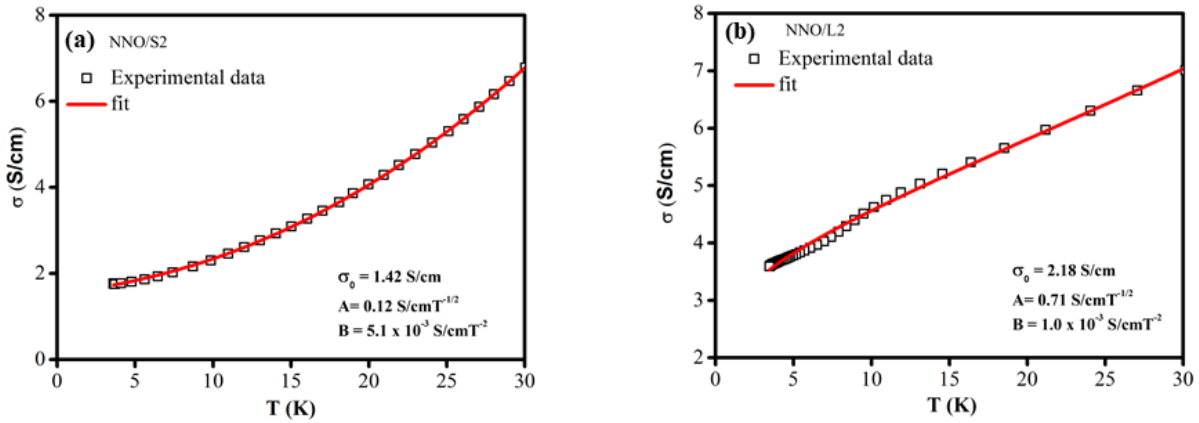

Figure 4.14: (a) The low-temperature fit of the data to equation 4.4 for (a) NNO/S2 and (b) NNO/L2.

Despite having low conductivity (high resistivity), the samples that have been irradiated with the highest fluences do not exhibit a clear insulating behavior (activated transport), in contrast to the pristine samples, which exhibit a VRH type of conduction [Eq. (4.1)]. Instead, these samples exhibit a power-law conductivity [Eq. (4.2)] with a finite conductivity $\sigma(0)$ as $\rightarrow 0$. A small value of $\sigma(0)$ in the range of 10^{-2} to 5×10^{-3} S/cm would require comments, even though this is predicted in samples that exhibit weak localization or approach the Anderson insulator state. This Mott minimum conductivity (σ_{Mott}) value, which is typically in the range of $\sigma_{Mott} \leq 100$ S/cm in disordered oxides [16], is substantially lower than those observed in such materials. As the system $Nd_{0.7}La_{0.3}NiO_3$ passes through a region of substitution-induced continuous MI transition, it is noted that a low value of $\sigma(0) \leq 10$ S/cm has also been observed [28]. A low value of $\sigma(0)$ may arise from two sources. It might be caused by extremely low DOS at E_F, which could occur given that the collapse of the insulating state would require filling the hole in Fermi level DOS. It is possible that the emergence of significant disorder will cause the samples to become inhomogeneous, resulting in the coexistence of insulating and conducting (but low conductivity) regions. It has been demonstrated in the context of rare-earth manganites that the presence of a minority phase conducting region at low temperatures in the majority phase of an insulating solid can result in a situation at low T where the current is predominately carried in the regions of higher conductivities, which can lead to a finite $\sigma(0)$ [59].

4.5 Conclusion

To summarize, we show that ion irradiation-induced disorder in an insulator such as $NdNiO_3$, which is similar to a Mott insulator, can lead to the collapse of the insulating state and a crossover to a disordered conductor that approaches Anderson localization due to increasing disordering. It has been suggested that radiation-induced disordering is a better technique to disorder a correlated insulator than the more traditional process of ionic substitution, which may introduce additional variables. It is conventional wisdom that when a solid is disordered it leads to a lowering (raising) of conductance (resistance). We, however, make a counterintuitive observation that at lower fluence at low T the conductivity enhanced on irradiation. This develops, as was previously discussed when the insulating state collapses under disordering. Using noise spectroscopy, it has also been found that the non-Gaussian content of the resistance fluctuation, which comes from the correlated character of the fluctuation in pristine films and is readily seen at $T \approx T_{MI}$, is suppressed in the irradiated films.

References:

[1] N. F. Mott, *Metal-Insulator Transition* (Taylor and Francis, London, 1990).

[2] M. Imada, A. Fujimori, and Y. Tokura, Rev. Mod. Phys. **70**, 1039 (1998).

[3] P. A. Lee and T. V. Ramakrishnan, Rev. Mod. Phys. **57**, 287 (1985).

[4] P. P. Edwards, J. R. L., C. N. R. Rao, D. P. Tunstall, and F. Hensel, Philos. Trans. R. Soc. London. Ser. A Math. Phys. Eng. Sci. **356**, 5 (1998).

[5] P. Edwards and C. N. R. Rao, Eds., *Metal-Insulator Transitions Revisited* (Taylor and Francis, Bristol, 1955).

[6] R. E. Peierls, *Quantum Theory of Solids* (Oxford University Press, New York, 1955). p. 108.

[7] N. F. Mott, Proc. Phys. Soc. Sect. A **62**, 416 (1949).

[8] N. F. MOTT, Rev. Mod. Phys. **40**, 677 (1968).

[9] P. W. Anderson, Phys. Rev. **109**, 1492 (1958).

[10] F. Evers and A. D. Mirlin, Rev. Mod. Phys. **80**, 1355 (2008).

[11] D. Belitz and T. R. Kirkpatrick, Rev. Mod. Phys. **66**, 261 (1994).

[12] K. Byczuk, W. Hofstetter, and D. Vollhardt, Phys. Rev. Lett. **94**, 056404 (2005).

[13] H. Bragança, M. C. O. Aguiar, J. Vučičević, D. Tanasković, and V. Dobrosavljević, Phys. Rev. B **92**, 125143 (2015).

[14] A. E. Antipov, Y. Javanmard, P. Ribeiro, and S. Kirchner, Phys. Rev. Lett. **117**, 146601 (2016).

[15] D. I. Khomskii, *Transition Metal Compounds* (Cambridge University Press, Cambridge, 2014).

[16] A. K. Raychaudhuri, Adv. Phys. **44,** 21 (1995).

[17] C. N. R. Rao and J. Gopalakrishnan, *New Directions in Solid State Chemistry* (Cambridge University Press, 1997).p. 200.

[18] T. Sasaki, Crystals **2**, 374 (2012).

[19] Y. Kumar, R. J. Choudhary, A. P. Singh, G. Anjum, and R. Kumar, J. Appl. Phys. **108**, 083706 (2010).

[20] Y. Kumar, R. J. Choudhary, and R. Kumar, J. Appl. Phys. **112**, 073718 (2012).

[21] Y. Kumar, R. J. Choudhary, and R. Kumar, J. Appl. Phys. **120**, 115306 (2016).

[22] S. Middey, J. Chakhalian, P. Mahadevan, J. W. Freeland, A. J. Millis, and D. D. Sarma, Annu. Rev. Mater. Res. **46,** 305 (2016).

[23] S. Catalano, M. Gibert, J. Fowlie, J. Iguez, J. M. Triscone, and J. Kreise, Rep. Prog. Phys. **81,** 046501 (2018).

[24] H. Park, A. J. Millis, and C. A. Marianetti, Phys. Rev. Lett. **109**, 156402 (2012).

[25] I. I. Mazin, D. I. Khomskii, R. Lengsdorf, J. A. Alonso, W. G. Marshall, R. M. Ibberson, A. Podlesnyak, M. J. Martínez-Lope, and M. M. Abd-Elmeguid, Phys. Rev. Lett. **98**, 176406 (2007).

[26] V. Bisogni, S. Catalano, R. J. Green, M. Gibert, R. Scherwitzl, Y. Huang, V. N. Strocov, P. Zubko, S. Balandeh, J. Triscone, G. Sawatzky, and T. Schmitt, Nat. Commun. **7**, 13017 (2016).

[27] A. S. Disa, D. P. Kumah, J. H. Ngai, E. D. Specht, D. A. Arena, F. J. Walker, and C. H. Ahn, APL Mater. **1**, 032110 (2013).

[28] R. S. Bisht, G. N. Daptary, A. Bid, and A. K. Raychaudhuri, J. Phys.: Condens. Matter 31, 145603 (2019).

[29] Z. Wang, Y. Okada, J. O'Neal, W. Zhou, D. Walkup, C. Dhital, T. Hogan, P. Clancy, Y.-J. Kim, Y. F. Hu, L. H. Santos, S. D. Wilson, N. Trivedi, and V. Madhavan, Proc. Natl. Acad. Sci. **115**, 11198 (2018).

[30] R. S. Bisht, S. Samanta, and A. K. Raychaudhuri, Phys. Rev. B **95**, 115147 (2017).

[31] S. Chatterjee, R. S. Bisht, V. R. Reddy, and A. K. Raychaudhuri, Phys. Rev. B **104**, 155101 (2021).

[32] J. F. Ziegler, J. P. Biersack, and M. D. Ziegler, *SRIM-The Stopping and Range of Ions in Matter* (Ion Implantation Press, 2008).

[33] J. F. Ziegler, J. P. Biersack, and U. Littmark, *The Stopping and Range of Ions in Matter*

(Pergamon, New York. 1985).

[34] J. H. Scofield, Rev. Sci. Instrum. **58**, 985 (1987).

[35] A. K. Raychaudhuri, Curr. Opin. Solid State Mater. Sci. **6**, 67 (2002).

[36] A. Ghosh, S. Kar, A. Bid, and A. K. Raychaudhuri, arXiv:cond-mat/0402130.

[37] F. X. Zhang, H. Xue, J. K. Keum, A. Boulle, Y. Zhang, and W. J. Weber,J. Phys. Condens. Mater **32,** 355405 (2020).

[38] Ravindra Singh Bisht, Investigation of Metal Insulator Transition in 3D Transition Metal Oxides, Ph.D. thesis, University of Calcutta, India (2019).

[39] M. Zaghrioui, A. Bulou, P. Lacorre, and P. Laffez, Phys. Rev. B **64,** 081102(R) (2001).

[40] C. Girardot, J. Kreisel, S. Pignard, N. Caillault, and F. Weiss, Phys. Rev. B **78**, 104101 (2008).

[41] J. Fowlie, B. Mundet, C. Toulouse, A. Schober, M. Guennou, C. Domínguez, M. Gibert, D. T. L. Alexander, J. Kreisel, and J.-M. Triscone, APL Mater. **9**, 081119 (2021).

[42] M. Zhang, Raman Study of the crystalline-to-amorphous state in alpha-decay-damaged materials, http://dx.doi.org/10.5772/65910.

[43] A. Stupakov, O. Pacherova, T. Kocourek, M. Jelinek, A. Dejneka, and M. Tyunina, Phys. Rev. B **99**, 085111 (2019).

[44] K. Ramadoss, N. Mandal, X. Dai, Z. Wan, Y. Zhou, L. Rokhinson, Y. P. Chen, J. Hu, and S. Ramanathan, Phys. Rev. B **94**, 235124 (2016).

[45] R. M. Hill, Phys. Status Solidi (a) **34,** 601 (1976).

[46] A. Möbius, Crit. Rev. Solid State Mater. Sci. **44**, 1 (2019).

[47] W. N. Shafarman and W. Koon, **40**, 1216 (1989).

[48] S. Samanta, A. K. Raychaudhuri, X. Zhong, and A. Gupta, Phys. Rev. B **92**, 195125 (2015).

[49] A. Sahoo, S. D. Ha, S. Ramanathan, and A. Ghosh, Phys. Rev. B **90**, 085116 (2014).

[50] A. M. Alsaqqa, S. Singh, S. Middey, M. Kareev, J. Chakhalian, and G. Sambandamurthy, Phys. Rev. B **95**, 1 (2017).

[51] G. N. Daptary, S. Kumar, M. Kareev, J. Chakhalian, A. Bid, and S. Middey, Phys. Rev. B **100**, 125105 (2019).

[52] S. Kundu, T. Bar, R. K. Nayak, and B. Bansal, Phys. Rev. Lett. **124**, 095703 (2020).

[53] A. Ghosh, A. K. Raychaudhuri, R. Sreekala, M. Rajeswari, and T. Venkatesan, J. Phys. D (Appl. Phys.) **30,** L75 (1997).

[54] A. Ghosh and A. K. Raychaudhuri, Phys. Rev. B **64**, 104304 (2001).

[55] E. A. Kotomin and A. I. Popov, Nucl. Instrum. Methods Phys. Res. B **141**, 1 (1998).

[56] K. E. Sickafus, L. Minervini, R. W. Grimes, J. A. Valdez, M. Ishimaru, F. Li, K. J. Mcclellan, and T. Hartmann, **289**, 748 (2000).

[57] K. E. Sickafus, R. W. Grimes, J. A. Valdez, A. Cleave, M. Tang, M. Ishimaru, S. M. Corish, C. R. Stanek, and B. P. Uberuaga, Nat. Mater. **6**, 217 (2007).

[58] M. M. Rahman, W. Chen, L. Mu, Z. Xu, Z. Xiao, M. Li, X. Bai, and F. Lin, Nat. Commun. **11**, 4548 (2020).

[59] T. Sarkar, A. K. Raychaudhuri, A. K. Bera, and S. M. Yusuf, New J. Phys. **12**, 123026 (2010).

Chapter 5 Anomalous Hall effect in topological Weyl and nodal-line semimetal Heusler compound Co_2VAl

In this chapter, we present a thorough investigation of the anomalous Hall effect (AHE) in the ferromagnetic full Heusler compound Co_2VAl. Experimentally, it has been found that the longitudinal resistivity (ρ_{xx}) scales quadratically with the anomalous Hall resistivity (ρ_{xy}^{A}). Our experimental findings further indicate that the anomalous Hall conductivity is approximately 85 S/cm, with an intrinsic contribution of approximately 75.6 S/cm at 2 K. The first-principles calculations suggest that the Berry curvature originated from a gapped nodal line and symmetry-protected Weyl nodes near the Fermi level are the main source of the observed AHE in the studied compound.

Content of this chapter has been published in: **S. Chatterjee**, J. Sau, S. Ghosh, S. Samanta, B. Ghosh, M. Kumar, and K. Mandal, "Anomalous Hall effect in topological Weyl and nodal-line semimetal Heusler compound Co_2VAl," **J. Phys.: Condens. Matter** 35, 035601 (2023).

5 Anomalous Hall effect in topological Weyl and nodal-line semimetal Heusler compound Co_2VAl

5.1 Preface

Magnetic topological semimetals (TSMs) display remarkable quantum transport properties due to the topological structure of their electronic bands in the presence of ferromagnetic ordering, which breaks the system's time-reversal symmetry [1–4]. The valence and conduction bands of magnetic TSMs have linear band dispersion at the crossing point due to their nontrivial topology, and the crossing points may form zero-dimensional discrete points [5], one-dimensional continuous or extended lines [6] in the Brillouin zone (BZ). Since the ferromagnetic TSMs with broken time-reversal symmetry include nontrivial electronic structures in addition to intrinsic magnetic order [7,8], they may be prospective materials for next-generation spintronic devices. Hence, identifying compounds with readily visible ferromagnetic Weyl or nodal fermions constitutes a key issue in the investigation of this topological phase. For their high Curie temperature and tunability in structural, electrical, and magnetic properties, cobalt (Co_2)-based ferromagnetic full Heusler compounds have recently gained attention [9–12]. Several of these Co_2-based ferromagnetic full Heusler compounds have also been expected to host the Weyl fermions in their electronic band structure [13], and their unusual half-metallic feature makes them attractive candidates for device applications [14,15]. While examples of Weyl fermionic materials with broken inversion symmetry abound in the literature [16–20], examples with broken time-reversal symmetry are very rare [21,22]. These nontrivial topological materials result in numerous unusual phenomena, including the anomalous Hall effect (AHE), anomalous Nernst effect, Fermi arc surface states, the chiral anomaly effect, etc [2,23–29].

One of the most intriguing topics in condensed matter physics is the genesis of AHE in magnetic materials, and it is still ambiguous whether AHE contributes in an intrinsic or extrinsic way. Along with the ordinary Hall effect that results from the Lorentz force deflecting moving charge carriers in a magnetic field, ferromagnetic materials also exhibit an anomalous term that is proportional to spontaneous magnetization. The AHE is caused by three

mechanisms, namely skew scattering, side jump, and intrinsic deflection [30]. Karplus and Luttinger originally suggested a model related to the band structure of ferromagnetic metals with the spin-orbit interaction (the intrinsic Karplus-Luttinger (KL) mechanism) [31], and it is demonstrated that the anomalous Hall resistivity (ρ_{xy}^{A}) grows quadratically with the longitudinal resistivity (ρ_{xx}). Eventually, Smit [32,33] and Berger [34] found two fundamental extrinsic mechanisms, skew-scattering, and side-jump, respectively. These mechanisms can be explained as asymmetric scattering caused by the spin-orbit interaction acting on conduction electrons or impurities. However, side-jump scattering is proportional to ρ_{xx}^{2}, which is identical to the intrinsic KL mechanism, whereas the ρ_{xy}^{A} for skew-scattering is linearly proportional to ρ_{xx}. The intrinsic KL mechanism is intimately related to the Berry curvature of the occupied electronic Bloch states [35–37]. AHE has been considered the primary signature of finite magnetization in ferromagnetic materials for a very long time. However, it has been established in recent years that the intrinsic contribution of AHE is not directly related to magnetization but is instead determined by its nonvanishing Berry curvature [38]. Hence, by carefully modifying a material's electronic band structures and symmetries, it is possible to regulate the Berry curvature and intrinsic AHE [39].

The AHE in a few Co_2-based ferromagnetic full Heusler compounds has been explored both experimentally and theoretically [6,40–47]; nonetheless, their non-trivial topological and magneto-transport features depend substantially on their electronic band structure, despite their belonging to the same space group, $Fm\bar{3}m$. For instance, the AHE in Co_2MnAl is dominated by the intrinsic mechanism [46], whereas Co_2TiAl exhibits skew-scattering dominated AHE [45]. The temperature-dependent skew-scattering similarly dominates the AHE in Co_2FeSi and Co_2FeAl [42], in contrast to Co_2CrAl, where the intrinsic mechanism predominates [40]. In a different investigation on Co_2TiSi and Co_2TiGe, the intrinsic mechanism is discovered to be the predominant mechanism for AHE [44], however, for Co_2MnSi and Co_2MnGe, the skew scattering is discovered to be the dominant mechanism for AHE [41]. Furthermore, while a number of these full Heusler compounds have topological nontrivial states in their band structure, they are fundamentally different from one another. Co_2FeGe, for example, is a nodal-line TSM [47], but Co_2MnAl has both a topological Weyl and a nodal-line semimetallic state [46]. Thus, the topological and magneto-transport properties of these compounds are strongly influenced by the electronic band dispersion of

these compounds. As a result, the phenomenon of AHE in these compounds is intriguing due to the rich physics and intricacy connected with understanding its origin in specific compounds.

The primary purpose of this chapter is to investigate the topological origin of AHE in the Co_2-based ferromagnetic full Heusler compound Co_2VAl both theoretically and experimentally. The majority of previous investigations on this system have been limited to magnetic properties [48,49], but the topological nature of this system has remained unexplored so far. We observed that the experimental anomalous Hall conductivity (AHC), which has an intrinsic contribution of about 75.6 S/cm and exhibits weak temperature dependency, is about 85 S/cm at 2 K. Our ab initio first-principles simulations of the electronic structure reveal a magnetization-induced gapped nodal-line in the electronic band dispersion close to the Fermi level (E_F) as well as symmetry-protected Weyl points. We further demonstrate that the significant Berry curvature along the nodal-line and at the Weyl points is the primary source of AHE in Co_2VAl, implying that the intrinsic KL mechanism is prominent in this system. We also determine the charge chirality of the Weyl points at the E_F and compare it to the calculated intrinsic AHC using the Green-Kubo formalism, which is 64 S/cm and is in good agreement with the experimentally obtained result.

5.2 Experimental and theoretical details

High-purity Co (99.99%), V (99.9%), and Al (99.99%) components were utilized in a typical arc-melting furnace containing a high-purity argon environment to produce polycrystalline Co_2VAl. To ensure a uniform melting, the sample was repeatedly remelted. The ingot was then vacuum-sealed in a quartz tube and annealed at 1173 K for five days before being quenched in cold water. The structure and phase purity of polycrystalline Co_2VAl were determined using the X-ray diffraction (XRD) technique (Rigaku SmartLab) with Cu K_α radiation. The FULLPROF software was used to perform Rietveld refinements on the experimentally obtained XRD data. A vibrating sample magnetometer was used in a physical property measurement system (PPMS, Quantum Design, USA) to measure the magnetization. The magnetization measurements were performed as a function of the applied field up to 5 T and temperature down to 2 K. The magnetic measurements were performed on a sample with approximate dimensions of 0.4 × 0.5 × 4.2 mm^3. To obtain a good thermal equilibrium, we stabilized the temperature for at least 45 minutes for each M(H) isotherm. We found no difference in M(H) isotherms between rising and decreasing fields. Using a 9-T PPMS (Quantum Design, USA)

equipped with the AC transport option down to 2 K and magnetic field up to 9 T, electrical and magnetic transport measurements were conducted. A conventional four-probe technique was used to measure both the longitudinal and the Hall resistivity. The final Hall resistivity (ρ_{xy}) was computed using the difference between the transverse resistance obtained at the positive and negative fields to completely rule out the longitudinal resistivity (ρ_{xx}) contribution caused by the voltage probe misalignment.

Using first-principles electronic structure simulations[1], we also studied the electronic band structures and transport characteristics of Co_2VAl. The calculations were done using the projected augmented wave method, which was implemented in the Vienna ab-initio simulation package [50]. The exchange-correlation function was approximated by a generalized gradient of the Perdew-Burke-Ernzerhof type. Using a plane-wave basis, the kinetic energy cut-off is 600 eV. The BZ sampling was performed on a 6 × 6 × 6 k-point mesh, and the electrical integral across BZ was computed using the Gaussian smearing method with a width of 0.05 eV. Cell parameters and internal atomic positions were thoroughly relaxed until all-atom forces were less than 0.01 eV A^{-1}. Using Wannier90 [51,52] and Wanniertools [53] starting with the plane wave basis state, the AHC, the chirality of the Weyl fermion, and Berry curvature were computed. Using the limit of the tight-binding model, the AHC computations were performed using a dense k-grid of 501 × 501 × 501.

5.3 Results

5.3.1 Structural and magnetization properties

Figure 5.1(a) depicts the room temperature XRD pattern of the polycrystalline Co_2VAl compound, as well as its Rietveld refinement, the difference between observed and fitted patterns, and the Bragg peak positions. There are no impurity peaks seen in the observed XRD pattern. The single-phase character of the compound and its crystallization in cubic $L2_1$ structure with a space group $Fm\bar{3}m$ are confirmed by the Rietveld refinement of the XRD pattern. The existence of (111) and (200) superlattice reflections [inset of Fig. 5.1(a)] demonstrates that this material organizes in an $L2_1$-type structure. Co atoms occupy (0, 0, 0) and (1/2, 1/2, 1/2) sites, respectively, whereas V and Al atoms occupy (1/4, 1/4, 1/4) and (3/4, 3/4, 3/4) sites. The lattice parameter obtained from the refinement is determined to be 5.7732 Å, which is in good accordance with the previously reported works [48,49,54]. Figure

[1] All the first-principles calculations used in this chapter has been done by the Prof. Manoranjan Kumar's group (in collaboration) at S. N. Bose National Centre for Basic Sciences, Kolkata.

5.1(b) depicts the magnetic field dependence of dc magnetization at 2 K. It is also noteworthy that the half-metallic full Heusler compounds obey the Slater-Pauling (SP) type behavior of magnetization [15]: $M_{tot}^{SP} = Z_{tot} - 24$ μ_B/f.u. where, M_{tot}^{SP} is the total magnetic moment and Z_{tot} is the total number of valance electrons in the unit cell of the compound. The value of Z_{tot} for Co_2VAl is 26. As a result, the total magnetic moment should be 2 μ_B/f.u. according to the above-mentioned formula. The value of saturation magnetization (M_s) is inferred from Fig. 1(b) to be around 1.86 μ_B/f.u., which is compatible with the SP rule. The magnetic behavior seen here is consistent with what has been reported in the literature [48].

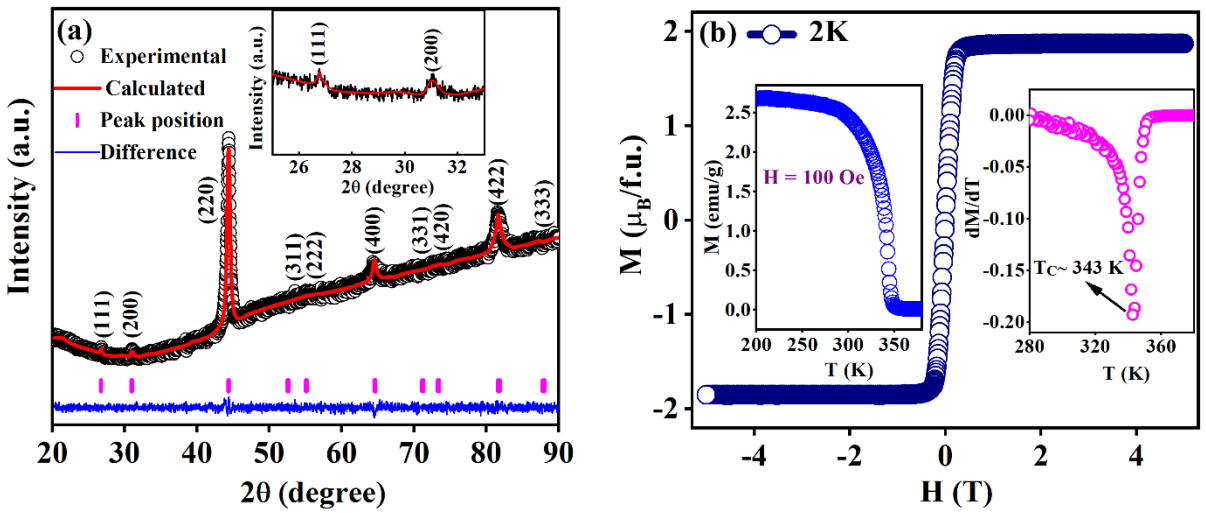

Figure 5.1: (a) Room temperature Rietveld refinement of the XRD pattern for Co_2VAl. The experimental data are represented by black circles, while the calculated result is shown by a solid red line. The vertical magenta lines represent Bragg positions, and the solid blue line at the bottom represents the difference in intensities between the experiment and the fitted intensities. The presence of (111) and (200) superlattice reflections in Co_2VAl is shown in the inset. (b) Magnetic field dependency of dc magnetization (M vs H) at 2 K. The temperature dependence of dc magnetization (M versus T) measured at 100 Oe is shown in the left inset, while the derivative magnetization dM/dT vs T is shown in the right inset.

The temperature dependence of dc magnetization under a 100 Oe applied magnetic field is illustrated in the left inset of Fig. 5.1(b). This indicates a continuous change from the paramagnetic (PM) to the ferromagnetic (FM) phase. The Curie temperature (T_C) is predicted to be around 343 K based on the temperature derivative of the magnetization curve, as seen in the right inset of Fig. 5.1(b).

5.3.2 Resistivity, magneto-transport, and anomalous Hall

Figure 5.2(a) depicts the change in longitudinal resistivity (ρ_{xx}) as a function of temperature from 2 to 380 K. At 2 K, the residual resistivity value is calculated to be around 176 μΩ cm, yielding a residual resistivity ratio of 1.14 [RRR = ρ_{xx}(300 K)/ ρ_{xx}(2 K)]. Though the magnetization curve [left inset of Fig. 5.1(b)] shows a clear continuous PM to FM phase transition around 343 K, we have not found such behavior in the ρ_{xx}; rather, the longitudinal resistivity exhibits a broad maximum at ~ 200 K, well below the Curie temperature. A similar type of behavior in the ρ_{xx} has already been reported in Co_2VAl [55]. The broad platform in ρ_{xx} about 200 K, which is significantly below its Curie temperature (343 K), emerges due to a major change in the electronic band structure near the E_F as for a half-metallic ferromagnet there is a vanishing of the energy gap in one sub-band of electrons with spin down [56]. At lower temperatures, the electron-magnon contribution of a half-metallic ferromagnetic compound is generally nonexistent. As a result, the predominant contribution to the ρ_{xx} is attributable to (a) electron-electron (T^2 dependence), (b) electron-phonon (T dependency), and (c) double magnon scattering ($T^{9/2}$ dependence at lower temperatures and $T^{7/2}$ dependence at higher temperatures) [57].

To investigate the various scattering mechanisms of the ρ_{xx}, we fitted the temperature-dependent ρ_{xx} curve in three different temperature ranges of 2 K - 230 K (region I), 230 K - 325 K (region II), and 325 K - 380 K (region III), as shown in Fig. 5.2(a). In the low-temperature range, i.e., 2 K to 230 K, the ρ_{xx} fits well with the relation, $\rho(T) = \rho_0 + AT + BT^2 + CT^{9/2}$, while in the temperature range 230 K to 325 K, the best fit is given by, $\rho(T) = \rho_0 + DT + ET^{7/2}$, and in the high-temperature range, i.e. 325 K to 380 K, the ρ_{xx} fits very well with the relation, $\rho(T) = \rho_0 + FT$. Here, ρ_0 is the residual resistivity, A, D, and F are the temperature coefficients for electron-phonon scattering, B is the temperature coefficient for electron-electron scattering, and C and E are the temperature coefficients for two magnon scattering. As a result, the temperature-dependent ρ_{xx} data clearly show the presence of multiple scattering mechanisms in the present compound. Figure 5.2(b) depicts the isothermal magnetization (M) curves as a function of the applied field (H) for various temperatures. $M(H)$ isotherms demonstrate a dramatic increase with an increasing applied field in the low field area and saturation-like behavior begins to develop in the high field region far below T_C. With increasing temperature, the saturation magnetization decreases gradually. When we get closer

to the T_C, the overall character of the $M(H)$ isotherms in both the low and high field areas changes dramatically.

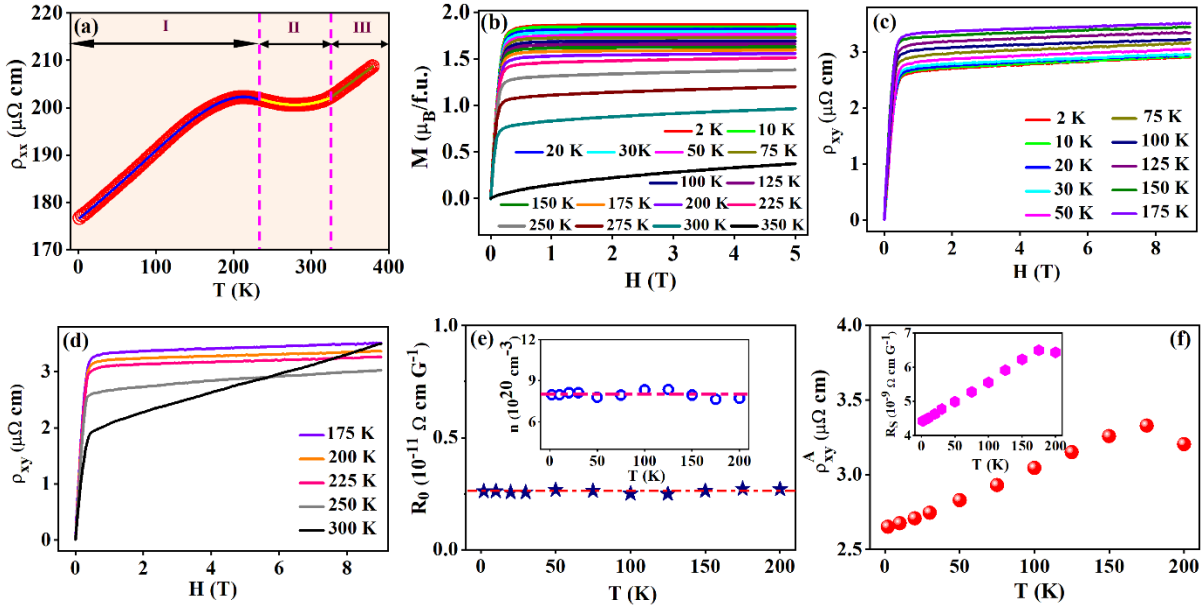

Figure 5.2: (a) Dependence of the longitudinal resistivity (ρ_{xx}) on temperature. The fittings in three temperature ranges are shown by the solid red (2 to 230 K), yellow (230 to 325 K), and dark yellow (325 to 380 K) lines. (b) Magnetic field dependency of dc magnetization (M vs. H) at the temperatures indicated. (c) and (d) Magnetic field-dependent Hall resistivity (ρ_{xy}) at different temperatures. (e) Temperature dependency of the ordinary Hall coefficient (R_0). The temperature-dependent carrier density n is shown in the inset. (f) Obtained temperature-dependent anomalous Hall resistivity (ρ_{xy}^A). The temperature dependency of the anomalous Hall coefficient is shown in the inset (R_S).

The Hall resistivity (ρ_{xy}) as a function of an applied magnetic field is shown in Fig. 5.2(c) and (d) at various temperatures. With a small applied magnetic field, the $\rho_{xy}(H)$ grows sharply, and anomalous behavior is observed up to 0.6 T. Up to 9 T, $\rho_{xy}(H)$ in the high field area exhibits a very weak linear field dependence. Similarities between the shapes of the $\rho_{xy}(H)$ and $M(H)$ curves indicate the existence of AHE in this compound. In contrast to magnetization, the value of $\rho_{xy}(H)$ increases monotonically with increasing temperature up to 175 K. As the temperature rises further, $\rho_{xy}(H)$ starts decreasing gradually. In general, the Hall resistivity ρ_{xy} in ferromagnetic materials receives a contribution from the spontaneous magnetization M, which is empirically described as [30],

$$\rho_{xy} = \rho_{xy}^{0} + \rho_{xy}^{A} = R_0 H + R_S \mu_0 M \quad (5.1)$$

where ρ_{xy}^{0} and ρ_{xy}^{A} are the ordinary and anomalous contributions to Hall resistivity, R_0 and R_S are the normal and anomalous Hall coefficients, and μ_0 is magnetic permeability in a vacuum. From the expression $R_0 = 1/ne$, where e is the electronic charge, we can determine the carrier density (n) and carrier type (electrons or holes) as a function of temperature. The linear fit of the $\rho_{xy}(H)$ curve in the high field region yields the values of R_0 and ρ_{xy}^{A}. The slope and y-axis intercept of the linear fit correspond to R_0 and ρ_{xy}^{A}, respectively. When we go closer to the T_C, the magnetic transition has a greater impact on the overall nature of the Hall resistivity, hence R_0 and R_S change dramatically. As a result, such an analysis is impossible to execute when the magnetization does not saturate in the high-field region [44]. Hence, near the Curie temperature, R_0 and ρ_{xy}^{A} cannot be extracted. The R_S can be calculated using the formula $\rho_{xy}^{A} = R_S \mu_0 M_S$ at temperatures much below the Curie temperature. We estimated the M_S from the $M(H)$ curves at H = 5 T [44,58]. Figure 5.2(e) depicts the R_0 as a function of temperature. Positive R_0 values indicate that holes are the majority charge carriers over the whole temperature range of 2 to 200 K. The carrier density n is calculated using R_0 values, as illustrated in the inset of Fig. 5.2(e). It is nearly temperature independent, with an estimated carrier density of $\sim 8 \times 10^{20}$ cm^{-3} at the lowest temperature (2 K). At 2 K, the associated carrier mobility (μ_h) is calculated to be $\sim$ 44.32 $cm^2\ V^{-1}\ S^{-1}$. Figure 5.2(f) depicts the extracted anomalous Hall resistivity (ρ_{xy}^{A}) as a function of temperature, demonstrating that the ρ_{xy}^{A} increases monotonically with temperature increase from 2 K to 175 K and then begins to decrease above 175 K. This is also reflected in the obtained anomalous Hall coefficient R_S, as seen in the inset of Fig. 5.2(f).

To understand the origin of AHE in Co_2VAl, we investigated the scaling behavior of ρ_{xy}^{A} on a double logarithmic scale in the temperature range of 2-175 K. However, we assume that the magnetic transition comes into effect above 175 K, and ρ_{xy}^{A} begins to decrease at higher temperatures [Fig. 5.2(f)]. Hence, for a valid comparison, the plot between ρ_{xy}^{A} and ρ_{xx} is confined to the temperature range of 2 to 175 K [43,44]. As shown in Fig. 5.3(a), a linear fitting is used to obtain the exponent based on the scaling relation $\rho_{xy}^{A} \propto \rho_{xx}^{\alpha}$ [30]. The almost quadratic dependence between ρ_{xy}^{A} and ρ_{xx} (i.e. $\alpha \approx 2$) implies that the intrinsic KL or the extrinsic side-jump mechanism, rather than the extrinsic skew-scattering mechanism, dominates the AHE in this material, rather than the linear dependence between ρ_{xy}^{A} and ρ_{xx}.

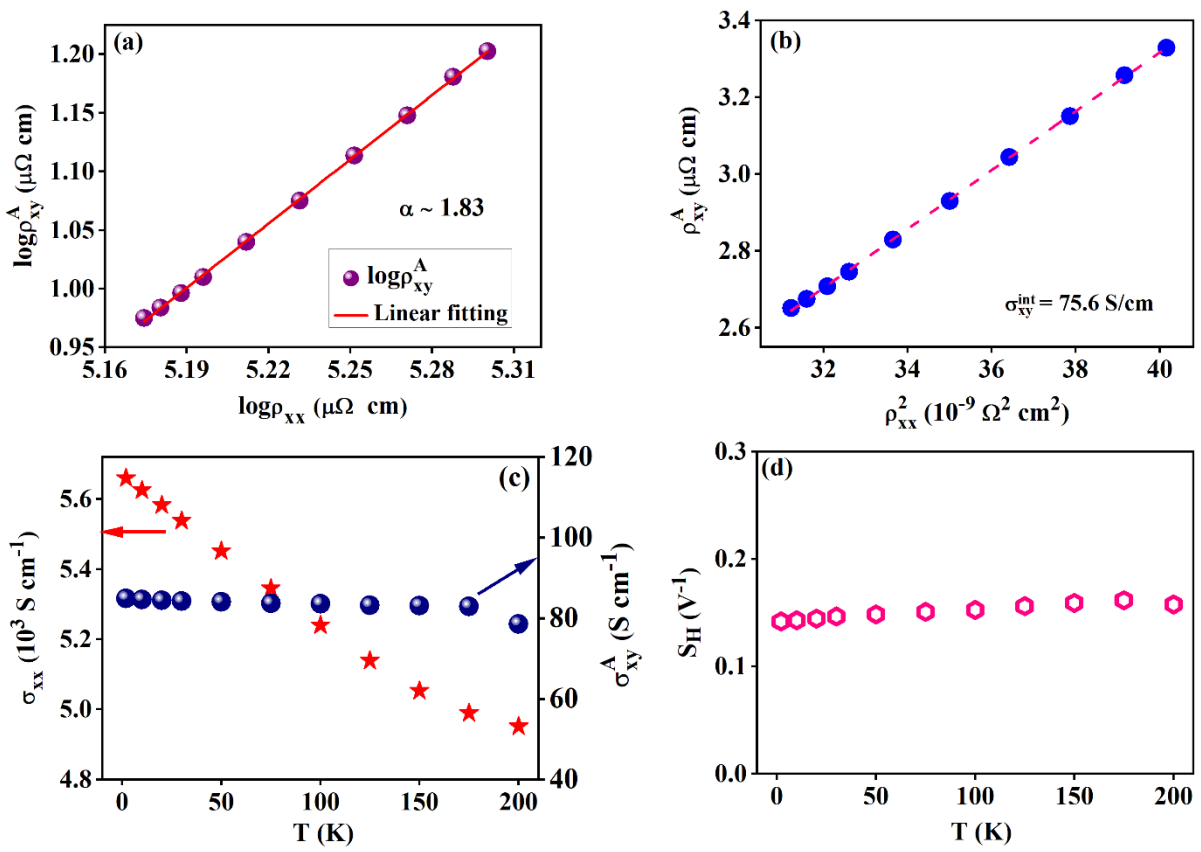

Figure 5.3: (a) log $\rho_{xy}^{A}(T)$ vs. log $\rho_{xx}(T)$ plot. According to the relation "$\rho_{xy}^{A} \propto \rho_{xx}^{\alpha}$", the solid red line represents the fit. (b) The fitting using equation (5.2) is represented by the dotted magenta line in the plot between ρ_{xy}^{A} and ρ_{xx}^{2}. The intrinsic AHC, σ_{xy}^{int}, is provided by the appropriate slope. (c) Temperature-dependent longitudinal conductivity σ_{xx} and anomalous Hall conductivity σ_{xy}^{A}. (d) Temperature dependency of the scaling coefficient (S_H).

To estimate the intrinsic AHC value, we plotted ρ_{xy}^{A} with ρ_{xx}^{2} as shown in Fig. 5.3(b) and fitted with the equation [43],

$$\rho_{xy}^{A} = f(\rho_{xx0}) + \sigma_{xy}^{int}\rho_{xx}^{2} \tag{5.2}$$

where $f(\rho_{xx0})$ is a function of residual resistivity ρ_{xx0}, including contributions from skew-scattering and side-jump mechanisms, and σ_{xy}^{int} is the AHC caused solely by the Berry curvature effect. For this compound, we determined an intrinsic AHC σ_{xy}^{int} of ~ 75.6 S/cm. It has been demonstrated that the extrinsic side-jump contribution of the AHC $|\sigma_{xy,sj}^{A}|$ is in the order of $\frac{e^2}{ha}(\frac{\varepsilon_{SO}}{E_F})$, where ε_{SO}, h, a and E_F are the spin-orbit interaction, Planck constant, lattice

constant, and Fermi energy, respectively [59,60]. For metallic ferromagnets, $\frac{\varepsilon_{SO}}{E_F}$ is typically of the order of 10^{-2} [44,58]. Using the lattice constant $a \sim 5.7732$ Å for the investigated compound and $(\frac{\varepsilon_{SO}}{E_F}) \sim 10^{-2}$, the derived side-jump contribution $|\sigma^{A}_{xy,sj}|$ is only approximately 6.7 S/cm. As a result, the extrinsic side-jump contribution to overall AHC is negligible when compared to the intrinsic AHC. Consequently, the intrinsic Berry-phase driven KL contribution dominates the AHE in Co_2VAl. Furthermore, to understand the microscopic origin of the AHE in this compound, we must investigate the variation of AHC with temperature and with longitudinal conductivity (σ_{xx}). For this, we estimated the AHC ($\sigma^{A}_{xy} \approx -\frac{\rho^{A}_{xy}}{\rho^{2}_{xx}} \approx -\frac{R_S \mu_0 M_S}{\rho^{2}_{xx}}$) at various temperatures [44]. Figure 5.3(c) depicts the temperature dependence of AHC and longitudinal conductivity. The resulting AHC is nearly temperature independent, but the longitudinal conductivity is temperature dependent, implying that the intrinsic process dominates the origin of AHE in Co_2VAl [5,47,61]. Since the intrinsic AHC $|\sigma^{int}_{xy}|$ is nearly proportional to magnetization, the scaling coefficient ($S_H = \frac{R_S \mu_0}{\rho^{2}_{xx}} = \frac{\sigma^{A}_{xy,in}}{M}$) should be constant and temperature independent [44,62,63]. Figure 5.3(d) shows that S_H is almost temperature independent, confirming the dominant intrinsic Berry phase contribution to AHC in Co_2VAl. The computed value of S_H is comparable to that reported in the literature for numerous Heusler systems and ferromagnetic materials ($\sim 0.01 - 0.2$ V^{-1}) [40,44,58]. We performed the first principles calculation on Co_2VAl since the intrinsic AHE depends on the band structure of a material to gain a better understanding of its origin.

5.3.3 First-principles calculations

Understanding the magnetic properties of the compound under study is crucial because of the strong correlation between intrinsic AHE and magnetism [46]. Figure 5.4(a) depicts the crystal structure of Co_2VAl as well as the associated high symmetry point in the BZ. Magnetic moments of Co_2VAl are calculated using the first-principles calculations and transition metal atoms Co and V atoms have major contributions to magnetic moments μ_{Co} = 0.911 μ_B/f.u. and μ_V = 0.210 μ_B/f.u. respectively. Al acts like a non-magnetic atom, with a total magnetic moment per formula unit of 2.02 μ_B/f.u. Whereas one Al atom gives three valence electrons, the two Co and one V atoms each donate 18 and 5 valence electrons. The effective magnetic moment of Co_2VAl is therefore predicted to be around 2 μ_B/f.u.

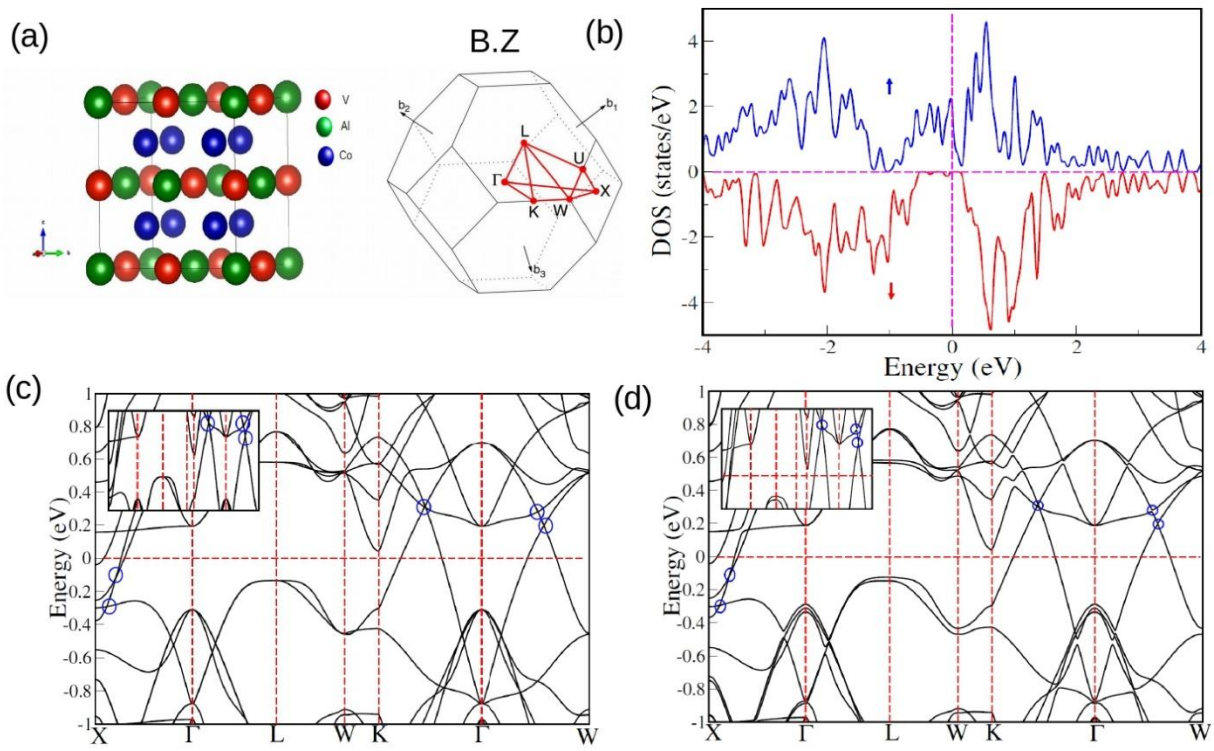

Figure 5.4: (a) The Co_2VAl crystal structure with the $Fm\bar{3}m$ space group. Co, Al, and V atoms are depicted in blue, green, and red, respectively, and the Brillouin zone (BZ) of the crystal Co_2VAl. (b) The total density of state (DOS) of Co_2VAl. The blue and red curves reflect the total DOS for the majority and minority spins, respectively. (c) Co_2VAl band structure in the absence of SOC (crossing points are marked by blue circles). The magnified picture of the crossing points is shown in the inset. (d) The band structure of Co_2VAl in the presence of SOC (gapped nodal lines are shown in blue circles). The magnified view of gapped nodal lines is shown in the inset.

Our calculations suggest that this material is a half-metallic system with a magnetic moment of 2.02 μ_B/f.u. and follows the SP rule. The observed magnetic behavior is consistent with previous work [49]. The estimated magnetic moment for Co_2VAl agrees well with our experimentally determined value. Figure 5.4(b) depicts a spin-resolved density of state (DOS), and we find that the DOS is entirely gapped for minority spin but metallic for majority spin.

To understand the topological aspects of the compound, the band dispersions are computed in the absence and presence of spin-orbit coupling (SOC) using plane wave-based pseudopotential [64]. In the absence of SOC, there are several band crossings from nodal lines. All nontrivial crossing places around Fermi energy are designated by a blue circle without SOC along high symmetry points in Fig. 5.4(c), and the inset gives an expanded view of the crossing

spots. However, except for a few Weyl points that are symmetry-protected, the nodal lines are gapped out in the presence of SOC. The nodal line stays gapless in the k_z = 0 plane when the SOC and magnetic polarisation direction are taken into account along the [001] direction. Figure 5.4(d) depicts the band dispersions in the presence of SOC near the Fermi energy. Gapped-out band crossings are indicated by blue circles along the Γ–W and Γ–X symmetry paths. The expanded picture of the gapped nodal lines may be seen in the inset of Fig. 5.4(d). In the absence of finite magnetization, the Co_2VAl point group crystal symmetry is $Fm\bar{3}m$ (space group 225) and features three mirror planes [65], M_x (k_x = 0), M_y (k_y = 0), and M_z (k_z = 0), as well as three C_4 rotation axes. The gapless nodal lines in the band structure in the k_x, k_y, and k_z = 0 planes are protected by these mirror planes.

The presence of SOC along the [001] direction only preserves the mirror symmetry M_z = 0 and the C_{4z} rotational symmetry. As a result, it is anticipated that two nodal lines on the k_x = 0 and k_y = 0 planes will gap out, and the nodal line along the k_z = 0 plane should be intact, and some Weyl points will be present outside of the k_z = 0 plane. We investigated the electronic band structure of the tight-binding model Hamiltonian calculated with Wannier90 [51,52] and Wanniertools [53]. Figure 5.5(a) depicts the color plot of the energy gap at the k_x = 0 plane, with SOC present, between the lowest conduction and topmost valence bands, using a logarithmic scale. The oval structure seen in Fig. 5.5(b) is generally gapped except for Weyl points, which are regarded to be gapless for gaps smaller than 10^{-4} eV. Figures 5.5(b) and 5.5(d) demonstrate the considerable Berry curvature in the k_x = 0 and k_y = 0 planes caused by minor gaps at the nodal lines. Figures 5.5(b) and 5.5(d) exhibit the Weyl points with chiral charges +1 and -1 in k_x = 0 and k_y = 0 by filled and open circles. Table 5.I show the position of the energy and momentum coordinates of the Weyl points. To corroborate the chirality at Weyl points, Wannier charge centers are also calculated. The Berry curvature, which is a geometrical characteristic of energy bands, is proportional to the AHC. The electronic motion exhibits a transverse anomalous velocity due to the Berry curvature, which results in a significant AHC.

The intrinsic AHC can be assessed using Kubo formalism's [37] linear response theory, and the intrinsic AHC in the xy plane can be described as

$$\sigma_{xy} = -\frac{e^2}{\hbar} \int \frac{d^3k}{(2\pi)^3} \sum_n \Omega_n^z(k) f_n(k) \tag{5.3}$$

Ω_n^z is the Berry curvature and it can be written as

$$\Omega_n^z = -2i \sum_{m \neq n} \frac{<\Psi_{nk}|v_x|\Psi_{mk}><\Psi_{mk}|v_y|\Psi_{nk}>}{[E_m(k) - E_n(k)]^2} \quad (5.4)$$

where $f_n(k)$ represents the Fermi–Dirac distribution function, n is for the occupied band's index, $E_n(k)$ is the eigenvalue of the n^{th} eigenstate $\Psi_n(k)$, $v_i = \frac{1}{\hbar}\frac{\partial H(k)}{\partial k_i}$ is the velocity operator along the i $(i = x, y, z)$ direction.

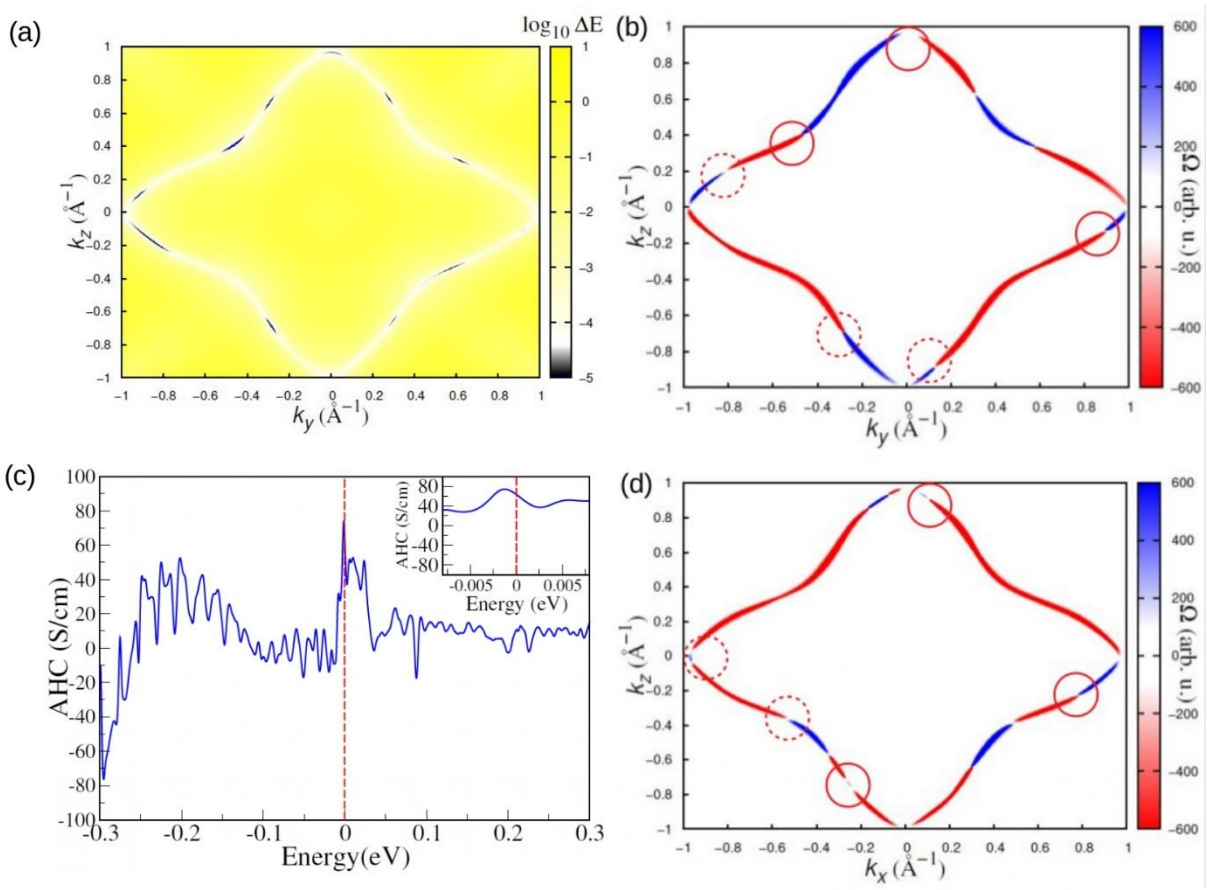

Figure 5.5: (a) The energy gap ΔE (k_y, k_z) is plotted in k_y - k_z plane at k_x = 0 with SOC. (b) and (d) The Berry curvature distribution in k_y - k_z plane and k_x - k_z plane. (c) Energy (E - E_F) dependence of the AHC. The inset represents the enlarged view of the energy dependence of the AHC close to the E_F.

In order to calculate AHC, the spin-orbit coupling is taken into account along the [001], which is also a magnetic polarisation direction. As seen in Figs. 5.5(b) and 5.5(d), almost degenerate bands in the k_x = 0, k_y = 0 planes have large Berry curvature and contribute to the intrinsic AHC.

Table 5.I: The Weyl points' positions, Chern numbers, and the energy relative to the E_F of Co_2VAl.

Weyl points	k_x	k_y	k_z	Chern number	E - E_F (eV)
1	-0.52	0.009	-0.36	-1	0.26
2	-0.23	-0.007	-0.76	+1	0.04
3	0.78	-0.004	-0.22	+1	0.07
4	0.10	0.01	0.91	+1	-0.20
5	-0.0006	-0.27	-0.69	-1	0.14
6	-0.009	0.89	-0.12	+1	-0.16
7	0.01	0.13	-0.88	-1	-0.15
8	0.0009	-0.46	0.40	+1	0.29
9	-0.95	-0.05	0.03	-1	-0.26
10	0.008	-0.81	0.20	-1	-0.03

The calculated AHC value of Co_2VAl at the E_F is $\sim$ 64 S/cm, which agrees well with the experimentally determined intrinsic AHC of $\sim$ 70 S/cm. The experimentally estimated AHC is equivalent to that reported for several Co_2-based ferromagnetic full Heusler compounds and other magnetic materials [43,44,47,66,67]. Figure 5.5(c) illustrates the energy dependence of AHC for Co_2VAl, and the inset depicts a zoomed view of the energy dependence of AHC near the E_F.

5.4 Conclusion

To summarise, we explored the AHE in the half-metallic full Heusler compound Co_2VAl experimentally and performed first principle calculations to understand the origin of AHE in this compound. The dominant intrinsic Berry phase contribution to the AHC is confirmed by the quadratic dependence ($\alpha \approx 2$) between ρ_{xy}^{A} and ρ_{xx} and the nearly temperature-independent character of the scaling coefficient S_H. Experimentally, it is found that the AHC is around 85 S/cm at 2 K with an intrinsic contribution of 75.6 S/cm. Our electronic structure calculation indicates that the intrinsic mechanism dominates the AHE in Co_2VAl, and the AHC estimated using Berry curvature yields 64 S/cm, which is comparable with the experimentally measured

value. We further demonstrate that the electronic band structure features gaped nodal lines and symmetry-protected Weyl points near the E_F in the presence of finite internal magnetization and SOC. The charge chirality of these Weyl points has also been determined. It is extremely rare for gapped nodal lines and symmetry-protected Weyl points to coexist in full Heusler compounds. Our detailed analysis reveals that the half-metallic full Heusler compound Co_2VAl exhibits intrinsic AHE resulting from non-trivial band topology and features a rare co-existence of gapped nodal lines and symmetry-protected Weyl points in its electronic bands. Lastly, our findings corroborate current studies on the Berry curvature origin of AHE and give a viable platform for exploring TSMs both theoretically and experimentally.

References:

[1] G. Xu, H. Weng, Z. Wang, X. Dai, and Z. Fang, Phys. Rev. Lett. **107**, 186806 (2011).

[2] X. Wan, A. M. Turner, A. Vishwanath, and S. Y. Savrasov, Phys. Rev. B **83**, 205101 (2011).

[3] D. Zhang, M. Shi, T. Zhu, D. Xing, H. Zhang, and J. Wang, Phys. Rev. Lett. **122**, 206401 (2019).

[4] S. Nie, Y. Sun, F. B. Prinz, Z. Wang, H. Weng, Z. Fang, and X. Dai, Phys. Rev. Lett. **124**, 76403 (2020).

[5] Q. Wang, Y. Xu, R. Lou, Z. Liu, M. Li, Y. Huang, D. Shen, H. Weng, S. Wang, and H. Lei, Nat. Commun. **9**, 3681 (2018).

[6] B. Ernst, R. Sahoo, Y. Sun, J. Nayak, L. Müchler, A. K. Nayak, N. Kumar, J. Gayles, A. Markou, G. H. Fecher, and C. Felser, Phys. Rev. B **100**, 054445 (2019).

[7] G. Chang, S. Y. Xu, X. Zhou, S. M. Huang, B. Singh, B. Wang, I. Belopolski, J. Yin, S. Zhang, A. Bansil, H. Lin, and M. Z. Hasan, Phys. Rev. Lett. **119**, 1 (2017).

[8] Y. J. Jin, R. Wang, Z. J. Chen, J. Z. Zhao, Y. J. Zhao, and H. Xu, Phys. Rev. B **96**, 2 (2017).

[9] T. Graf, C. Felser, and S. S. P. Parkin, Prog. Solid State Chem. **39**, 1 (2011).

[10] J. Kübler, G. H. Fecher, and C. Felser, Phys. Rev. B **76**, 024414 (2007).

[11] H. C. Kandpal, G. H. Fecher, and C. Felser, J. Phys. D. Appl. Phys. **40**, 1507 (2007).

[12] R. Sahoo, L. Wollmann, S. Selle, T. Höche, B. Ernst, A. Kalache, C. Shekhar, N. Kumar, S. Chadov, C. Felser, S. S. P. Parkin, and A. K. Nayak, Adv. Mater. **28**, 8499 (2016).

[13] Z. Wang, M. G. Vergniory, S. Kushwaha, M. Hirschberger, E. V. Chulkov, A. Ernst, N. P. Ong, R. J. Cava, and B. A. Bernevig, Phys. Rev. Lett. **117**, 236401 (2016).

[14] R. A. de Groot, F. M. Mueller, P. G. van Engen, and K. H. J. Buschow, Phys. Rev. Lett. **50**, 2024 (1983).

[15] I. Galanakis, P. H. Dederichs, and N. Papanikolaou, Phys. Rev. B **66**, 174429 (2002).

[16] B. Q. Lv, H. M. Weng, B. B. Fu, X. P. Wang, H. Miao, J. Ma, P. Richard, X. C. Huang,

L. X. Zhao, G. F. Chen, Z. Fang, X. Dai, T. Qian, and H. Ding, Phys. Rev. X **5**, 031013 (2015).

[17] H. Weng, C. Fang, Z. Fang, B. A. Bernevig, and X. Dai, Phys. Rev. X **5**, 011029 (2015).

[18] S.-Y. Xu, N. Alidoust, I. Belopolski, Z. Yuan, G. Bian, T.-R. Chang, H. Zheng, V. N. Strocov, D. S. Sanchez, G. Chang, C. Zhang, D. Mou, Y. Wu, L. Huang, C.-C. Lee, S.-M. Huang, B. Wang, A. Bansil, H.-T. Jeng, T. Neupert, A. Kaminski, H. Lin, S. Jia, and M. Zahid Hasan, Nat. Phys. **11**, 748 (2015).

[19] S. Y. Xu, I. Belopolski, D. S. Sanchez, C. Zhang, G. Chang, C. Guo, G. Bian, Z. Yuan, H. Lu, T. R. Chang, P. P. Shibayev, M. L. Prokopovych, N. Alidoust, H. Zheng, C. C. Lee, S. M. Huang, R. Sankar, F. Chou, C. H. Hsu, H. T. Jeng, A. Bansil, T. Neupert, V. N. Strocov, H. Lin, S. Jia, and M. Zahid Hasan, Sci. Adv. **1**, (2015).

[20] K. Zhang, C. Bao, Q. Gu, X. Ren, H. Zhang, K. Deng, Y. Wu, Y. Li, J. Feng, and S. Zhou, Nat. Commun. **7**, 13552 (2016).

[21] S. Borisenko, D. Evtushinsky, Q. Gibson, A. Yaresko, K. Koepernik, T. Kim, M. Ali, J. van den Brink, M. Hoesch, A. Fedorov, E. Haubold, Y. Kushnirenko, I. Soldatov, R. Schäfer, and R. J. Cava, Nat. Commun. **10**, 3424 (2019).

[22] N. Morali, R. Batabyal, P. K. Nag, E. Liu, Q. Xu, Y. Sun, B. Yan, C. Felser, N. Avraham, and H. Beidenkopf, Science (80-.). **365**, 1286 (2019).

[23] T. Suzuki, R. Chisnell, A. Devarakonda, Y.-T. Liu, W. Feng, D. Xiao, J. W. Lynn, and J. G. Checkelsky, Nat. Phys. **12**, 1119 (2016).

[24] E. Liu, Y. Sun, N. Kumar, L. Muechler, A. Sun, L. Jiao, S. Y. Yang, D. Liu, A. Liang, Q. Xu, J. Kroder, V. Süß, H. Borrmann, C. Shekhar, Z. Wang, C. Xi, W. Wang, W. Schnelle, S. Wirth, Y. Chen, S. T. B. Goennenwein, and C. Felser, Nat. Phys. **14**, 1125 (2018).

[25] C. Helman, A. Camjayi, E. Islam, M. Akabori, L. Thevenard, C. Gourdon, and M. Tortarolo, Phys. Rev. B **103**, 134408 (2021).

[26] A. Sakai, Y. P. Mizuta, A. A. Nugroho, R. Sihombing, T. Koretsune, M. T. Suzuki, N. Takemori, R. Ishii, D. Nishio-Hamane, R. Arita, P. Goswami, and S. Nakatsuji, Nat. Phys. **14**, 1119 (2018).

[27] H. Zhang, C. Q. Xu, and X. Ke, Phys. Rev. B **103**, L201101 (2021).

[28] M. Hirschberger, S. Kushwaha, Z. Wang, Q. Gibson, S. Liang, C. A. Belvin, B. A. Bernevig, R. J. Cava, and N. P. Ong, Nat. Mater. **15**, 1161 (2016).

[29] R. Singha, S. Roy, A. Pariari, B. Satpati, and P. Mandal, Phys. Rev. B **99**, 035110 (2019).

[30] N. Nagaosa, J. Sinova, S. Onoda, A. H. MacDonald, and N. P. Ong, Rev. Mod. Phys. **82**, 1539 (2010).

[31] R. Karplus and J. M. Luttinger, Phys. Rev. **95**, 1154 (1954).

[32] J. Smit, Physica **21**, 877 (1955).

[33] J. Smit, Physica **24**, 39 (1958).

[34] L. Berger, Phys. Rev. B **2**, 4559 (1970).

[35] T. Jungwirth, Q. Niu, and A. H. MacDonald, Phys. Rev. Lett. **88**, 4 (2002).

[36] N. Nagaosa, J. Phys. Soc. Japan **75**, 1 (2006).

[37] M. Gradhand, V. Fedorov, F. Pientka, P. Zahn, I. Mertig, L. Györffy, M. Gradhand, D. V. Fedorov, F. Pientka, P. Zahn, I. Mertig, and B. L. Györffy, J. Phys. Condens. Matter **24**, (2012).

[38] J. Kübler and C. Felser, Epl **108**, (2014).

[39] R. Shindou and N. Nagaosa, Phys. Rev. Lett. **87**, 116801 (2001).

[40] A. Husmann and L. J. Singh, Phys. Rev. B **73**, 172417 (2006).

[41] M. Obaida, K. Westerholt, and H. Zabel, Phys. Rev. B **84**, 184416 (2011).

[42] I. M. Imort, P. Thomas, G. Reiss, and A. Thomas, J. Appl. Phys. **111**, 2 (2012).

[43] K. Manna, L. Muechler, T.-H. Kao, R. Stinshoff, Y. Zhang, J. Gooth, N. Kumar, G. Kreiner, K. Koepernik, R. Car, J. Kübler, G. H. Fecher, C. Shekhar, Y. Sun, and C. Felser, Phys. Rev. X **8**, 041045 (2018).

[44] S. Roy, R. Singha, A. Ghosh, A. Pariari, and P. Mandal, Phys. Rev. B **102**, 085147 (2020).

[45] R. P. Jena, D. Kumar, and A. Lakhani, J. Phys. Condens. Matter **32**, 365703 (2020).

[46] P. Li, J. Koo, W. Ning, J. Li, L. Miao, L. Min, Y. Zhu, Y. Wang, N. Alem, C.-X. Liu, Z. Mao, and B. Yan, Nat. Commun. **11**, 3476 (2020).

[47] G. K. Shukla, J. Sau, N. Shahi, A. K. Singh, M. Kumar, and S. Singh, Phys. Rev. B **104**, 195108 (2021).

[48] T. Kanomata, Y. Chieda, K. Endo, H. Okada, M. Nagasako, K. Kobayashi, R. Kainuma, R. Y. Umetsu, H. Takahashi, Y. Furutani, H. Nishihara, K. Abe, Y. Miura, and M. Shirai, Phys. Rev. B **82**, 144415 (2010).

[49] H. Han, Z. Bai, and K. L. Yao, J. Alloys Compd. **576**, 93 (2013).

[50] J. Hafner, J. Comput. Chem. **29**, 2044 (2008).

[51] G. Pizzi, V. Vitale, R. Arita, S. Blügel, F. Freimuth, G. Géranton, M. Gibertini, D. Gresch, C. Johnson, T. Koretsune, J. Ibañez-Azpiroz, H. Lee, J.-M. Lihm, D. Marchand, A. Marrazzo, Y. Mokrousov, J. I. Mustafa, Y. Nohara, Y. Nomura, L. Paulatto, S. Poncé, T. Ponweiser, J. Qiao, F. Thöle, S. S. Tsirkin, M. Wierzbowska, N. Marzari, D. Vanderbilt, I. Souza, A. A. Mostofi, and J. R. Yates, J. Phys. Condens. Matter **32**, 165902 (2020).

[52] N. Marzari and D. Vanderbilt, Phys. Rev. B **56**, 12847 (1997).

[53] Q. Wu, S. Zhang, H.-F. Song, M. Troyer, and A. A. Soluyanov, Comput. Phys. Commun. **224**, 405 (2018).

[54] M. Meinert, J. M. Schmalhorst, G. Reiss, and E. Arenholz, J. Phys. D. Appl. Phys. **44**, (2011).

[55] V. V. Marchenkov, Y. A. Perevozchikova, N. I. Kourov, V. Y. Irkhin, M. Eisterer, and T. Gao, J. Magn. Magn. Mater. **459**, 211 (2018).

[56] N. I. Kourov, Y. A. Perevozchikova, H. W. Weber, and V. V. Marchenkov, Phys. Solid State **58**, 1355 (2016).

[57] L. Bainsla, K. G. Suresh, A. K. Nigam, M. Manivel Raja, B. S. D. C. S. Varaprasad, Y. K. Takahashi, and K. Hono, J. Appl. Phys. **116**, 203902 (2014).

[58] Q. Wang, S. Sun, X. Zhang, F. Pang, and H. Lei, Phys. Rev. B **94**, 075135 (2016).

[59] P. Nozières and C. Lewiner, J. Phys. **34**, 901 (1973).

[60] S. Onoda, N. Sugimoto, and N. Nagaosa, Phys. Rev. Lett. **97**, 126602 (2006).

[61] X. Chen, M. Wang, C. Gu, S. Wang, Y. Zhou, C. An, Y. Zhou, B. Zhang, C. Chen, Y. Yuan, M. Qi, L. Zhang, H. Zhou, J. Zhou, Y. Yao, and Z. Yang, Phys. Rev. B **100**, 165145 (2019).

[62] N. Manyala, Y. Sidis, J. F. DiTusa, G. Aeppli, D. P. Young, and Z. Fisk, Nat. Mater. **3**, 255 (2004).

[63] C. Zeng, Y. Yao, Q. Niu, and H. H. Weitering, Phys. Rev. Lett. **96**, 037204 (2006).

[64] P. E. Blöchl, Phys. Rev. B **50**, 17953 (1994).

[65] G. Chang, S.-Y. Xu, H. Zheng, B. Singh, C.-H. Hsu, G. Bian, N. Alidoust, I. Belopolski, D. S. Sanchez, S. Zhang, H. Lin, and M. Z. Hasan, Sci. Rep. **6**, 38839 (2016).

[66] Y. Liu, E. Stavitski, K. Attenkofer, and C. Petrovic, Phys. Rev. B **97**, 165415 (2018).

[67] Y. Liu, H. Tan, Z. Hu, B. Yan, and C. Petrovic, Phys. Rev. B **103**, 045106 (2021).

Chapter 6 Nodal-line and triple point fermion induced anomalous Hall effect in topological Heusler compound Co_2CrGa

In this chapter, we present a comprehensive study of the anomalous Hall effect (AHE) in the ferromagnetic full Heusler compound Co_2CrGa, based on both experimental and theoretical findings. Our experimental results indicate that the intrinsic Berry phase mechanism dominates the AHE in Co_2CrGa. Experimental results further indicate that the anomalous Hall conductivity (AHC) at 10 K is as high as 569 S/cm, with an intrinsic Berry phase contribution of 526 S/cm. According to first-principles calculations, the observed large AHC in this compound is caused by the Berry curvature originating from a gapped nodal line as well as Weyl nodes generated from the triple point near the Fermi level in the presence of spin-orbit coupling.

Content of this chapter has been published in: **S. Chatterjee**, J. Sau, S. Samanta, B. Ghosh, N. Kumar, M. Kumar, and K. Mandal, "*Nodal-line and triple point fermion induced anomalous Hall effect in topological Heusler compound Co_2CrGa*," ***Phys. Rev. B*** *107, 125138 (2023).*

6 Nodal-line and triple point fermion induced anomalous Hall effect in topological Heusler compound Co_2CrGa

6.1 Preface

In recent years, three-dimensional topological semimetals (TSMs), a new class of gapless quantum states, have been the subject of significant investigation in condensed matter physics as they exhibit fundamentally new physical phenomena with potential applications [1–4]. These TSMs have an intriguing band dispersion with linear crossing, and they are categorized into three categories based on the degeneracy of the band crossing points and their distribution in the Brillouin zone (BZ). The first one is zero-dimensional (0D) nodal points, which comprise Weyl points [1,5], Dirac points [6,7], triple points [8], and other higher degeneracy nodal points [9]. The second category is one-dimensional (1D) nodal-line systems, which constitute nodal rings [10], nodal chains [11], and nodal nets [11]. Two-dimensional (2D) nodal surfaces [12] are the third type. Because of their nontrivial topological features and unusual transport phenomena, 0D nodal point systems have been widely explored over the last decade [6,13,14], whereas 1D nodal-line systems have just recently been investigated [15,16]. The previously mentioned classification of fermions has recently been extended to include triply-degenerate nodal points. This three-fold degeneracy generates triple-point (TP) fermions [17], which have been experimentally validated [18]. However, in cobalt (Co_2)-based full Heusler compounds, the existence of TP fermions and their consequences in transport properties is yet to be understood.

Co_2-based Heusler compounds have piqued the interest of researchers because of their high Curie temperature (T_C) and tunable magnetic and electric characteristics [19,20]. As a result, these materials have the potential to be very useful for spin manipulation and spintronic devices. Recently, a few Co_2-based full Heusler compounds were predicted to feature Weyl fermions in their band structure [21]. The Berry curvature (BC) associated with this topologically nontrivial state results in a variety of exotic transport phenomena, including anomalous Hall effect (AHE), anomalous Nernst effect, and chiral anomaly, [22–30]. The AHE in these compounds is caused by either an intrinsic mechanism [31] that can be explained by

the Berry phase effect of the occupied electronic Bloch states [32,33], or by extrinsic mechanisms that can be understood as a result of asymmetric scattering of conduction electrons in the presence of spin-orbit coupling (SOC) or impurities [34–36]. The AHE in a few Co_2-based full Heusler compounds is investigated both theoretically and experimentally [22–27]; however, these materials have largely different electronic band structures, resulting in substantial differences in the AHE's magnitude. For instance, Co_2MnAl exhibits a large anomalous Hall conductivity (AHC) of around 1300 S/cm at ambient temperature because of a gapped nodal ring [26]. Co_2MnGa exhibits an AHC of 1600 S/cm at 2 K due to a large BC in momentum space, whereas Co_2VGa displays an AHC of approximately 137 S/cm at 2 K due to a slightly gapped nodal line [23].

In this chapter, we present a comprehensive investigation of the AHE on ferromagnetic full Heusler compound Co_2CrGa utilizing both experimental and theoretical analysis. Experimentally, we observed a large AHC of ~ 569 S/cm at 10 K, with an intrinsic contribution of ~ 526 S/cm exhibiting weak temperature dependence. At ambient temperature, we also noticed an exceptionally large anomalous Hall angle (AHA) of ~ 8.5 % and a large anomalous Hall factor (AHF) of ~ 0.23 V^{-1}. Additionally, we have used density functional theory (DFT) based on a first-principles analysis and have shown topologically protected TP fermion in the BZ without SOC. In the presence of SOC, we explored the creation of Weyl nodes from this triple point. We also discuss the presence of a few symmetry-protected Weyl nodes and their effect on anomalous transport features.

6.2 Experimental and theoretical methods

Using 99.99% pure individual elements, the polycrystalline Co_2CrGa compound is synthesized in a typical arc-melting furnace in a high-purity argon atmosphere. The sample is re-melted six to seven times to ensure chemical homogeneity. After being obtained, the ingot is sealed in an evacuated quartz tube and annealed for five days at 1173 K before being quenched in cold water. The magnetization of the sample is measured using a vibrating sample magnetometer (VSM) in a physical property measurement system (PPMS, Quantum Design, USA). Magnetization data are recorded as a function of the applied field up to 5 T and temperature down to 10 K. The sample utilized for the magnetic measurements is approximately 0.4 × 0.6 × 4.0 mm^3 in size. To obtain a proper thermal equilibrium, we stabilized the temperature for at

least 30 minutes for each M(H) isotherm. The transport measurements are performed with a 9-T Dynacool PPMS (Quantum Design, USA) equipped with the electrical transport option (ETO). The electrical contacts for both the longitudinal and Hall resistivity measurements are made using a standard four-probe method with conductive silver epoxy and copper wires. To effectively eliminate the longitudinal resistivity (ρ_{xx}) contribution owing to voltage probe misalignment while measuring the Hall resistivity (ρ_{xy}), the final Hall resistivity is determined as the difference of transverse resistance measured at positive and negative fields.

We also investigated the electronic band structures and transport properties of Co_2CrGa using first-principles electronic structure calculations[1]. The projected augmented wave approach is used to depict ion-electron interactions. Vienna ab-initio simulation package (VASP) [37] is used to do the calculations. For the electronic exchange-correlation functional, the generalized gradient approximation (GGA) [38] of the Perdew-Burke-Ernzerhof (PBE) [39] type is utilized. The plane-wave basis uses the kinetic energy cutoff of 600 eV. The electronic integral over BZ is estimated using the Gaussian smearing method with a width of 0.05 eV, and a 12 × 12 × 12 Monkhorst-pack k-point mesh with a Γ-centered is utilized for the BZ sampling. Cell parameters and internal atomic positions were thoroughly relaxed until the forces on all atoms were less than 0.01 eV/A. Both with and without SOC are considered in the calculation. Starting from the plane wave basis state, the AHC, energy gap, BC, and Wannier charge center (WCC) are calculated using Wannier90 [40,41] and Wanniertools [42]. A dense 501 × 501 × 501 k-grid was used for the AHC calculations, with the tight-binding model's limit.

6.3 Results and Discussions

6.3.1 Structural, magnetization, and longitudinal resistivity

The room-temperature X-ray diffraction (XRD) pattern of the sample is collected for structural investigation and phase purity. The FULLPROF software is used to do the Rietveld analysis of the XRD pattern. Figure 6.1 depicts the XRD pattern of the sample as well as its Rietveld refinement, and the crystal structure of the compound is presented in the right corner. The crystallographic coordinates of the Co atoms are (0, 0, 0) and (1/2, 1/2, 1/2), while the Cr and Ga atoms are (1/4, 1/4, 1/4) and (3/4, 3/4, 3/4), respectively. The Rietveld refinement of the XRD data verifies the single-phase nature of the present sample and its crystallization in the cubic $L2_1$ structure with the space group $Fm\bar{3}m$. Generally, the ordered structure of full Heusler

[1] All the first-principles calculations used in this chapter has been done by the Prof. Manoranjan Kumar's group (in collaboration) at S. N. Bose National Centre for Basic Sciences, Kolkata.

alloys is characterized by (111) and (200) superlattice reflections [27]. The existence of both (111) and (200) superlattice reflections in Co_2CrGa implies that this material organizes perfectly in the cubic $L2_1$ structure. The refined lattice parameter was found to be 5.796 Å, which is consistent with previously reported works [43,44].

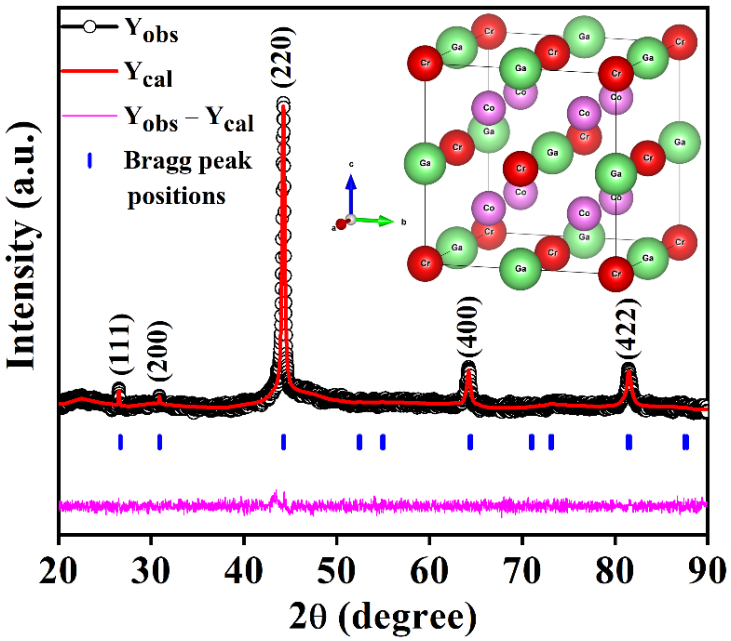

Figure 6.1: Rietveld refinement of the room temperature XRD pattern for Co_2CrGa. The black circles represent the experimental data, and the solid red line illustrates the calculated result. The vertical blue lines represent the Bragg peak positions, and the solid magenta line at the bottom corresponds to the difference between the experimental and calculated data. The inset shows the crystal structure of Co_2CrGa.

As topology and magnetism are interrelated, we measured the magnetization of the sample to determine its magnetic properties. Figure 6.2(a) represents the magnetic field dependence of dc magnetization up to a field of 5 T at 10 K. Co_2-based full Heusler compounds often obey the Slater-Pauling (SP) magnetization rule [45], which states that $M_t = Z_t - 24$ μ_B/f.u., where M_t is the total magnetic moment and Z_t is the total number of valance electrons in the unit cell of the compound. The value of Z_t for Co_2CrGa is 27. Hence, if the SP rule is followed, the total magnetic moment should be 3 μ_B/f.u. According to Fig. 6.2(a), the saturation magnetization (M_S) is calculated to be around 3.01 μ_B/f.u. at 10 K, which is in accordance with the SP rule.

The temperature-dependent dc magnetization under a field of 500 Oe is also shown in the left inset of Fig. 6.2(a).

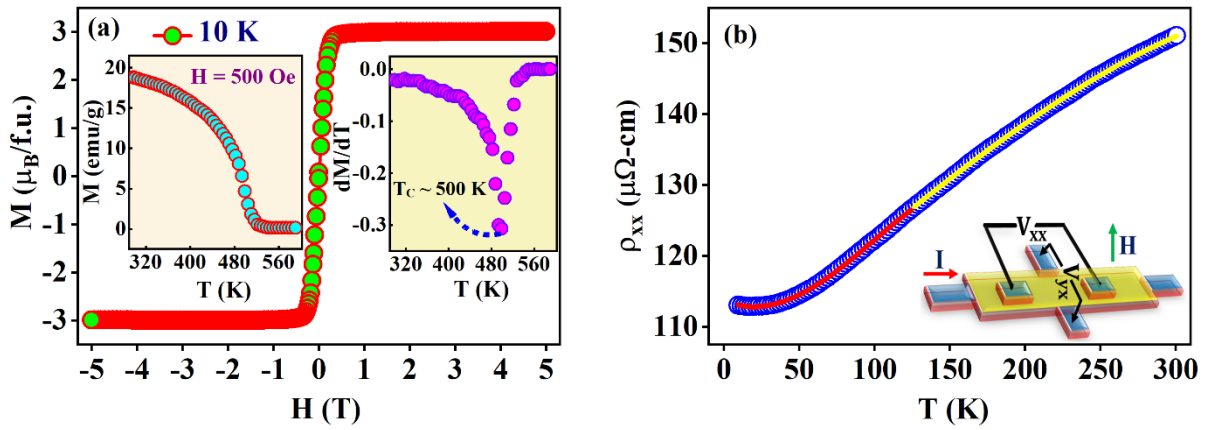

Figure 6.2: (a) Magnetic field-dependent dc magnetization (M vs H) at 10 K. The left inset depicts the temperature-dependent dc magnetization (M vs T) measured at 500 Oe, and the right inset represents the derivative magnetization dM/dT vs T. (b) Temperature dependence of the longitudinal resistivity ρ_{xx}. The solid red and yellow lines illustrate the fittings in two different temperature regions. The inset represents the schematic diagram of the sample device used for longitudinal voltage V_{xx} and Hall voltage V_{yx} measurements.

It undergoes a continuous paramagnetic (PM) to ferromagnetic (FM) phase transition at T_C ~ 500 K, as seen by the $\frac{dM}{dT}$ curve in the right inset of Fig. 6.2(a). The measured magnetic behavior is quite similar to previous investigations [43,44]. Figure 6.2(b) exhibits the temperature variation of the longitudinal resistivity (ρ_{xx}) from 10 K to 300 K. The schematic diagram of the sample device utilized for longitudinal voltage (V_{xx}) and Hall voltage (V_{yx}) measurements is given in the inset of Fig. 6.2(b). The residual resistivity value at 10 K is 113 μΩ-cm, resulting in a residual resistivity ratio [RRR = ρ_{xx} (300 K)/ρ_{xx} (10 K)] of ~ 1.34, which is comparable to previously reported values for other Co_2-based full Heusler compounds [25,46]. For a half-metallic ferromagnetic material, the electron-magnon contribution is typically absent at low temperatures. As a result, the main contribution to the ρ_{xx} comes from (i) electron-electron scattering (T^2 dependence), (ii) electron-phonon scattering (T dependency), and (iii) double magnon scattering ($T^{9/2}$ dependence at lower temperatures and $T^{7/2}$ dependence at higher temperatures) [47]. So, in order to comprehend the various scattering mechanisms to the ρ_{xx} in Fig. 6.2(b), we fitted the data in two distinct

temperature ranges, namely between 10 K and 125 K and 125 K to 300 K. In the temperature range of 10 K to 125 K, the ρ_{xx} fits very well with the relation, $\rho_{xx}(T) = \rho_0 + AT^{1/2} + BT^2 + CT^{9/2}$ (shown in a solid red line in Fig. 6.2(b)), while in the high-temperature range, i.e. 125 K to 300 K, the best fit is given by $\rho_{xx}(T) = \rho_0 + DT + ET^{7/2}$ (shown in a solid yellow line in Fig. 6.2(b)). Here, ρ_0 denotes the residual resistivity, A denotes the temperature coefficient for the disorder present in the system, B denotes the temperature coefficient for electron-electron scattering, D is the temperature coefficient for electron-phonon scattering, and C and E denote the respective temperature coefficients for two magnon scattering. Thus, the temperature-dependent ρ_{xx} data strongly suggests the presence of a variety of scattering mechanisms in the present compound.

6.3.2 Anomalous Hall Effect

After studying the sample's structural and magnetic properties, we performed thorough magneto-transport measurements at temperatures ranging from 10 K to 300 K to investigate the AHE in Co_2CrGa. The field-dependence of Hall resistivity (ρ_{yx}) up to a field of 9 T at various specified temperatures is depicted in Fig. 6.3(a). At a low field of ~ 0.7 T, the ρ_{yx}(H) sharply increases as the field increases, and in the high field region over ~ 1 T, the ρ_{yx}(H) exhibits a weak linear field dependence up to 9 T. The field-dependent dc magnetization at various temperatures is illustrated in the inset of Fig. 6.3(a). The shape of the ρ_{yx}(H) and $M(H)$ curves in the low field area are identical, confirming the presence of AHE in this compound. In addition to the ordinary Hall effect, the Hall resistivity ρ_{yx} in a ferromagnetic material receives an additional contribution from spontaneous magnetization M and is given as [48],

$$\rho_{yx} = \rho_{yx}^0 + \rho_{yx}^A = R_0 H + R_S \mu_0 M, \tag{6.1}$$

where ρ_{yx}^0 and ρ_{yx}^A are the ordinary and anomalous contributions to total Hall resistivity, respectively, and R_0 and R_S are the ordinary and anomalous Hall coefficients. The linear fit of the ρ_{yx} vs H curve in the high-field region yields the values of ρ_{yx}^A and R_0. The intercept of the y-axis and the slope of the linear fit are denoted by ρ_{yx}^A and R_0, respectively. The temperature-dependent carrier density n and carrier type can be calculated using the equation $R_0 = 1/ne$, where e is the electronic charge. The temperature variation of R_0 from 10 to 300 K is shown in Fig. 6.3(b). The positive R_0 values suggest that throughout the whole temperature range, holes predominate as charge carriers. The carrier density n is calculated using the values of R_0,

as demonstrated in the inset of Fig. 6.3(b). The estimated carrier density at 10 K is ~ 1.37 × 10^{20} cm^{-3}, and it is nearly temperature-independent. The associated carrier mobility (μ_h) is determined to be around 340 $cm^2\ V^{-1}\ S^{-1}$.

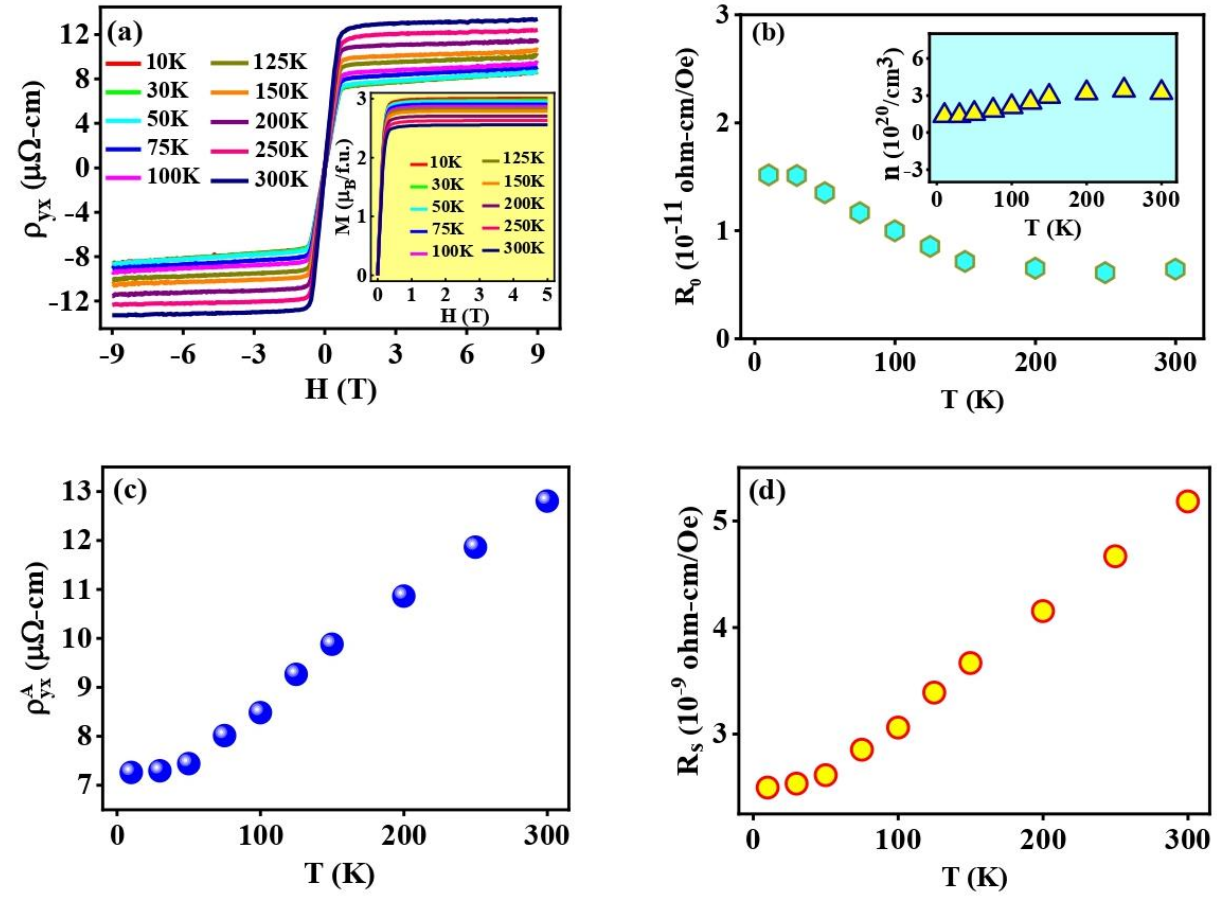

Figure 6.3: (a) Magnetic field-dependent Hall resistivity ρ_{yx} at various temperatures. The inset shows the magnetic field dependence of dc magnetization at different temperatures. (b) Temperature-dependent ordinary Hall coefficient R_0. The inset shows the calculated temperature-dependent carrier concentration n. (c) Anomalous Hall resistivity (ρ_{yx}^A) as a function of temperature. (d) Temperature dependence of anomalous Hall coefficient (R_S).

The obtained temperature-dependent ρ_{yx}^A is illustrated in Fig. 6.3(c), and it increases monotonically with increasing temperature from 10 K to 300 K. The R_S can be calculated using the equation $\rho_{yx}^A = R_S \mu_0 M_S$. We have estimated the M_S using $M(H)$ curves at H = 5 T, similar to many other ferromagnetic systems [25,49,50]. The determined R_S is shown as a function of temperature in Fig. 6.3(d), and it rises with temperature from 10 to 300 K.

To identify the mechanism responsible for the observed AHE in Co_2CrGa, we examine the scaling behavior between ρ_{yx}^{A} and ρ_{xx} over the entire temperature range on a double logarithm scale. As shown in Fig. 6.4(a), a linear fitting is employed to determine the exponent β according to the scaling relation $\rho_{yx}^{A} \propto \rho_{xx}^{\beta}$ [48].

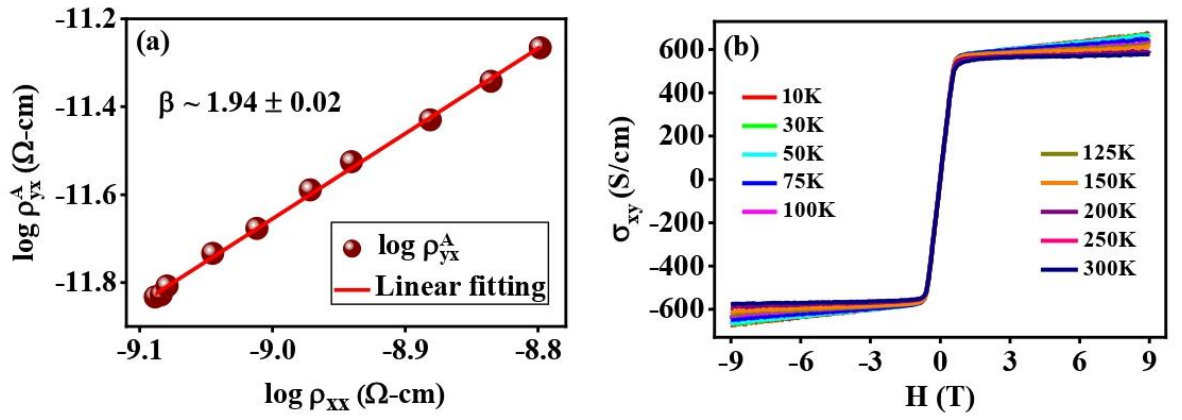

Figure 6.4: (a) Plot of log $\rho_{yx}^{A}(T)$ vs log $\rho_{xx}(T)$; the solid red line is the fit using the relation $\rho_{yx}^{A} \propto \rho_{xx}^{\beta}$. (d) Field-dependent Hall conductivity σ_{xy} at various indicated temperatures.

It is generally known that if β = 1, the origin of the AHE is due to skew scattering, and if β = 2, the origin of the AHE is due to intrinsic or side-jump mechanisms [25,27,48]. We determined the exponent β = 1.94, which indicates that intrinsic Karplus-Luttinger (KL) or extrinsic side-jump mechanisms dominate the AHE in Co_2CrGa. It has been demonstrated that the extrinsic side-jump contribution of the AHC is on the order of $\frac{e^2}{ha}(\frac{\varepsilon_{SO}}{E_F})$, where ε_{SO} is the spin-orbit interaction and E_F is the Fermi energy [51,52]. The terms e, h, and a are the electronic charge, Planck's constant, and the lattice parameter, respectively. The term $(\frac{\varepsilon_{SO}}{E_F})$, is typically in the order of 10^{-2} for most of the ferromagnetic materials [25,49,50]. Hence, compared to the intrinsic AHC, the extrinsic side-jump contribution should be very small or insignificant. Therefore, the intrinsic Berry phase-driven KL mechanism dominates the AHE in Co_2CrGa.

In order to understand the microscopic origin of the observed AHE in Co_2CrGa, we need to investigate how the AHC changes with temperature and ρ_{yx}^{A} in this compound. Hence, we calculate the Hall conductivity σ_{xy} using the tensor conversion relation [23,53].

$$\sigma_{xy} = \frac{\rho_{yx}}{(\rho_{xx}^2 + \rho_{yx}^2)} \tag{6.2}$$

The field-dependent Hall conductivity at different temperatures is shown in Fig. 6.4(b). In Fig. 6.5, the field-dependent ρ_{xx} data are presented. At a given temperature, the ρ_{xx} does not change significantly with the magnetic field.

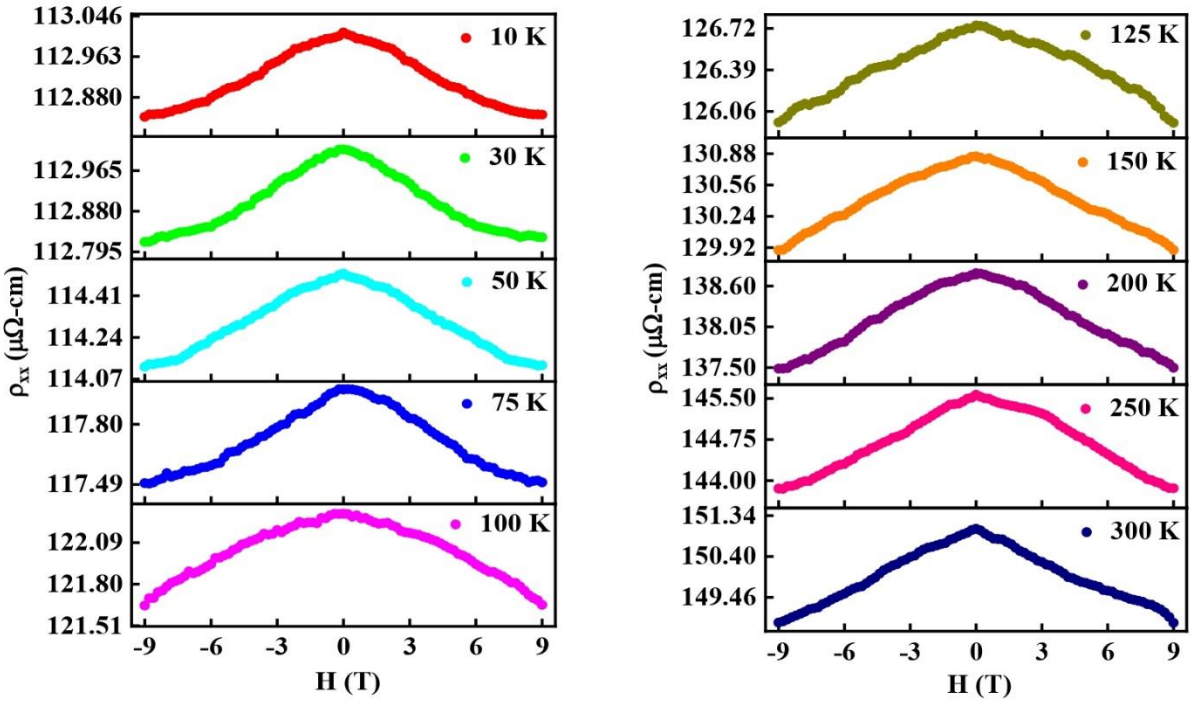

Figure 6.5: Field dependence of the longitudinal resistivity (ρ_{xx}) at indicated temperatures.

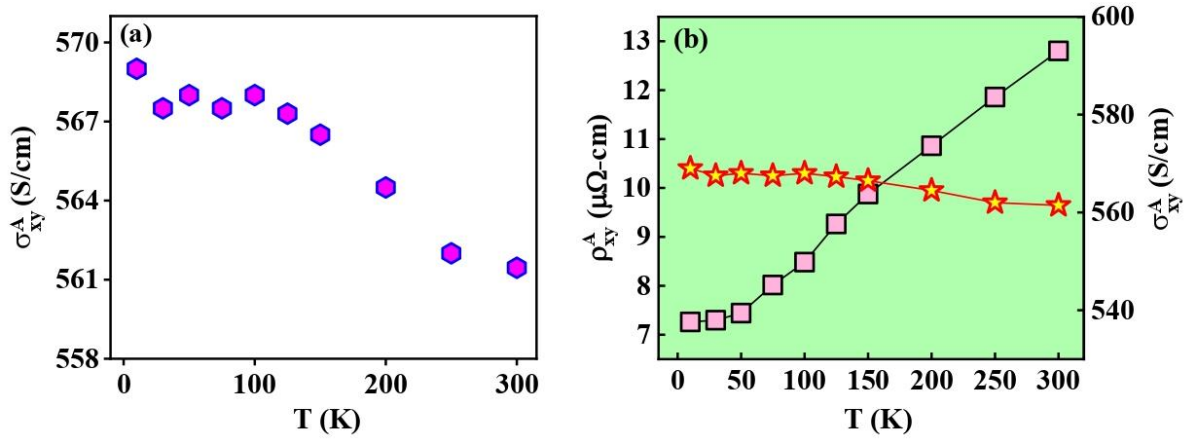

Figure 6.6: (a) Anomalous Hall conductivity (σ_{xy}^{A}) as a function of temperature for Co_2CrGa. (b) Anomalous Hall resistivity ρ_{yx}^{A} and anomalous Hall conductivity σ_{xy}^{A} as a function of temperature.

The AHC (σ_{xy}^{A}) is calculated using zero-field extrapolation of high-field Hall conductivity data on the y-axis. AHC is determined to be ~ 569 S/cm at 10 K and does not change significantly up to room temperature (~ 561 S/cm). Figure 6.6(a) depicts the temperature dependence of the AHC. In general, the AHC changes significantly towards T_C, but not much below T_C, as has been seen before in numerous Heusler compounds [25,50]. The temperature-dependent AHC and ρ_{yx}^{A} are presented in Fig. 6.6(b), and the change of AHC is almost temperature independent, showing that the genesis of AHE in Co_2CrGa is intrinsic in nature [54,55].

To differentiate the intrinsic and extrinsic components of the AHC, we plot ρ_{yx}^{A} with ρ_{xx} in Fig. 6.7 and fit it with the equation [27,56,57],

$$\rho_{yx}^{A} = a^{skew}\rho_{xx} + b^{int}\rho_{xx}^{2}, \tag{6.3}$$

where a^{skew} and b^{int} stand for the skew-scattering coefficient and intrinsic AHC, respectively. We found a^{skew} of ~ 0.005 and an intrinsic AHC b^{int} of ~ 526 S/cm. Therefore, the intrinsic Berry phase-driven mechanism is responsible for more than 92% of the total AHC. Theoretically, the intrinsic AHC under resonance conditions is of the order of $\frac{e^2}{ha}$, where e is the electronic charge, h is Planck's constant, and a is the lattice constant [52,58]. Using a = 5.796 Å for the investigated compound, we estimate the intrinsic AHC for Co_2CrGa to be around 669 S/cm, which is comparable to our experimentally obtained value of 526 S/cm.

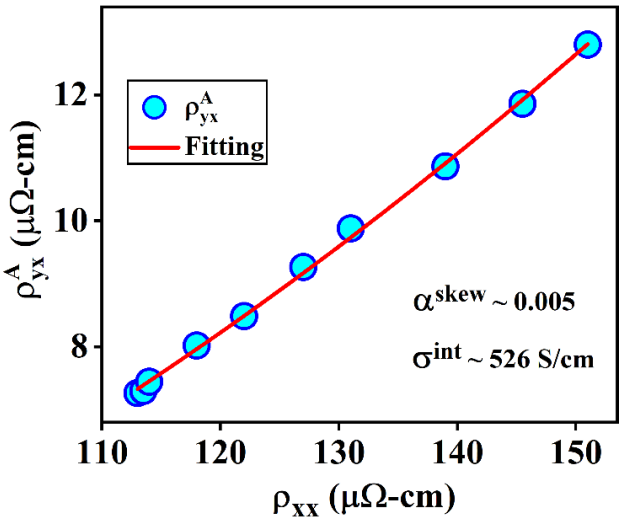

Figure 6.7: Plot of ρ_{yx}^{A} vs ρ_{xx}, and the fitted curve using equation 6.3 is shown in red.

Finally, the AHE of Co_2CrGa is compared to that of other ferromagnetic systems. Here, we focus on two characteristic factors, specifically the anomalous Hall angle Θ_{AH} and the anomalous Hall factor S_H. The Θ_{AH} can be calculated using the formula $\Theta_{AH} = \frac{\sigma_{xy}^A}{\sigma_{xx}}$, which estimates the relative contribution of the anomalous Hall current to the normal current [48]. Similarly, the S_H can be calculated using the equation $S_H = \frac{R_S \mu_0}{\rho_{xx}^2} = \frac{\sigma_{xy}^A}{M_S}$, which estimates the relative magnitude of the anomalous Hall current with respect to magnetization [59]. In light of this, these two variables help to assess the relative strength of the AHE in a compound, which is crucial for practical applications [60]. The temperature-dependent variation of Θ_{AH} is shown in Fig. 6.8(a), and the temperature-dependent variation of S_H is shown in the inset of Fig. 6.8(a).

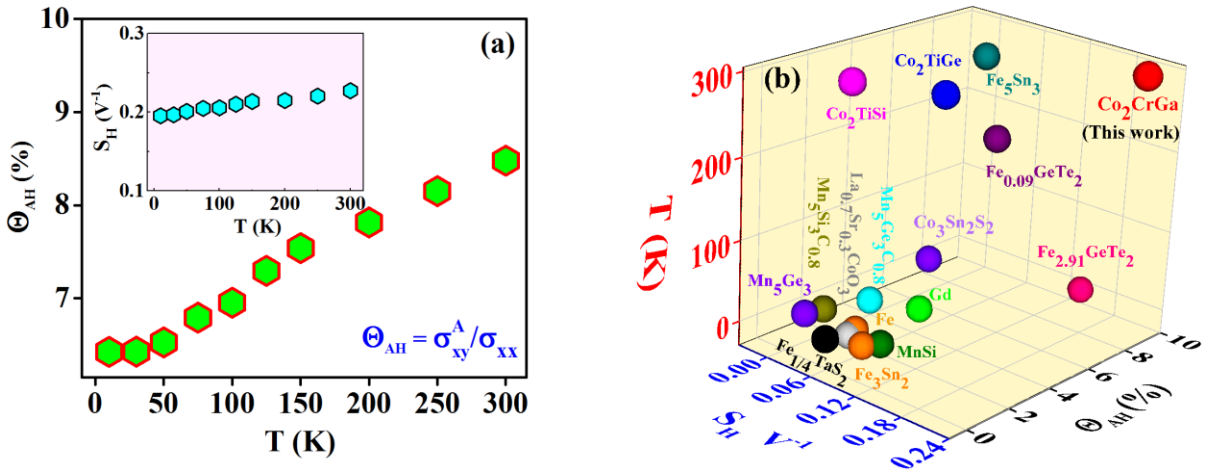

Figure 6.8: (a) Temperature-dependent anomalous Hall angle ($\Theta_{AH} = \frac{\sigma_{xy}^A}{\sigma_{xx}}$). The inset shows the temperature dependence of the anomalous Hall factor S_H. (b) Θ_{AH} and S_H for Co_2CrGa are plotted as a function of temperature along with other reported metallic ferromagnets.

The parameter S_H exhibits a very weak temperature dependence, and a similar type of temperature dependence in S_H was previously observed in other metallic ferromagnets where the intrinsic Berry phase mechanism dominates the AHE [25,50,60,61]. At room temperature, the maximum values of Θ_{AH} ~ 8.5% and S_H ~ 0.23 V^{-1} are obtained, which are among the highest among metallic ferromagnets. It is quite uncommon to find a metallic ferromagnetic system with high S_H and Θ_{AH} at ambient temperature. Even recently discovered Mn-based

antiferromagnets, or half-Heusler antiferromagnets, have either a large Θ_{AH} with a small S_H or vice versa [62,63]. We additionally compare the Θ_{AH} and S_H values in Fig. 6.8(b) with values for several ferromagnetic compounds that have been previously reported [25,49,54,59–61,64–68]. In the next subsection, we discussed the first-principles calculations for Co_2CrGa since the intrinsic AHE depends on the band structure of a material to better understand the origin of the observed large intrinsic AHE.

6.3.3 First-principles calculations

Using the first-principles method, the magnetic moments of Co_2CrGa are determined. The transition metal atoms Co and Cr contribute significantly to the magnetic moments, with values of μ_{Co} = 0.706 μ_B/f.u. and μ_{Cr} = 1.701 μ_B/f.u., respectively. Ga acts like a nonmagnetic atom, with a total magnetic moment per formula unit of 3.019 μ_B/f.u. Two Co and one Cr atom contribute 18 and 6 valance electrons, respectively, while one Ga atom contributes 3 valance electrons. Co_2CrGa is therefore anticipated to have an effective magnetic moment of about 3 μ_B/f.u. According to our calculations, this compound is a half-metallic system that obeys the SP rule and has a magnetic moment of 3.019 μ_B/f.u.

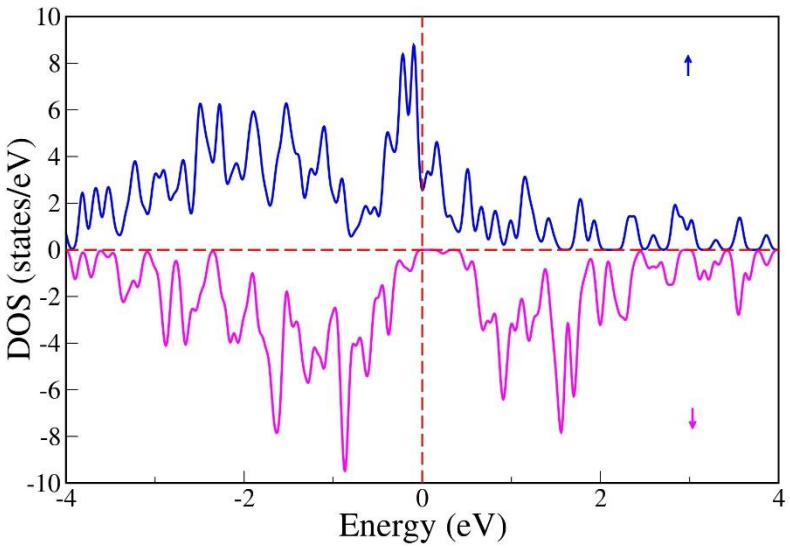

Figure 6.9: Total density of states (DOS) of Co_2CrGa. Blue and magenta curves represent the total DOS for the majority and minority spins.

The estimated magnetic moment for Co_2CrGa agrees well with the results of our experimental study. The spin-resolved density of states (DOS) is shown in Fig. 6.9, and it can be seen that while the DOS is metallic for majority spins, it is entirely gapped for minority spins. The partial density of states (PDOS) calculation shows that near the E_F DOS is mostly produced from Cr d orbitals with a majority contribution from spin electrons. To understand the topological characteristics of the compound, band dispersions are estimated in the absence and presence of SOC using a plane wave-based pseudopotential [69]. In the absence of SOC, numerous band crossings produce nodal lines, as seen in Fig. 6.10(b). In the presence of SOC, several topological nontrivial crossings exist, as indicated by the blue, green, and magenta circles in Fig. 6.10(c), and substantial BC is seen in the vicinity of these nontrivial crossings.

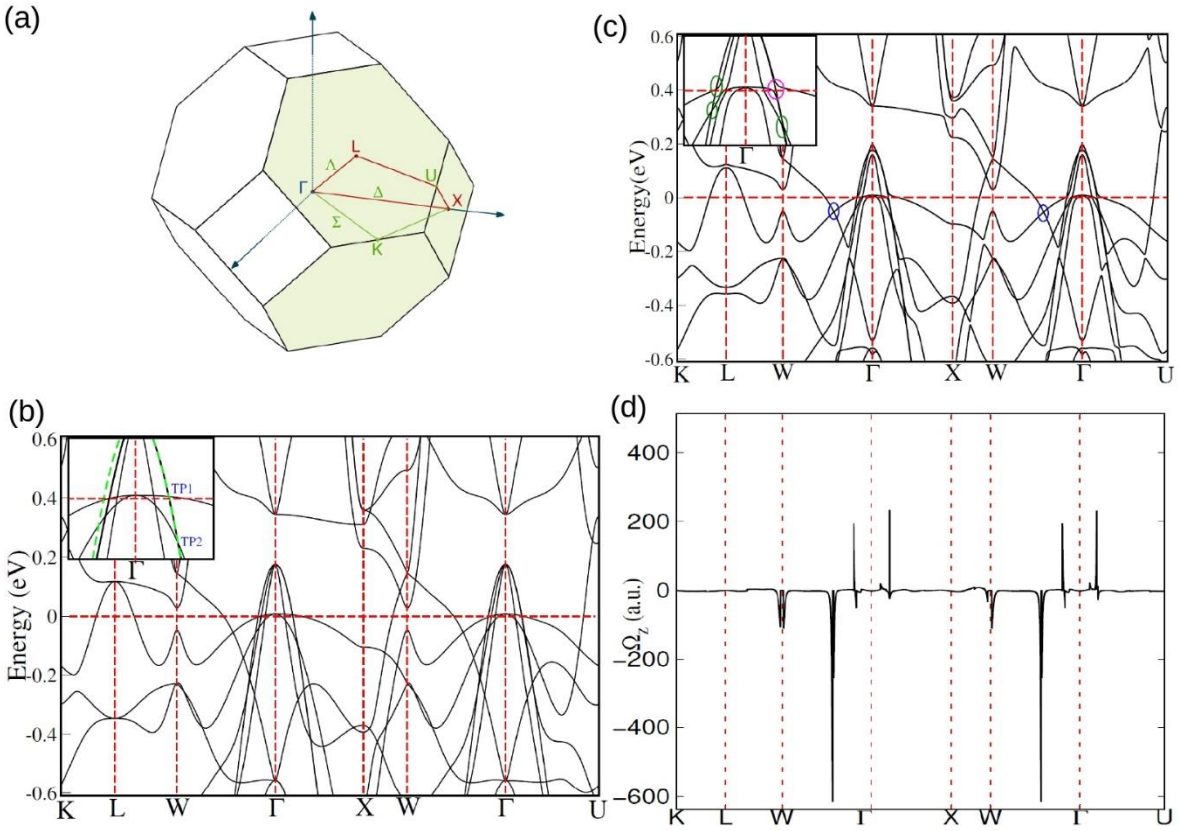

Figure 6.10: (a) Brillouin zone of Co_2CrGa. (b) The band structure of Co_2CrGa without SOC. In the inset, we also point out the triple points (TPs). (c) The band structure of Co_2CrGa with SOC. The Weyl points and the gapped nodal lines are shown by green and blue circles. (d) The Berry curvature along the high-symmetry lines due to the nontrivial crossings.

Crystal symmetries are considered to further characterize the class of these nontrivial crossing points. Co_2CrGa has the space group $Fm\bar{3}m$ (space group number 225), and the associated BZ

with a high-symmetry point is illustrated in Fig. 6.10(a). In the absence of finite magnetization, this symmetry group has three M_x (k_x = 0), M_y (k_y = 0), and M_z (k_z = 0) mirror planes in addition to three C_4 rotation axes [70]. These mirror planes in the k_x = 0, k_y = 0, and k_z = 0 planes protect the gapless nodal lines in the band structure. Only the mirror symmetry M_z = 0 and the rotational symmetry C_{4z} are preserved in the presence of SOC along the [001] direction. As a result, two nodal lines on the k_x = 0 and k_y = 0 planes are expected to gap out, while the nodal line along the k_z = 0 plane should be intact. The band dispersions around the Fermi energy in the presence of SOC are depicted in Fig. 6.10(c), and the blue circles along the Γ-W high-symmetry path denote band crossings that are gapped out. A large negative BC is detected along the high-symmetry path Γ-W in Fig. 6.10(d), corresponding to gapped nodal lines. A large Berry curvature in the k_x = 0 plane is observed because of small gaps along the nodal lines. The energy gap and corresponding BC in the k_x = 0 plane are shown in Fig. 6.11(a) and (b).

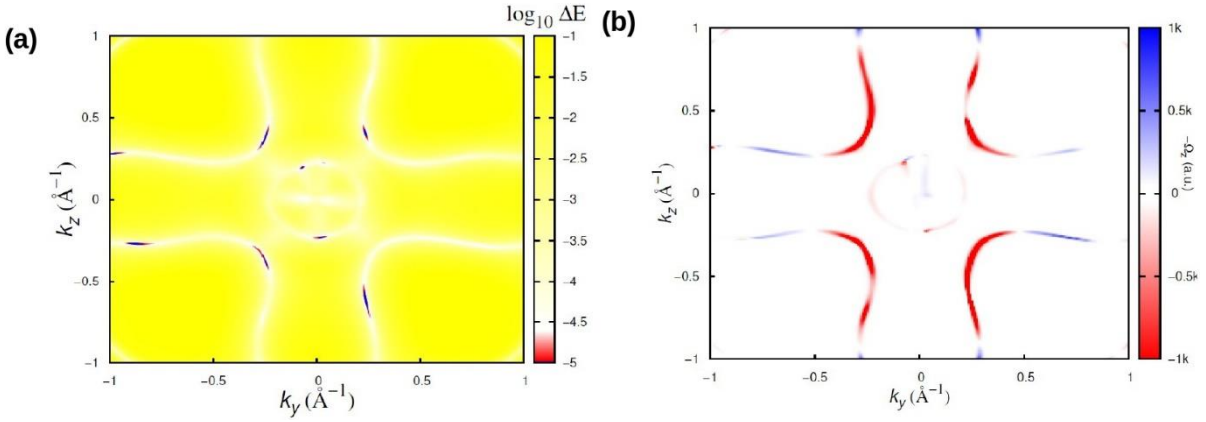

Figure 6.11: For Co_2CrGa with SOC (a) Energy gap, between two crossing bands at E = -0.045 eV and white line represents gapped out nodal line. (b) Along the gapped nodal line, the Berry curvature distribution is shown at k_x = 0 plane.

This crystal structure also features a C_{3v} point group high-symmetry axis, which possesses threefold rotational symmetry (C_3) along the [111] direction. This symmetry results in twofold degenerate bands, which are indicated by the thick, solid black and dashed green lines in the inset of Fig. 6.10(b). In the absence of SOC, the crossing point of this doubly degenerate band with a nondegenerate band yields a pair of triple points [17], denoted as TP1 and TP2 in the inset of Fig. 6.10(b). In the presence of SOC along the [001] direction, TP1 splits out as depicted in the inset of Fig. 6.10(c) inside the magenta circle and TP2 separates into a pair of

Weyl points as depicted in the inset of Fig. 6.10(c) inside the green circle at around 0.08 eV. To better comprehend the texture of these Weyl points, we calculate the normalized BCs that represent the flux at these two opposite-chirality Weyl points, and their precise position and topological charges are shown in Table 6.I. As illustrated in Fig. 6.12(a), W_1+ is a source type, where the flux is in the outward direction, whereas W_1- is a sink type, where the flux is along the inward

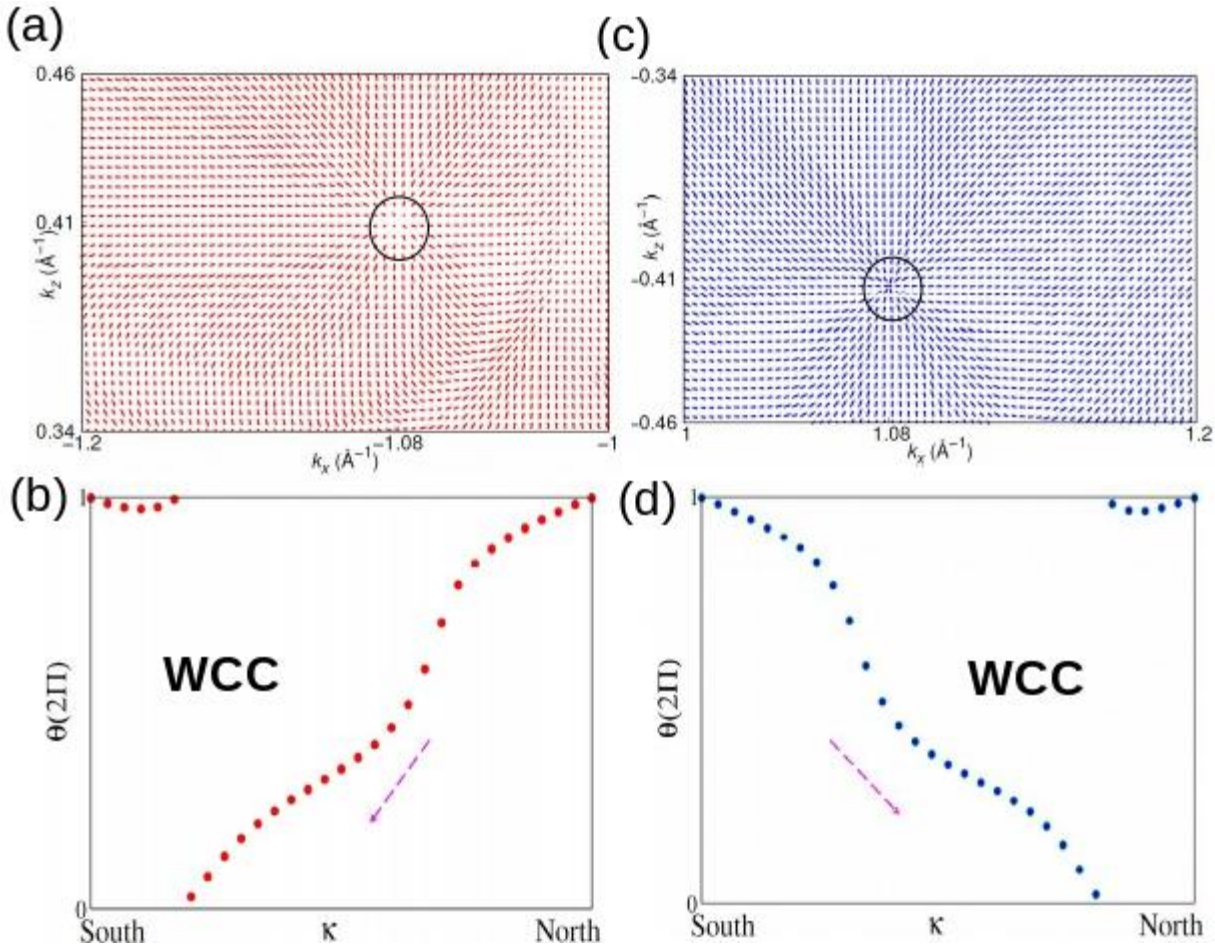

Figure 6.12: For Co_2CrGa with SOC normalized Berry curvatures are shown for Weyl point W_1. (a) Source type (W_1+), which is indicated by outward red arrows from the marked black circle. (b) Average position of the Wannier charge center (WCC) corresponding to the +1 Chern number. (c) Sink type (W_1−), which is indicated by inward blue arrows from the marked black circle. (d) Average position of the WCC corresponding to −1 Chern number.

direction in Fig. 6.12(c). Furthermore, we investigate the average position of the WCC computed using the Wilson-loop approach on a sphere enclosing these two nodes of opposite chirality. As can be seen in Fig. 6.12(b), the average WCC is observed to shift from north to

south when the Chern number of W_1 is +1, while it shifts from south to north when the Chern number of W_1 is -1 as shown in Fig. 6.12(d).

Table 6.I: The Weyl point positions, Chern numbers, and energy relative to E_F of Co_2CrGa.

Weyl points	k_x	k_y	k_z	Chern number	E - E_F (eV)
W_1	1.080	-0.0014	-0.41	-1	-0.10
W_2	-1.080	-0.0077	0.41	+1	-0.11
W_3	-0.004	1.0811	0.41	+1	-0.06
W_4	0.005	-1.0815	-0.4165	-1	-0.04
W_5	-0.0139	-0.9110	-0.0062	+1	-0.01
W_6	-0.01	0.910	-0.014	-1	-0.02

The AHC is proportional to the BC, resulting in a transverse anomalous velocity in the electronic motion and a large AHC. The intrinsic AHC can be assessed using Kubo formalism's linear response theory, and the intrinsic AHC in the xy plane can be expressed as

$$\sigma_{xy} = -\frac{e^2}{\hbar}\int \frac{d^3k}{(2\pi)^3}\ \sum_n \Omega_n^z(k) f_n(k) \tag{6.4}$$

Ω_n^z is the Berry curvature and it can be written as

$$\Omega_n^z = -2i\ \sum_{m\neq n} \frac{<\Psi_{nk}|v_x|\Psi_{mk}><\Psi_{mk}|v_y|\Psi_{nk}>}{[E_m(k) - E_n(k)]^2} \tag{6.5}$$

where $f_n(k)$ is the Fermi-Dirac distribution function, n is the index of the occupied bands, $E_n(k)$ is the eigenvalue of the n^{th} eigenstate $\Psi_n(k)$, $v_i = \frac{1}{\hbar}\frac{\partial H(k)}{\partial k_i}$ is the velocity operator along the i $(i = x, y, z)$ direction. To determine the AHC, the SOC is taken along the magnetic polarization direction [001]. As demonstrated in Fig. 6.11, nearly degenerate bands along the nodal line in the k_x = 0, k_y = 0 planes have large BC and contribute to the intrinsic AHC. The energy dependency of the AHC is shown in Fig. 6.13. The giant value (~ 1000 S/cm) of the AHC near the gapped nodal line (~ 0.05 eV below the E_F) is shown inside the red circle in Fig. 6.13. This AHC value is supposed to be large due to the maximum BC value at that point, as described above, but at E_F, the AHC value reduces to ~ 504 S/cm due to the positive BC near

the Weyl point crossing. The experimentally found intrinsic AHC value is comparable to the theoretically calculated intrinsic AHC value for this ferromagnetic full Heusler compound.

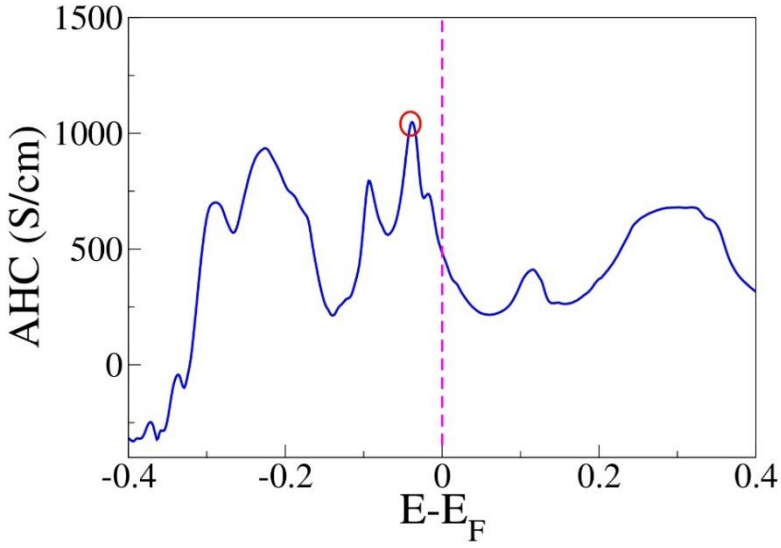

Figure 6.13: Energy ($E - E_F$) dependence of the AHC for Co_2CrGa, where the red circle is the position of the gapped nodal line (at an energy of −0.05 eV).

6.4 Conclusion

In summary, we explored the AHE in the ferromagnetic full Heusler compound Co_2CrGa both experimentally and theoretically. ρ_{yx}^{A} scales quadratically with ρ_{xx}, and our extensive experimental analysis revealed that the observed AHE is generated by the intrinsic Berry curvature-driven KL mechanism. At 10 K, an AHC σ_{xy}^{A} ~ 569 S/cm with an intrinsic contribution of ~ 526 S/cm is seen experimentally. The observed AHC is almost temperature-independent up to room temperature. Moreover, at room temperature, an exceptionally large AHA of ~ 8.5 % and a large AHF of ~ 0.23 V^{-1} is observed, which is rarely present in metallic ferromagnets. First-principles calculations revealed that the AHC in Co_2CrGa is ~ 504 S/cm, which is compatible with the experimentally obtained intrinsic AHC value. Theoretical calculations revealed that the BC contributes most significantly to the AHC and has a substantial value close to the gapped nodal line. In the absence of SOC, we detected the

topologically protected TP fermion in its band structure, and in the presence of SOC, we demonstrated the formation of Weyl points from this TP. Furthermore, the impact of these nontrivial crossings on anomalous transport features was discussed. In addition, we noted that hole doping causes the E_F to shift to 0.05 eV, which results in the system's AHC value reaching its maximum (~1000 S/cm). Consequently, future material engineering of this molecule would give a feasible pathway to tune its multiple fascinating topological features both theoretically and experimentally.

References:

[1] X. Wan, A. M. Turner, A. Vishwanath, and S. Y. Savrasov, Phys. Rev. B **83**, 205101 (2011).

[2] G. Xu, H. Weng, Z. Wang, X. Dai, and Z. Fang, Phys. Rev. Lett. **107**, 186806 (2011).

[3] N. P. Armitage, E. J. Mele, and A. Vishwanath, Rev. Mod. Phys. **90**, 015001 (2018).

[4] B. Q. Lv, T. Qian, and H. Ding, Rev. Mod. Phys. **93**, 025002 (2021).

[5] S. M. Huang, S. Y. Xu, I. Belopolski, C. C. Lee, G. Chang, B. Wang, N. Alidoust, G. Bian, M. Neupane, C. Zhang, S. Jia, A. Bansil, H. Lin, and M. Z. Hasan, Nat. Commun. **6**, 7373 (2015).

[6] Z. Wang, Y. Sun, X.-Q. Chen, C. Franchini, G. Xu, H. Weng, X. Dai, and Z. Fang, Phys. Rev. B **85**, 195320 (2012).

[7] S. M. Young, S. Zaheer, J. C. Y. Teo, C. L. Kane, E. J. Mele, and A. M. Rappe, Phys. Rev. Lett. **108**, 140405 (2012).

[8] H. Weng, C. Fang, Z. Fang, and X. Dai, Phys. Rev. B **93**, 241202(R) (2016).

[9] B. Bradlyn, J. Cano, Z. Wang, M. G. Vergniory, C. Felser, R. J. Cava, and B. A. Bernevig, Science **353**, aaf5037 (2016).

[10] J. Hu, Z. Tang, J. Liu, X. Liu, Y. Zhu, D. Graf, K. Myhro, S. Tran, C. N. Lau, J. Wei, and Z. Mao, Phys. Rev. Lett. **117**, 016602 (2016).

[11] T. Bzdušek, Q. S. Wu, A. Rüegg, M. Sigrist, and A. A. Soluyanov, Nature **538**, 75 (2016).

[12] Q.-F. Liang, J. Zhou, R. Yu, Z. Wang, and H. Weng, Phys. Rev. B **93**, 085427 (2016).

[13] Z. Wang, H. Weng, Q. Wu, X. Dai, and Z. Fang, Phys. Rev. B - Condens. Matter Mater. Phys. **88**, 125427 (2013).

[14] H. Weng, C. Fang, Z. Fang, B. A. Bernevig, and X. Dai, Phys. Rev. X **5**, 011029 (2015).

[15] C. Fang, Y. Chen, H.-Y. Kee, and L. Fu, Phys. Rev. B **92**, 081201 (2015).

[16] Z. Yan, R. Bi, H. Shen, L. Lu, S.-C. Zhang, and Z. Wang, Phys. Rev. B **96**, 041103(R) (2017).

[17] Z. Zhu, G. W. Winkler, Q. Wu, J. Li, and A. A. Soluyanov, Phys. Rev. X **6**, 031003 (2016).

[18] B. Q. Lv, Z. L. Feng, Q. N. Xu, X. Gao, J. Z. Ma, L. Y. Kong, P. Richard, Y. B. Huang, V. N. Strocov, C. Fang, H. M. Weng, Y. G. Shi, T. Qian, and H. Ding, Nature **546**, 627 (2017).

[19] J. Kübler, G. H. Fecher, and C. Felser, Phys. Rev. B **76**, 024414 (2007).

[20] T. Graf, C. Felser, and S. S. P. Parkin, Prog. Solid State Chem. **39**, 1 (2011).

[21] Z. Wang, M. G. Vergniory, S. Kushwaha, M. Hirschberger, E. V. Chulkov, A. Ernst, N. P. Ong, R. J. Cava, and B. A. Bernevig, Phys. Rev. Lett. **117**, 236401 (2016).

[22] A. Husmann and L. J. Singh, Phys. Rev. B **73**, 172417 (2006).

[23] K. Manna, L. Muechler, T.-H. Kao, R. Stinshoff, Y. Zhang, J. Gooth, N. Kumar, G. Kreiner, K. Koepernik, R. Car, J. Kübler, G. H. Fecher, C. Shekhar, Y. Sun, and C. Felser, Phys. Rev. X **8**, 041045 (2018).

[24] B. Ernst, R. Sahoo, Y. Sun, J. Nayak, L. Müchler, A. K. Nayak, N. Kumar, J. Gayles, A. Markou, G. H. Fecher, and C. Felser, Phys. Rev. B **100**, 054445 (2019).

[25] S. Roy, R. Singha, A. Ghosh, A. Pariari, and P. Mandal, Phys. Rev. B **102**, 085147 (2020).

[26] P. Li, J. Koo, W. Ning, J. Li, L. Miao, L. Min, Y. Zhu, Y. Wang, N. Alem, C.-X. Liu, Z. Mao, and B. Yan, Nat. Commun. **11**, 3476 (2020).

[27] G. K. Shukla, J. Sau, N. Shahi, A. K. Singh, M. Kumar, and S. Singh, Phys. Rev. B **104**, 195108 (2021).

[28] J. Hu, B. Ernst, S. Tu, M. Kuveždić, A. Hamzić, E. Tafra, M. Basletić, Y. Zhang, A. Markou, C. Felser, A. Fert, W. Zhao, J.-P. Ansermet, and H. Yu, Phys. Rev. Appl. **10**, 044037 (2018).

[29] A. Sakai, Y. P. Mizuta, A. A. Nugroho, R. Sihombing, T. Koretsune, M. T. Suzuki, N. Takemori, R. Ishii, D. Nishio-Hamane, R. Arita, P. Goswami, and S. Nakatsuji, Nat. Phys. **14**, 1119 (2018).

[30] K. Manna, Y. Sun, L. Muechler, J. Kübler, and C. Felser, Nat. Rev. Mater. **3**, 244 (2018).

[31] R. Karplus and J. M. Luttinger, Phys. Rev. **95**, 1154 (1954).

[32] T. Jungwirth, Q. Niu, and A. H. MacDonald, Phys. Rev. Lett. **88**, 207208 (2002).

[33] N. Nagaosa, J. Phys. Soc. Japan **75**, 042001 (2006).

[34] J. Smit, Physica **21**, 877 (1955).

[35] J. Smit, Physica **24**, 39 (1958).

[36] L. Berger, Phys. Rev. B **2**, 4559 (1970).

[37] J. Hafner, J. Comput. Chem. **29**, 2044 (2008).

[38] J. P. Perdew and Y. Wang, Phys. Rev. B **98**, 244 (2018).

[39] J. P. Perdew, K. Burke, and M. Ernzerhof, Phys. Rev. Lett. **77**, 3865 (1996).

[40] G. Pizzi, V. Vitale, R. Arita, S. Blügel, F. Freimuth, G. Géranton, M. Gibertini, D. Gresch, C. Johnson, T. Koretsune, J. Ibañez-Azpiroz, H. Lee, J.-M. Lihm, D. Marchand, A. Marrazzo, Y. Mokrousov, J. I. Mustafa, Y. Nohara, Y. Nomura, L. Paulatto, S. Poncé, T. Ponweiser, J. Qiao, F. Thöle, S. S. Tsirkin, M. Wierzbowska, N. Marzari, D. Vanderbilt, I. Souza, A. A. Mostofi, and J. R. Yates, J. Phys. Condens. Matter **32**, 165902 (2020).

[41] N. Marzari and D. Vanderbilt, Phys. Rev. B **56**, 12847 (1997).

[42] Q. Wu, S. Zhang, H.-F. Song, M. Troyer, and A. A. Soluyanov, Comput. Phys. Commun. **224**, 405 (2018).

[43] R. Y. Umetsu, K. Kobayashi, A. Fujita, K. Oikawa, R. Kainuma, K. Ishida, N. Endo, K. Fukamichi, and A. Sakuma, Phys. Rev. B **72**, 214412 (2005).

[44] Y. V. Kudryavtsev, N. V. Uvarov, V. N. Iermolenko, and J. Dubowik, J. Appl. Phys. **108**, (2010).

[45] I. Galanakis, P. H. Dederichs, and N. Papanikolaou, Phys. Rev. B **66**, 174429 (2002).

[46] A. Markou, D. Kriegner, J. Gayles, L. Zhang, Y. C. Chen, B. Ernst, Y. H. Lai, W. Schnelle, Y. H. Chu, Y. Sun, and C. Felser, Phys. Rev. B **100**, 54422 (2019).

[47] L. Bainsla, K. G. Suresh, A. K. Nigam, M. Manivel Raja, B. S. D. C. S. Varaprasad, Y. K. Takahashi, and K. Hono, J. Appl. Phys. **116**, 203902 (2014).

[48] N. Nagaosa, J. Sinova, S. Onoda, A. H. MacDonald, and N. P. Ong, Rev. Mod. Phys. **82**, 1539 (2010).

[49] Q. Wang, S. Sun, X. Zhang, F. Pang, and H. Lei, Phys. Rev. B **94**, 075135 (2016).

[50] S. Chatterjee, J. Sau, S. Ghosh, S. Samanta, B. Ghosh, M. Kumar, and K. Mandal, J. Phys. Condens. Matter **35**, 035601 (2023).

[51] P. Nozières and C. Lewiner, J. Phys. **34**, 901 (1973).

[52] S. Onoda, N. Sugimoto, and N. Nagaosa, Phys. Rev. Lett. **97**, 126602 (2006).

[53] S. N. Guin, K. Manna, J. Noky, S. J. Watzman, C. Fu, N. Kumar, W. Schnelle, C. Shekhar, Y. Sun, J. Gooth, and C. Felser, NPG Asia Mater. **11**, 16 (2019).

[54] Q. Wang, Y. Xu, R. Lou, Z. Liu, M. Li, Y. Huang, D. Shen, H. Weng, S. Wang, and H. Lei, Nat. Commun. **9**, 3681 (2018).

[55] D. F. Liu, A. J. Liang, E. K. Liu, Q. N. Xu, Y. W. Li, C. Chen, D. Pei, W. J. Shi, S. K. Mo, P. Dudin, T. Kim, C. Cacho, G. Li, Y. Sun, L. X. Yang, Z. K. Liu, S. S. P. Parkin, C. Felser, and Y. L. Chen, Science **365**, 1282 (2019).

[56] S. Singh, J. Noky, S. Bhattacharya, P. Vir, Y. Sun, N. Kumar, C. Felser, and C. Shekhar, Adv. Mater. **33**, 2104126 (2021).

[57] G. K. Shukla, A. K. Jena, N. Shahi, K. K. Dubey, I. Rajput, S. Baral, K. Yadav, K. Mukherjee, A. Lakhani, K. Carva, S. C. Lee, S. Bhattacharjee, and S. Singh, Phys. Rev. B **105**, 035124 (2022).

[58] T. Miyasato, N. Abe, T. Fujii, A. Asamitsu, S. Onoda, Y. Onose, N. Nagaosa, and Y. Tokura, Phys. Rev. Lett. **99**, 086602 (2007).

[59] M. Lee, Y. Onose, Y. Tokura, and N. P. Ong, Phys. Rev. B - Condens. Matter Mater. Phys. **75**, 172403 (2007).

[60] K. Kim, J. Seo, E. Lee, K. T. Ko, B. S. Kim, B. G. Jang, J. M. Ok, J. Lee, Y. J. Jo, W. Kang, J. H. Shim, C. Kim, H. W. Yeom, B. Il Min, B. J. Yang, and J. S. Kim, Nat. Mater. **17**, 794 (2018).

[61] H. Li, B. Zhang, J. Liang, B. Ding, J. Chen, J. Shen, Z. Li, E. Liu, X. Xi, G. Wu, Y. Yao, H. Yang, and W. Wang, Phys. Rev. B **101**, 140409 (2020).

[62] S. Nakatsuji, N. Kiyohara, and T. Higo, Nature **527**, 212 (2015).

[63] T. Suzuki, R. Chisnell, A. Devarakonda, Y.-T. Liu, W. Feng, D. Xiao, J. W. Lynn, and J. G. Checkelsky, Nat. Phys. **12**, 1119 (2016).

[64] C. Sürgers, G. Fischer, P. Winkel, and H. V. Löhneysen, Phys. Rev. B - Condens. Matter Mater. Phys. **90**, 104421 (2014).

[65] S. A. Baily and M. B. Salamon, Phys. Rev. B **71**, 104407 (2005).

[66] Y. Onose and Y. Tokura, Phys. Rev. B - Condens. Matter Mater. Phys. **73**, 174421 (2006).

[67] J. G. Checkelsky, M. Lee, E. Morosan, R. J. Cava, and N. P. Ong, Phys. Rev. B - Condens. Matter Mater. Phys. **77**, 014433 (2008).

[68] S. Sangiao, L. Morellon, G. Simon, J. M. De Teresa, J. A. Pardo, J. Arbiol, and M. R. Ibarra, Phys. Rev. B - Condens. Matter Mater. Phys. **79**, 014431 (2009).

[69] P. E. Blöchl, Phys. Rev. B **50**, 17953 (1994).

[70] G. Chang, S.-Y. Xu, H. Zheng, B. Singh, C.-H. Hsu, G. Bian, N. Alidoust, I. Belopolski, D. S. Sanchez, S. Zhang, H. Lin, and M. Z. Hasan, Sci. Rep. **6**, 38839 (2016).

Chapter 7 Conclusion and scope for future work

In this chapter, we provide a summary of all the findings from previous chapters and draw a conclusion. We also point out a few areas where future work can be done.

7 Conclusion and scope for future work

7.1 Summary

This thesis work primarily focused on two physical phenomena, namely the metal-insulator transition (MIT) and the anomalous Hall effect (AHE) in various 3d-transition metal-based compounds. The main observations of this thesis are listed below.

I. The results obtained in *Chapter* 3 for $NdNiO_3$ films grown on crystalline $SrTiO_3$ substrates with different crystallographic orientations reveal the emergence of large thermal noise $\left(\zeta(T) \equiv \frac{S_{th}(T)}{4k_BTR}\right)$ close to the temperature-driven MIT. The ratio ζ reaches a maximum value of ζ_M at a temperature T^* that is close but distinct from the MIT temperature T_{MI}. It has been observed that the ratio $\frac{T^*}{T_{MI}}$ and ζ_M are highly dependent on the in-plane strain of the films. The enhanced thermal noise and large correlated flicker noise both arise from slow kinetics of relaxation, as determined by the temperature dependence of the correlation time (τ), which grows much larger in the temperature range around T^*, reaching a maximum at $T = T^*$. It has been proposed that the presence of significantly large noise (both thermal and flicker noise) is due to the existence of electronic phase separation (EPS) near the MIT. A physical model has also suggested that EPS near the MIT temperature can give rise to a sparse phase of nanometric small pockets of metallic phases (nanopuddles) that are surrounded by and embedded within the minority insulating phase. Such isolated metallic nanopuddles can be Coulomb-charged if the charging energy $E_C \geq k_BT$ and have slow relaxation of fluctuations acting as a source of large noise.

II. The results obtained in *Chapter* 4 show that an introduction of disorder using 1 MeV argon (Ar) ion irradiation, suppresses the correlation-driven MIT in $NdNiO_3$ films. The films make a crossover to a heavily disordered conductor governed by weak localization (WL) and at even higher disorder, an Anderson

localized state. The pristine films of $NdNiO_3$ exhibit an MIT with the conduction process being governed by variable range hopping. For disorders up to 1%, the insulating state arising from a gap in the density of states (DOS) at the Fermi level (E_F) as in a Mott insulator is suppressed and the conduction in the film shows a WL behavior with finite conductivity at temperature $T \rightarrow 0$. This behavior is expected in a disordered conductor that does not have a gap in DOS at E_F. At higher fluences, the conductivity reduces substantially but the electrical conduction shows a power-law temperature dependence with a small but finite zero temperature conductivity σ $(T = 0)$ which is expected in a solid with electrons that are Anderson localized. A similar experiment was performed on La substituted $NdNiO_3$ films ($Nd_{1-x}La_xNiO_3$) with x = 0.3 that are grown in the same way. Evidence of suppression of correlated behavior can also be seen in the irradiated films where the non-Gaussian nature of resistance fluctuation at $T \sim T_{MI}$, a signature of correlated electron systems, is suppressed on irradiation leading to a collapse of the MIT.

III. In *Chapter* 5, we report a comprehensive study of the topology-induced AHE in the half-metallic ferromagnetic full Heusler compound Co_2VAl. The anomalous Hall resistivity ρ_{xy}^A is observed to scale quadratically with the longitudinal resistivity ρ_{xx}. Our experimental results also reveal that the anomalous Hall conductivity (AHC) is ~ 85 S/cm at 2 K with an intrinsic contribution of ~ 75.6 S/cm, and is nearly insensitive to temperature. The first principle calculations note that the Berry curvature originated from a gapped nodal line and symmetry-protected Weyl nodes in the presence of spin-orbit coupling near the E_F is the main source of AHE in this compound. The theoretically calculated AHC is in good agreement with the experimentally obtained AHC.

IV. In *Chapter* 6, we present a systematic investigation of the AHE in the Co_2-based ferromagnetic full Heusler compound Co_2CrGa using combined experimental and theoretical studies. The anomalous Hall resistivity ρ_{yx}^A is observed to scale nearly quadratically with the longitudinal resistivity ρ_{xx}, and further experimental analysis suggests that the AHE in Co_2CrGa should be dominated

by the intrinsic Karplus-Luttinger Berry phase mechanism. Experimental results also reveal that AHC is as large as ~569 S/cm at 10 K with an intrinsic contribution of ~526 S/cm and the observed AHC is nearly temperature-independent. In addition to the large AHC, we also found an exceptionally large anomalous Hall angle of ~8.5% and a large anomalous Hall factor of ~0.23 V^{-1} simultaneously at room temperature. First-principles calculations suggest that the Berry curvature originates from a gapped nodal line and that Weyl nodes which are generated from the triple point near the E_F in the presence of spin-orbit coupling are responsible for the observed large AHC in this compound.

7.2 Future directions

- It is interesting to study the effect of disorder on the thermal noise as well as the flicker noise close to MIT.
- It is also very intriguing to understand the disorder-induced crossover of the Mott insulator to weak Anderson localized regime through scanning tunneling microscope (STM) measurements.
- The effect of disorder in the Berry curvature as well as in the AHE of Co_2-based full Heusler compounds. It is also very interesting to study the effect of disorder on the half-metallicity of these compounds.
- More experimental and theoretical studies are needed to understand the effect of triple point fermion in transport and magneto-transport properties in Co_2-based ferromagnetic Heusler compounds.

Appendix A: X-ray diffraction data of nickelates nanopowder and rocking curves of nickelates thin films

Here, we present the X-ray diffraction (XRD) data of the rare-earth nickelates nanopowder. Figure A.1 represents the room temperature Rietveld profile refinement of the XRD patterns for $NdNiO_3$ and $Nd_{0.7}La_{0.3}NiO_3$ nanopowder, respectively. It shows that the structure follows the Pbnm symmetry at room temperature.

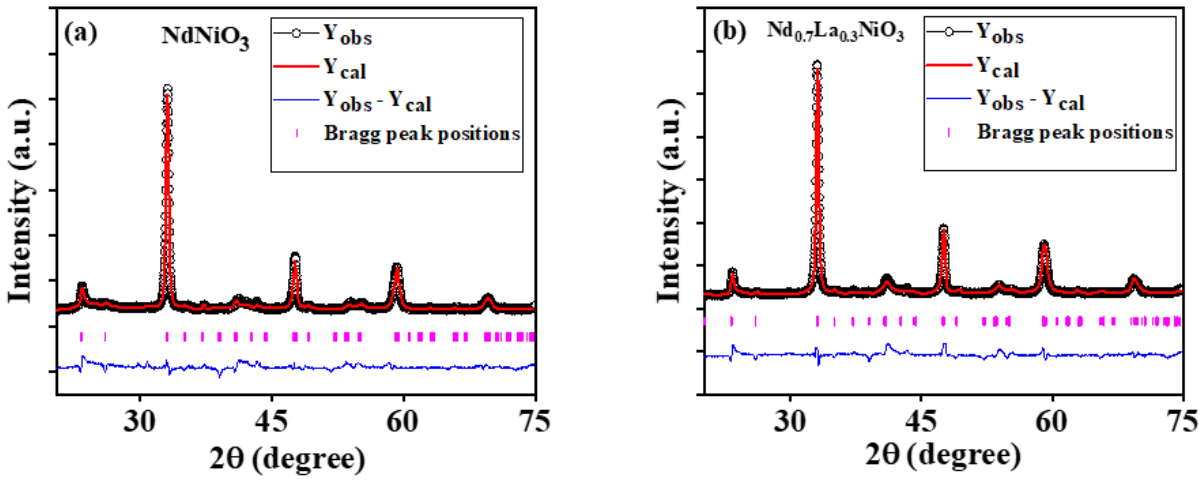

Figure A.1: Rietveld refinement of the XRD pattern for (a) $NdNiO_3$ and (b) $Nd_{0.7}La_{0.3}NiO_3$ at room temperature. The black circles represent the experimental data, and the solid red line depicts the calculated result. The vertical magenta lines show the Bragg peak positions and the blue line at the bottom corresponds to the difference between experimental and calculated data.

In Table A.I, we summarize the lattice parameters of the $NdNiO_3$ and $Nd_{0.7}La_{0.3}NiO_3$ nanopowder after Rietveld refinement. The obtained lattice parameters match well with the earlier reports [1]

Table A.I: The obtained lattice parameters from Rietveld refinement

Lattice parameters (Å)	$NdNiO_3$	$Nd_{0.7}La_{0.3}NiO_3$
a	5.417	5.453
b	5.365	5.377
c	7.621	7.611

Figure A.2(a)-(c) represents the rocking curves obtained from high-resolution XRD (Reciprocal space mapping) measurements of all three $NdNiO_3$ (NNO) films grown on $SrTiO_3$ substrates with different orientations. The full width at half-maximum is given below in Table A.II of all three films. It suggests that there is progressive disordering in the films of NNO grown on STO with different orientations in the order (100) → (110) → (111).

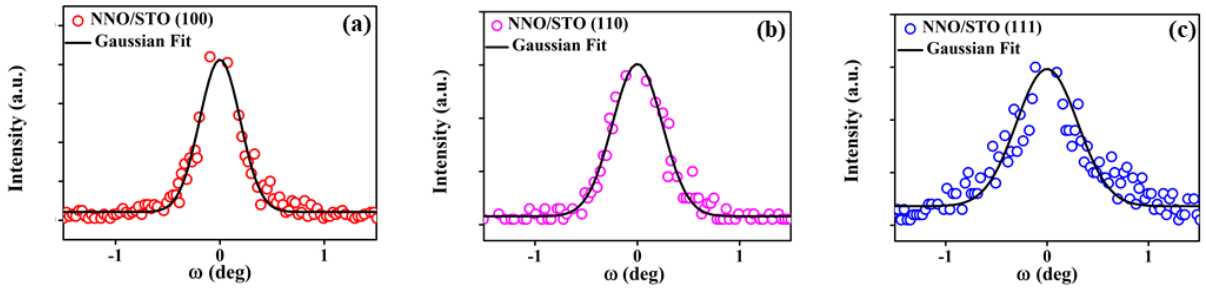

Figure A.2: (a)-(c) Rocking curves obtained from high-resolution XRD data for $NdNiO_3$ (NNO) films grown on $SrTiO_3$ (STO) substrates with different orientations. The fit to the data is a Gaussian from which the full width at half-maximum $\delta\omega$ given in Table 3.I (*Chapter 3*) have been obtained.

Table A.II: The full width at half-maximum $\delta\omega$ of all the NNO films grown on STO substrate with different orientations.

Sample	$\delta\omega$ (°)
NNO/STO (100)	0.373
NNO/STO (110)	0.489
NNO/STO (111)	0.607

References:

[1] G. Catalan, Phase Transitions **81**, 729 (2008)

Appendix B: Scanning electron microscope and energy dispersive X-ray spectroscopy data for nickelates nanopowder and Co_2-based Heusler alloys

Figure B.1(a)-(b) represents the scanning electron microscope (SEM) image of $NdNiO_3$ and $Nd_{0.7}La_{0.3}NiO_3$ nanopowder, respectively. Figures B.1(c)-(d) show the SEM image of bulk polycrystalline Co_2VAl and Co_2CrGa respectively.

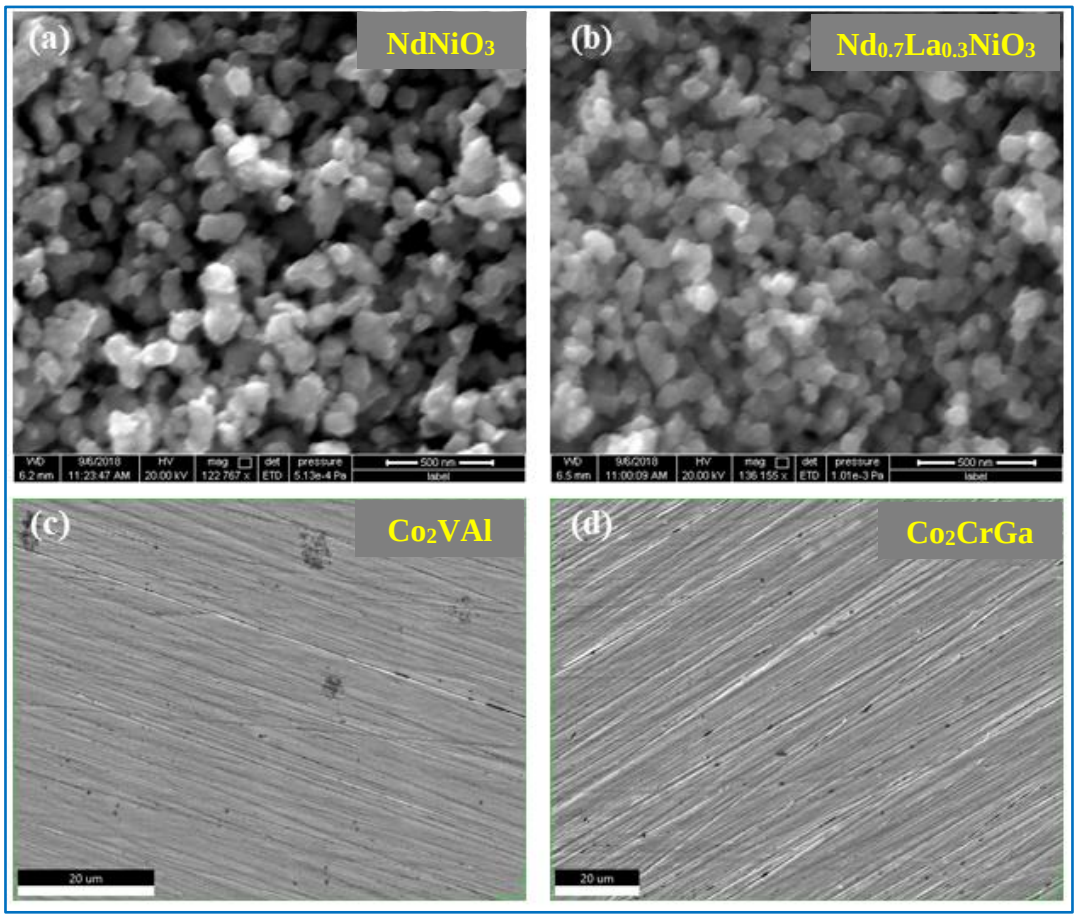

Figure B.1: SEM image of (a) $NdNiO_3$ and (b) $Nd_{0.7}La_{0.3}NiO_3$ nanopowder at room temperature. SEM image of bulk polycrystalline (c) Co_2VAl and (d) Co_2CrGa.

In Figs. B.2(a) and (b) we show the energy dispersive analysis of X-ray (EDAX) spectra for the $NdNiO_3$ and $Nd_{0.7}La_{0.3}NiO_3$ nanopowder, respectively. Figure B.3(a) and (b) represent the EDAX spectra for the bulk polycrystalline Co_2VAl and Co_2CrGa, respectively. The corresponding atomic percentage is also given in the table for each of the compounds. The atomic percentage shows that the samples are highly stoichiometric.

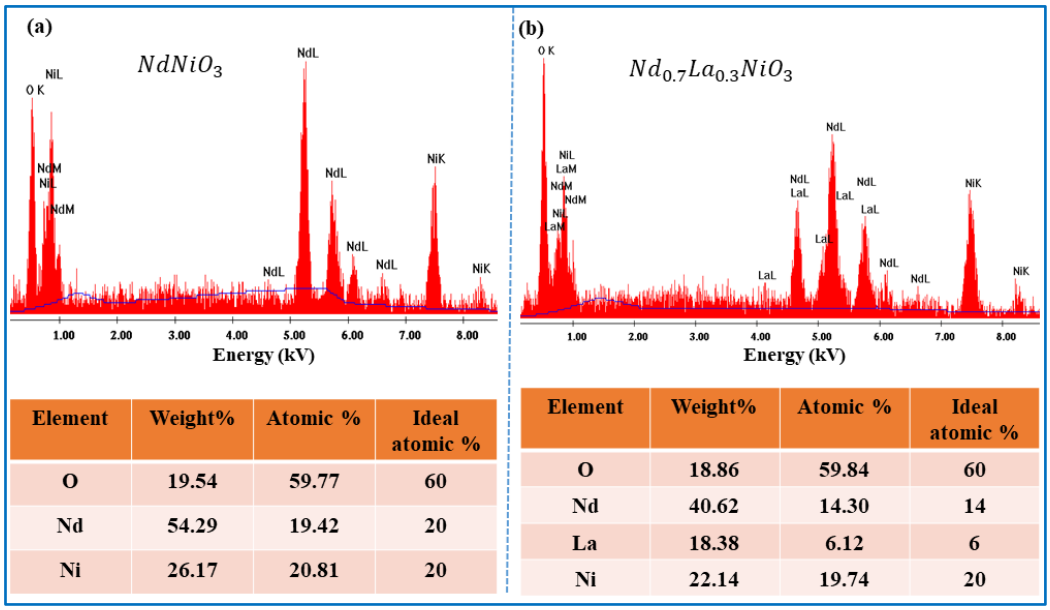

Element	Weight%	Atomic %	Ideal atomic %
O	19.54	59.77	60
Nd	54.29	19.42	20
Ni	26.17	20.81	20

Element	Weight%	Atomic %	Ideal atomic %
O	18.86	59.84	60
Nd	40.62	14.30	14
La	18.38	6.12	6
Ni	22.14	19.74	20

Figure B.2: EDAX spectra for the as-prepared (a) $NdNiO_3$ and (b) $Nd_{0.7}La_{0.3}NiO_3$ nanopowder, respectively.

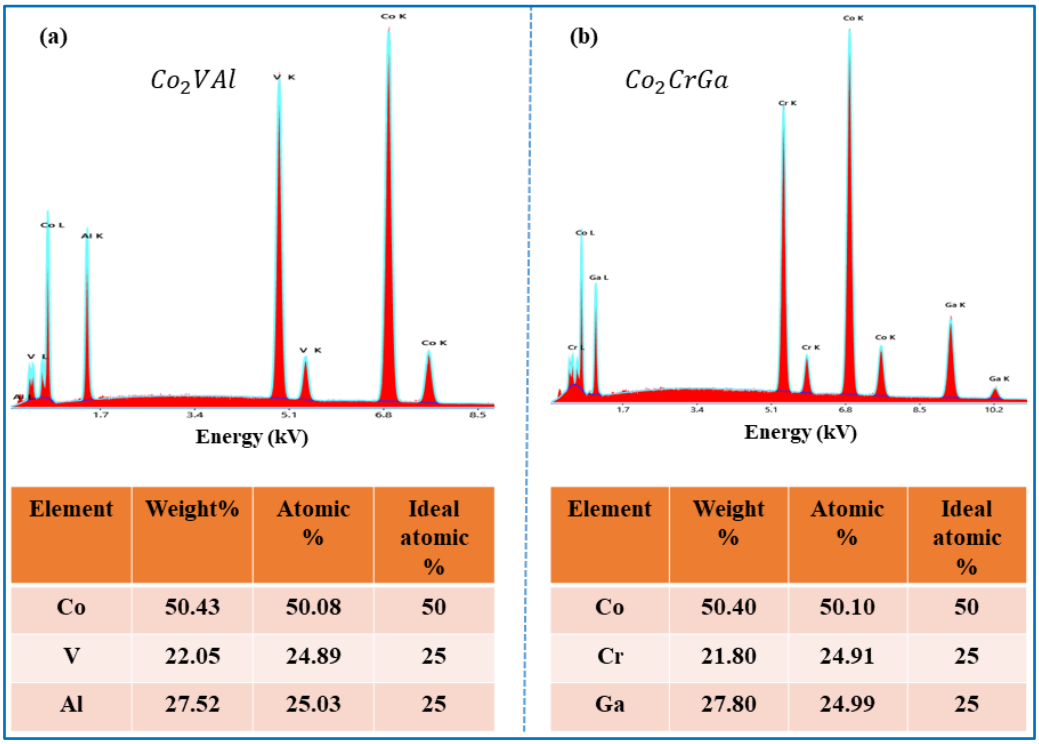

Element	Weight%	Atomic %	Ideal atomic %
Co	50.43	50.08	50
V	22.05	24.89	25
Al	27.52	25.03	25

Element	Weight %	Atomic %	Ideal atomic %
Co	50.40	50.10	50
Cr	21.80	24.91	25
Ga	27.80	24.99	25

Figure B.3: EDAX spectra for bulk polycrystalline (a) Co_2VAl and (b) Co_2CrGa compounds, respectively